University of Turin, Department of Earth Science
Thesis in co-tutele with University of São Paulo, Geoscience Institute

PhD program in Earth Science

CYCLE XXXIV

KINEMATICS AND P-T-t EVOLUTION IN HOT COLLISIONAL FRAMEWORKS – A COMPARISON BETWEEN A NEOPROTEROZOIC AND A PHANEROZOIC LARGE HOT OROGENS

By

Beatriz Yuri Benetti Silva

Supervisor: Rodolfo Carosi
Co-supervisors: Mário da Costa Campos Neto, Salvatore Iaccarino and Chiara Montomoli
PhD programme coordinator: Francesco Dela Pierre

Code of the scientific discipline: GEO/03 – STRUCTURAL GEOLOGY

2022

UNIVERSITÀ DEGLI STUDI DI TORINO, E CO-TUTELLA CON LA UNIVERSIDADE DE SÃO PAULO

DIPARTIMENTO DI SCIENZA DELLA TERRA (UNITO) E ISTITUTO DI GEOSCIENZE (USP)

DOTTORATO DI RICERCA IN SCIENZA DELLA TERRA

CICLO XXXIV

TITOLO DELLA TESI: KINEMATICS AND P-T-T EVOLUTION IN HOT COLLISIONAL FRAMEWORKS – A COMPARISON BETWEEN A NEOPROTEROZOIC AND A PHANEROZOIC LARGE HOT OROGENS

TESI PRESENTATA DA: BEATRIZ YURI BENETTI SILVA

TUTORS: RODOLFO CAROSI, MÁRIO DA COSTA CAMPOS NETO, SALVATORE IACCARINO E CHIARA MONTOMOLI

COORDINATORE DEL DOTTORATO: Francesco Dela Pierre

ANNI ACCADEMICI: 2018

SETTORE SCIENTIFICO-DISCIPLINARE DI AFFERENZA: GEO/03 GEOLOGIA STRUTTURAL

Serviço de Biblioteca e Documentação do IGc/USP
Ficha catalográfica gerada automaticamente com dados fornecidos pelo(a) autor(a)
via programa desenvolvido pela Seção Técnica de Informática do ICMC/USP

Bibliotecários responsáveis pela estrutura de catalogação da publicação:
Sonia Regina Yole Guerra - CRB-8/4208 | Anderson de Santana - CRB-8/6658

Benetti Silva, Beatriz Yuri
KINEMATICS AND P-T-t EVOLUTION IN HOT COLLISIONAL FRAMEWORKS ? A COMPARISON BETWEEN A NEOPROTEROZOIC AND A PHANEROZOIC LARGE HOT OROGENS / Beatriz Yuri Benetti Silva; orientador Mario da Costa Campos Neto; coorientador Rodolfo Carosi. -- São Paulo, 2022.
184 p.

Tese (Doutorado - Programa de Pós-Graduação em Mineralogia e Petrologia) -- Instituto de Geociências, Universidade de São Paulo, 2022.

1. Orogeno quente. 2. Trajetória P-T-t. 3. Modelagem metamórfica. 4. Petrocronologia. I. da Costa Campos Neto, Mario, orient. II. Carosi, Rodolfo, coorient. III. Título.

UNIVERSIDADE DE SÃO PAULO
INSTITUTO DE GEOCIÊNCIAS

"KINEMATICS AND P-T-t EVOLUTION IN HOT COLLISIONAL FRAMEWORKS –A COMPARISON BETWEEN A NEOPROTEROZOIC AND A PHANEROZOIC LARGE HOT OROGENS"

BEATRIZ YURI BENETTI SILVA

Orientador: Prof. Dr. Mário da Costa Campos Neto
Co-orientador: Prof. Dr. Rodolfo Carosi

Tese de Doutorado

Nº 662

COMISSÃO JULGADORA

Dr. Alessandro Borghi

Dr. Hans-Joachim Massone

Dr. Gabriele Cruciani

Dr. Rodolfo Carosi

Dr. Mário da Costa Campos Neto

SÃO PAULO
2022

ABSTRACT

Large hot orogens (LHO) are characterized by an increase in heat the production and thickness of the lithosphere. The increase in heat production, related to the accretion of high-radiogenic continental crust, leads to middle and lower crust partial melt and consequently decreases their strength. The gradient in lithostatic pressure between the thickened crust and its foreland will result in the ductile flow of the partially molten and weakened middle and lower crust. The rocks from the orogen wedge hinterland are constituted by crustal material detached from the subducted lithosphere, accreted, and stored within the orogenic system. Therefore, the hinterland rocks are able to record pressure (*P*) and temperature (*T*) changes during the orogen development as well as its kinematics history. In order to explore the lithosphere modifications during this mature stage of the continental collision, it was investigated hinterland sections of two large hot orogens, the Himalayan Orogen and the Southern Brasilia Orogen.

In the Himalayan Orogen, a transect of the Greater Himalayan Sequence was described in the Alaknanda valley, localized in the Garhwal region, NW India. A *P-T-t-D* study was addressed for these rocks and allowed us to reveal the occurrence of a newly described high-temperature shear zone, called Badrinath Shear Zone, within the Greater Himalayan Sequence. The occurrence of a high-temperature shear zone, the contrast in exhumation onset (*ca.* 3 Ma), and the apparent geothermal gradient difference between the Lower and Upper Greater Himalayan Sequence set up a tectonic-metamorphic discontinuity inside the Greater Himalayan Sequence in the study area. The Badrinath Shear Zone characteristics match with the High Himalayan Discontinuity geological features and, thus is here suggested that it represents its prolongation in Garhwal Himalaya (NW India). The Badrinath Shear Zone is interpreted as the High Himalayan Discontinuity branch in NW Himalaya. It corroborates with the regional extent of the High Himalayan Discontinuity accomplishing an important role during the GHS exhumation. Such findings support that the deformation was accommodated by high-temperature shear zones during progressive mid-crust exhumation from top to bottom in the GHS, as highlighted by the model “in-sequence shearing”.

In the Southern Brasilia Orogen an exposition of the Andrelândia Nappe System, localized in Pouso Alto county, southeast Brazil, was studied. In the area, the three structural levels of the nappe system crop out from top to bottom: the Pouso Alto, Liberdade, and Andrelândia Nappes. The obtained *P-T-t-D* results indicate an "in-sequence" propagation of the nappes stack toward the Andrelândia Nappe System bottom. The spread of ages within the orogen would represent different periods in which each nappe from the system attained prograde and retrograde metamorphism. This new dataset reinforces the idea that Southern Brasilia Orogen evolved by the progressive evolution of the continental collision between the Paranapanema and São Francisco cratons.

Furthermore, the provided data from the Pouso Alto Nappe records HP-UHT metamorphic conditions for the first time within the Southern Brasilia Orogen. The *P-T* data indicate that this rock was part of the continental subduction channel and reached crustal depths of *ca.* 70 km, corresponding to the interface between the lower crust and lithospheric mantle in a double-thickened crust. It is suggested that the UHT metamorphic condition was attained by combining heat production elements accumulation and minor mantle heat flow. The previous melt-weakened rocks from the Pouso Alto Nappe onset their flow outward likely driven by the gravitational force. Lastly, it is proposed that the exhumation onset would record the transition from a wedge-shaped orogenic belt to an orogenic plateau during the continental collision development.

The results from this thesis indicate that the Large Hot Orogens can display a wedge-shaped (i.e., Himalayan Orogen) and fold-nappe (i.e., Southern Brasilia Orogen) hinterland geometry. The hinterland can be constituted by middle (i.e., Himalayan Orogen) and/or lower (i.e., Southern Brasilia Orogen) crustal rocks. The geothermal gradients vary within the Barrovian field, and the perturbed isotherms remained in a time range of 35 to 50 Ma until they started re-equilibrating. In both of the study cases, they evolved by progressive metamorphism and deformation owing to a single continental collision event. Folds and shear zones played a first-order role in accommodating ductile deformation during the assembly and the exhumation of the middle and lower crust. The studied examples of large hot orogens followed an "in-sequence" propagation pattern from the hinterland toward the foreland, and it is suggested that their exhumation was driven mainly by the gravitational force.

RESUMO

Grandes orógenos quentes (LHO) são caracterizados por um aumento na produção de calor e na espessura da litosfera. O aumento na produção de calor, relacionado à acreção de crosta continental com alto conteúdo radiogênico, leva a fusão parcial da crosta média e inferior e, consequentemente, diminui sua resistência. O gradiente na pressão litostática entre a crosta espessada e seu "foreland" resultará no fluxo dúctil da crosta média e inferior parcialmente fundida e enfraquecida. As rochas que fazem parte do "hinterland" da cunha orogênica são constituídas por material crustal desprendido da litosfera subductada, agregado e armazenado dentro do sistema orogênico. Portanto, as rochas do "hinterland" são capazes de registrar mudanças de pressão(P) e temperatura(T) durante o desenvolvimento do orógeno, bem como sua história cinemática. A fim de explorar as modificações da litosfera durante este estágio maduro da colisão continental, investigamos seções do interior de dois grandes orógenos quentes, o Orógeno Himalaia e o Orógeno Brasília Meridional.

No Orógeno Himalaiano, um transecto da Grande Sequência do Himalaia foi descrito no vale de Alaknanda, localizado na região de Garhwal, noroeste da Índia. Um estudo *P-T-t-D* foi endereçado para essas rochas e nos permitiu revelar a ocorrência de uma zona de cisalhamento de alta temperatura recentemente descrita, chamada zona de Badrinath, dentro da Grande Sequência do Himalaia. A ocorrência de uma zona de cisalhamento de alta temperatura, o contraste no início da exumação (*ca.* 3 Ma) e a aparente diferença de gradiente geotérmico entre a porção inferior e superior da Grande Sequência do Himalaia configuraram uma descontinuidade tectônico-metamórfica na área de estudo. As características da zona de cisalhamento de Badrinath combinam com as feições geológicas da descontinuidade do alto Himalaia e, portanto, sugere-se que ela represente seu prolongamento no Garhwal Himalaya (NW Índia). A zona de cisalhamento de Badrinath é interpretada como um ramo da descontinuidade do alto Himalaia no noroeste do Himalaia. Isso corrobora com a extensão regional da Descontinuidade do Alto Himalaia, desempenhando um papel importante durante a exumação da grande sequência do Himalaia. Tais achados suportam que a deformação foi acomodada por zonas de cisalhamento de alta temperatura durante a exumação progressiva da crosta média do topa para base na Grande Sequência do Himalaia, conforme destacado pelo modelo "cisalhamento em sequência".

No Orógeno Brasília Meridional foi estudada uma exposição do Sistema de Nappes Andrelândia, localizado no município de Pouso Alto, sudeste do Brasil. Na área, os três níveis estruturais do sistema de nappes afloram do topo para base: as nappes Pouso Alto, Liberdade e Andrelândia. Os resultados *P-T-t-D* obtidos indicam uma propagação "em sequência" da pilha de nappes em direção a base do Sistema de Nappes Andrelândia. A propagação das idades dentro do orógeno representaria diferentes períodos em que cada nappe do sistema atingiu metamorfismo progressivo e retrógrado. Este novo conjunto de dados reforça a ideia de que o Orógeno Brasília Sul foi produto da evolução progressiva da colisão continental entre os crátons Paranapanema e São Francisco.

Além disso, os dados fornecidos da Nappe Pouso Alto registram condições metamórficas HP-UHT pela primeira vez dentro do Orógeno Brasília Meridional. Os dados *P-T* indicam que esta rocha fazia parte do canal de subducção continental e atingiu profundidades crustais de *ca.* 70 km, correspondente à interface entre a crosta inferior e o manto litosférico em uma crosta duplamente espessada. Sugere-se que a condição metamórfica de UHT foi alcançada pela combinação de acúmulo de elementos de produção de calor e menor fluxo de calor do manto. As rochas enfraquecidas pela fusão parcial iniciaram seu fluxo para fora, provavelmente impulsionadas pela força gravitacional. Por fim, propõe-se que o início da exumação registraria a transição de um cinturão orogênico em cunha para um platô orogênico durante a colisão continental.

Os resultados desta tese indicam que os LHO podem apresentar uma geometria em forma de cunha (Orógeno Himalaia) e "fold-nappe" (Orógeno Brasília). O "hinterland" pode ser constituído por rochas da crosta média (Orógeno Himalaia) e/ou inferior (Orógeno Brasília). Os gradientes geotérmicos variam dentro do campo Barroviano, e as isotermas permaneceram perturbadas em um intervalo de tempo de 35 a 50 Ma até começarem a se reequilibrar. Em ambos os casos estudados, eles evoluíram por metamorfismo progressivo e deformação devido a um único evento de colisão continental. As dobras e zonas de cisalhamento desempenharam um papel de primeira ordem na acomodação da deformação dúctil durante a montagem e a exumação da crosta média e inferior. Os exemplos estudados seguem uma propagação "em sequência" do hinterland para o foreland, e sugere-se que sua exumação foi impulsionada principalmente pela força gravitacional.

ACKNOWLEDGMENTS

After a change of country, a pandemic, a broken leg and so many other things, my PhD journey finally comes to an end. I could not fail to thank in a few lines all those who have accompanied me on this long journey. I had the incredible opportunity to have four mentors during my doctorate, and thank you all for your guidance throughout this process. Rodolfo and Chiara for giving me this incredible opportunity to work with Himalayan rocks which was a long-time dream. My co-supervisor Salvatore, always very enthusiastic, a big thank you for all the papers he referred to me, the coffees we had together, and the fruitful discussions on metamorphic modeling. Mário for his longtime partnership and guidance since I was a bachelor student.

I would like to thank Antonio Langone for the support during laser analysis and very interesting discussion about monazite behavior during the HP-granulite metamorphism. A very big thank you for George Luvizotto for opening his EMPA lab during the middle of the pandemic crisis, and performed so much more analysis than I previously thought. The incredible X-ray monazite maps and quantitative compositional maps improved a lot my work would not be possible without you, thanks a lot!

The friends that I have done during my period in Turin Antoine, Michele, Andrea, Claudio, Lukardis, Elen, Matteo, Ito, and Helena made my days always more fun with lunches at the park, or at an “apericena”. My best friend Gabriella for all the support conversation, laughs, and all the times you put me up. My childhood friend Camilo for always worrying about me.

A special thank you to Christophe Real, my alpine guide, ski instructor, nurse (when I broke my leg), and boyfriend. Without your support, in this final moment, the thesis conclusion would have been impossible!

My beloved family which also supported me and believe in my decisions! It certainly would have been impossible to have come this far without being the daughter and granddaughter of such incredible women who have always inspired me to go further!

For my dear mother, who taught me that knowledge is the greatest wealth.

Table of contents

List of figures

List of tables

List of figures in Appendix A

List of figures in Appendix B

List of figures in Appendix C

CHAPTER 1

INTRODUCTION

1 GENERAL INTRODUCTION

Orogenesis is the product of interaction between two convergent plates, which leads to the growth of a mountain chain during the activity of Plate Tectonics on our planet (Coney, 1970; Dewey and Bird, 1970). The mountain uplift is related to several important processes on the Earth, such as mineral deposits formation (Bradley et al., 2017; Richards, 2015), climate changes (Armijo et al., 2015; Miao et al., 2012), life spread on Earth (Squire et al., 2006). The collisional orogenesis is considered the final stage of a Wilson cycle and is preceded by passive margin inversion, subduction of oceanic crust, and terrane/arc accretion (Wilson, 1966). After the accretionary phase and ocean consumption, the orogenic system evolves following horizontal shortening, vertical thickening, heating production, and metamorphic rock exhumation (Johnson and Harley, 2012; Mooney and Vidale, 2003; Sandiford and McLaren, 2002). Moreover, structural and metamorphic patterns differences in the orogens geological record are observed through the Earth history (Brown, 2007a, 1993; Brown and Johnson, 2018; Chardon et al., 2009; Gerya, 2014; Sizova et al., 2014). The final orogenic architecture will be controlled by several factors such as the lithosphere rheology, temperature, inheritance structures, fluid presence in the system, erosion, and convergence rates.

A global classification of the orogens is proposed by Beaumont et al. (2006), taking into account the orogen magnitude (M), which corresponds to the deformed lithosphere thickness, and the temperature (T) (Fig. 1). According to this classification, the orogenesis style can be divided into two end members, small cold (SMO) and large hot orogens (LHO). The small cold orogens are characterized by low levels of radioactive heating, high denudation rates, and low- to intermediate magnitude thickness. For instance, the Southern Alps of New Zealand, Pyrenees, and European Alps are classified as small and cold orogenic belts (Fig. 1). In contrast, the large hot orogens (LHO) are characterized by middle and lower crust high heat production and a high-altitude gradient between the mean hinterland elevation and the foreland. Consequently, a plateau tends to be built due to an altitude contrast and decreased strength and viscosity in the partially melted middle/lower crust due to a high-temperature gradient. The joining of these factors leads to gravitationally driven ductile flow

of the middle/lower crust. The hot style of orogenesis has been spread in the Earth history since the Proterozoic (e.g., the Grenvillian, Variscan orogens), and even though it is not the predominant style after the Phanerozoic (Gerya, 2014; Sizova et al., 2014), in which the cold orogenesis dominates, there is still a modern example of it, the Himalayan belt, recognized as the classic example of continent-continent collision.

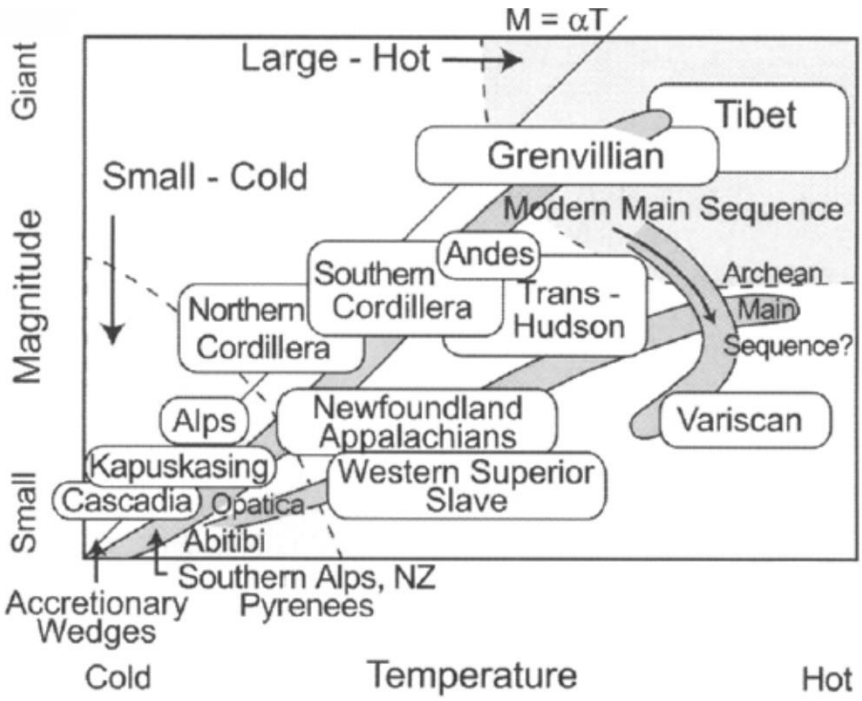

Figure 1 - Temperature-Magnitude (T-M) orogenic classification diagram by Beaumont et al.,2006. The small cold orogens field (SCO) is marked at the left bottom, while the large hot orogen (LHO) field is at the right top. The diagram displays the classification of several orogenic belts.

Exhumed sections of the middle and lower crust exposed in hot collisional belts offer us unique opportunities to study such crustal portions, which can be difficult using indirect methodologies. In this study, it is provided Pressure-Temperature-Time-Deformation (*P-T-t-D*) data of middle and lower crust rocks in two different collisional hot orogens. The first study case is a Phanerozoic LHO, the Himalaya Orogen, in which the orogenesis is still an ongoing process, and the second study case is the Southern Brasilia Orogen, built during the Proterozoic. The addressed methodology provides information about kinematics, rheological characteristics of the middle/lower crust, *P-T* paths, and finally, time constraints of related processes such as prograde burial, partial melting, and exhumation. All these data are input

parameters for building tectonic-metamorphic models able to explain LHO evolution. The comparative study of geological processes, in this case, the continental collision, has proven a valuable approach to understanding structural and thermal changes in the lithosphere during the Earth history.

1.1 LARGE HOT COLLISIONAL OROGENY

1.1.1 Force balance, lithosphere rheology, and structural architecture

During the collision, two continental blocks get in contact along convergent plates boundary. Due to the low density of the continental crust, its subduction is slowed down or even ceased, even though tomography seismic profiles demonstrate that the subduction can carry on in the lower crust and lithospheric mantle (Kind et al., 2002; Li et al., 2008; Wortel and Spakman, 2000). Three main forces will be responsible for controlling the lithosphere deformation within collisional belts: the tectonic, gravity, and buoyancy forces (Beaumont et al., 2006; Dielforder et al., 2020; Dielforder and Hampel, 2021; Jamieson and Beaumont, 2013a; Piccolo et al., 2018; Vanderhaeghe, 2012; Vanderhaeghe and Teyssier, 2001; Warren, 2013). The tectonic forces are the basal traction, the wedge bottom shear stress, and the horizontal compression, the integral of horizontal normal stress through the crust thickness. Whereas the basal traction will be the primary driving force controlling the crust thickness, the horizontal responses will depend on rock rheology. The gravity force results from lateral topographic variations. It is measured by the differential lithostatic pressure gradient between the maximum elevation of a mountain belt and its foreland. Finally, the buoyancy force is controlled by the density contrast between the rocks. The buoyancy force is usually relevant in low-density rocks buried, as well as in those affected by partial melting and magma development.

The hot collisional orogeny will evolve by sediment and crustal material accretion, leading to thickening and increasing in heat production. The accretion of crustal material (e.g., granitoid and pelite) with high concentrations of radioactive elements, such as U, Th and K, recognized as the main crustal heat sources, will enhance the heat production within the orogenic belt (England and Thompson, 1984; Rudnick and Fountain, 1995). Besides the

accumulation of radioactive elements, the high-strain production within an orogenic belt can play a minor role in the increase of heat production (Faccenda et al., 2008). The middle and lower crust temperatures can achieve temperatures higher than 700°C after 20-25 m.y interval of crustal thickness, and at these conditions, the rocks will undergo partial melt (Jamieson and Beaumont, 2013a).

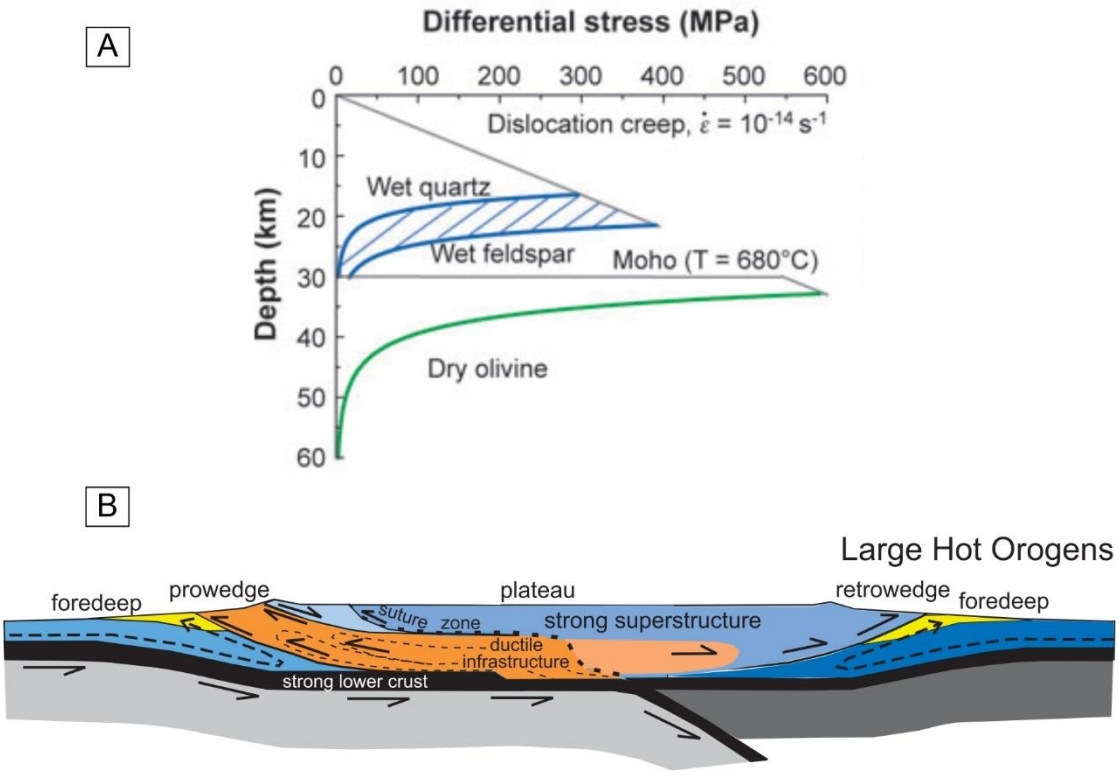

Figure 2 - a) The jelly sandwich rheological envelope displaying a weak middle and lower-crust, and a strong upper mantle (Bürgmann and Dresen, 2008; Hirth and Kohlstedf, 2003). *b) LHO crustal architecture* (Jamieson and Beaumont, 2013a).

The aforementioned mechanical and thermal framework will result in the rheological lithospheric profile known as the jelly sandwich, in which a weak middle and lower crust are strongly decoupled by the overlain cool and strong upper crust and the lithospheric mantle (Fig. 2a; Bürgmann and Dresen, 2008; Hirth and Kohlstedf, 2003). The partial melting of the middle and/or lower crust decreases the viscosity (Rosenberg and Handy, 2005) and basal traction of these layers, which are not able to sustain the topographic gradients, leading to a

plateau formation (Vanderhaeghe, 2012). Moreover, the lithostatic gradient (gravitational force) and the rheological characteristics will result in the ductile flow of the weakened and partially molten middle and lower crust (Beaumont et al., 2001; Jamieson et al., 2011a). The erosion may cause the exhumation of the high-grade rocks from the middle and lower crust in the plateau flanks (Jamieson et al., 2002). The described mechanisms result in the formation of a large hot orogen, characterized by an elevated plateau flanked by thrust-sense wedges (Fig. 2b). The upper crust rocks present steep structures, while the expositions of middle and lower crustal rocks will show shallow-dipping foliation and ductile flow structures.

1.1.2 Metamorphism

Due to orogenesis intrinsic processes, such as the upper mantle subduction, thrusting, doming, and magma intrusions, the thermal architecture, and thickness of the crust are modified over time (Brown, 2007b, 1993). The temperature (*T*) and pressure (*P*) variations across the time are going to control the metamorphic evolution (*P*-*T*-*t* path) of the belt. The metamorphic core of hot orogenic belts, called hinterland, is characterized by the presence of migmatites, usually associated with leucogranites emplacement. The metamorphic gradients are moderate-to-high-*dT/dP* and are related to radiogenic elements accumulation and shear heating leading to T>700°C and partial melt in the middle crust (Jamieson et al., 2011b; Jamieson and Beaumont, 2013a; Vanderhaeghe, 2012, 2009). Even though low-*dT/dP* rocks, which underwent high-pressure (*HP*) metamorphism, can be observed as relics of the subduction phase (Leech et al., 2005). The time range in which rocks within LHO were submitted to high temperature and suprasolidus conditions is variable. For instance, in the Himalayan orogen, high temperature and suprasolidus conditions were sustained for 25 Ma to <10 Ma (Weinberg, 2016), while in the Grenville Province, such conditions were maintained from approximately 40-70 Ma (Turlin et al., 2018).

1.1.3 Crustal flow pattern and exhumation of deep-seated crustal rocks

The ductile flow of the weakened mid- and lower crust in LHO can be divided into three groups according to what will be the primary driving force of this process. The flow mechanisms are: channel flow, driven by gravity force; hot nappe emplacement, driven by tectonic forces; the diapiric domal flow, driven by buoyancy forces (Fig. 3; Beaumont et al., 2006; Jamieson and Beaumont, 2013).

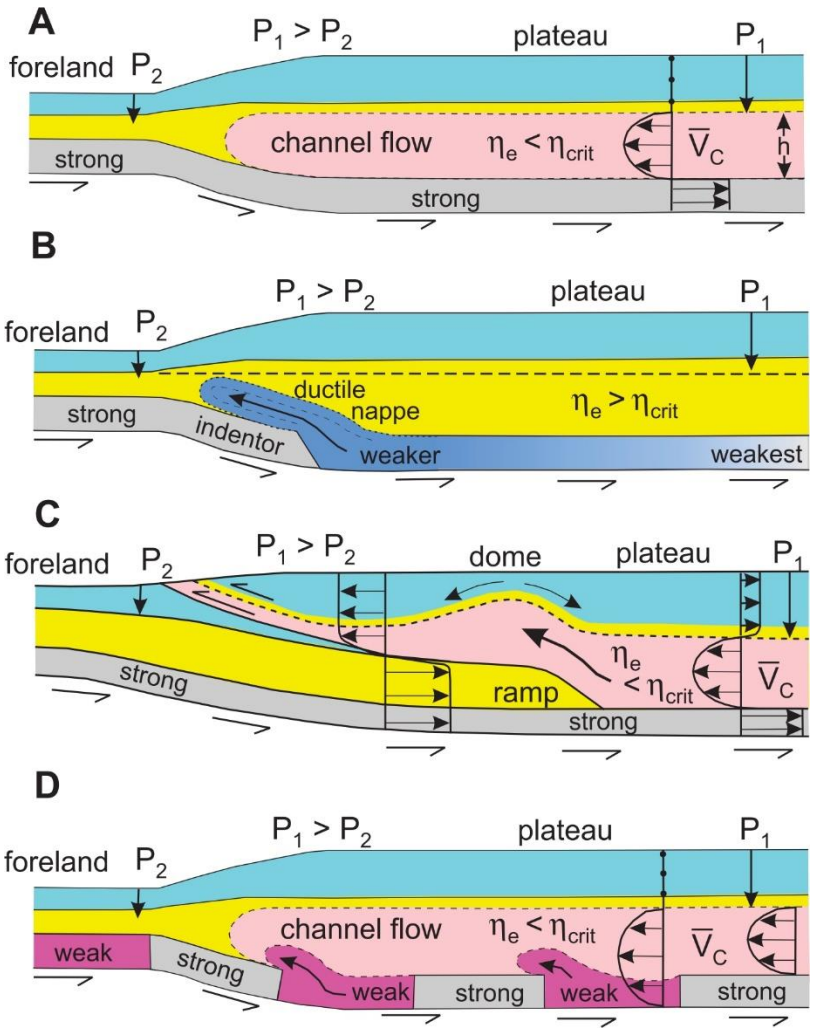

Figure 3 - Crustal ductile flow modes (adapted from Jamieson & Beaumont 2013). a) Channel flow model; b) Hot nappe model; c) Diapiric domal flow; d) Heterogeneous flow. η_c= effective viscosity of middle crust; η_{crit}=threshold viscosity required for efficient channel flow ($\leq 10^{19}$ Pa s); Vc=mean velocity of the channel.

The channel flow model (Fig. 3a) was elaborated mainly taking into account the Himalaya Orogen architecture, and it assumes that the flow of the partially molten and weakened middle crust takes place due to the differential pressure gradient between the plateau and the foreland (Beaumont et al., 2001, 2006; Jamieson and Beaumont, 2013b). Within the channel, there is a balance and competition between two end-members flow regimes, the Poiseuille flow (or Pipe flow), in which the maximum velocity is placed in the center of the channel and decreases toward the boundaries, and the Couette flow, which has homogenous vorticity, and the velocity increases toward the channel bottom. The channel flow in LHO requires bounding ductile shear zones with coeval and opposite sense of motion, being the one in the bottom a thrust-sense in which the Poiseuille flow is predominant, whereas the one at the top is a normal-sense where the Couette flow prevails. Moreover, the **incubation time**, the necessary time range for thickening, heating, and weakening of the crust before a decrease of the thermal perturbation owing to thermal relaxation, must be 10-20 Ma to induce channel development and motion.

The hot nappe model for the lateral ductile flow of mid- and lower crust presumes that a strong indentor is inserted under crustal levels, which will lead to the expulsion of the weakened material (Fig. 3b; Beaumont et al., 2006; Jamieson et al., 2004). As a result of such process, a fold-nappe structure, in which thrust-sense shear zones imbricate weaker material over stronger one. Such kind of flow, driven by tectonic instead of gravitational forces, takes place in LHO that is not hot enough or does not have large topographic gradients and likely did not achieve the plateau formation stage. The stiff indentor may represent a cratonic core or a cold oceanic crust lately carried into the orogen crust. Previously of the strong material to be brought, the orogenic belt might undergo a long incubation period, equal to or higher than 20-30 Ma. The hot nappe flow model has been applied to several LHO, such as the Mesoproterozoic Grenville Belt, some portions of the Appalachian belt, and the Canadian Cordilleran Belt.

The last driven force that can induce crustal flow is the buoyancy one, which usually forms a domal structure, and the process responsible for it is known as diapirism (Fig. 3c). The diapirism takes place due to gravitational instabilities proceeded by density contrast

between two materials (Weinberg and Podladchikov, 1994; Weinberg and Schmeling, 1992). A density contrast of $0.1 g/cm^3$ is enough for the diapiric process to carry out (Fletcher, 1972). In LHO, the crustal gravitational instability can be provoked by the partial melt of the orogen infrastructure (middle and lower crust), which is responsible for decreasing the density and viscosity (Vanderhaeghe, 2009), as well as the density contrast between crustal deep-seat rocks, which underwent UHP metamorphism, and the mantle ones (Warren, 2013). It is essential to highlight that the domal rise is facilitated by a detachment (Couette flow). The diapiric domal flow is used to explain gneissic domes of partially melted rocks, metatexite/diatexite, and (U)HP crustal rocks flow. For instance, the Himalaya, North American Cordillera, Appalachians, and Iberian and French Variscides are examples of LHO in which the gneiss domes presence have been explained by buoyancy force activity.

In fact, more than one process can act at the same or different times and localities within an orogenic system, how it has been demonstrated already in numerical models (Fig. 3d). It is important to highlight that natural processes are much more complex and can include other elements that were not considered in simplified numerical modeling. However, numerical models can point to important factors that control orogenesis. Their results may be confronted against the reality of the orogenic belts to become more sophisticated and realistic.

Middle and lower crust exhumation will respond to erosion and orogen extension, which can be coeval or post-convergence (Ring et al., 1999). Syn-convergence exhumation can be related to high erosion rates (Beaumont et al., 2001) or geodynamics processes (Ring et al., 1999), such as slab rollback and upper plate retreat that cause crustal extension (Brun and Faccenna, 2008). The orogenic collapse is linked to post-convergence exhumation and is a consequence of force balance change (Rey et al., 2001). For instance, the convergence end will decrease the basal traction tectonic force responsible for sustaining the orogen topography, shifting from a compressional to an extensional setting. Another example of force balance is an increase in orogen buoyancy force due to slab breakoff, causing detachment and exhumation. The post-convergence erosion can help to expose the orogen infrastructure as well.

1.2 STATEMENTS OF OBJECTIVES AND JUSTIFICATIVE

The uniformitarianism concept elaborated by James Hutton that says, “The present is key to past” is applied here in this study. Despite nowadays is known the earth geodynamics underwent some secular changes (e.g., Archean to Proterozoic transition), and this principle can not be applied for those periods after the modern tectonic has been established (Gerya, 2014; Palin et al., 2020; Palin and Santosh, 2021), in this study this principle remains valid and can be applied. The Himalaya Orogen is a modern example of LHO where the continental collision is a process that is still going on, and it has been used as the primary parameter to understand the Southern Brasilia Orogen evolution. The Himalaya Orogen was chosen because most structural, petrologic, and tectonics models for LHO evolution were elaborated to fit it. Moreover, those models are widely used to interpret old collisional orogens.

To understand the lithosphere modifications during the large hot orogenesis development, it was applied a multidisciplinary methodology consisting of field mapping, meso-and microstructural analysis, thermodynamic metamorphic modeling, and U-(Th)-Pb monazite geochronology (chemistry and isotopic dating) to the Himalayan Orogen and the Southern Brasilia Orogen (SBO) focus on them orogenic wedge hinterland. The orogen hinterland represents the exhumed deep-seated rocks, recording wealthy information about their geodynamic setting. Four questions were addressed:

- How is the architecture of the orogenic hinterland? Is there any evidence of a plateau formation in the SBO?
- How varies the *P-T* gradient within the orogenic hinterland? Which are the structures controlling its change?
- How long was the incubation time for each one of the studied LHO? Was it enough to generate widespread partial melting and weaken the middle and lower crust?
- How was the strain distributed in such LHO? What was the flow mode acting in which one of the studied LHO systems?

1.3 THESIS ORGANIZATION

The thesis is organized into six different chapters, in which the analysis results are presented in the chapters 3 to 5 in the form of manuscripts submitted/accepted by periodicals. Below, it is provided a summary of the subject of each chapter:

Chapter 2 – Geological background. This chapter brought a brief overview of both orogenic systems accumulated knowledge focused on their orogenic wedges, which are the target of this study.

Chapter 3 is entitled "Mapping tectono-metamorphic discontinuities in orogenic belts: implications for mid-crust exhumation in NW Himalaya." This chapter presents structural, metamorphic petrology, and monazite petrochronology data for a shear zone within the Great Himalayan Sequence (GHS). From those data, an exhumation model for the ductile flow of mid-crust in the Alaknanda Valley (NW India) is proposed, corroborating with the "in-sequence shearing" for the GHS exhumation. This chapter is a version of a paper published in the periodical LITHOS.

Chapter 4 is entitled "Tectono-metamorphic evolution of Andrelândia Nappe System (SE Brazil) constraint by metamorphic iterative thermodynamic modeling and monazite petrochronology". This chapter addressed a *P-T-t-D* study for two nappes from the Andrelândia Nappe System, the Southern Brasilia Orogen wedge hinterland. By integrating the results, it is provided a discussion about the progressive evolution of the deformation and metamorphism during the continental collision between the Paranapanema and São Francisco cratons.

Chapter 5 is entitled **"** HP-UHT granulites from Pouso Alto Nappe, SE Brazil: insights into the heat drivers and exhumation of lower crust". In this chapter, the same multidisciplinary approach is applied to the Pouso Alto Nappe, the upper structural level of the Andrelândia Nappe System. The Pouso Alto granulite *P-T-t* trajectory is reconstructed, and it is recognized for the first time a rock that experienced HP-UHT metamorphism within the SBO.

In addition, a geodynamic model in which the Pouso Alto Granulite would record the transition from a wedge-shaped to plateau orogen is proposed.

Chapter 6- Conclusion. In the last chapter, the results presented and discussed in chapters 3, 4, and 5 are summarized through a comparative view regarding the factors which controlled the evolution of both large orogenic belts.

CHAPTER 2

GEOLOGICAL BACKGROUND

2 GEOLOGICAL BACKGROUND

2.1 Himalaya Orogen

The Himalaya Orogen, the most impressive present mountain chain, is the archetype of continent-continent collision (Dewey and Bird, 1970; Dewey and Burke, 1973). The mountain belt has approximately 2,500 km. From the west to the east, it crosses the following countries: Pakistan, India, Nepal, and Bhutan. It is limited to northeastern by Tibet and southeastern by India. The orogen is resulted from India and Asia continental margins ongoing collision, leading to the Paleo-Tethys ocean closure (le Fort, 1975; Searle et al., 1987). Although the age of the collision onset is still a target of many discussions, several geological criteria have been applied to assess it. For instance, ultra-high pressure metamorphism timing (Leech et al., 2005; St-Onge et al., 2013), paleomagnetism constraint (Yi et al., 2015), magmatism source change (Zhu et al., 2015), detrital provenance shift (Decelles et al., 2014; Hu et al., 2015) and marine sedimentation cessation (Garzanti et al., 1987) are some of the processes used to estimate the collision age. However, the stratigraphic methods have provided the most accurate ages, around 59 Ma, for the initial collision (Hu et al., 2016).

The orogen comprises four main tectonic units separated by orogen-scale shear zones dipping to the north (Fig. 4 and 5). The four tectonic units are from the bottom to the top: the Sub-Himalaya, the Lesser Himalaya Sequence (LHS), the Greater Himalaya Sequence (GHS), and Tethyan Sedimentary Sequence (Fig. 4). In addition, the shear zones separating the geological units are respectively: the Main Boundary Thrust, the Main Central Thrust (MCT), and the Southern Tibetan Detachment system (STDs) (Hodges, 2000; Le Fort, 1975). Those units are bounded in the north by the Indus suture zone and in the south by the Main Frontal Thrust (MFT) and were deformed and metamorphosed coeval and after the India-Asia collisional process.

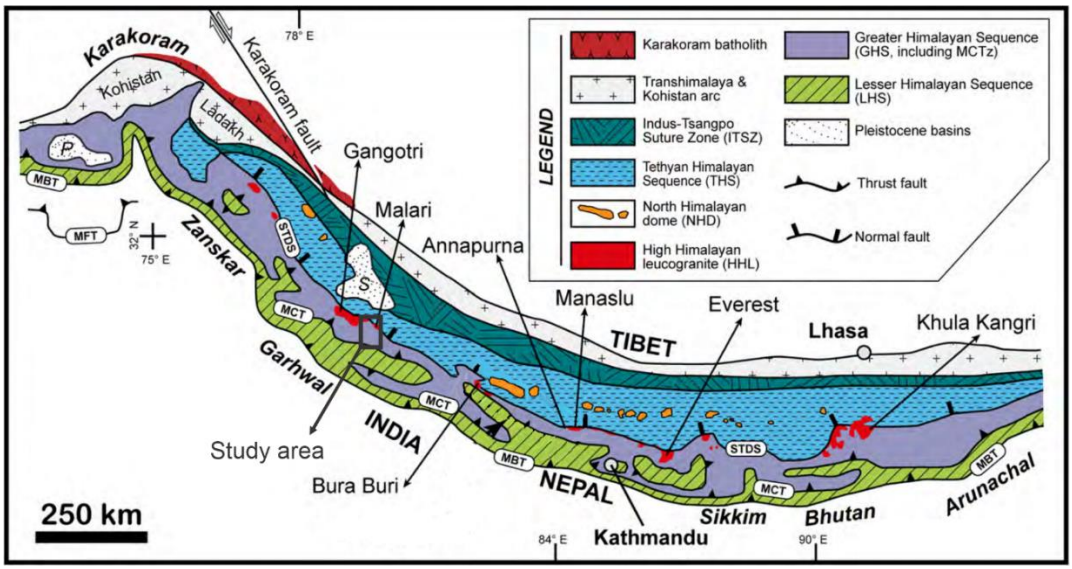

Figure 4 - Simplified geological map of Himalaya Orogen, after Carosi et al. (2019). MBT-Main Boundary Thrust; MCT – Main Central Thrust; STDS- South Tibetan Detachment system; P- Peshawar basin; S- Sutlej basin.

The basal tectonic unit is the Sub-Himalaya molasses constituted by the Siwalik Group, a Tertiary syn-orogenic sequence deposited in the orogen foreland basin (Hodges, 2000). At the top of the Sub-Himalaya molasses is located the Main Boundary Thrust, a top-to-the-south shear zone that separates the Sub-Himalaya from the Lesser Himalaya Sequence (LHS). The LHS is made up by impure quartzite, phyllite, schist and orthogneiss. The LHS rocks were metamorphosed in lower-greenschist to lower-amphibolite facies and vary in age from the Mesoproterozoic to the Miocene (Hodges, 2000).

The Greater Himalayan Sequence (GHS) is the metamorphic core of the belt. The GHS is separated by other units by two shear zones with opposite senses, the Main Central Thrust zone (MCTz) at the bottom and the Southern Tibetan Detachment system (STDs) at the top. Internally, the GHS is divided into two structural levels, the Lower (GHS_L) and Upper (GHS_U) (Benetti et al., 2021; Carosi et al., 2019; Larson et al., 2010; Waters, 2019). The GHS_L has at its bottom the MCTz hanging-wall and is characterized by metapelites interlayered with quartzite and calcsilicate rocks. An inverted metamorphic pattern is observed, grading from the garnet isograd at the bottom to the kyanite isograd close to the top.

The uppermost GHS structural level, the $GHS_{U,}$ is characterized by the sillimanite+K-feldspar-isograd appearance that grades toward the kyanite+K-feldspar close to the top. A remarkable GHS_U feature is the increase of partial melting in comparison with those rocks from the GHS_L. The GHS_L and GHS_U are separated by the High Himalayan Discontinuity (HHD), a high-temperature ductile thrust-sense shear zone (Carosi et al., 2019, 2018; Montomoli et al., 2015, 2013). Although some authors considered the HHD a cryptic structure, the enhancement of HHD works have shown that this tectonic-metamorphic discontinuity can be identified, based on metamorphic and structural features, from a macro- to microscopic scale (Carosi et al., 2019, 2018; Montomoli et al., 2013).

The Tethyan Sedimentary Sequence is the belt uppermost structural level, is bounded in the southern part by the STDs and toward the Northern by the Indus Yarlung Suture Zone (Antolín et al., 2011; Hodges, 2000). The Tethyan Sedimentary Sequence comprises siliciclastic and carbonate sedimentary rocks, with Cambrian to early Cenozoic age, and volcanic rocks from the Paleozoic and Mesozoic (Garzanti, 1999). The metamorphic conditions vary from non-metamorphosed, close to the STDs, to amphibolite facies toward the Indus Yarlung Suture Zone (Dunkl et al., 2011; Montomoli et al., 2017). The Tethyan Sedimentary Sequence records several stages of the Tethys ocean evolution, since its opening stages, passing through a passive margin, and finally, it has a syn-collisional sequence (Garzanti, 1999).

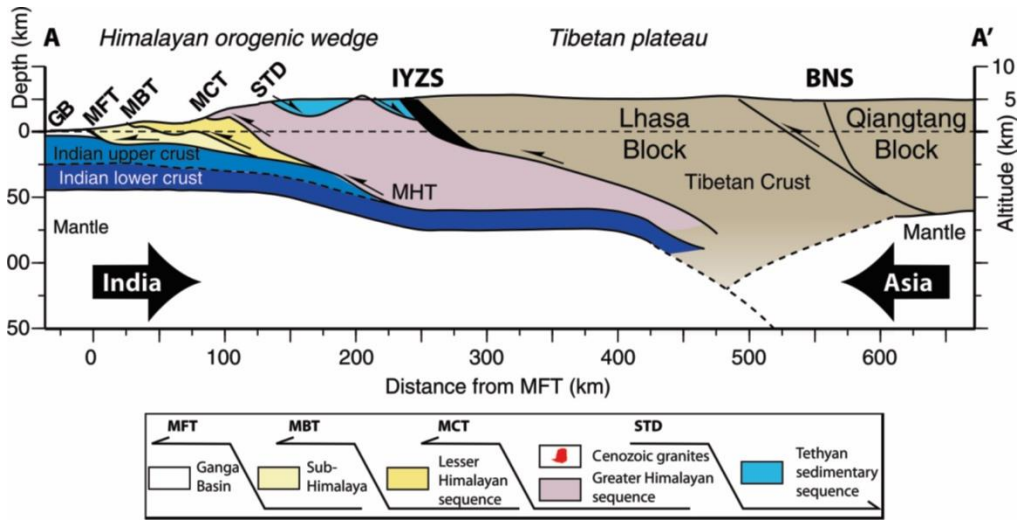

Figure 5 - Himalaya belt cross-section showing the major upper crustal features from Godin et al. (2019).

2.1.1 Greater Himalaya Sequence: P-T-t paths and tectonic evolution

Fig. 6 displays a schematic view of the main metamorphic and structural features of the Greater Himalaya Sequence (GHS). The high-grade rocks from the GHS are bounded by two medium-to low-grade sequences, the LHS at the bottom and the Tethyan Sedimentary Sequence at the top (Kohn, 2014). The bottom division between the GHS and LHS is the MCTz, a tectonic discontinuity crossing ~2400 km along the belt strike. The MCTz is a top-to-the-south/southwest thrust-sense shear zone in which one of the most remarkable features of the GHS is observed, the inverse metamorphic pattern (Carosi et al., 2007; Iaccarino et al., 2020, 2017a; Searle et al., 2008). The Barrovian inverted metamorphism is characterized by the low-grade rocks in the biotite/garnet zone overlapped by higher grades ones up to the kyanite zone (Kohn, 2014). The GHS lower structural level (GHS_L) includes the MCTz hanging-wall and goes until the HHD onset.

The HHD can be identified based on its deformation, metamorphic and geochronology features (Carosi et al., 2019, 2018; Montomoli et al., 2015, 2013). Regarding the HHD deformational characteristics, it is a high-temperature thrust-sense shear zone, quartz displays microstructures compatible with the GBM_{II} regime, the sillimanite is one of the main minerals growing along the mylonitic foliation, and its kinematic indicators point-to-the-south/southwest sense of shear. In concern of the metamorphism, the HHD is distinguished by the contrast of 2-3 kbar between the rocks from its hanging-wall, which are re-equilibrated within the sillimanite field, and those from its footwall, equilibrated in the kyanite stability field. In addition, the HHD marks the widespread of partially molten rocks. Lastly, there is a time difference between the HHD hanging-wall and footwall metamorphism peak. It is observed that when the HHD hanging-wall rocks onset their exhumation, the ones from its footwall were still being buried during the prograde metamorphism.

The Upper GHS structural level (GHS_U) has the HHD at its bottom and the South Tibetan Detachment System (STDs) at the top. The STDs is characterized by ductile-to-brittle low-angle structures dipping toward the north that cut the GHS in the top (Burchfiel et al., 1992; Carosi et al., 1998; Iaccarino et al., 2017b; Kellett et al., 2015). The GHS_U rocks are sillimanite/kyanite-bearing migmatite, calcsilicate, and quartzite, in which the

metamorphic grade increases upward (Carosi et al., 2019, 2018; Waters, 2019). Granite bodies of Oligo-Miocene ages are emplaced in the GHS_U, close to its top boundary, and are called the High Himalayan Leucorgranites (HHL) (Visonà et al., 2012; Weinberg, 2016). Some examples of these leucogranites are the Manaslu, Bura Bura, Makalu, and Malari. The HHL are divided into two groups: the white mica+biotite±tourmaline leucogranites and the tourmaline leucogranites. Whereas the two micas leucogranites yield older ages between 24-19 Ma, the tourmaline-bearing leucogranites are often younger, from 14 Ma to 7 Ma.

The age of the GHS metamorphic peak decreases structurally downward, and its history is usually divided into two episodes (Carosi et al., 2015; Iaccarino et al., 2015; Kohn, 2014; Vannay and Hodges, 1996). The first one (M1), called Eohimalayan, is considered an episode of crustal thickening in the kyanite isograd during the late Eocene to Oligocene. The Neohimalayan stage is the second metamorphic stage (M2) recorded, is a high-temperature stage related to the sillimanite isograd, anatexis, and granite emplacement from early to middle Miocene (Groppo et al., 2009; Kohn, 2014, 2008; Warren et al., 2011).

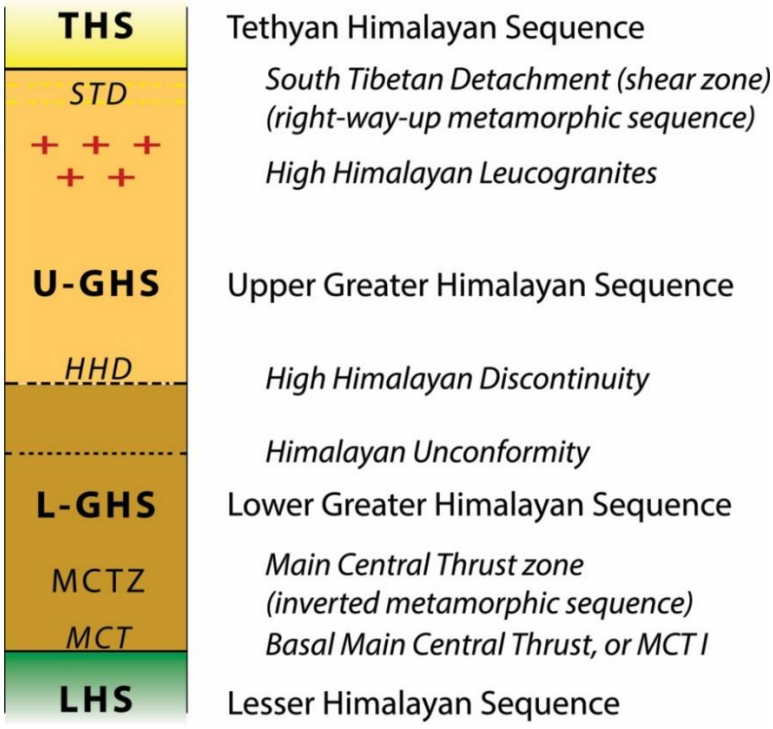

Figure 6 - Summary of GHS main structural and metamorphic features from Waters (2019).

Tectonic models attempting to describe the GHS flow and exhumation may comprise its complex framework: the two opposite sense shear zones bounding the GHS (MCTz and STDs), an internal tectono-metamorphic discontinuity (HHD), an inverted metamorphic gradient, partial melting, and leucogranites emplacement. Moreover, the whole sequence *P-T* path and the time processes (e.g., partial melting, exhumation, etc.) should also be considered to elaborate a model consistent with reality.

Two models are regarded to fit most of the concerns related to GHS evolution, the channel flow and the critical taper (Beaumont et al., 2001; Grujic et al., 1996; Jamieson et al., 2011; Searle et al., 2003). In the channel flow model, the flow of weakened mid-crust is gravity driven. The two opposite sense shear zones correspond to the bottom and top boundaries of the channel. The inverted metamorphic pattern results from isotherms fold during the upward channel motion. At last, the partial melt and leucogranites emplacement would be the outcome of 10-20 m.y of crustal thickening and heating (Beaumont et al., 2001; Grujic et al., 1996; Jamieson et al., 2011; Searle et al., 2003). In opposite, the critical taper model claims that the orogen will answer to changes in the wedge taper angle by propagating the deformation by thrust faults toward the foreland if you increase the taper angle or forming out-of-sequence thrust faults if there is a decrease in the taper angle (Dahlen, 1990; Kohn, 2008; Robinson et al., 2006; Sachan et al., 2010). The factors that are able to disturb the critical taper angle are erosion, the addition of crustal material, rock strength, shortening rate, and balance friction at the wedge bottom. The critical taper principle has been applied to Himalaya kinematic models, mainly to explain the inverted metamorphism pattern as well as the MCTz motion. Notwithstanding, some authors shedded light on the fact that both models are not exclusives and that both tectonic models should coexist in nature (Cottle et al., 2015; Waters, 2019). Models considering the HHD presence and MCTz and STDS no coeval motion are still scarce.

2.2 Southern Brasilia Orogen (SBO)

The Pan African-Brasilian orogenic cycle is the name given to a series of diachronic collisions during the West Gondwana assemblage (Cordani et al., 2013, 2003; Ganade De Araujo et al., 2014). The cycle initiated at *ca.* 900 Ma during Rodinia breaks up and was completed in the Neoproterozoic era. The Rodinia block pieces were amalgamated against cratonic blocks to give rise to the western part of the paleocontinent Gondwana.

The Brasilia Orogen (BO) is one of the thrust fold belts associated with the West Gondwana built during the Pan African-Brasiliano event (Alkmim et al., 2001; Brito Neves et al., 1999; Cordani et al., 2003). The BO is located in central and southeast Brazil between the parallels 10° and 26°S and has an extension of *ca.* 1800 km. The Brasilia Orogen has been segmented into two domains, the Northern Brasilia and the Southern Brasilia Orogens. Whereas in the Northern sector, the Amazonian and São Francisco paleoplates collided frontally to build such domain (Fuck et al., 2017), in the Southern, a lateral collision between the Paranapanema and São Francisco cratonic blocks was responsible for its setup (Valeriano, 2017).

The Southern Brasilia Orogen (SBO) final architecture resulted in an almost flat-lying fold-nappe pile with top-to-the-east/northeast tectonic transport (Fig. 7). Based on the tectonic paleo-geographic interpretations, the nappes pile is divided into three tectonic domains (Fig. 7; Campos Neto, 2000; Campos Neto et al., 2011; Trouw et al., 2013, 2000), the Socorro-Guaxupé Nappe related to the roof of a magmatic arc, the Andrelândia Nappe System, a metasedimentary sequence interpreted as the orogen hinterland, and the passive margin domain, which comprises Archean and Paleoproterozoic orthogneisses from the basement and metasedimentary rocks from the São Vicente group, Carrancas, and Lima Duarte Nappes.

The Socorro-Guaxupé Nappe is separated in two lobes by the Ouro Fino shear zone, the Socorro in the north and Guaxupé to the south, and is made by migmatites and granulites intruded by syn-to post-collisional metaluminous granitoid plutons. The rocks from this unit underwent ultra-high temperature (UHT) metamorphism, whose temperature peak was estimated between 900-1040°C and pressure at 10-12 kbar (Del Lama et al., 2000; Garcia

and Campos Neto, 2003; Motta et al., 2021; Reno et al., 2009; Rocha et al., 2018, 2017a; Tedeschi et al., 2018). The UHT metamorphism age was constrained, using monazite and zircon geochronology, between a time range of 630 and 620 Ma (Motta et al., 2021; Rocha et al., 2018, 2017b; Salazar Mora et al., 2014; Tedeschi et al., 2018). The Socorro-Guaxupé Nappe UHT metamorphism is interpreted to have occurred in a deep root of a magmatic arc setting.

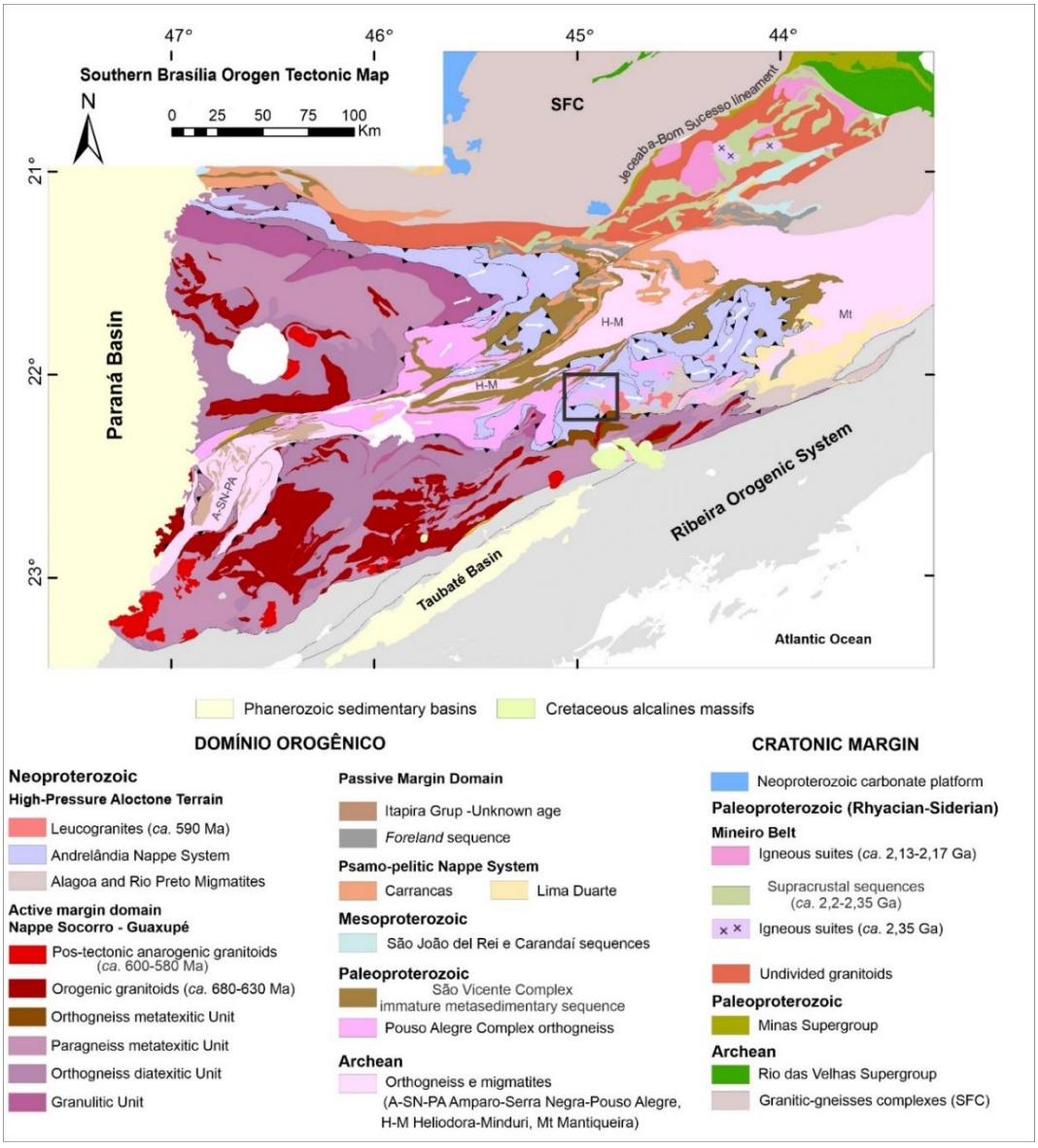

Figure 7 – Geological map of the Southern Brasilia Orogen (Modified by Cioffi et al., 2019). The black square corresponds to the study area.

The Andrelandia Nappe System (ANS) is divided from the bottom to the top in Andrelandia (AN), Liberdade (LN), and Três Pontas-Varginha (or Pouso Alto how is called when associated with the Socorro lobe) Nappes and related klippes. The metamorphism within ANS varies from high-pressure granulite (Pouso Alto and Três Pontas-Varginha Nappes and the Carvalho, Serra da Natureza and Aiuruoca Klippes) to amphibolite toward the bottom (Andrelândia Nappe). It sets up an inverted metamorphic gradient to the sequence. The timing of metamorphism peak varies in the nappe stacks, with a spread of time from 650 Ma to 586 Ma (Campos Neto et al., 2011; Coelho et al., 2017; Li et al., 2021; Motta and Moraes, 2017; Reno et al., 2012, 2009; Westin et al., 2021). Metric-to kilometric leucogranite bodies were described within the ANS emplaced around 596-586 Ma (Campos Neto et al., 2011; Coelho et al., 2017).

A tectonic window divides the Socorro-Guaxupé Nappe into two lobes and exposes the migmatitic orthogneiss from the basement, which crop out between ANS rocks. These orthogneisses are separated into the Archean domains, the Amparo-Serra Negra and Heliodora-Minduri complexes, and the Pouso Alegre Complex from the Paleoproterozoic (Cioffi et al., 2016a, 2016b; Westin et al., 2016). The peak conditions of the Pouso Alegre Complex were constrained around 770°-775°C and 10-12 kbar at 630-620 Ma (Cioffi et al., 2019). These orthogneiss complexes are interpreted as parts of the paleocontinent São Francisco that were incorporated and reworked in the Brasilia orogeny and then exhumed together with ANS.

The Carrancas and Lima Duarte Nappes are metasedimentary sequences that crop out in the orogen northeast, close to the São Francisco Craton border. The Lima Duarte Nappe is a metapsammitic sequence interlayered with metapelite and calcsilicate rocks, metamorphosed under upper amphibolite and granulite facies with evidence of partial melting. The Carrancas Nappe is mainly composed of quartzite and graphite-bearing metapelite. It displays in its front an inverted metamorphic pattern from greenschist to lower amphibolite facies (Campos Neto et al., 2004; Trouw et al., 2000; Westin et al., 2019; Westin and Campos Neto, 2013). The peak conditions in this section were achieved between 590-575 Ma (Campos Neto et al., 2011; Machado et al., 1996; Valeriano et al., 2004; Valladares et al., 2004). Both sequences are interpreted as deposited in the passive margin of the São

Francisco paleocontinent (Campos Neto et al., 2011; Westin et al., 2019; Westin and Campos Neto, 2013).

2.2.1 Andrelândia Nappe System (ANS): P-T-t paths and tectonic evolution

The Andrelândia Nappe System (ANS) is divided into two sectors separated by basement inliers. In the north sector, the ANS is bounded by the Guaxupé Lobe of the Socorro-Guaxupé Nappe at its top, by the Carrancas Nappe at its bottom, and it is internally divided into the Três Pontas-Varginha and Carmo da Cachoeira Nappes. Whereas in the southern sector, the Socorro lobe of Socorro-Guaxupé Nappe is located at ANS bottom and the basement rocks from the São Vicente Complex at its top. The ANS in its southern sector is divided, from uppermost structural level to the bottom, in the Pouso Alto (or Aiuruoca, Carvalhos and Serra da Natureza Klippes equivalent), Liberdade and Andrelândia Nappes.

The ANS uppermost structural nappe is represented by K-feldspar+garnet+kyanite+rutile-bearing paragneiss, interpreted as a residual HP-granulite. The HP-granulite constitutes the Passos Nappe and Três Pontas-Varginha Nappe in the northern part of the SBO, whereas, in the southern portion, the HP-granulite is part of Pouso Alto Nappe (PAN), and the klippes of Auiruoca, Carvalhos, and Serra da Natureza. The K-feldspar+garnet+kyanite+rutile-bearing gneiss reached metamorphic conditions around 850°-900°C and 12-16 kbar (Campos Neto et al., 2010; Campos Neto and Caby, 2000; Cioffi et al., 2012; Fumes et al., 2021; Garcia and Campos Neto, 2003; Li et al., 2021; Reno et al., 2009). The timing of this HP-HT metamorphic event is variable in the literature. Proposed ages, based on monazite geochronology, are 660-650 Ma by Reno et al. (2012, 2009), 635 Ma by Fumes et al. (2021), 617 Ma by Campos Neto et al. (2010), and 604 Ma by Motta and Moraes (2017). Li et al. (2021) suggested two metamorphic loops for developing the HP-granulites based on the age spread. According to the latter authors, the first loop, with peak *P-T* conditions around 500-600°C and 11-20 kbar, occurred at *ca.* 660-650 Ma. The first cycle ended around 617 Ma when the second loop was initiated, reaching peak condition of *ca.* 13 kbar and 830°C at *ca.* 605 Ma.

The Liberdade Nappe (LN), the intermediate unit of ANS, is composed of garnet+kyanite+ilmenite(±sillimanite±rutile)-bearing gneiss/schist with subordinate

quartzite, metamafic, and calc-silicate lenses. The metamorphic conditions in metapelites are constrained in the *P-T* range of 642-715°C and 6-10 kbar (Coelho et al., 2017; Motta and Moraes, 2017; Rodrigues et al., 2019; Santos et al., 2004). Zircon and monazite U-Pb dating retrieved ages around 620-615 Ma (Coelho et al., 2017; Motta and Moraes, 2017; Westin et al., 2021). Moreover, the metamafic rocks, interpreted as retroeclogites (Campos Neto and Caby, 1999; Coelho et al., 2017; Reno et al., 2009; Trouw et al., 2013), experienced *P-T* conditions around 700°-800°C and 12-16 kbar (Coelho et al., 2017; Reno et al., 2009; Tedeschi et al., 2017). The metamafic rocks present two clusters of metamorphic ages, the first around 680-660 Ma (Campos Neto et al., 2011; Reno et al., 2009) and the other around 630-625 Ma (Coelho et al., 2017; Tedeschi et al., 2017).

The Andrelândia (AN) and Carmo da Cachoeira Nappes are at the bottom of the ANS stack. They are internally divided into three lithostratigraphic units. From the top to the base they are: the Rio Capivari, Santo Antonio, and Serra da Boa Vista. The Andrelândia Nappe displays an inverted metamorphic gradient in which "peak" mineral assemblages vary from garnet+biotite+staurolite at its bottom and kyanite+garnet+melt at the top. The Andrelândia and Carmo da Cachoeira Nappes attained peak conditions around 650-670°C and 9-10 kbar in *ca.* 600 Ma, followed by almost isothermal decompression in the period of 600-575 Ma (Frugis et al., 2018; Motta and Moraes, 2017; Reno et al., 2012; Santos et al., 2004; Westin et al., 2021). In summary, the ANS displays an inverted metamorphic pattern, in which rocks in high-P granulite metamorphic facies overlaps structurally those in amphibolite facies conditions. Although, internally the nappes stack, the inverted metamorphic behavior is observed just in the Andrelândia Nappe (Motta and Moraes, 2017).

The ANS provenance study reveals information about the tectonic sedimentation settings and likely source areas. The Liberdade Nappe has maximum depositional age of 760 Ma, and isotopic and rare elements analyses point to sediments derived from a continental magmatic arc and erosion of an active margin basement localized in the east-northeastern Paranapanema margin (Frugis et al., 2018). In opposite, the Andrelândia Nappe maximum depositional age was constrained at *ca.* 680-670 Ma. In addition, the Santo Antônio unit has isotopic signatures of sedimentation in an intraoceanic convergent setting with direct contribution from island arcs (Mara Rosa-Type). Whereas the isotopic characteristics of the

Serra da Boa Vista Unit suggest syn-collisional sedimentation with sources in the Paranapanema and São Francisco paleo-continents (Frugis et al., 2018).

Two models are proposed to address the issues related to the Andrelândia Nappe System tectono-metamorphic evolution (Fig. 8 and 9) and contrast ideas of progressive versus polyphase deformation within the Southern Brasilia Orogen (SBO). One of the views suggests that the ANS would represent a distal passive margin deposit with the main source in the São Francisco Craton and the suture between Socorro-Guaxupé and the Três Pontas-Varginha/Pouso Alto Nappes (Fig. 8; Marimon et al., 2021). The SBO collision onset would take place at *ca.* 625 Ma, based on the age of the high-pressure metamafic rocks emplaced within the Liberdade Nappe, and the exhumation occurred from 620 to 600 Ma (Fig. 8; Coelho et al., 2017). Between 600-580 Ma, the ANS underwent a second episode of metamorphism and deformation due to an interference of the collisional processes in the Central Ribeira Orogen (Fontainha et al., 2020; Hackspacher et al., 2004; Trouw et al., 2013). The main features related to the Central Ribeira Orogeny interference would be the leucogranites crystallization in 590-580 Ma and NW-SE shortening structures related to the sillimanite isograd (Fig. 8; Coelho et al., 2017; Fontainha et al., 2020; Hackspacher et al., 2004; Trouw et al., 2013).

Another view proposes that the ANS is resulted of the progressive deformation migration from WSW to ENE into a single orogenic event (Fig. 9). The ANS metasedimentary rocks would have provenance from different sedimentary settings (Campos Neto et al., 2011; Frugis et al., 2018; Westin et al., 2021). The ANS maximum depositional age, in conjunction with the high-P metamafic rocks metamorphism age, were used to estimate the SBO collision onset at *ca.* 670 Ma (Frugis et al., 2018; Reno et al., 2009). The nappes exhumation and migration initiated around 630 and goes until 590 Ma, a protected period of *ca.* 40 Ma, driven by channel flow mechanism (Fig. 9; Campos Neto et al., 2011; Westin et al., 2021). The orogenic collapse took place around *ca.*590 Ma and led to leucogranites emplacement, and the sillimanite widespread through the ANS would result of retrometamorphism and exhumation (Fig. 9; Campos Neto et al., 2011; Frugis et al., 2018; Westin et al., 2021).

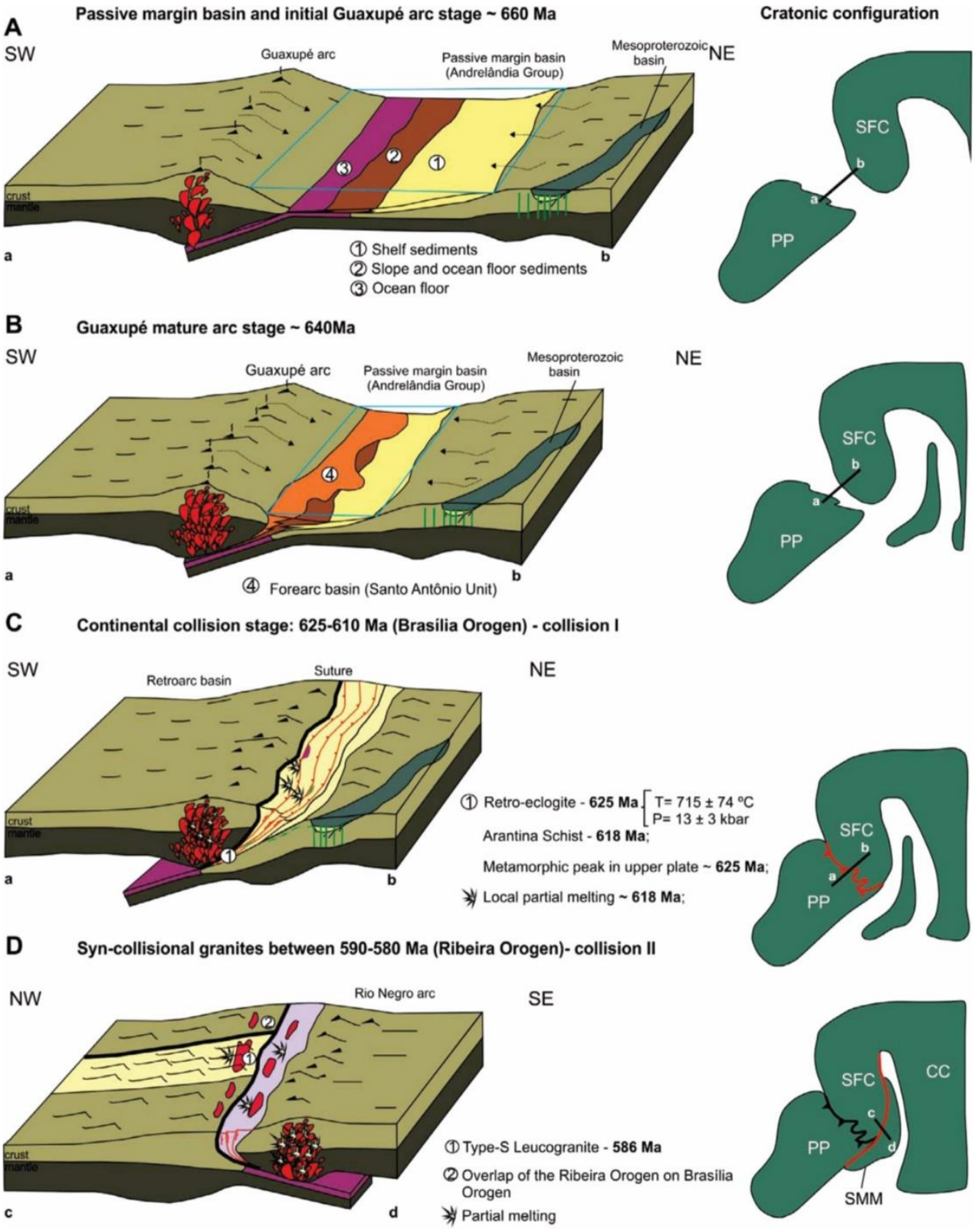

Figure 8 - Southern Brasilia Orogen tectonic evolution model taking into account the interference by the Central Ribeira Orogeny from Coelho et al.(2017).

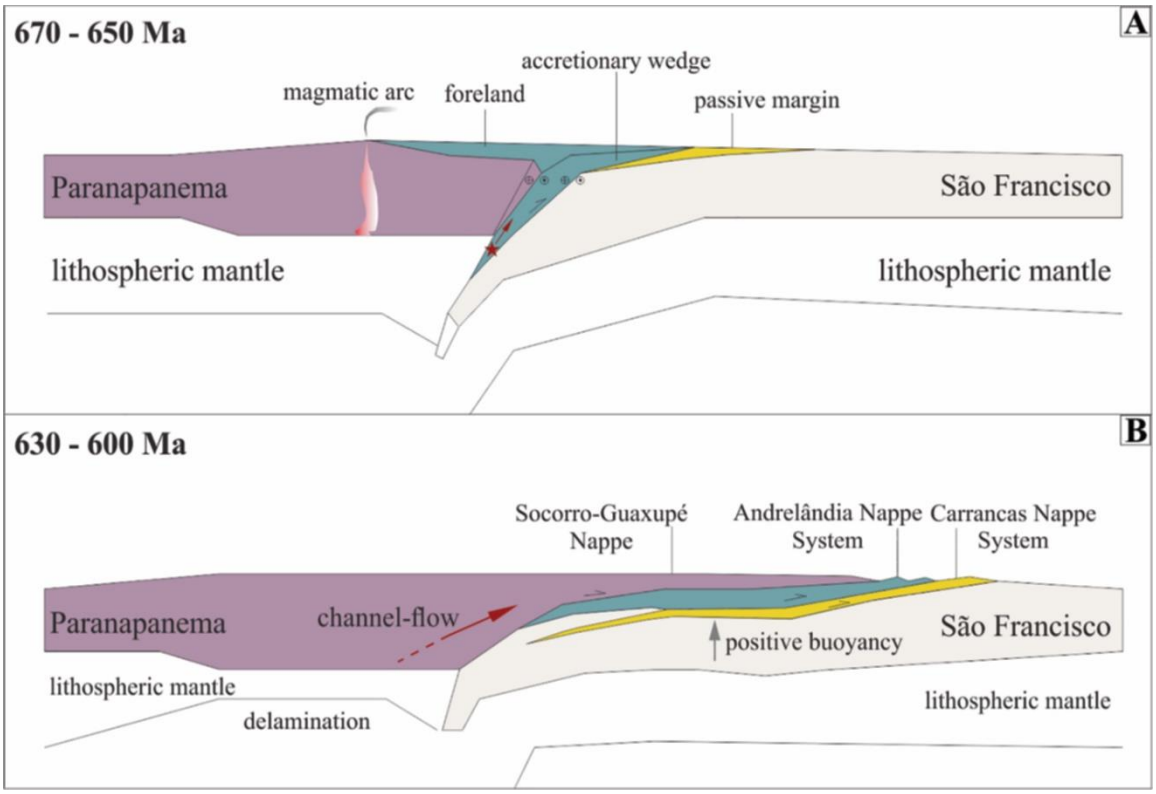

Figure 9- Tectonic evolution of the Southern Brasilia Orogen based on the progressive deformation migration during a single orogenic event from Westin et al.(2021).

CHAPTER 3

MAPPING TECTONO-METAMORPHIC DISCONTINUITIES IN OROGENIC BELTS: IMPLICATIONS FOR MID-CRUST EXHUMATION IN NW HIMALAYA

3.1 Abstract

A newly identified high-temperature shear zone, the Badrinath shear zone (BSZ), is described within the metamorphic core of the Himalayan belt along the Alaknanda valley, Garhwal Himalaya (NW India). A multidisciplinary approach comprising fieldwork, microstructural analyses, petrology, and *in situ* monazite geochronology was addressed to this high-strain zone to understand better its role in the evolution of the Greater Himalayan Sequence (GHS) along the study area. The Badrinath mylonite displays top-to-the-south thrust-sense of shear and affects a sillimanite-bearing gneiss showing evidence of partial melting.

The data integration allowed us to reconstruct the following model for BSZ development: the pre-mylonitic stage took place during prograde metamorphic path reaching conditions of 700-720°C and 10 kbar during the time interval of 34 and 23 Ma, with incipient partial melting, followed by nearly-isothermal decompression triggered by the shear activity between 23-19 Ma, with exhumation rate of ±0.3 cm yr^{-1}. Moreover, the rocks from the lower part of GHS, in the BSZ footwall, experienced metamorphic conditions of *ca.* 660-700°C and *ca.* 10-11 kbar, the partial melting and exhumation took place ~3 Ma after the BSZ. Such findings led us to correlate the BSZ with the High Himalayan Discontinuity (HHD) of the Central Himalaya. The BSZ is the first reported HHD branch in NW Himalaya (Garhwal). It corroborates the regional extent of the HHD accomplishing an important role during the GHS exhumation. In the Alaknanda valley, the BSZ activity accommodated deformation during early exhumation stages, 3 Ma before the MCTz and STDs coeval motion took place. Our observations point to a shift in time and place of the deformation responsible for triggering the GHS exhumation.

3.2 Introduction

In collisional settings, shear zones are structures usually associated with burial and exhumation processes. Two of the most known and studied shear zones in the largest modern collisional setting, the Himalaya, are the Main Central Thrust Zone (MCTz) and the South Tibetan Detachment system (STDs). Whereas the MCTz represents a thrust-sense shear zone, the STDS is a low angle normal-sense shear zone. One of the main reasons making the MCTz

and STDS so well studied is that current tectonic models focus on their coupled role during the exhumation of the medium-to high-grade core of the Himalaya belt. MCTz and STDS would represent respectively the lower and upper channel boundary where low viscosity/partially melted rocks from the mid-crust were extruded (Beaumont et al., 2001; Jamieson et al., 2004; Godin et al., 2006).

Notwithstanding the identification of an inner shear zone in the metamorphic core, the High Himalayan Discontinuity (HHD), enhances the complexity of the Himalayan orogenic system (Montomoli et al., 2013, 2015). The HHD is a tectono-metamorphic discontinuity, and several studies were done regarding its structural (Carosi et al., 2007, 2010; Goscombe et al., 2018; Montomoli et al., 2013, 2015), metamorphic (Kohn, 2008, 2014; Waters, 2019) and geochronological characteristics (Kohn, 2014, 2016; Wang et al., 2015). However, the multidisciplinary approach allowed to fully understand the HHD features (Carosi et al., 2010; Larson et al., 2015; Montomoli et al., 2013; Iaccarino et al., 2015, 2017a; Wang et al., 2015). In summary, the HHD is characterized, according to Carosi et al. (2018, 2019) and Montomoli et al. (2013, 2015), by a) kinematic indicators showing top-to-the south/southwest sense of shear, b) synkinematic growth of sillimanite along mylonitic foliation and quartz microstructures compatible with GBM_{II} regime (Stipp et al., 2002a); c) different *P-T* paths for the HHD hanging-wall and footwall rocks. Usually, the hanging-wall rocks are sillimanite- or kyanite-bearing migmatite that reached peak conditions in the sillimanite-stability field and experienced pressure of 2-3 kbar lower than the footwall rocks; d) the HHD was active at different times during the interval of ~28/27-17 Ma. The HHD tectonic activity previous to MCTz along the same structural section is one of its remarkable features. The HHD was traced in central and eastern Himalaya, but it has never been reported in the NW Himalaya, raising the question if the tectonic behavior of the GHS was different in the NW portion of the belt or if it was not yet detected in the field.

In order to assess the HHD presence in the western portion of the belt, a pressure-temperature-time-deformation (*P-T-t-D*) study was performed in the Garhwal Himalaya, focusing on the GHS. In this study, we coupled meso- and microstructural analyses with *P-T* paths, built using isochemical phase diagrams, and U-(Th)-Pb monazite *in situ* geochronology data as suggested by Montomoli et al. (2013). This applied integrative

methodology allowed us to reveal the occurrence of the HHD in the studied transect and to highlight its role during mid-crust rocks exhumation.

3.3 Geology of Alaknanda Valley

The study area, the Alaknanda valley, is localized in the Garhwal region, NW India. The main Himalayan units cropping out are: the Lesser Himalaya Sequence (LHS) and the Greater Himalaya Sequence (GHS) (Fig. 10).

The LHS is divided into three formations, from bottom to top they are (Jain et al., 2014): the Mandhali Formation, made up of marble, shale, and limestone, the Berinag Formation, made of quartzite, and the Munsiari Formation, which comprises orthogneiss and mylonitic garnet-bearing paragneiss. Detrital zircon crystals from LHS display Paleoprotezoic provenance ages spread in the time range of 2.70 to 1.60 Ga (Spencer et al., 2012a; Mukherjee et al., 2019).

The MCTz is delimited by lower and upper shear zones. The downward Munsiari thrust (MT) separates the Berinag quartzite from the Munsiari formation and the upper Vaikrita thrust (VT) at the bottom of the Joshimath Formation. Kinematic indicators, such as *S-C* shear band and minor asymmetric fold, point to a top-to-the-south sense of shear. Inside MCTz, the quartz deformation mechanisms vary from the subgrain rotation (SGR) to the grain boundary migration (GBM) recrystallization, and the metamorphic peak temperatures are from 450°C at the bottom to 750°C at the top of the shear zone (Célérier et al., 2009; Spencer et al., 2012b; Thakur et al., 2015; Hunter et al., 2018, 2019; Iaccarino et al., 2020). The shear activity took place in Munsiari, and Vaikrita thrusts at different times: 5-4 Ma and 20-9 Ma, respectively (Montemagni et al., 2018a, 2020; Iaccarino et al., 2020).

The GHS is divided into three formations (Jain et al., 2014 and references therein): the Joshimath, Suraithota (or Pandukeshawar, according to Spencer et al. (2012a), Thakur et al. (2015), Hunter et al. (2018)) and Bhapkund formations. The Joshimath Formation is the lower unit just above the VT. It is made up of kyanite-biotite bearing gneiss. The upward unit is the Suraithota Formation, constituted by kyanite-garnet-white mica gneiss interlayered with quartzite and amphibolite. The uppermost formation is the Bhapkund Formation, made

of garnet-biotite-sillimanite±kyanite-bearing migmatitic gneiss with intrusions of tourmaline-bearing leucogranite.

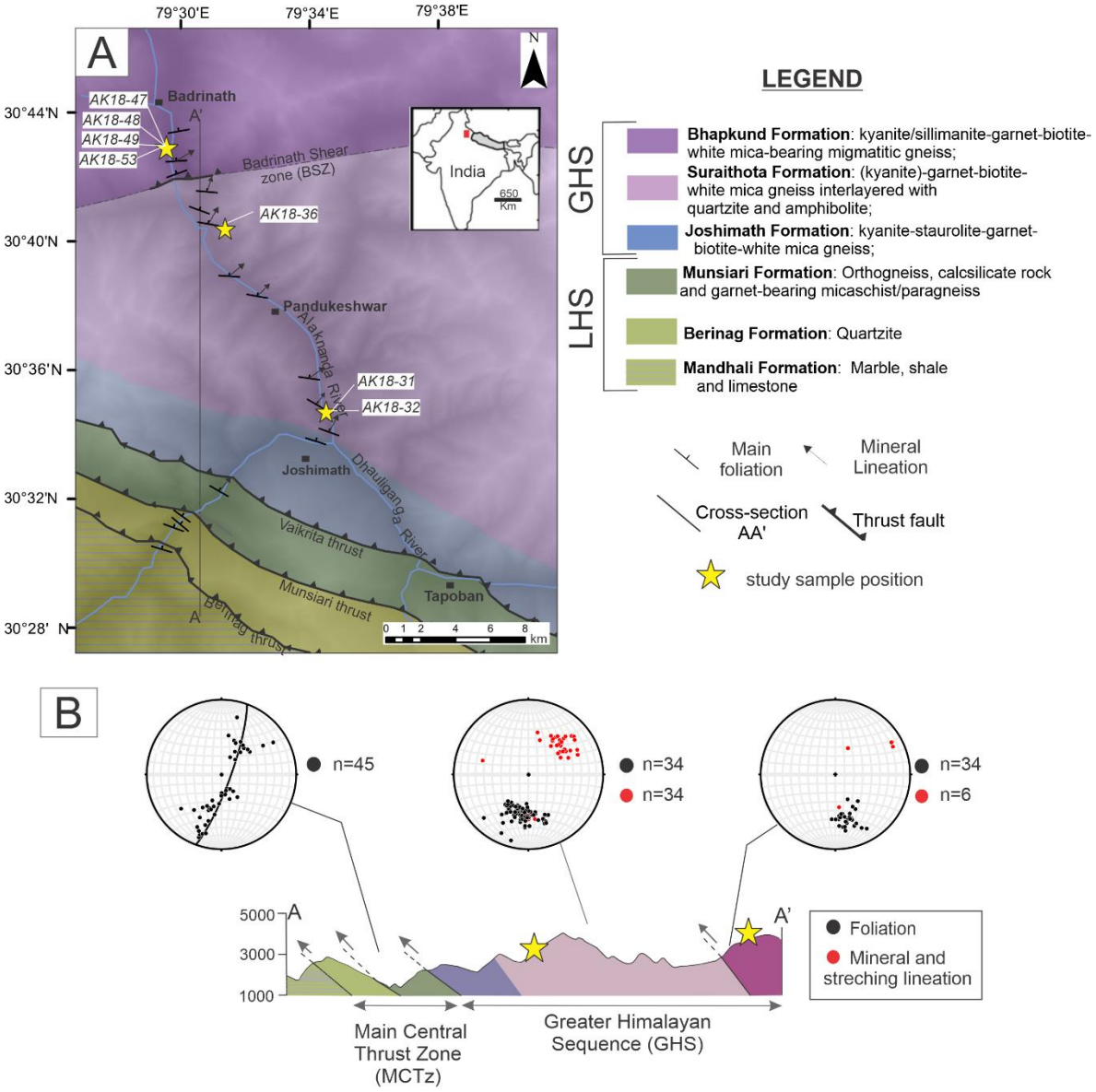

Figure 10 - a) Schematic geological map of the Alaknanda valley, including sample location (modified from Hunter et al., 2018b; Jain et al., 2014; and Iaccarino et al., 2020); b) Geological cross-section of the area and stereographic projections (lower hemisphere) of collected structural data.

The *P-T* evolution of the GHS in the Alaknanda-Duali Ganga valleys was studied by Hodges and Silverberg (1988) and Spencer et al. (2012b). The GHS metamorphic conditions estimated by Hodges and Silverberg (1988) vary from 645-550°C and 6-9 kbar, for rocks in the MCTz hanging-wall, and to 640-500°C and 3-5 kbar in the GHS upper structural level. According to Spencer et al. (2012b), the temperature ranges from 700°C to 800°C in the basal formation (Joshimath), reaching values between 800°C and 860°C in the middle (Suraithota) and the upper units (Bhapkund). Whereas the pressure condition goes from 10 to 14 kbar at the bottom, and the intermediary structural position decreases at the top of the sequence with values ranging from 8 to 10 kbar in the Bhapkund Formation. The ductile STDS activity was constrained in the nearby Dhauli Ganga valley between ~20 and 15 Ma (Iaccarino et al., 2017b; Montemagni et al., 2018b).

3.4 Sample description

Seven samples, four from Bhapkund Formation and three from the Suraithota Formation, were selected for detailed analyses. The sample positions are shown in Fig. 10. Table 1 summarizes the main features and applied methodology for each studied sample. Mineral abbreviations in the figures and text follow Whitney and Evans (2010).

3.4.1 Bhapkund Formation - Badrinath shear zone (BSZ)

The contact between the Bhapkund and Suraithota Formations near the Badrinath village (Fig. 10) is characterized by mylonite developed in a hectometer-thick shear zone, firstly described in this paper. This shear zone is named Badrinath shear zone (BSZ) and mainly affects sillimanite-garnet-bearing migmatitic gneiss of the Bhapkund Formation (Fig. 11a, b, and c). The mylonitic foliation (Sm) (Fig. 11b) strikes WNW-ESE and dips 40-60° toward N, while the mineral lineation trends NE-SW and plunges 15°-60° to NE (Fig. 10b). Quartz-feldspar-bearing stretched and rotated coarse-grained pods, wrapped by the mylonitic foliation (Fig. 11c and 12d), are interpreted as former leucosome. Macro and microscale kinematics indicators are observed, such as shear bands, asymmetric (sigma-type) polimineralic clast aggregates, rotated porphyroclasts, and group 1 mica-fish and feldspar fish (Passchier and Trouw, 2005) (Fig. 11a, 12a and 12b). All the kinematics indicators point to the top-to-the-south and southwest sense of shear.

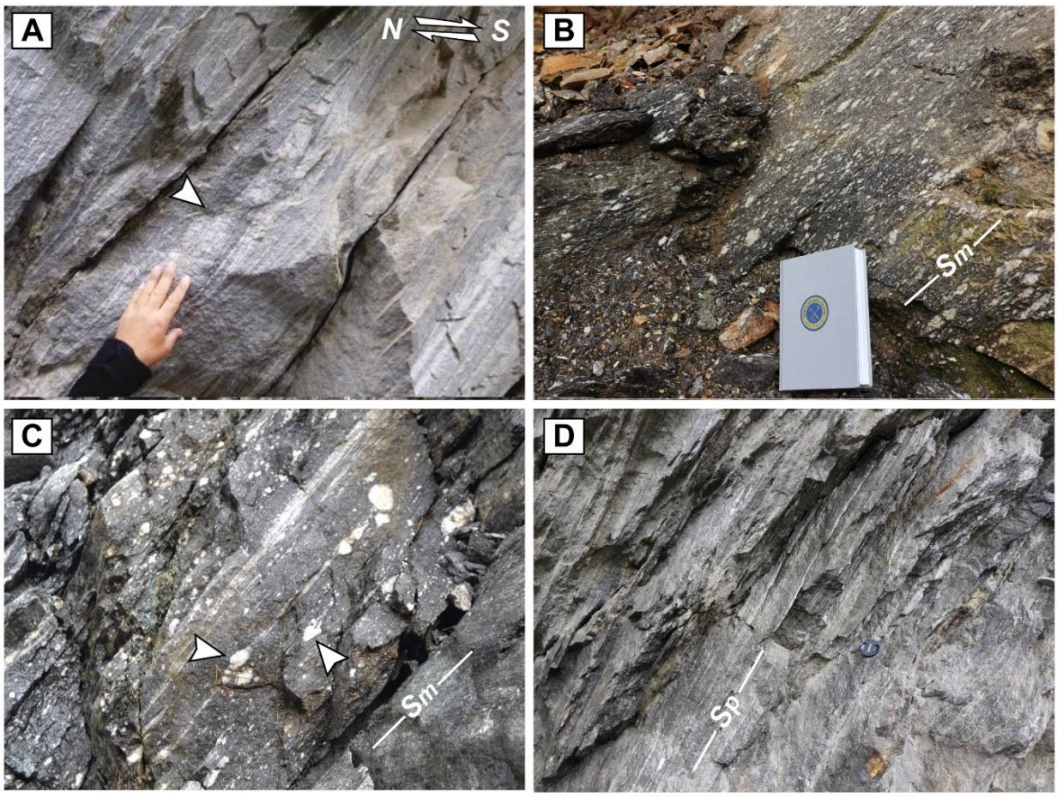

Figure 11-a) Top-to-the-south shear band (arrow) in sillimanite-bearing gneiss from Bhapkund Formation; b) Mylonitic foliation (S_m) of sillimanite-bearing migmatitic gneiss (BSZ – Bhapkund Formation); c) stretched and rotated deformed leucosome (arrows) wrapped by the mylonitic foliation of the BSZ; d) Main foliation (S_p) of garnet-biotite-muscovite gneiss from the Suraithota Formation in the BSZ footwall.

The main matrix mineralogy in the mylonite is quartz, plagioclase, white mica, biotite, garnet, ilmenite and sillimanite, with minor apatite, allanite, zircon, tourmaline and monazite. Quartz has irregular contacts and displays in some portions chessboard extinction (Fig. 12c), highlighting the high-T deformation (Law, 2014). Feldspar shows evidence of ductile deformation as supported by intergrowth between quartz and plagioclase forming myrmekites and the formation of plagioclase-fishes (Fig. 12b and d). Both quartz and feldspar microstructures point out a high-T deformation regime in the studied mylonitic samples.

Table 1- Summary of structural position, mineral assemblage, and main microstructures for selected samples.

	Sample	Structural position	Mineral Assemblage	Microstructures	Analysis
Bhapkund Formation - Badrinath Shear Zone (BSZ)	AK18-47	Hanging-wall	Qz-Pl-Ms-Bt-Sil-Ilm	Anastomosed disjunctive schistosity (S_m) defined by sillimanite and mica. The kinematic indicators are: S-C fabric mica fish and asymmetric sigma porphyroclasts.	Microstructure
	AK18-48	Hanging-wall	Qz-Pl-Ms-Bt-Grt-Ilm	Anastomosed disjunctive schistosity (S_m) defined by mica. S-C fabric, shear bands, and muscovite fish are the main kinematics indicators. Quartz chessboard extinction. Allanite inclusions in garnet.	Microstructure, *P-T* estimate, isochemical diagrams, and Mnz geochronology
	AK18-49	Hanging-wall	Qz-Pl-Ms-Bt-Grt-Ilm	Anastomosed disjunctive schistosity defined (S_m) by mica. S-C fabric, shear band, plagioclase, and muscovite fishes are the main kinematics indicators. Quartz chessboard extinction. Coarse-grained recrystallized leucosome layer.	Microstructure and *P-T* estimate
	AK18-53	Hanging-wall	Qz-Pl-Ms-Bt-Grt-Sil-Ilm	Anastomosed disjunctive schistosity (S_m) defined by sillimanite and mica. Quartz chessboard extinction. The kinematic indicators are S-C fabric, shear bands, and asymmetric sigma porphyroclasts. Disequilibrium textures developed during the cooling and melt crystallization are mymerkite and white mica, quartz, and plagioclase symplectite.	Microstructure, *P-T* estimate, isochemical diagram, and Mnz geochronology
Suraithota Formation	AK18-31	Footwall	Qz-Pl-Ms-Bt-Grt-Ilm-Rt	Anastomosed schistosity defined by mica. Intertectonic garnet with internal foliation (S_{p-1}) truncated by the external (S_p) one. Allanite inclusion in garnet.	Microstructure, *P-T* estimate, and isochemical diagrams
	AK18-32	Footwall	Qz-Pl-Ms-Bt-Grt-Ilm	Anastomosed schistosity, garnet both with internal foliation (S_{p-1}), which truncates the external (S_p) and snowball structure.	Microstructure and *P-T* estimate
	AK18-36	Footwall	Qz-Pl-Ms-Bt-Grt-Ilm	Anastomosed schistosity defined by mica (S_p).	Microstructure

Sillimanite, occurring as fibrolite, is orientated along the mylonitic foliation (Fig. 12e), and it is interpreted as a synkinematic mineral. Besides the sillimanite, biotite and white mica define the anastomosed disjunctive schistosity. In some portions, the white mica, quartz, and plagioclase made up symplectites (Fig. 12f), likely replacing K-feldspar, a microstructure interpreted as formed due to melt crystallization during the cooling/retrogression stage (Brown, 2002; Phillips et al., 1972). Garnet porphyroblasts, wrapped by the mylonitic foliation, are 1-2 mm in size. They show non-oriented inclusions of quartz, feldspar, white mica, biotite monazite, and allanite.

In summary, based on microstructural observations, three stages for the BSZ rocks are recognized: pre-mylonitic (pre-Dm), mylonitic (Dm), and post-mylonitic (post-Dm) (Fig. 13). The pre-mylonitic stage is represented by the assemblage enclosed in garnet with quartz, feldspars, allanite/monazite, white mica, biotite, and ilmenite as part of the equilibrium assemblage. The occurrence of highly sheared leucosome suggests that also partial melt took place before the mylonitic stage, and thus this stage is likely related to prograde burial. The mylonitic stage is characterized by the assemblage quartz+plagioclase+sillimanite+ biotite+garnet+white mica+ilmenite±K-feldspar. Metamorphic retrogressive textures of possible melt/K-feldspar replacement by white mica, quartz, and plagioclase and few thin allanite rims on monazite are related to the post-mylonitic stage (post-Dm).

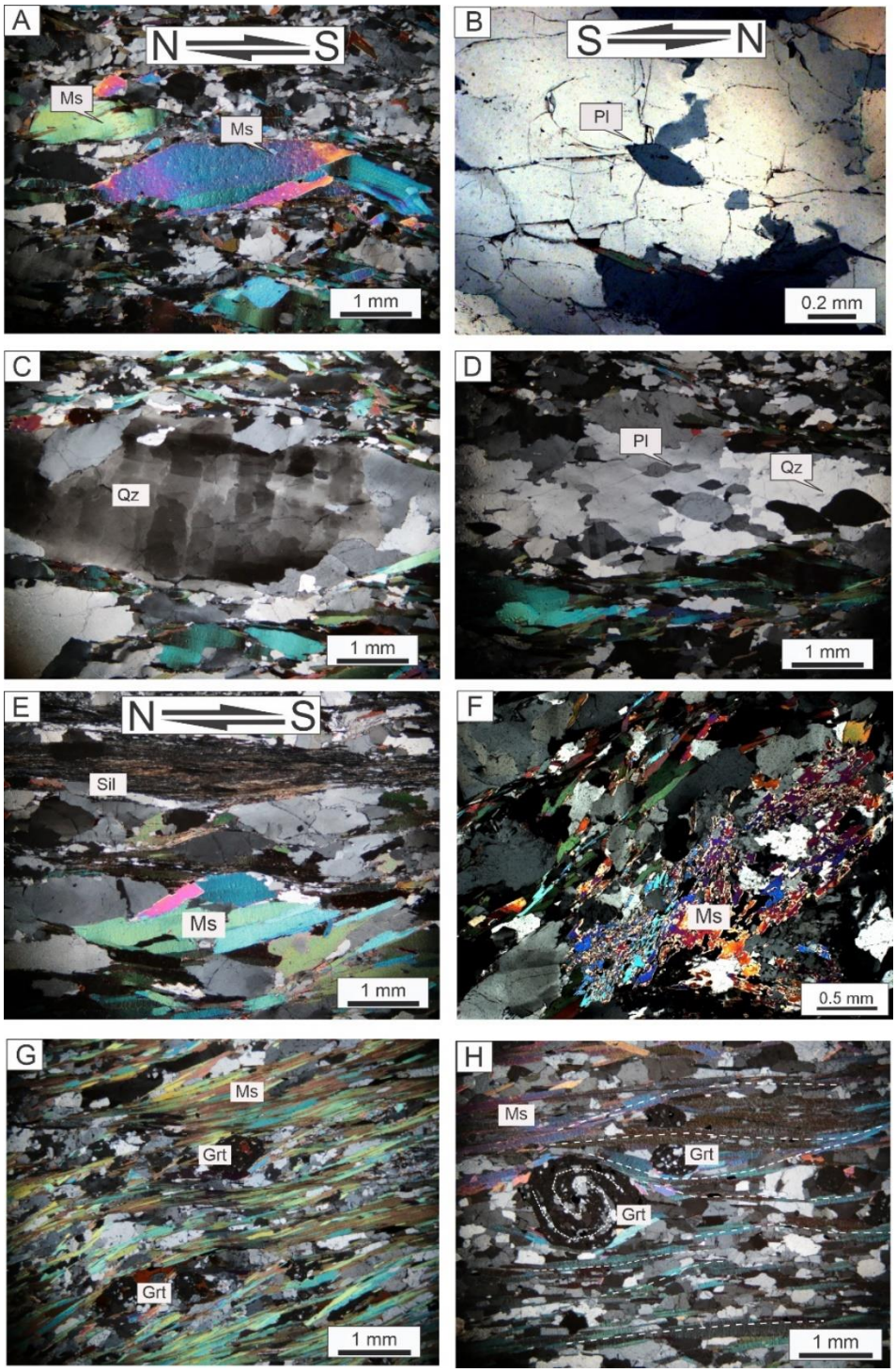

Figure 12 -a) White mica fish indicating a top-to-the-south sense of shear (BSZ, AK18-48); b) plagioclase fish pointing top-to-the-south sense of shear (BSZ, AK18-49); c) quartz with chessboard extinction pattern (BSZ, AK18-49); d) leucosome layer with coarse-grained quartz and plagioclase fishes (BSZ, AK18-49); e) sillimanite defining the mylonitic foliation and white mica aggregate in sigma (BSZ, AK18-47); f) white mica, quartz, and feldspar symplectite replacing K-feldspar (BSZ, AK18-53); g) anastomosed disjunctive foliation defined by biotite and white mica. in the paragneiss from the Suraithota Formation (AK18-36); h) snowball garnet from the Suraithota Formation (AK18-32).

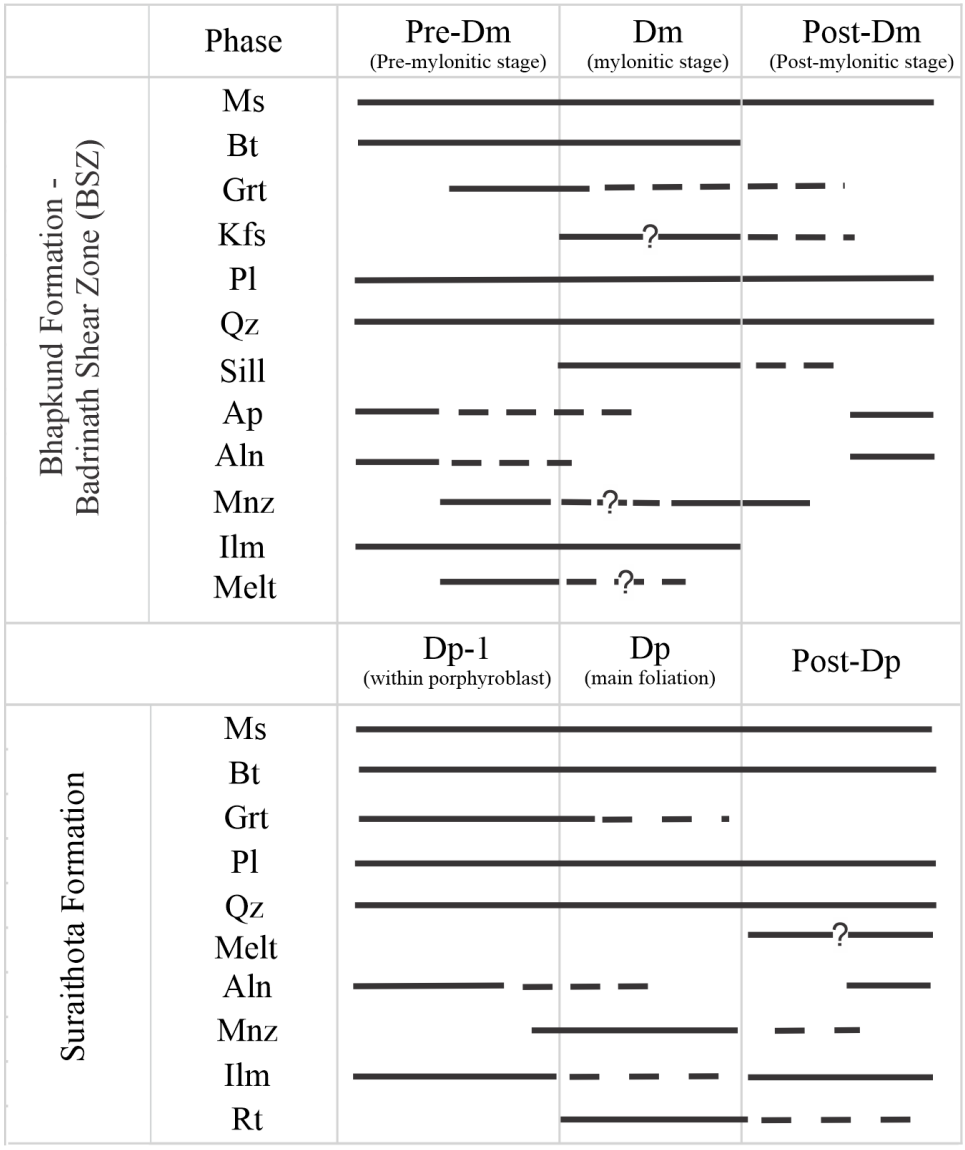

Figure 13 - Deformation-mineral growth relationships in the BSZ mylonite and the Suraithota Formation.

3.4.2 Suraithota Formation

Structurally beneath BSZ mylonites, garnet-biotite-muscovite schist/paragneiss, quartzite, and amphibolite, belonging to the Suraithota Formation, crop out (Fig. 11d). In order to check differences of metamorphism and deformation between the mylonites in the BSZ and the below paragneiss from the Suraithota Formation, the latter was also chosen as a target of this study. The main foliation (Sp) (Fig. 11d) strikes WNW-ESE and dips 40°-60° to NE, and the mineral lineation trends N20°-70° and plunges 30-50° to NE (Fig. 10b). Paragneiss has an anastomosed disjunctive schistosity, defined by white mica and biotite (Fig. 12g). Mineral assemblage is quartz, feldspar, white mica, biotite, garnet, ilmenite, rutile and as minor phases allanite and zircon. The rock matrix is characterized by a millimeter compositional banding between granoblastic and lepidoblastic layers, made by quartz+plagioclase, and white mica+biotite, respectively. Quartz is medium- to fine-grained and presents irregular contacts compatible with the GBM dynamic recrystallization regime. Garnet porphyroblasts (0.5 to 2 mm in size) are wrapped by the main foliation (Sp). Garnet has an internal foliation (S_{p-1}), which is not continuous with the main external foliation (Sp), defined by the preferential orientation of the enclosed minerals quartz, plagioclase, ilmenite, white mica, biotite, and allanite. Some garnet presents snowball microstructure (Fig. 12h). Therefore, garnet is regarded as inter- to syn-tectonic porphyroblast. Rutile was observed in the matrix surrounded by ilmenite

Based on such observations, three tectonic-metamorphic stages were recognized (Fig. 13). In the first stage (D_{p-1}), an early metamorphic assemblage associated with garnet internal foliation (S_{p-1}) composed by Qz+Pl+Grt+Ms+Bt+Ilm. The second stage (D_p), regarded the metamorphic peak paragenesis, is defined by the matrix minerals forming the external main foliation (S_p) Qz+Bt+Ms+Grt+Rt+Pl. The last stage, post-Dp, is related to ilmenite, white mica, and allanite growth, replacing minerals rim.

3.5 METHODS

3.5.1 Mineral chemistry and compositional x-ray maps

X-ray compositional maps of garnet (Y, Fe, Mg, Mn, and Ca), monazite (Si, Y, Th, P, Ce, Nd, Ca, La and U), and chemical analysis for the main minerals were obtained with a JEOL 8200 Super Probe equipped with five WDS spectrometers hosted at Dipartimento di Scienza Della Terra "Ardito Desio" of Università di Milano (table 1). An accelerating voltage of 15kV, a beam current of 5 and 150 nA (respectively for chemical analysis and X-ray maps), and a spot size of 1µm were used. Structural formula of each mineral was recalculated using the software AX by Tim Holland (https://filedn.com/lU1GlyFhv3UuXg5E9dbnWFF/TJBHpages/ax.html). Monazite formula, normalized to 16 oxygens, was obtained with an in-house excel spreadsheet.

3.6 Strategy for P-T estimates

Pressure and temperature were estimated using isochemical phase diagrams (samples AK18-48, AK18-53, and AK18-31; table 1) calculated through the software PERPLEX_X_6.8.7 (Connolly, 2005; version from November 2019). The samples were modeled in the system MnNCKFMASHT (MnO-Na_2O-CaO-K_2O-FeO-MgO-Al_2O_3-TiO_2-SiO_2-H_2O) using the internally consistent thermodynamic database of Holland and Powell (2011) and activity model mainly of White et al. (2014). The solid solution model Bi(W) was used for biotite, Mica (W) for white mica, Gt (W) for garnet, Opx (W) for orthopyroxene, feldspar for the plagioclase, and alkali feldspar (Fuhrman and Lindsley, 1988), Crd (W) for cordierite, IlGkPy ideal model for ilmenite and melt (W) for the liquid phases.

The bulk compositions used for calculations (table 4) were based on whole rock analysis obtained by X-ray fluorescence (XRF) on ground thin-section chips (Massonne, 2014). A correction of CaO allocated to apatite was done, and the ferric iron was excluded because of Fe^{3+}-rich oxides lack. The loss-on-ignition (L.O.I) values, representing the maximum H_2O value (Clarke et al., 2007; Groppo et al., 2009), were used as input for modeling. T-M_{H2O} pseudosections (at fixed pressure) were built (Hasalová et al., 2007) in order to assess modeled assemblage sensitivity (including Grt (vol%), melt (vol%), and

composition of minerals such as garnet and white mica) to the used H_2O contents (**appendix A** figures A1, A2, and A3). Moreover, in the case of samples (AK18-48 and AK18-31) where garnet shows prograde growth zoning, two sets of pseudosections were calculated. In the first set, the original bulk composition was used for modeling prograde stages. In contrast, in the second one, a chemical fractionation correction was applied subtracting the garnet core from the original bulk composition, following Massonne (2014) for estimating peak to-retrograde metamorphic stages. Garnet (and garnet core) modal amount was obtained through the software PolyLX (https://petrol.natur.cuni.cz/~ondro/oldweb/polylx:home), a toolbox in MATLAB. All the modeled bulk compositions are presented in table 4. We note, as already suggested by Groppo et al. (2009) and Iaccarino et al. (2017a) that due to the low modal amount of garnet (AK18-31 garnet (vol%)- 4%; AK18-48 garnet (vol%)- 2%) no significant change in pseudosection topology was observed but only a slight shift in isopleths (particularly spessartine).

Optimal multiequilibrium average *P-T* calculations with THERMOCALC software (Powell and Holland, 2008) were also applied (table 1). Such estimates were done using end-member activities calculated with the aforementioned AX software. Selected mineral chemistry of garnet, plagioclase, white mica, biotite, and ilmenite were chosen using textural and chemical criteria for ensuring compositions closest to the metamorphic equilibration peak, such as garnet near-rim (or core in diffusional profile) with low Mn (a.p.f.u.) and highest pyrope content (Spear, 1995). Due to the anatectic nature of these samples at peak conditions, water activity was adjusted at 0.8 in order to guarantee ϭfit values at 95% of significance level (Palin et al., 2014).

3.6.1 U-(Th)-Pb monazite geochronology

Monazite is a light rare earth element (LREE)-bearing phosphate mineral and a common metapelite accessory phase. This mineral represents a useful tool in petrochronological studies because: (1) the low Pb diffusion rates at high temperatures (<900°C), which enables it to be used as a geochronometer (Parrish, 1990); (2) The presence of distinct compositional domains related with multiple (re-)crystallization episodes, that record different metamorphic and deformational events (Spear and Pyle, 2002; Williams and

Jercinovic, 2002, 2012). The *in-situ* dating allows us to recognize monazite textural and structural relations and provides arguments to link age, metamorphism, and deformation, enabling to trace a more detailed record of the geologic history of its host rock.

Monazite was identified through a Scanning Electron Microscope hosted at the Earth Science Department of the University of Turin. The further step was to investigate the chemistry and the zoning of each monazite crystal using the electronic microprobe (EMP) described above. The monazite U-(Th)-Pb *in-situ* analysis was carried out using a laser-ablation, inductively coupled, plasma mass spectrometry (LA-ICP-Ms) at CNR-Istituto di Geoscienze e Georisorse U.O. Pavia (Italy). The equipment used was Ar-F 193-nm excimer (Geolas 102 from Microlas) coupled with 8900 triple quadrupole ICP-MS (Agilent), and the spot size was 10µm. The software GLITTER ® was used for data reduction (van Achterbergh et al., 2001). The data treatment was done with IsoplotR (Vermeesch, 2018). The data was plotted in a $^{206}Pb/^{238}U$ vs. $^{208}Pb/^{232}Th$ concordia diagram as suggested by Foster et al. (2000). The $^{208}Pb/^{232}Th$ ages were used when the monazite population ages are mentioned to avoid age overestimation due to ^{206}Pb excess on young samples. Data with discordance higher than 10% and/or a spot overlap were excluded to prevent bias data.

3.7 Results of mineral chemistry

Five samples were selected for mineral chemistry analyses, among them three are sillimanite-bearing migmatitic gneiss from BSZ (AK18-48, AK18-49, and AK18-53) and two of them (AK18-31 and AK18-32) are garnet-biotite-white mica gneiss from the Suraithota Formation, structurally below (i.e. the footwall) (table 1). The largest garnet crystals were chosen for X-ray maps in two samples of each structural position (AK18-48 and AK18-53 from BSZ and AK18-31 and AK18-32 from Suraithota Formation) (Fig. 14). Fig. 15, table 2 and 3 summarize the chemical content of the analyzed minerals.

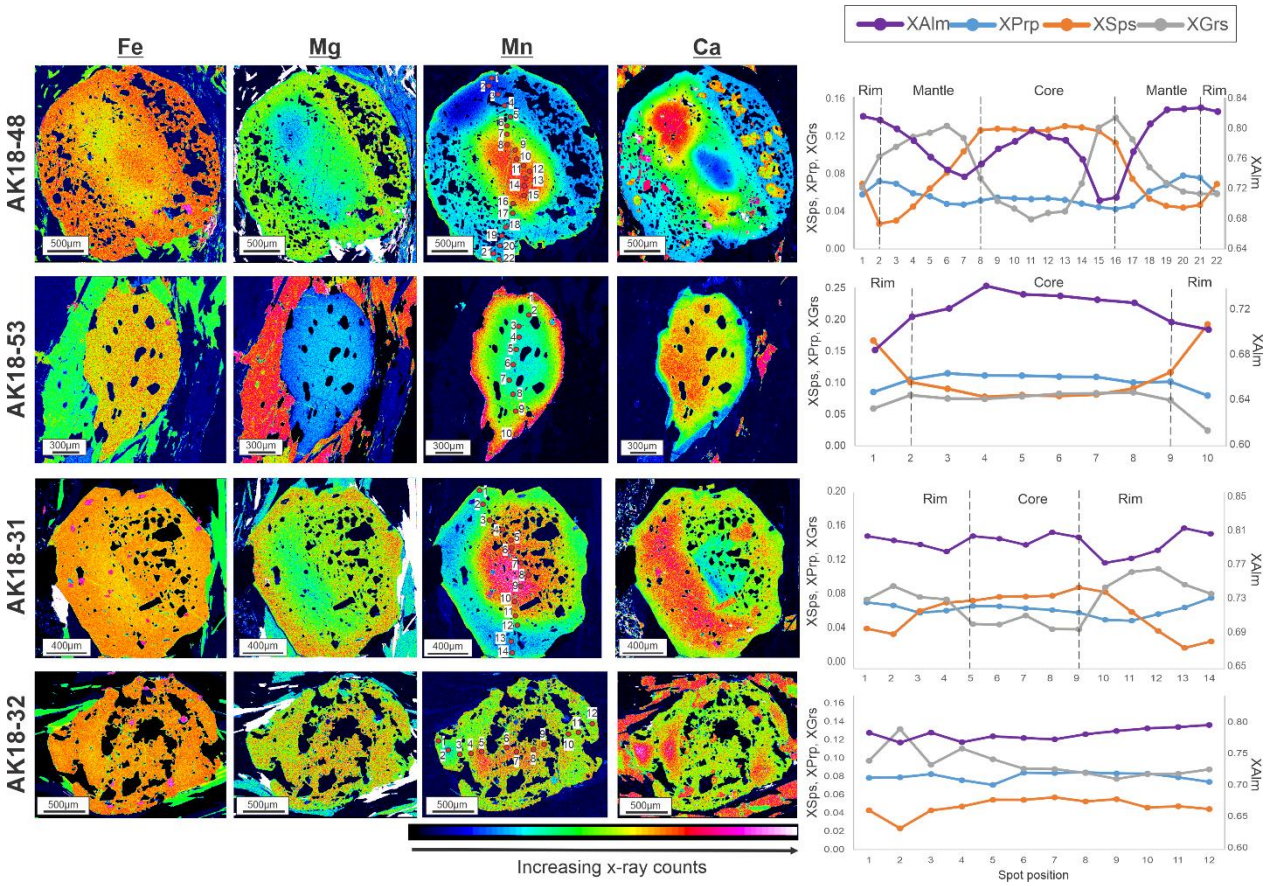

Figure 14 - Representative garnet X-ray compositional maps (elements: Mn, Ca, Mg, Fe) and related compositional profiles.

3.7.1 Badrinath Shear Zone mylonite (sillimanite-bearing migmatitic gneiss)

Sample AK18-48

Garnet in AK18-48 is almandine-rich and displays a core-rim zoning (Fig. 14), with increase of almandine (XAlm=Fe^{+2}/(Fe^{+2}+Mg+Mn+Ca)) and pyrope (XPrp=Mg/(Fe^{+2}+Mg+Mn+Ca)) toward the rim (Core–XAlm-0.69 and XPrp-0.03; Rim-XAlm-0.80 and XPrp-0.07) associated with a decrease of spessartine (XSps = Mn/(Fe^{+2}+Mg+Mn+Ca)) (core-XSps-0.08 and rim-XSps-0.02) (Fig. 14, 15a; Table 2). In the outermost rim an increase of spessartine (XSps-0.07) is observed, likely linked to requilibration during the retrograde path (Spear, 1995). The grossular (XGrs=(Ca/(Fe^{+2}+Mg+Mn+Ca)) in garnet shows a complex distribution, with some off-center enriched domains (XGrs-0.20), a core depleted in the grossular (XGrs-0.03), a mantle enriched (XGrs-0.12) followed by rim decrease in the Ca content (XGrs-0.06) (Fig. 14).

The plagioclase composition varies from anorthite (An = Ca/(Ca+Na+K)) 0.16 up to 0.86, with an increase in Ca from core to rim (Fig. 15b). This large compositional zoning occurs mainly in plagioclase enclosed in garnet, which has the highest An variations, between 0.22-0.86, whereas the matrix crystals have An values ranging from 0.16 to 0.33 (Fig. 14 and 15b; table 2).

Matrix biotite has Mg# (=Mg/Fe+Mg) values between 0.24-0.29 and Ti values of 0.10-0.20 (a.p.f.u), lower values of Mg# and higher-Ti is observed in biotite crystal within garnet (Mg#=0.35and Ti (a.p.f.u)=0.07) (Fig. 15c; Table 2). White mica has #Mg between 0.31 and 0.45, Si^{4+} content varying from 3.01 to 3.14 (a.p.f.u.) and Na^{+} varies from 0.06 to 0.08 (a.p.f.u.) (Fig. 15d). No correlation is observed between the chemistry ($Na^{+,}$ Si^{4+} and Mg#) and the structural position of white mica.

Sample AK18-49

Garnet in sample AK18-49 presents core enriched in spessartine (XSps-0.09) which decreases toward rim (XSps-0.04), while pyrope, grossular, and almandine display the opposite behavior, with increasing amounts from core to rim (Core-XAlm-0.78, XGrs-0.05 and XPrp-0.08; Rim-XAlm-0.80, XGrs-0.07, and XPrp-0.10) (Fig. 14 and 15a; Table 2). Values of An in matrix plagioclase are between 0.16 and 0.28 (Table 2; Fig. 15b). Internal zoning of plagioclase with a decreasing of An toward the core (from $An_{0.28}$ to $An_{0.16}$) is common. Biotite has Mg# between 0.29 and 0.34 and Ti (a.p.f.u.) from 0.11 to 0.23 (Fig. 15c; Table 2). Biotite crystals enclosed in garnet or close to its rims show higher Mg# (0.32-0.34) and lower Ti (0.12-0.13 a.p.f.u). It is not observed a clear compositional trend for white mica crystals, in which Mg# varies from 0.37 to 0.51, Si^{+4} (a.p.f.u.) ranges from 3.03 to 3.11 and Na^{+}(a.p.f.u.) is between 0.08 and 0.11 (table 2; Fig. 15d).

Sample AK18-53

Garnet shows a slight decrease of almandine, grossular, and pyrope from core (XAlm-0.74, XPrp-0.11, and XGrs-0.07) to rim (XAlm-0.68, XPrp-0.08, and XGrs-0.02) and an increase of spessartine from core (XSps-0.08) to rim (XSps-0.19) (Fig. 14, 15a; Table 2). The AK18-53 zoning pattern is typical of diffusional modified zoning (Spear, 1995). Plagioclase has a homogenous composition ($An_{0.15-0.20}$) (Fig. 15b; Table 2). The biotite (Mg#=0.35-0.40 and Ti (a.p.f.u.)=0.15-0.20) and white mica (Mg# = 0.40-0.56, Na^{+} = 0.07-0.10 a.p.f.u. and Si^{4+} = 3.00-3.16 a.p.f.u.) (Table 2; Fig. 15c and d) have no correlation between the crystal chemistry and microstructural position.

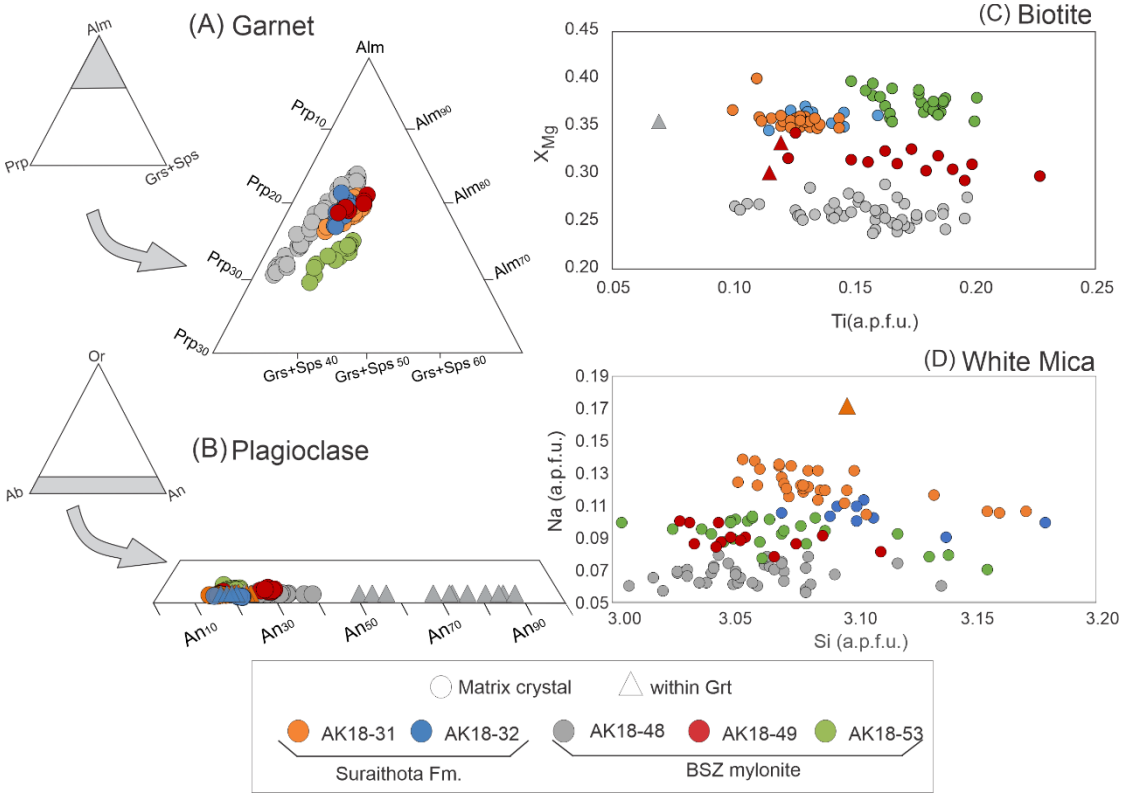

Figure 15 - Compositional diagrams for (a) garnet (b) plagioclase (c) biotite and (d) white mica.

Table 2 - Representative Electron Microprobe (EMP) analyses of minerals from BSZ. (b.d.l. - below detection limit).

Badrinath Shear Zone mylonites

	AK18-48									AK18-49								AK18-53					
	Grt - rim	Grt - core	Bt - matrix	Bt - within grt	Ms	Pl - matrix	Pl - within grt	Pl - within grt	Ilm	Grt - rim	Grt - core	Ms	Bt - matrix	Bt - within grt	Ilm	Pl - core	Pl - rim	Grt - core	Grt - rim	Ms	Bt	Pl	Ilm
SiO2	37.72	37.58	34.16	34.17	44.61	60.55	46.17	58.12	0.01	37.58	37.74	45.98	34.52	34.77	0.03	64.42	61.64	37.21	37.61	44.47	34.26	62.38	0.05
TiO2	0.05	0.02	3.34	1.19	0.71	b.d.l	b.d.l	b.d.l	52.19	0.06	b.d.l	0.96	3.90	2.13	52.56	b.d.l	b.d.l	0.03	0.03	1.09	3.44	b.d.l	51.79
Al2O3	21.64	21.51	18.13	18.78	36.01	24.14	33.61	25.26	0.03	22.05	21.69	36.50	17.79	19.88	b.d.l	22.52	24.81	21.54	21.61	34.32	18.75	22.30	0.04
Cr2O3	0.01	0.04	0.10	b.d.l	b.d.l	b.d.l	b.d.l	b.d.l	0.06	b.d.l	0.04	b.d.l	b.d.l	0.07	0.04	b.d.l	b.d.l	b.d.l	0.01	0.03	0.04	b.d.l	0.01
FeO_{Tot}	34.98	31.66	24.78	23.35	1.77	0.12	0.93	0.37	46.39	36.00	35.20	1.28	24.87	24.31	46.42	0.04	0.03	32.92	31.24	1.23	21.07	0.02	43.21
MnO	0.79	3.43	0.12	0.08	b.d.l	b.d.l	0.11	0.01	1.19	1.75	3.98	0.01	0.13	0.15	1.29	b.d.l	b.d.l	3.39	8.41	0.03	0.24	0.04	3.04
MgO	1.14	0.82	5.31	7.20	0.45	b.d.l	0.01	b.d.l	0.01	2.51	2.06	0.54	5.94	6.34	0.07	b.d.l	b.d.l	2.77	1.98	0.65	7.27	b.d.l	0.03
CaO	5.75	7	0.01	0.10	b.d.l	6.29	17.43	7.51	0.02	2.16	1.73	b.d.l	b.d.l	0.02	0.05	3.42	5.73	2.57	0.83	0.01	0.06	3.84	0.04
Na2O	b.d.l	b.d.l	0.09	0.12	0.46	7.90	1.53	7.28	0.01	b.d.l	b.d.l	0.79	0.08	0.10	0.01	9.84	8.01	0.06	0.04	0.76	0.18	9.35	0.02
K2O	b.d.l	b.d.l	9.22	9.45	10.29	0.14	0.02	0.17	b.d.l	b.d.l	b.d.l	10.05	9.41	8.96	0.01	0.07	0.18	b.d.l	0.02	9.85	9.12	0.14	0.04
Totals	102.09	102.06	95.26	94.43	94.3	99.14	99.8	98.72	99.9	102.11	102.45	96.1	96.64	96.74	100.49	100.31	100.4	100.48	101.77	92.44	94.43	98.07	98.27
Oxygens	12	12	11	11	11	8	8	8	3	12	12	11	11	11	3	8	8	12	12	11	11	8	3
Si	2.986	2.975	2.679	2.687	3.007	2.715	2.134	2.634	–	2.969	2.987	3.028	2.670	2.661	0.001	2.832	2.721	2.977	2.996	3.051	2.661	2.811	0.001
Ti	0.003	0.001	0.197	0.070	0.036	–	–	–	0.992	0.004	–	0.048	0.227	0.123	0.993	0.000	–	0.002	0.002	0.056	0.201	–	0.999
Al	2.019	2.008	1.677	1.741	2.862	1.276	1.831	1.349	0.001	2.054	2.024	2.834	1.622	1.794	–	1.167	1.291	2.032	2.030	2.776	1.717	1.185	0.001
Cr	0.001	0.002	0.006	0.000	–	–	–	–	0.001	–	0.002	–	–	0.004	0.001	–	–	–	0.001	0.002	0.002	–	–
Fe^{+3}	0.002	0.037	–	0.000	0.006	0.004	0.032	0.013	0.014	0.001	0.001	–	–	0.000	0.013	0.001	0.001	0.020	–	–	–	0.001	–
Fe^{+2}	2.314	2.055	1.626	1.535	0.094	–	–	–	0.965	2.377	2.329	0.070	1.609	1.556	0.960	–	–	2.180	2.081	0.070	1.369	–	0.927
Mn	0.053	0.230	0.008	0.005	–	–	0.004	–	0.026	0.117	0.267	–	0.009	0.010	0.027	–	–	0.230	0.568	0.002	0.016	0.002	0.066
Mg	0.135	0.097	0.621	0.844	0.045	–	–	–	–	0.296	0.243	0.053	0.685	0.723	0.003	–	–	0.330	0.235	0.066	0.842	–	0.001
Ca	0.488	0.594	0.001	0.008	–	0.302	0.863	0.365	0.001	0.183	0.147	–	–	0.002	0.001	0.161	0.271	0.220	0.071	0.001	0.005	0.185	0.001
Na	–	–	0.013	0.018	0.060	0.687	0.137	0.640	–	–	0.001	0.100	0.012	0.015	–	0.839	0.686	0.009	0.005	0.101	0.027	0.817	0.001
K	–	–	0.923	0.948	0.885	0.008	0.001	0.010	–	–	–	0.845	0.929	0.875	–	0.004	0.010	–	0.002	0.862	0.904	0.008	0.001
Sum	8.00	8.00	7.75	7.86	7.00	4.99	5.00	5.01	2.00	8.00	8.00	6.98	7.76	7.76	2.00	5.01	4.98	8.00	7.99	6.99	7.74	5.01	2.00
	XAlm-0.77	XAlm-0.69	XMg-0.28	XMg-0.35	XMg-0.32	XAn-0.30	XAn-0.86	XAn-0.36		XAlm-0.80	Xalm-0.78	XMg-0.43	XMg-0.30	XMg-0.32		An-0.16	An-0.28	Xalm-0.74	XAlm-0.70	XMg-0.49	XMg-0.38	An-0.18	
	XPrp-0.04	XPrp-0.03								XPrp-0.10	XPrp-0.08							XPrp-0.11	XPrp-0.08				
	XSps-0.02	XSps-0.08								XSps-0.04	XSps-0.09							XSps-0.08	XSps-0.19				
	XGrs-0.16	XGrs-0.20								XGrs-0.06	XGrs-0.05							XGrs-0.07	XGrs-0.02				

3.7.2 Suraithota Formation (garnet-biotite-muscovite gneiss in the BSZ footwall)

Sample AK18-31

Mn, Fe, and Mg display prograde zoning in garnet (Spear, 1995), with the pyrope and almandine increasing toward the rim associated with a spessartine decrease (Core- XAlm-0.77, XPrp-0.05, and XSps-0.09; Rim- XAlm-0.81, XPrp-0.09, and XSps-0.02) (Fig. 14, 15a; Table 3). Grossular is asymmetrically depleted in the core (XGrs-0.04) and enriched toward rim (XGrs-0.11). Plagioclase inside the garnet is An-rich ($An_{0.17-0.22}$) compared with those in the matrix ($An_{0.12-0.16}$) (Table 3; Fig. 15b). The Si^{4+} content in white mica increases from the core to rim and varies between 3.05 and 3.17 (a.p.f.u.). The Si^{4+} content in the white mica enclosed in garnet is 3.10 (a.p.f.u.). In addition, the white mica Na^{+} (a.p.f.u.) varies from 0.10 to 0.13 and Mg# ranges from 0.41 to 0.56 (Fig. 15d; Table 3). Biotite displays small compositional variations with Mg# varying from 0.35 to 0.40 and Ti between 0.10 and 0.14 (a.p.f.u.) (Table 3; Fig. 15c).

Sample AK18-32

X-ray map of a snowball garnet (Fig. 14) displays a decrease of Mn and Mg toward the rim (Core-XSps-0.06 and XPrp-0.08; Rim-XSps-0.02 and XPrp-0.06) compensated by an increase of Fe from core (XAlm-0.78) to rim (XAlm-0.80) (Fig. 15a; table 3). No zoning was detected for Ca in garnet, the grossular end-member has values between 0.08 and 0.13, and some off-center Ca-rich cores (XGrs=0.10-0.13) can be observed. Anorthite content in plagioclase varies from 0.14 to 0.21 (table 3; Fig. 15b), without a clear difference between crystals enclosed in garnet and those in the matrix. White mica Si^{+4} content is between 3.07 and 3.18 (a.p.f.u.), Na^{+} ranging from 0.09 to 0.11 (a.p.f.u.) and Mg# varies between 0.41 and 0.56 (Fig. 15d; Table 3). Biotite shows some variation with Mg# ranging from 0.34 to 0.38 and Ti varying from 0.11 to 0.16 (a.p.f.u.) (table 3; Fig. 15c).

Table 3 - Representative Electron Microprobe (EMP) analyses of minerals from Suraithota Formation. (b.d.l. - below detection limit).

Suraithota Formation

	AK18-31							AK18-32						
	Grt - rim	Grt - core	Bt	Ilm	Ms	Pl - matrix	Pl - within grt	Grt - rim	Grt - core	Bt	Ms	Ilm	Pl - matrix	Pl - within garnet
SiO2	37.95	37.37	35.98	0.08	46.67	64.51	62.43	37.64	37.63	35.51	46.30	0.06	62.90	64.11
TiO2	0.04	b.d.l	2.52	52.48	0.82	0.03	0.01	0.05	0.06	2.77	0.80	52.14	b.d.l	0.02
Al2O3	21.87	22.05	18.54	0.04	36.27	22.61	23.37	21.76	21.49	18.11	34.76	0.02	23.22	22.42
Cr2O3	b.d.l	b.d.l	0.04	b.d.l	b.d.l	b.d.l	b.d.l	b.d.l	b.d.l	b.d.l	0.01	0.02	b.d.l	b.d.l
FeOTot	36.25	36.17	23.30	47.34	1.55	b.d.l	0.45	34.40	34.48	22.89	1.58	46.12	0.03	0.18
MnO	1.38	3.65	0.10	0.51	0.04	b.d.l	0.03	1.03	2.52	0.03	0.02	0.64	b.d.l	b.d.l
MgO	2.03	1.67	7.33	0.09	0.77	b.d.l	0.01	1.99	2.10	7.30	0.73	0.16	b.d.l	b.d.l
CaO	2.99	1.57	b.d.l	0.05	b.d.l	3.39	4.71	4.62	3.07	b.d.l	b.d.l	0.02	4.26	3.14
Na2O	0.02	b.d.l	0.18	0.04	0.98	9.68	8.92	0.01	b.d.l	0.11	0.84	0.07	8.96	9.68
K2O	b.d.l	b.d.l	8.65	b.d.l	9.40	0.07	0.11	b.d.l	b.d.l	9.02	9.59	0.03	0.06	0.07
Totals	102.53	102.48	96.64	100.63	96.5	100.29	100.04	101.5	101.35	95.74	94.63	99.29	99.44	99.62
Oxygens	12	12	11	3	11	8	8	12	12	11	11	3	8	8
Si	2.989	2.964	2.734	0.002	3.052	2.834	2.767	2.983	2.996	2.729	3.093	0.002	2.793	2.835
Ti	0.003	–	0.144	0.989	0.040	0.001	–	0.003	0.004	0.160	0.040	0.995	–	0.001
Al	2.031	2.062	1.661	0.001	2.797	1.171	1.221	2.033	2.017	1.641	2.738	0.001	1.215	1.169
Cr	–	–	0.003	–	–	–	0.000	–	–	–	0.001	–	–	–
Fe^{+3}	–	0.01	–	0.018	0.010	–	0.015	–	–	–	–	0.011	0.001	0.006
Fe^{+2}	2.388	2.388	1.481	0.972	0.074	–	–	2.280	2.296	1.471	0.088	0.967	–	–
Mn	0.092	0.245	0.007	0.011	0.002	–	0.001	0.069	0.17	0.002	0.001	0.014	–	–
Mg	0.238	0.197	0.830	0.003	0.075	–	0.001	0.235	0.249	0.836	0.072	0.006	–	–
Ca	0.252	0.133	–	0.001	–	0.160	0.224	0.392	0.262	–	–	0.001	0.203	0.149
Na	0.003	–	0.026	0.002	0.124	0.825	0.767	0.002	–	0.016	0.109	0.004	0.771	0.830
K	–	–	0.838	–	0.784	0.004	0.006	–	–	0.884	0.817	0.001	0.003	0.004
Sum	8.00	8.00	7.72	2.00	6.96	4.99	5.00	8.00	7.99	7.74	6.96	2.00	4.99	4.99
	XAlm-0.80	XAlm-0.81	XMg-0.36		XMg-0.50	XAn-0.16	XAn-0.22	XAlm-0.77	XAlm-0.77	XMg-0.36	XMg-0.45		XAn-0.21	XAn-0.15
	XPrp-0.08	XPrp-0.07						XPrp-0.08	XPrp-0.08					
	XSps-0.03	XSps-0.08						XSps-0.02	XSps-0.06					
	XGrs-0.08	XGrs-0.04						XGrs-0.13	XGrs-0.09					

3.8 *P-T* conditions and Paths

Three samples were chosen to build isochemical diagrams (i.e., pseudosections), two of them from the BSZ (AK18-48 and AK18-53) and one from the Suraithota Formation (AK18-31) (table1). The isochemical diagrams were calculated for the *P-T* range of 3-12 kbar and temperatures of 650-900°C to the BSZ and 600-850°C to the Suraithota Formation. Quartz is observed in all fields. The T-M_{H2O} pseudosections (**appendix A** figures A1, A2, and A3) show that the peak metamorphic assemblage (including melt and observed volume of garnet) from the studied samples are stable in a wide range (~4-10 mol%) of H_2O amounts above the wet-solidus, attesting that the inferred water amount (based on L.O.I.) has no very large influence on our *P-T* estimates. The compositional isopleths of the main minerals are presented in **appendix A** figures A5, A6, and A7. Optimal average *P-T* estimations were performed on five samples, and the results are reported in Table 5.

Table 4 - Bulk rock compositions (mol%) of the studied samples used for pseudosection calculations. Original: XFR-based bulk composition – grt core: bulk composition corrected for garnet core (used for garnet rim calculations).

Sample	AK18-48		AK18-53	AK18-31	
(mol%)	original	− grt core	original	original	− grt core
SiO2	73.98	74.18	71.98	72.34	72.64
TiO2	0.57	0.57	0.75	0.45	0.45
Al2O3	7.51	7.47	8.24	8.87	8.82
FeO	4.44	4.29	4.96	3.5	3.20
MnO	0.06	0.03	0.08	0.09	0.05
MgO	1.48	1.47	2.74	1.22	1.21
CaO	1.24	1.23	0.94	1.18	1.17
Na2O	1.02	1.03	1.44	2.28	2.30
K2O	2.75	2.77	2.93	1.75	1.77
H2O	6.95	6.96	5.95	8.33	8.39

Table 5 - Summary of THERMOCALC optimal Average P-T *estimates for each studied sample.*

	Sample	"inferred" peak Assemblage	T(°C)	P(kbar)	SigFit	n° reactions
Badrinath shear zone (BSZ)	AK18-48	Qz+Pl+Grt+Ms+Bt+Ilm+L	719±45	7.8±1.3	1.12	4
	AK18-49	Qz+Pl+Grt+Ms+Bt+Ilm+L	678±35	6.5±1.1	1.01	4
	AK18-53	Qz+Sil+Pl+Grt+Ms+Bt+Ilm+L	723±53	6.2±1.8	1.49	5
Suraithota Formation	AK18-31	Qz+Pl+Grt+Ms+Bt+Rt+L	706±52	9.7±1.9	1.44	4
	AK18-32	Qz+Pl+Grt+Ms+Bt+Rt+L	701±51	8.5±1.7	1.40	4

3.8.1 Badrinath shear zone mylonite (sillimanite-bearing migmatitic gneiss)

Sample AK18-48

The isochemical diagram corresponding to this sample is shown in Fig. 16. The observed assemblage of this rock is Qz+Pl+Ms+Bt+Grt+Ilm(±L and Kfs), which is a triangular field in the isochemical diagram limited by ilmenite-in curve toward high pressure, by the melt-out at low temperatures and white mica-out at high temperatures. This field is quadri-variant constrained in the interval of 680-740°C and 5-11 kbar. Although the K-feldspar is not observed in this rock, it appears as a stable phase in the field. Three explanations can be given for this mineral lack in our sample: (1) K-feldspar low proportions in this field (<5%) is within the isochemical diagram uncertainties (Powell and Holland, 2008); (2) it could have been consumed during metamorphic back reactions and melt crystallization; (3) K-feldspar is present just as very fine grains hard to observe even with the microscope. The observed retrogressive textures, such as myrmekites and white mica symplectites with quartz and feldspar, support that the K-feldspar was a reactant phase during metamorphic back-reactions. Hence, according to these evidences, the most reasonable explanation for the lack of K-feldspar is option 2.

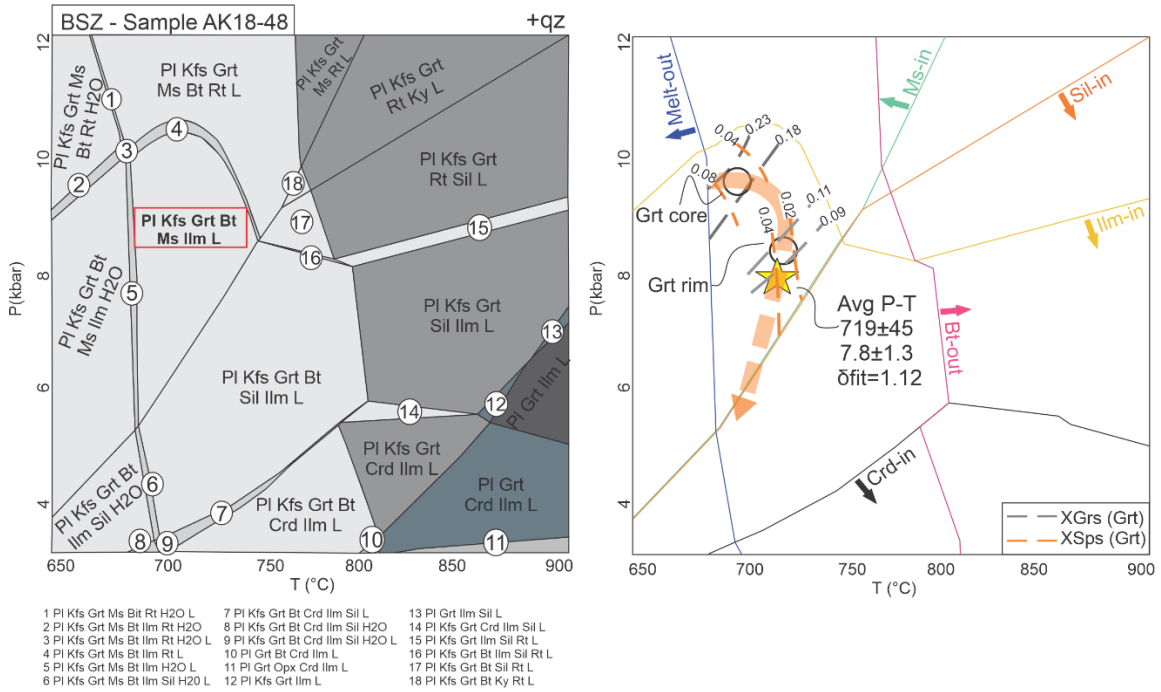

Figure 16 - P-T isochemical phase diagram in the MnNCKFMASHT system for AK18-48 (BSZ hanging-wall). The left diagram highlights the quadri-variant field for peak assemblage Qz+Pl+Kfs+Grt+Ms+Bt+Ilm+L. The right diagram shows the main minerals stability curves and P-T path based on mineral isopleths and THERMOCALC average P-T.

The distribution of garnet compositional isopleths intersected with garnet core composition (XGrs=0.23-0.18, XSps=0.04-0.08) suggests that the highest pressure achieved was 10 kbar in temperature interval between 690-710°C. Garnet rim (XGrs=0.09-0.11, XSps=0.02-0.04) provides metamorphic peak information and shows that the thermal peak was reached during the decompression at 720-730°C and ~8-9 kbar. The multiequilibrium average *P-T* calculation (719±45°C and 7.8±1.3 kbar) agrees with the results of the isochemical phase diagram (Fig. 16).

Sample AK18-53

The AK18-53 isochemical diagram is presented in Fig. 17. There are similar patterns between the AK18-48 (Fig. 16), and AK18-53 diagrams, and the larger changes are in the high-grade fields with the ilmenite stability field appearing at lower pressures. Even though the similarities between both isochemical diagrams, we decided to draw both due to high retrogressive features observed in AK18-53 compared with the AK18-48, which enabled us to better constrain the retrograde path.

The peak assemblage is Qz+Pl+Ms+Bt+Grt+Ilm+L, similarly to sample AK18-48, with the addition of sillimanite as a phase that grew during the development of the mylonitic foliation. The peak assemblage is comprised in the interval of 680-750°C and 5-10 kbar. This field is delimited on the high-pressure side by the ilmenite disappearance, while toward the high-temperature side by the white mica consumption and on the low-temperature side by the melt-in curve. A similar explanation of the AK18-48 could be given for lacking K-feldspar in the thin section.

Garnet porphyroclast composition presents a diffusional-modified profile hampering us to reconstruct the prograde segment of the path, which is inferred to be similar to sample AK18-48. The compositional isopleth matches garnet compositions (XAlm- 0.68 and XGrs-0.04) at 720°C and 7 kbar close to the Sil-in curve. The multiequilibrium average *P-T* obtained is inside the field where Qz+Pl+Ms+Bt+Sil+Grt+Ilm+L are in equilibrium at *P-T* conditions of 6.2±1.8 kbar and 726±53°C, respectively. These data, in agreement with isochemical diagrams results, record post-peak, retrograde conditions.

In summary, the BSZ *P-T* path, based on both isochemical phase diagrams (Fig. 16 and 17) and average *P-T*, evolved following a clockwise path, with decompression associated with the development of a sillimanite-bearing mylonitic foliation. The maximum pressure was reached at conditions of 10 kbar before the metamorphic peak temperature (between 700-730°C) achieved during the decompression with the development of mylonitic foliation related to top-to-the-S shearing.

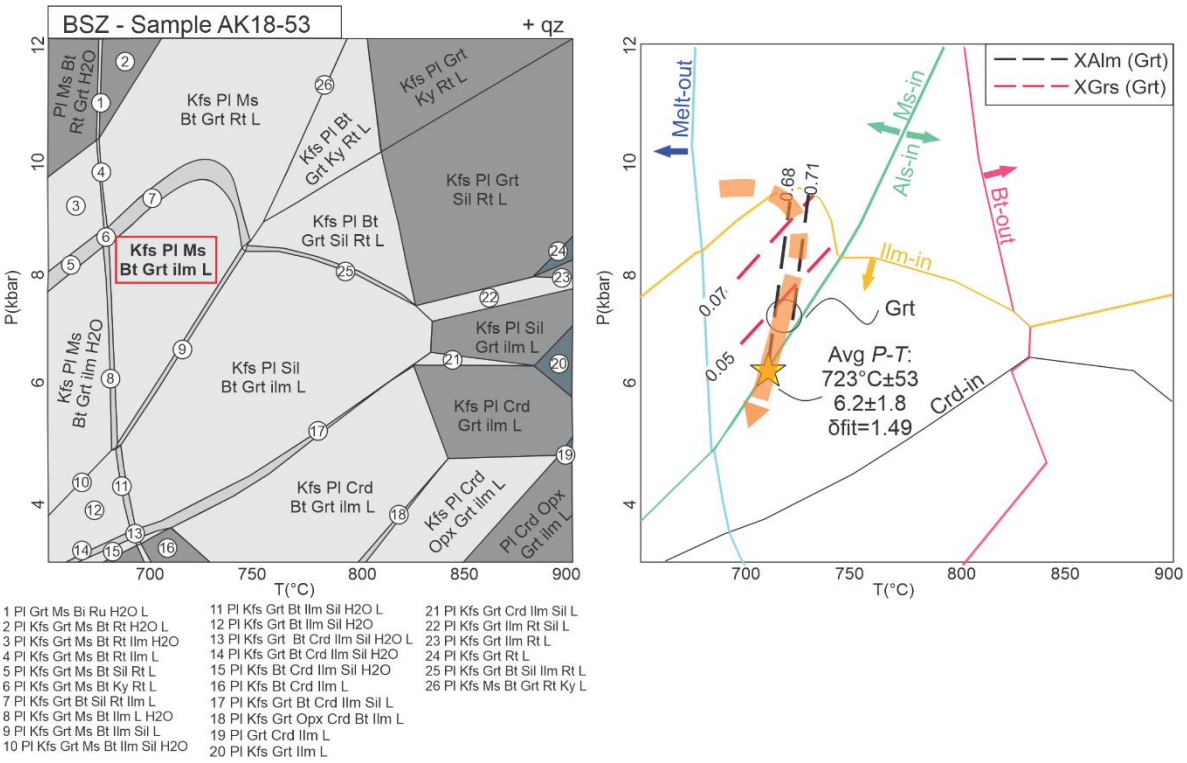

Figure 17 - P-T isochemical phase diagram in the MnNCKFMASHT system for AK18-53 (BSZ hanging-wall). The left diagram highlights the quadri-variant field for peak assemblage Qz+Pl+Kfs+Grt+Ms+Bt+Ilm+L. The right diagram shows the main minerals stability curves and P-T path based on mineral isopleths and THERMOCALC average P-T.

3.8.2 Suraithota Formation (garnet-biotite-muscovite gneiss in the BSZ footwall)

Sample AK18-31

Fig. 18 represents the isochemical diagram for sample AK18-31. The peak mineralogy observed in the thin section is Qz+Pl+Grt+Rt+Ms+Bt+L and is predicted within a *P-T* interval of ~8-12 kbar and 700-750°C. It is a penta-variant field delimited toward low temperature by the H_2O-in curve, in high grade by the Bt-out curve, and in low pressures by the Ky-in and Ilm-in curves.

The garnet core compositional isopleths (XAlm-0.79, XGrs-0.05, and XPrp-0.05) and Si^{+4} in white mica (~3.05) crossed in ~620°C and ~7 kbar in the field where Qz+Pl+Grt+Ms+Bt+Ilm+H_20 are the predicted stable phases and may yield information about the prograde path.

The intersection between garnet rim (XSps-0.02 and XGrs-0.08) and Si^{+4} in white mica (~3.13) compositions with compositional isopleths provides constraints for peak conditions of ~660°C and ~11 kbar. The average *P-T* calculations result is 706±52°C and 9.7±1.9 kbar, which is similar, within the relative uncertainties, to the pseudosection results. In summary, rocks in the BSZ footwall experienced a clockwise *P-T* path (Fig. 18). The *P-T* path evolved following pressure increase, starting from 7 kbar up to ~11 kbar with temperatures varying from 620°C to 700°C during the prograde metamorphism, likely associated with a deformation testified by garnet internal foliation. A near-isothermal decompression is suggested, in which rutile is consumed, and ilmenite grows, supported by texture observed at the microscale.

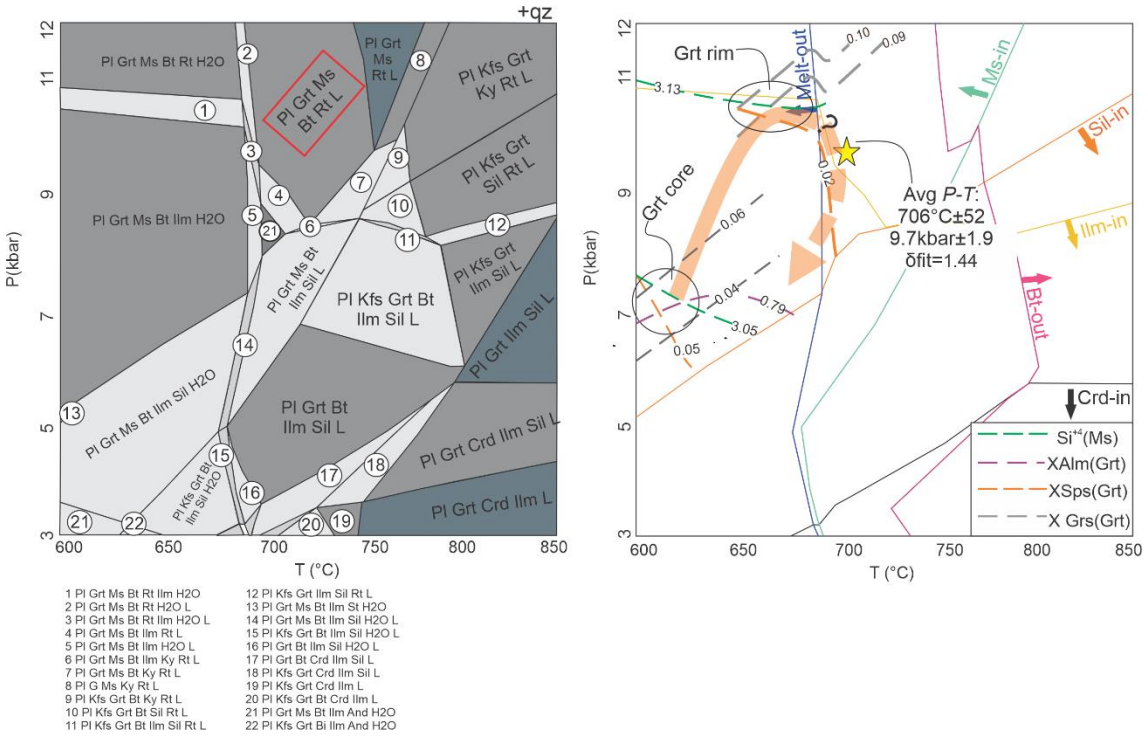

Figure 18 - P-T isochemical phase diagram in the MnNCKFMASHT system for AK18-31 (BSZ footwall). The left diagram highlights the quadri-variant field for peak assemblage Qz+Pl+Kfs+Grt+Ms+Bt+Ilm+L. The right diagram shows the main minerals stability curves and P-T path based on mineral isopleths and THERMOCALC average P-T.

3.9 Monazite composition and age

3.9.1 Monazite textural setting, chemistry, and zoning

The mylonites from the BSZ, samples AK 18-48 and AK 18-53, were analyzed for *in-situ* geochronology. The monazites from the sample AK18-48 have a length between 30 and 130 μm. They occur between quartz, plagioclase, biotite, and white mica in the matrix, usually laying along the mylonitic foliation. Two crystals of monazite are included in garnet. Allanite, apatite, and Th-oxide are observed forming rims in monazite. Zircon inclusion is found in the rim of one crystal.

The monazites from the sample AK18-53 have a length between 30 to 200 μm. The crystals in matrix layers are within quartz-rich domains or biotite and white mica layers within the mylonitic foliation. One monazite grain is associated with white mica forming a symplectic texture, intergrowth with quartz and sillimanite. Quartz, zircon, apatite, biotite, graphite, white mica, and sillimanite are recognized as inclusions in monazite. The crystals with sillimanite inclusion are particularly interesting because the sillimanite growth is concomitant with the shearing event.

The electronic microprobe analysis revealed that the monazite composition is mainly controlled by the cheralite substitution (Fig. 19a; $Th^{+4}+Ca^{+2}=2REE^{+3}$). The exchange between monazite and apatite in fluid presence is governed by the monazite loss of Ca+P going to apatite, compensated by the enrichment of Y+Si+REEs in monazite (Dumond et al., 2008). This correlation is not observed in the sample AK18-53, while the AK18-48 has rims enriched and cores depleted in Ca+P (Fig. 19b).

Three chemical zoned domains are recognized based on Y, Th, and REE content (Fig. 19c and d) and in X-ray maps (Fig. 20). In the sample AK18-48, only two of these domains (domain 2 and domain 3) have been identified. The domain 2 is characterized by cores with low Y content ranging from 0.02 to 0.07 (a.p.f.u.), Th between 0.12-0.25 (a.p.f.u.) and Y+HREE low amounts vary from 0.09 to 0.20 (a.p.f.u.). The second domain recognized is the domain 3 related with monazite rim, is characterized by high Y and Y+HREE content, $0.09<Y<0.28$ (a.p.f.u.) and $0.23<Y+HREE<0.45$ (a.p.f.u.), and low Th values $0.13<Th<0.19$

(a.p.f.u.). The monazites enclosed in garnet crystals follow the same zoning pattern as the other matrix crystals, in which the cores show low Y and Y+HREE (0.02<Y<0.07 a.p.f.u.; 0.11<Y+HREE<0.19 a.p.f.u.) and the rims are enriched of these same elements (0.20<Y<0.27 a.p.f.u.; 0.25<Y+HREE<0.38 a.p.f.u.).

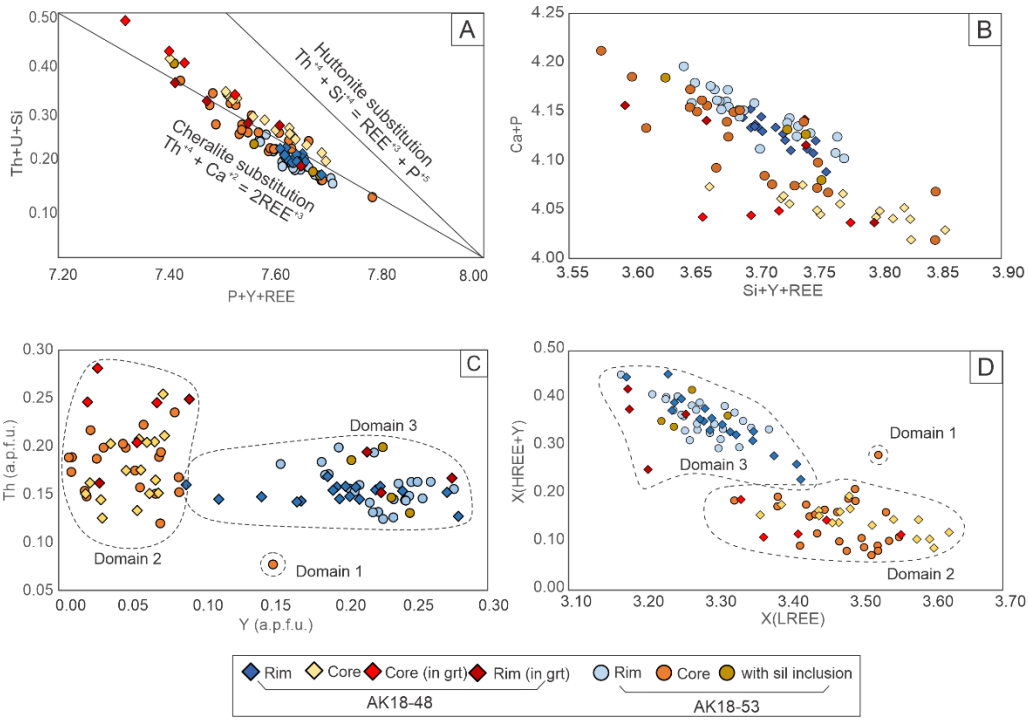

Figure 19 - Chemical monazite variations (monazite cations plot normalized to 16 oxygens). a) cheralite and huttonite exchange vectors are plotted; b) Ca+P vs. Si+Y+REE plot; c) Y vs. Th plot; d) Y+HREE vs. LREE plot; in c) and d) monazite compositional domains are highlighted: domain 1 is present only in the core observed of sample AK 18-53, domain 2 corresponds to monazite cores from sample AK 18-48 and sample AK 18-53; domain 3 represented by monazite rims of both samples and by a single grain located on the foliation containing sillimanite inclusions.

The sample AK18-53 displays three different chemical domains (Fig. 19). Domain 1, as documented by X-ray maps, occurs in the grain core with intermediate Y (*ca.* 0.15 a.p.f.u.) and low Th amount (*ca.* 0.08 a.p.f.u.) and Y+HREE ~0.31 (a.p.f.u.). Domain 2 is also related to monazite cores, however, it is characterized by low Y (<0.08 a.p.f.u.), a wide range of Th content (0.12<Th<0.24), and Y+HREE ranging from 0.07 to 0.21 (a.p.f.u). Discontinuous rims with medium to high Y values (0.15<Y<0.27 a.p.f.u.), Th values from 0.12 to 0.20 (a.p.f.u) and Y+HREE between 0.30< Y+HREE<0.45 are the main features of domain 3. The crystal with sillimanite inclusions has a homogenous growth correlated with domain 3 (0.20<Y<0.25 a.p.f.u.; 0.13<Th<0.20 a.p.f.u. and 0.34<Y+HREE<0.42 a.p.f.u.).

3.9.2 U-(Th)-Pb in situ Monazite Geochronology

Eight grains from the matrix aligned along the mylonitic foliation (S_m) and one crystal within garnet were selected from the sample AK18-48 to perform *in situ* LA-ICP-MS analysis, with a total of twenty-four spots (Table 6). The obtained ages are scattered in a narrow interval between 25 Ma and 19 Ma (Fig. 20a). The ages from domain 2, characterized by cores with low Y and Y+HREE contents, are spread between 25-22 Ma. Domain 3, distinguished by monazites rims with high Y and Y+HREE, has ages ranging from 22 Ma to 19 Ma. The crystal within garnet presented core age of 23 Ma and 21 Ma to the rim.

The *in-situ* analysis in the AK18-53 was carried out in matrix monazite that are preferentially elongated along the mylonitic foliation. Twenty-seven spots in seven different crystals were analyzed (Table 7). The ages are spread in an interval from 34 to 19 Ma (Fig. 20b). The oldest ages between 34-29 Ma correspond to domain 1 monazite cores with intermediate Y and low Th amounts. The ages from monazite core, with low Y and Y+HREE, related to domain 2 vary from 29 to 23 Ma. The obtained ages corresponding to domain 3, characterized by high Y and HREE contents, range from 23 to 19 Ma. The spots in monazite with sillimanite inclusion vary between 20 and 19 Ma, and both chemistry and age correspond to domain 3.

Table 6- LA-ICP-MS *U-(Th)-Pb* in situ *geochronological results for sample AK18-48.*

		AK18-48										
			ISOTOPES RATIOS						AGE ESTIMATES (Ma)			
Mnz Grain	Textural relation	Spot position	$^{207}Pb/^{235}U$	1 sigma	$^{206}Pb/^{238}U$	1 sigma	$^{208}Pb/^{232}Th$	1 sigma	$^{206}Pb/^{238}U$	1 sigma	$^{208}Pb/^{232}Th$	1 sigma
1.1	matrix	rim	0.04078	0.00121	0.00337	0.00007	0.00103	0.00001	21.7	0.43	20.8	0.25
1.2		rim	0.03320	0.00102	0.00316	0.00006	0.00099	0.00001	20.4	0.37	20.0	0.25
1.3		rim	0.04086	0.00120	0.00329	0.00006	0.00106	0.00001	21.1	0.38	21.4	0.25
17.1	matrix	rim	0.03860	0.00113	0.00315	0.00006	0.00101	0.00001	20.3	0.37	20.3	0.25
17.2		rim	0.03767	0.00111	0.00327	0.00006	0.00103	0.00001	21.0	0.38	20.7	0.25
17.3		core	0.10655	0.00305	0.00392	0.00007	0.00121	0.00001	25.2	0.47	24.5	0.27
17.4		rim	0.02993	0.00088	0.00299	0.00006	0.00095	0.00001	19.2	0.36	19.1	0.24
27.1	matrix	rim	0.03143	0.00103	0.00325	0.00006	0.00098	0.00001	20.9	0.42	19.8	0.25
27.2		core	0.02967	0.00108	0.00331	0.00007	0.00102	0.00001	21.3	0.42	20.6	0.25
19.1	matrix with Zr rim	rim	0.03063	0.00106	0.00318	0.00006	0.00095	0.00001	20.5	0.37	19.3	0.24
19.2		rim	0.02901	0.00096	0.00320	0.00006	0.00098	0.00001	20.6	0.38	19.8	0.25
19.3		rim	0.03238	0.00106	0.00324	0.00006	0.00101	0.00001	20.9	0.38	20.5	0.25
14.1	matrix	rim	0.02408	0.00073	0.00302	0.00006	0.00098	0.00001	19.4	0.36	19.7	0.24
14.2		rim	0.02547	0.00077	0.00306	0.00006	0.00097	0.00001	19.7	0.36	19.6	0.25
23.1	matrix	rim	0.03602	0.00113	0.00316	0.00006	0.00103	0.00001	20.4	0.37	20.8	0.25
23.2		core	0.04042	0.00125	0.00343	0.00007	0.00109	0.00001	22.1	0.43	22.0	0.26
22.1	matrix	rim	0.03156	0.00095	0.00318	0.00006	0.00101	0.00001	20.5	0.37	20.4	0.25
22.2		rim	0.03226	0.00105	0.00307	0.00006	0.00098	0.00001	19.8	0.37	19.7	0.24
20.1	matrix	rim	0.04182	0.00126	0.00310	0.00006	0.00101	0.00001	20.0	0.37	20.5	0.25
20.2		rim	0.04135	0.00128	0.00334	0.00006	0.00106	0.00001	21.5	0.39	21.4	0.25
20.3		core	0.18421	0.00515	0.00434	0.00008	0.00126	0.00001	27.9	0.51	25.4	0.27
20.4		core	0.14684	0.00410	0.00428	0.00008	0.00125	0.00001	27.5	0.50	25.2	0.27
24.1	Enclosed in garnet	core	0.06497	0.00185	0.00356	0.00007	0.00112	0.00001	22.9	0.44	22.7	0.26
24.2		rim	0.04320	0.00132	0.00338	0.00007	0.00104	0.00001	21.7	0.43	21.0	0.25

Table 7 - LA-ICP-MS *U-(Th)-Pb* in situ *geochronological results for sample AK18-53.*

		AK18-53										
			ISOTOPES RATIOS						AGE ESTIMATES(Ma)			
Mnz Grain	Textural relation	Spot position	$^{207}Pb/^{235}U$	1 sigma	$^{206}Pb/^{238}U$	1 sigma	$^{208}Pb/^{232}Th$	1 sigma	$^{206}Pb/^{238}U$	1 sigma	$^{208}Pb/^{232}Th$	1 sigma
13.1	matrix	rim	0.02833	0.00068	0.00331	0.00004	0.00106	0.00001	21.3	0.28	21.4	0.27
13.2		core	0.03962	0.00089	0.00371	0.00005	0.00113	0.00001	23.9	0.34	22.8	0.28
12.1	matrix	rim	0.03077	0.00102	0.00318	0.00005	0.00101	0.00001	20.5	0.32	20.4	0.30
12.2		core	0.04526	0.00139	0.00437	0.00007	0.00138	0.00002	28.1	0.44	27.9	0.36
12.3		rim	0.03730	0.00123	0.00333	0.00005	0.00099	0.00001	21.5	0.33	20.0	0.29
10.1	matrix	rim	0.03505	0.00120	0.00343	0.00006	0.00107	0.00002	22.1	0.38	21.6	0.31
10.2		core	0.04091	0.00135	0.00389	0.00006	0.00114	0.00002	25.1	0.41	22.9	0.31
10.3		rim	0.02539	0.00092	0.00301	0.00005	0.00095	0.00001	19.4	0.31	19.2	0.29
10.4		rim	0.03291	0.00112	0.00340	0.00005	0.00108	0.00002	21.9	0.34	21.8	0.31
10.5		rim	0.02555	0.00091	0.00330	0.00005	0.00104	0.00001	21.3	0.33	20.9	0.30
21.1	matrix	rim	0.02619	0.00098	0.00324	0.00005	0.00099	0.00001	20.8	0.33	19.9	0.29
21.2		core	0.04769	0.00150	0.00445	0.00007	0.00142	0.00002	28.6	0.45	28.7	0.36
21.3		core	0.04342	0.00147	0.00384	0.00006	0.00114	0.00002	24.7	0.41	23.0	0.32
21.4		core	0.04624	0.00147	0.00434	0.00007	0.00140	0.00002	27.9	0.44	28.3	0.36
25.1	matrix	rim	0.02897	0.00113	0.00308	0.00005	0.00101	0.00001	19.8	0.32	20.4	0.30
*25.2	grain	rim	0.11113	0.00378	0.00366	0.00006	0.00092	0.00001	23.6	0.40	18.6	0.28
25.3	with Sil	rim	0.02453	0.00098	0.00298	0.00005	0.00099	0.00001	19.2	0.31	20.0	0.29
25.4	inclusion	rim	0.03758	0.00142	0.00300	0.00005	0.00093	0.00001	19.3	0.31	18.7	0.28
*26.1	matrix	rim	0.06491	0.00257	0.00355	0.00007	0.00128	0.00002	22.9	0.43	25.8	0.49
*26.2	grain	core	0.04454	0.00181	0.00444	0.00008	0.00169	0.00003	28.6	0.49	34.1	0.54
*26.3	with Sil inclusion	core	0.04656	0.00151	0.00443	0.00007	0.00164	0.00003	28.5	0.44	33.1	0.53
16.1		core	0.03905	0.00126	0.00378	0.00006	0.00116	0.00002	24.3	0.40	23.5	0.32
16.2		core	0.04537	0.00148	0.00418	0.00007	0.00126	0.00002	26.9	0.43	25.5	0.34
16.3	matrix	core	0.04761	0.00159	0.00476	0.00008	0.00158	0.00003	30.6	0.50	31.8	0.52
16.4		core	0.04242	0.00139	0.00459	0.00007	0.00156	0.00003	29.5	0.45	31.5	0.52
16.5		core	0.04403	0.00141	0.00378	0.00006	0.00119	0.00002	24.3	0.40	24.0	0.32
16.6		core	0.04852	0.00156	0.00462	0.00007	0.00145	0.00003	29.7	0.46	29.4	0.51

* Discordant ages did not take into account

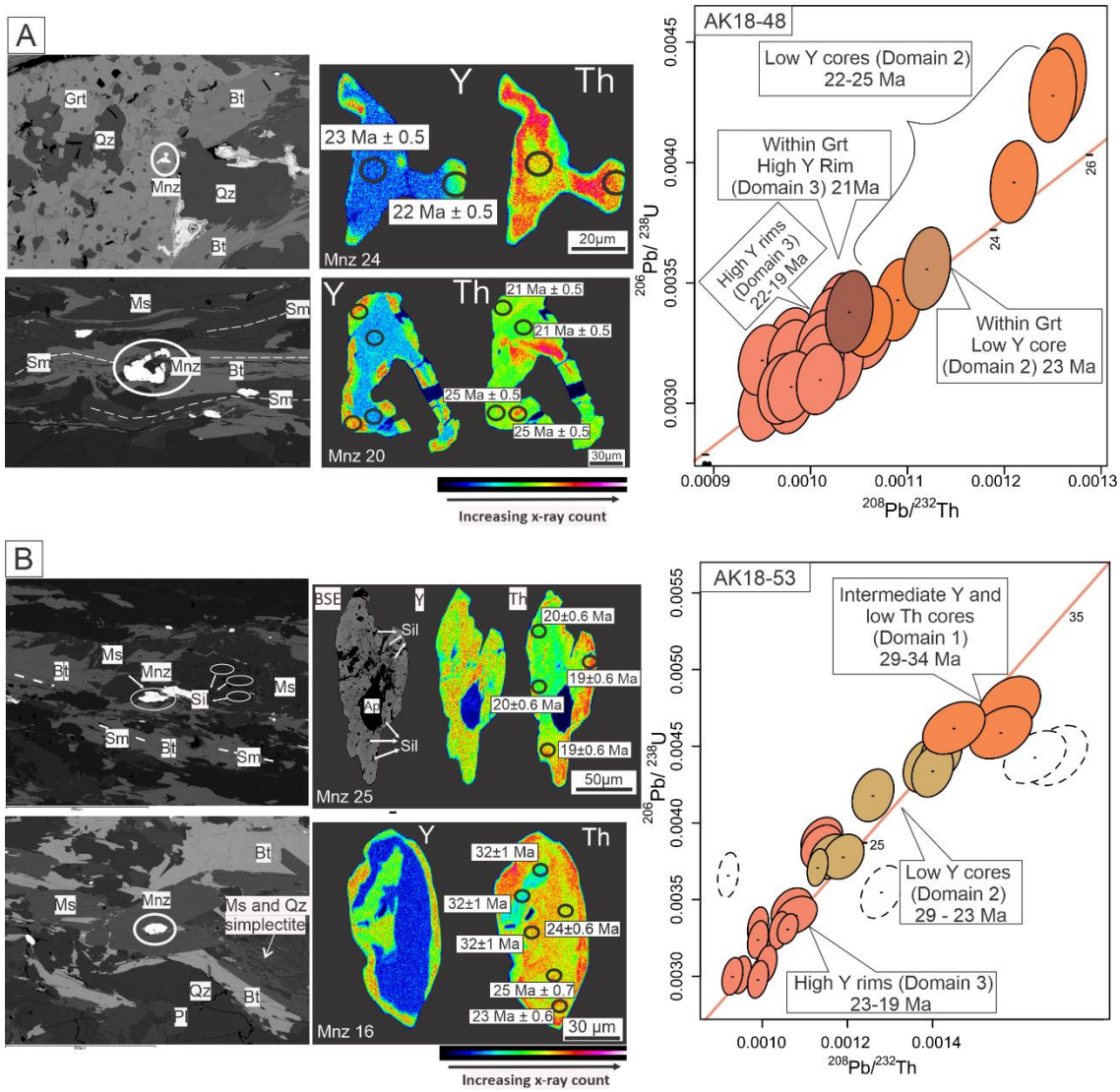

Figure 20 - BSE images, X-ray maps (Y and Th) of representative monazites showing structural position, textural relationships, and internal zoning. $^{206}Pb/^{238}U$ versus $^{208}Pb/^{232}Th$ concordia diagrams for: a) sample AK18-48; b) sample AK18-53.

3.10 Discussion

3.10.1 Monazite age interpretation

Several works reported the monazite behavior during metamorphism and its application in petrochronological studies (Williams and Jercinovic, 2002, 2012; Dumond et al., 2008; Gasser et al., 2012). The basic observation is that Y and HREE partition preferably into garnet structure, thus, monazite enrichment or depletion in such elements is highly dependent on garnet stability in the system. The first appearance of monazite during the prograde metamorphism in a pelitic system is close to the staurolite isograd (Wing et al., 2003; Kohn and Malloy, 2004; Janots et al., 2008; Spear, 2010; Gasser et al., 2012), at lower amphibolite facies. The reaction of allanite and/or xenotime (and apatite) provides Y and REE content enough to monazite growth at temperatures between ~500°C-600°C. During the allanite/xenotime reaction forming monazite, the monazite is expected to be Y- and HREE-rich. In garnet presence during prograde metamorphism, monazite will display an opposite chemical pattern, being Y- and HREE-depleted. Monazite will be dissolved in the peraluminous melt when the rock reaches metamorphic conditions to be partially molten. During cooling and melt crystallization, monazite will recrystallize, with garnet consumption during this process (Spear, 2010). Moreover, a monazite recrystallization stage will be expected during decompression due to garnet breakdown, which turns the system Y- and HREE-rich.

Besides Y and HREE zoning in monazite, Th chemical zoning also can give useful information to interpret monazite absolute ages. Monazite is a Th-rich mineral, and one factor that controls Th-zoning is the reactant phase (e.g., allanite or REE oxide) responsible for releasing Th in the system to form monazite (Catlos, 2013). Monazite crystals that have grown during the prograde metamorphism path display a Th-rich core and low-Th rim pattern (Kohn and Malloy, 2004; Catlos, 2013). The domain with the lowest Th and Y contents records the immediate pre-melting stage (Kohn, 2008).

Hence, monazite recrystallized during the *P-T* path has different chemical fingerprints for linking absolute ages with metamorphic reactions and deformation events. Based on the above description, the intermedium Y and HREE cores with ages ranging from

34 Ma to 29 Ma from domain 1 are correlated to the early prograde metamorphic stage, in which monazite grew before or concomitant with garnet in the system in subsolidus conditions. In the sample AK18-48, these domains are absent, while in the AK18-53 few cores are still preserved. The bulk rock and mineral chemical differences between both samples are the key to comprehending the AK18-48 lack of domain 1 ages, as well as enabling us to have interesting insights about the allanite-monazite transition. Spear (2010) modeled the allanite to monazite transition in metapelite and concluded that it strongly depends on Ca and Al contents. He demonstrated that an increase of Ca can shift the allanite-monazite transition to a higher grade, in the opposite, an increment of Al amount switches this transition toward low temperature. The sample AK18-48 has higher CaO and lower Al_2O_3 (CaO-1.22 wt% and Al_2O_3-12.35 wt%) content than AK18-53 (CaO-0.94 wt% and Al_2O_3-13.39wt%), such differences allow allanite to be preserved in higher grades during the prograde metamorphism in sample AK18-48. Janots et al. (2008) reported the plagioclase behavior after allanite-monazite transition, in which the Ca-rich plagioclase end-member (anorthite) tends to be one of the growing phases after allanite replacement. According to Janots et al. (2008), An values between 0.23 and 0.86 are reported in samples where the allanite was preserved at higher temperatures. Garnet from AK18-48 (Fig. 14) displays off-center domains enriched in Ca and An-rich plagioclase inclusions within garnet. Both features could be linked to the breakdown of a Ca-rich phase (likely allanite and/or apatite, still partially preserved enclosed in garnet) during the progressive metamorphism yielding local Ca enrichment. The plagioclase enclosed in garnet composition (from sample AK18-48) has An values ranging from 0.22 and 0.86, exactly the An interval described by Janots et al. (2008) in rocks where the allanite was stable longer in the system. The observations described above about allanite-monazite transition allow us to presume that the lack of domain 1 in AK18-48 is a consequence of allanite breakdown shifted toward higher grades in this sample (compared with sample AK18-53) due to its bulk composition. The monazite in sample AK18-48 grew later when garnet was already a stable phase in the system, and the domain 1 ages may have been preserved in allanite crystals in this sample.

Domain 2, consisting of cores with low Y and HREE time spreading between 29 Ma and 23 Ma, is considered to have grown during the prograde path in subsolidus conditions when garnet was already an equilibrium phase in the system. Domain 3, characterized by Y-

and HREE-rich rims time span from 23 Ma to 19 Ma, records a new event of monazite recrystallization during the decompression path due to garnet breakdown and melt crystallization conditions. The monazite crystal with sillimanite inclusions (Sample AK18-53- Mnz 25) has a uniform chemical variation compatible with domain 3 and ages ranging from 20 to 19 Ma, which is interpreted as growing in the same tectono-metamorphic context. Even though both samples record the timing of domain 2 and domain 3, some contrasts between monazite chemical features are observed. The sample AK18-48 displays a fractionation in Ca+P (a.p.f.u.) between domains 2 and 3, which is not seen in sample AK18-53 (Fig. 19b). Because of the high apatite solubility in anatectic metapelite this phase tends to be dissolved during the partial melting (Spear and Pyle, 2002) turning the melt Ca- and P-rich. The monazite recrystallized from this melt will be Ca+P enriched related to the older domains. The above explanation can be given for domain 3 rims enhancement in Ca+P compared with depleted cores from domain 2 in sample AK18-48. Such behavior is less evident in sample AK18-53, where a lower modal amount of apatite is observed, and this mineral is often shielded in other grains. Allanite, apatite, and Th-oxide rims on monazite are formed during cooling in the lower amphibolite/greenschist facies, after 19 Ma, during the latest metamorphic stage.

3.10.2 Pressure-Temperature-Deformation-time path (P-T-t-D) of Badrinath shear zone

The BSZ evolution was traced coupling time of monazite metamorphic reactions, with *P-T* and deformation data exhibited in this paper. The earliest prograde metamorphic pre-mylonitic stage (Dm-1) recorded in monazite crystals occurred between 34 and 29 Ma before or concomitant with garnet growth at lower amphibolite facies conditions (~550°C; Gasser et al., 2012) (Fig. 21a). The partial melting took place before or around 23 Ma during the prograde metamorphism at conditions of 700-720°C and 8-10 kbar (Fig. 21b). The isochemical diagram displays that 5-15% volume of melt (see **appendix A** figure A8) was produced at those conditions, consistent with field observations. The maximum pressure, reached during the prograde stage earlier than the metamorphic peak, was at ~10 kbar. Assuming a crust density of 2700 kg $m^{-3,}$ this pressure can be translated to a maximum burial depth of *ca.* 38 km (Spear, 1995).

Peak conditions obtained here, ~720°C and ~6.5-8 kbar, contrast with Spencer et al. (2012a) and Hodges and Silverberg (1988) data in the same structural level (Fig. 22). The discrepancy between these data may be due to the use of conventional thermobarometry by them, whereas in this paper we applied the average *P-T* method (Powell and Holland, 1994) coupled with isochemical diagrams. Moreover, the estimated *P-T* conditions and timing for partial melting in this paper for the upper part of the GHS are consistent with the results of Iaccarino et al. (2017b), who studied sheared aluminosilicate bearing-migmatitic gneiss in the nearby Dhauli Ganga valley, located in the uppermost part of GHS affected by STDS deformation.

The microstructural investigation demonstrated that the mylonitic stage (Dm) took place in a high-temperature ductile regime, as supported by quartz microstructures compatible with the GBM_{II} regime (Stipp et al., 2002a), feldspar microstructures, and synkinematic recrystallization of sillimanite along the main foliation. All the kinematic indicators, mica-fish, feldspar-fish, and *S-C* fabric reveal a contractional activity (with top-to-the-south/southwest kinematics) to the BSZ. Thus, the BSZ shear activity can be related to crustal thickening and shortening. Based on these premises and the *P-T* calculations, it is possible to link the BSZ shear activity to hanging wall (the Bhapkund Formation) decompression in high-temperature conditions and starting around ~23 Ma (Fig. 21b). The sillimanite grew later, after shear activity beginning at depths around ~25 km between 20 Ma and 19 Ma (Fig. 21c). Assuming a P decrease of 10 to 6.5 kbar (corresponding to an exhumation of 38 to 25 km) occurring in the period of 4 Ma (23 Ma to 19 Ma), the exhumation rate during BSZ shearing was estimated at *ca.* 0.3 cm yr^{-1}.

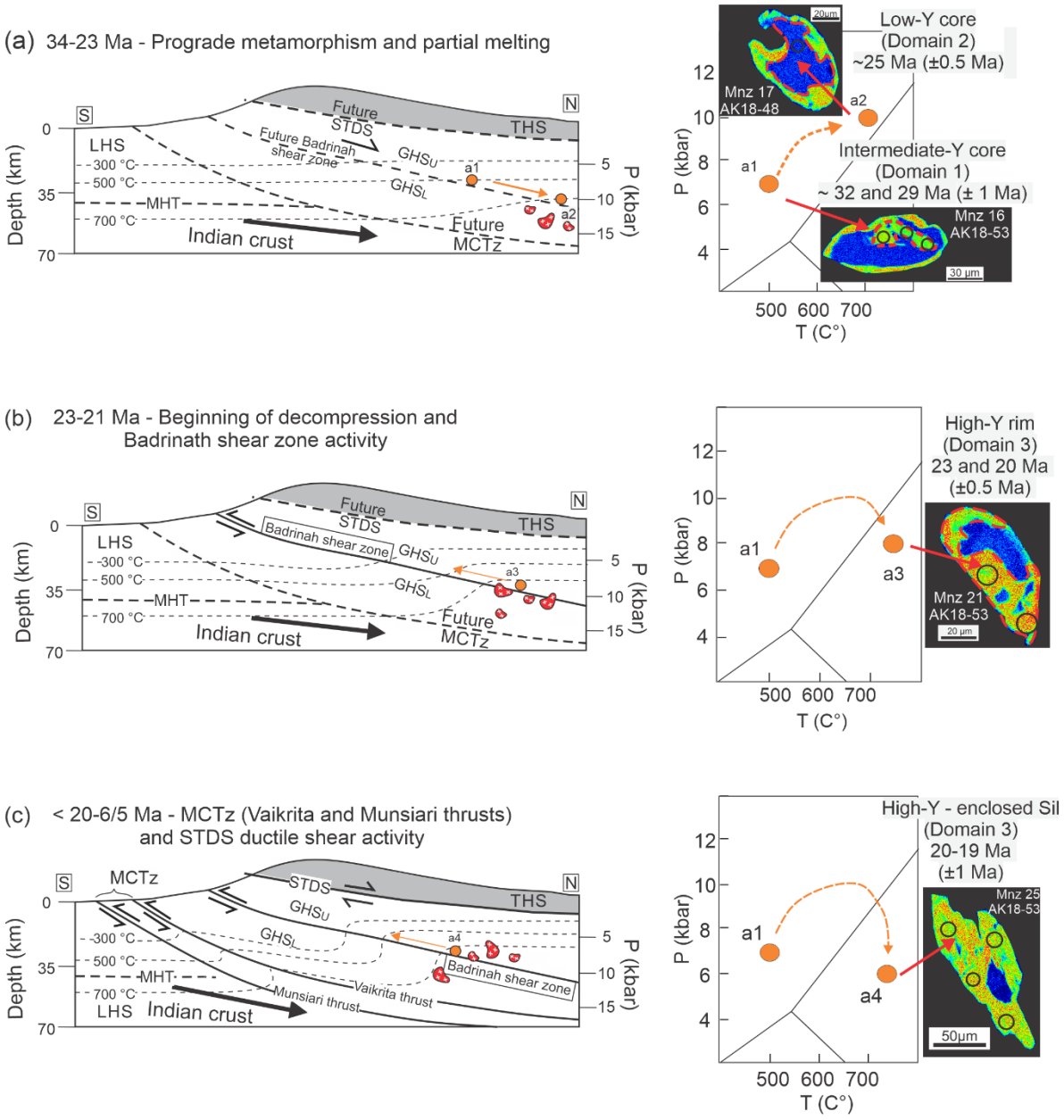

Figure 21 - Different stages of tectonic evolution in the Alaknanda-Dhauli Ganga valleys and P-T-t-D paths showing monazite textural zoning in each stage. a) 34-29 Ma: early prograde stage in amphibolite facies; 29-24 Ma: pre-mylonitic late prograde metamorphism stage; b) 23-21 Ma: BSZ contractional activity and GHS_U exhumation began; c) < 20-6/5 Ma: MCTz shearing and STDS (ductile to brittle) contemporaneous motion.

The rocks structurally below, the Suraithota Formation, reached simultaneous temperature and pressure peak conditions around ~660-700°C and up to 11 kbar, and the decompression path triggered partial melting in this rock. This result for the lower GHS is in agreement with previous estimates of Thakur et al. (2015, 2018) and Iaccarino et al. (2020) (Fig. 22). Iaccarino et al. (2020) analyzed a rock from the upper part of the MCTz, which is

the closest sample to the one from Suraithota Formation investigated in this work. Using U-(Th)-Pb monazite data, they suggest that exhumation started at 20 Ma. We assumed that both rocks were exhumed during the same time span. Hence there is a time gap of *ca.* 3 Ma in the exhumation and anatexis beginning between the BSZ and rocks structurally below.

The contrast in exhumation age (*ca.* 3 Ma) and peak pressure conditions (around 3 kbar) between Suraithota Formation rocks and the BSZ mylonite, structurally upward, set up a tectono-metamorphic discontinuity inside the GHS in this area. Even though *P-T* differences, the metamorphic data from Spencer et al. (2012b) and Hodges and Silverberg (1988) also support the occurrence of a metamorphic discontinuity (Fig. 22).

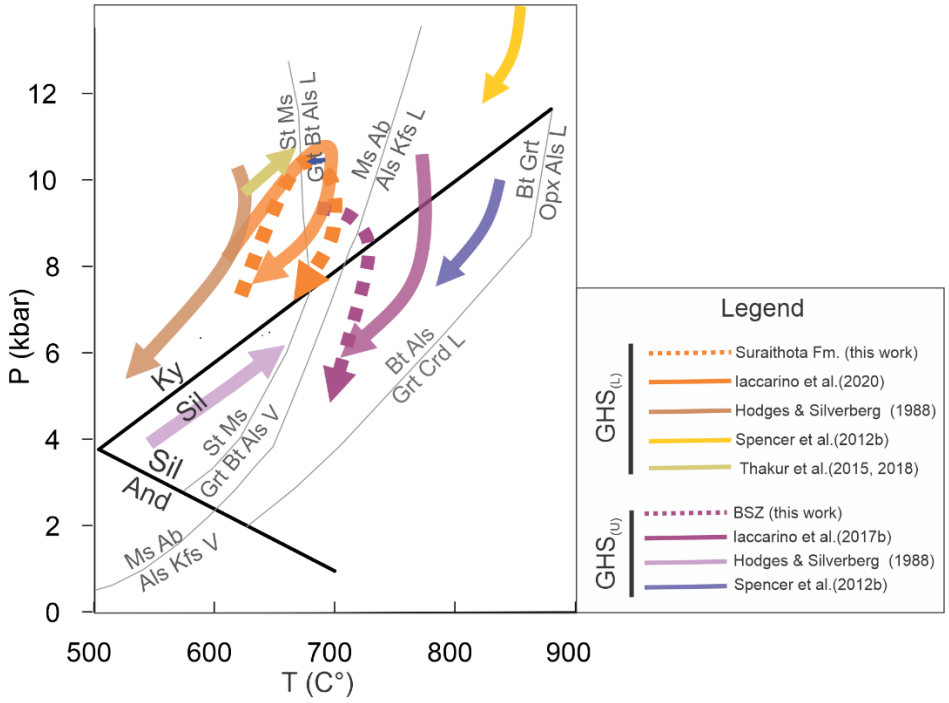

Figure 22 - Summary of GHS_L and GHS_U P-T paths from Alaknanda-Dhauli Ganga valleys (NW India).

3.10.3 Discontinuities within GHS

The idea of the GHS as a coherent tectonic unit has been challenged since the discovery of the High Himalayan Discontinuity (HHD) (Kohn, 2008, 2014; Montomoli et al., 2013, 2015; Wang et al., 2015; Waters, 2019). Authors who considered the HHD as a regional feature have made efforts to reconcile such structures and tectonics models (Montomoli et al., 2013, 2015; Cottle et al., 2015; Larson et al., 2015; Wang et al., 2015; Carosi et al., 2016, 2018, 2019).

The BSZ features match with the HHD geological features and represents its prolongation in Garhwal Himalaya, India. The HHD has been mapped in several localities such as Nepal (Carosi et al., 2007, 2010; Montomoli et al., 2013; Larson et al., 2015; Khanal et al., 2020), Sikkim (Chakraborty et al., 2019) and Bhutan (Zeiger et al., 2015; Agustsson et al., 2016), but our work brings the first report of the HHD in NW Himalaya (India). The HHD identification in Garhwal Himalaya confirms its regional feature that crosscuts the belt for more than 1400 km along strike, including NW India.

In the presence of the HHD, and taking into account the metamorphism and deformation of its hanging wall and footwall rocks, the GHS in our study area can be divided into upper and lower tectono-metamorphic units, respectively, the GHS_U and GHS_L (Figure 20c and 21), similarly to many other portions of the belt (Carosi et al., 2010, 2018; Larson et al., 2010; Montomoli et al., 2013; Wang et al., 2015; Iaccarino et al., 2017a; Waters, 2019). The GHS_L, comprising the Joshimath and Suraithota Formations, is composed of kyanite- to garnet-bearing micaschist/paragneiss interlayered with quartzite and amphibolite. A remarkable feature of the base of GHS_L is the inverted metamorphism pattern at its bottom (Iaccarino et al., 2020 and references therein). The GHS_U consists of sillimanite- and kyanite-bearing gneiss (Jain et al., 2014) of the Bhapkund Formation. In GHS_U, the anatexis is more pervasive, varying from 5 up to more than 20% of melt volume and leading to emplacement of leucogranite such as the Malari granite (~19 Ma; Sachan et al., 2010) close to the STDS (Jain et al., 2014; Iaccarino et al., 2017b).

3.10.4 Tectonic implications

The major shear zones bounding the GHS, the MCTz, and STDS, were studied by several authors in the Alaknanda-Dhauli Ganga valleys of Garhwal Himalaya (Sachan et al., 2010; Sen et al., 2015; Thakur et al., 2015; Iaccarino et al., 2017b, 2020; Hunter et al., 2018, 2019; Montemagni et al., 2018a, 2018b, 2020). The ductile activity of the STDS was constrained between ~20 and 15 Ma (Sen et al., 2015; Iaccarino et al., 2017b; Montemagni et al., 2018a), while the MCTz was active from 20 Ma to 5 Ma (Montemagni et al., 2018b, 2020; Iaccarino et al., 2020). Coupling literature data with our new data from the Alaknanda-Dhauli Ganga valleys, it was detected that the GHS_U exhumation and partial melting began at *ca.* 23 Ma, nearly 3 Ma before the GHS_L was exhumed (Fig. 21).

The data from Alaknanda valley demonstrate that BSZ accommodates deformation during the early stages of GHS rocks exhumation before MCTz and STDS activities. This supports the "in-sequence shearing" model in which the deformation was driven by high-temperature shear zones during progressive mid-crust exhumation from top to bottom in the GHS (Carosi et al., 2016, 2018, 2019; Montomoli et al., 2013, 2015). The recent dating of Vaikrita and Munsiari thrusts at 20-9 Ma and 5-4 Ma, respectively, further confirms and reinforces the progression of deformation downwards in the GHS and later in the LHS (Montemagni et al., 2018a, 2020).

In addition, the increase of partial melting in the GHS_U raises the question whether changes in the rock rheology, due to partial melting, would have been sustained for enough time to melt weak the mid-crustal rocks. Our monazite data show that the main partial melting event took place in a short period of time, likely after *ca.* 24 Ma and around 23 Ma, suddenly followed by the exhumation/retrograde path at least up to 19 Ma. Hence, the GHS_U rocks remained under suprasolidus conditions during a short period, *ca.* 5-4 Ma.

After 20 Ma, at the time of activation of the Vaikrita thrust (Iaccarino et al., 2020), during later stages of exhumation, the GHS behaved as a coherent tectonic unit (Fig. 21c). In other words, the synchronous MCTz and STDS activities played a role just during the latest stage of exhumation/extrusion, in the study transect. Such findings point to a shift in the mid-crust deformation active process responsible for the exhumation in different ages and localities.

The early shortening stages in the upper GHS by the BSZ contraction could have led to crustal thickening, which may have caused the activation of STDS coeval with MCTz in order to re-equilibrate the system as regarded in the critical taper model (Kohn et al., 2008).

3.11 Conclusion

The present contribution presents new *P-T-t-D* data to the inner portion of the GHS in the Garhwal Himalaya and led us to the following conclusions:

- A thrust-sense shear zone, the BSZ, has been detected in the core of the GHS. The timing history of BSZ rocks was recorded by monazite crystals returning ages from 34 to 19 Ma. The pre-mylonitic stage occurred during prograde metamorphism, in the time interval of 34-23 Ma, reaching conditions of ~700°C and 10 kbar. The contractional shear motion took place at high temperature (700-720 °C) conditions during the exhumation at 23-19 Ma. During this period, the exhumation rate has been estimated at around 0.3 cm yr^{-1}. The BSZ represents the first occurrence of the High Himalayan Discontinuity (HHD) in the western portion of the Himalayan belt.

- The BSZ partial melting occurred around 24-23 Ma, and the suprasolidus conditions were maintained until at least 19 Ma. Hence, the low-viscosity period due to partial melting was sustained for a short period of *ca.* 5-4 Ma.

- The metamorphic conditions of structural lower rocks in the GHS (GHS_L) show similar peak temperature but a pressure increase of *ca.* 3 kbar concerning the GHS upper portion. Partial melting and exhumation took place several Myrs later in this part, when the upper part of GHS was already experiencing retrograde metamorphism.

- The MCTz and STDS ductile activities in the Alaknanda valley were coeval but only at ~20 Ma, later than the BSZ ductile shear activity, which allowed the earlier exhumation of the upper GHS. Such findings point to a shift in time and space of deformation responsible for the exhumation within the GHS.

CHAPTER 4

TECTONO-METAMORPHIC EVOLUTION OF ANDRELÂNDIA NAPPE SYSTEM (SE BRAZIL) CONSTRAINTS BY METAMORPHIC ITERATIVE THERMODYNAMIC MODELING AND MONAZITE PETROCHRONOLOGY

4.1 Abstract

The medium-high grade rocks forming the hinterland of orogenic wedges are able to record pressure (*P*) and temperature (*T*) changes during the orogen development, as well as, its kinematics history. The Andrelândia Nappe System (ANS) is the hinterland of the Southern Brasilia Orogen (SBO). Its tectono-metamorphic evolution has been a target of intense debate in the past decades. Whereas some authors argue that the ANS features resulted from two tectonic-metamorphic events that affected the SBO, other scholars point out that ANS structural and metamorphic records were produced by the progressive deformation and metamorphism related to the Paranapanema block collision against the São Francisco craton. A *P-T-t-D* study was addressed to the ANS intermediate and bottom stacks. Field and microstructural observations were combined with metamorphic petrology (i.e., thermodynamic iterative modeling) and geochronology (i.e., monazite petrochronology) to reconstruct the ANS rocks tectono-metamorphic history. It was demonstrated that the Liberdade Nappe attained prograde metamorphism at *ca.* 610 Ma achieving peak conditions of ~650°C and 9.5-10 kbar. This stage was followed by isothermal decompression at *ca.* 570 Ma. On the contrary, the Andrelândia Nappe experienced prograde metamorphism later, at *ca.* 580 Ma, reaching peak conditions of *ca.* 680°C and 11-12 kbar. These results demonstrate that the spread of ages within the ANS is related to different periods in which the nappes of the system attained the prograde and retrograde metamorphism rather than a second tectono-metamorphic event. A rejuvenation of prograde and exhumation-related ages is observed towards the ANS bottom. This new dataset reinforces the idea that SBO evolved by the progressive evolution of the continental collision between the Paranapanema and São Francisco cratons.

4.2 Introduction

The mountain belt growth is controlled by the balance among accretion of crustal material, such as sediments and magma addition, and removal by erosion, tectonic and post-orogenic thinning (Jamieson and Beaumont, 2013; Vanderhaeghe, 2012). External (e.g., climate) and internal (e.g., structure and geodynamic) factors controlling mountain building play a main role in modifying the orogenic belt wedge's architecture (Carrapa, 2009; DeCelles and Mitra, 1995). An orogen wedge is constituted by crustal material mainly

detached from the subducted lithosphere, accreted, and stored within the orogenic system (Vanderhaeghe, 2012; Vanderhaeghe et al., 2003). During orogenesis, the balance of the orogen active forces leads to exhumation at the front of the crustal wedge (DeCelles and Mitra, 1995; Medvedev, 2002; Vanderhaeghe et al., 2003). Moreover, the accumulation of crustal material enriched in radioactive heat-production elements, such as U, Th, and K, modifies the crustal geothermal gradient (∂°C/ ∂km) (England and Thompson, 1984; Rudnick and Fountain, 1995). The aforementioned facts demonstrate that the deep-seated crustal rocks, stored within orogenic wedges, are able to record pressure (*P*) and temperature (*T*) changes during the orogen development as well as its kinematics history and crust internal structure (e.g., Catlos et al., 2018). Hence, the study of wedge deformation and metamorphism conditions is fundamental to comprehending the tectonic and geodynamic evolution of ancient and young orogenic belts.

The Andrelândia Nappe System (ANS) is interpreted as the Southern Brasilia Orogen (SBO) orogenic wedge hinterland. Its tectono-metamorphic evolution has been a target of intense debate in the past decades. Indeed, some researchers (Coelho et al., 2017; Fontainha et al., 2020; Trouw et al., 2013 and references therein) argue that the ANS evolution resulted from two separate tectono-metamorphic events. The first one is related to high-*P* metamorphic conditions testified by the HP-granulites and E/NE nappe stacking, owing to the Paranapanema and São Francisco Cratons collision. It was followed by a second event, characterized by medium pressure, greenschist- to amphibolite-facies conditions at the staurolite and sillimanite isograds, with NW-SE shortening direction. This second episode would be related to the Central Ribeira Orogeny. Meanwhile, the second viewpoint proposes that the ANS evolution results from a single orogenic event. According to them, the ANS evolved in a clockwise path to an isothermal decompression due to the Paranapanema craton collision against the São Francisco block (Campos Neto et al., 2011; Frugis et al., 2018; Westin et al., 2021 and references therein). The sillimanite and staurolite presence in the ANS rocks would result from the decompression rather than a second tectono-thermal event. The metamorphic ages indicate an in-sequence of thrust propagation from WSW to ENE toward the São Francisco Craton southern edge (Westin et al., 2021 and references therein).

The reconstruction of Pressure-Temperature-time-Deformation (*P-T-t-D*) paths provide elementary information to understand the tectonic and metamorphic events experienced by the orogenic wedge rocks. Primarily, the application of internal consistent databases to build pseudosection has been used to constrain metamorphic conditions (Powell and Holland, 2008; Waters, 2019). This data can be linked with microstructural observations to set up the rock fabric relationships with the metamorphic mineral assemblage, i.e., the so-called blastesis-deformation relationships (Passchier & Trouw, 2005). In addition, the *in-situ* dating of accessory minerals, such as monazite, zircon, or titanite, can be bound to metamorphic reactions and deformation events (e.g., Bosse and Villa, 2019; Kohn et al., 2017; Mottram et al., 2019; Williams and Jercinovic, 2012). This approach has been one of the most effective ways to understand the complex frameworks of collisional belts (Carosi et al., 2018; Montomoli et al., 2013; Waters, 2019).

In this contribution, we join the field and microstructural observations with modern techniques in metamorphic petrology and geochronology. This integrative approach provides the necessary information to reconstruct the tectono-metamorphic history of the ANS rocks.

4.3 Pouso Alto county geology

The study area is located in southeast Brazil, in the Minas Gerais state around Pouso Alto County (Fig. 23a). In the area, the three ANS structural levels crop out, which from top to bottom are: the Pouso Alto, Liberdade, and Andrelândia Nappes. The Diatexite Unit of the Socorro-Guaxupé Nappe, a slice of the basement, the Pouso Alegre Complex, and a large leucogranite body (Fig. 23a and b) are also present.

The Pouso Alto Nappe has a basin structure, as suggested by the main foliation dip direction variation interpreted as being a synform (Fig. 23a and b). Medium- to coarse-grained K-feldspar+garnet+kyanite+rutile(±ilmenite)-bearing gneiss represents the main lithotype of Pouso Alto Nappe. Kyanite and quartz alignments mark the lineation that mainly plunges, between 2-40°, toward SW.

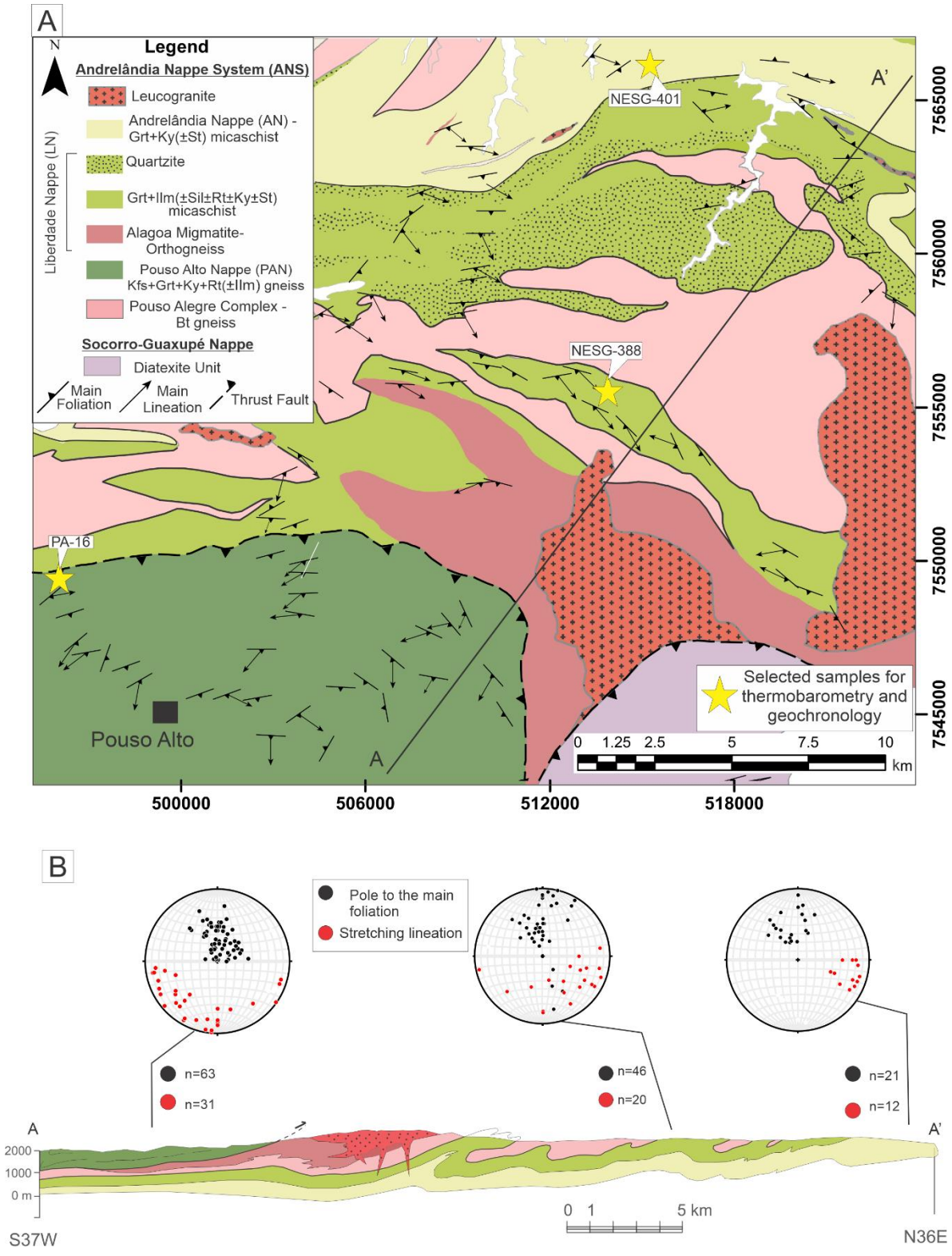

Figure 23 - a) Geological map of Pouso Alto county; b) Geological cross-section of the area and stereographic projections of collected structural data.

The Liberdade Nappe is represented by fine- to medium-grained garnet+ilmenite(±sillimanite±rutile±kyanite±staurolite)-bearing micaschist interlayered with quartzite. Micaschist displays a main spaced disjunctive schistosity, defined by biotite and white mica shape preferential orientation (SPO). Intrafolial stretched isoclinal passive folds are observed. The ensemble of the foliation describes a large cylindrical synform with an SW-oriented B-axis in a type-3 superposition pattern (Ramsay, 1962) over recumbent isoclinal folding between the basement nucleus and the metasedimentary sequence. The object lineation is marked by sillimanite, observed as fibrolite, white mica, and biotite. It trends mainly N82°-N180° and plunges 5°-70° toward SE (Fig. 23b). In the central portion of the study area crops out the Alagoa migmatite and the biotite gneiss of the Pouso Alegre Complex. A leucogranite body intrudes the micaschist of Liberdade Nappe, the Alagoa migmatite, and the Pouso Alegre Complex (Fig. 23a and b).

The Andrelândia Nappe crops out in the north of the study area (Fig. 23a and b). It is constituted by garnet+kyanite(±staurolite)-bearing micaschist. The main foliation is a spaced disjunctive schistosity identified by SPO on white mica, biotite, and kyanite. The schistosity strikes ENE-WNW with dips varying from low to high angles, between 20°-80° toward the north. White mica, biotite, quartz, and kyanite define the object lineation, which trends between N90°-N120° and plunges 10°-50° to SE.

4.4 Petrography, microstructural relationships, and mineral chemistry

In order to constrain the relationships between mineral blastesis and deformation, several samples from Liberdade and Andrelândia Nappes were collected and described with the help of a petrographic microscope. In total, 40 thin-sections were used to describe both units. One representative sample of each Nappe was selected for performing full thin-sections maps acquired using the Scanning Electron Microscopy and Mineral Liberation Analyzer (SEM-MLA) (appendix figure B1). The samples location is given in Fig. 23a. An area of each thin-section mapped containing the inferred peak mineral assemblage, avoiding retrometamorphic textures where possible, was investigated using X-ray maps acquired by an electron probe micro-analyzer (EMPA). Table 8 display some EMPA representative spots analysis. The analytical procedure employed for EMPA analysis is described in **appendix B**. The X-ray maps were converted into oxide weight percentage maps applying internal

standards (Andrade et al., 2006) in the software XMapTools 3.4 (Lanari et al., 2014, 2019). Such areas were the basis for estimating the Local Bulk Composition (LBC) needed for petrological modeling. The mineral abbreviations follow Whitney and Evans (2010).

4.4.1 Liberdade Nappe (LN)

The Liberdade Nappe micaschist is made up of quartz+plagioclase+white mica+biotite+garnet+ilmenite(±sillimanite±rutile+kyanite±staurolite). The rock has a S_2 schistosity transposed by structures of tectonic transport (Post-S_2) such as a *S-C* fabric (Fig. 24a) and isoclinal folds denoting top-to-the-SE motion. Quartz has slightly lobate contacts, and plagioclase has undulose extinction. The quartz features reveal that this mineral was recrystallized due to the grain boundary migration (GBM) regime and underwent grain boundary area reduction (GBAR; Passchier and Trouw, 2005). Garnet porphyroblast has a skeletal microstructure (Fig. 24b). It also shows S-shaped inclusions made of quartz (Fig. 24c), defining an internal foliation that is not continuous with the external schistosity. Then, garnet is regarded as an inter- to syn-tectonic with respect to the S_2 schistosity. Sillimanite is present as fibrolite, it replaces partial to completely garnet porphyroblasts, forming pseudomorphs (Fig. 24d), and also occurs as isoclinal folds (Fig. 24e). Subidiomorphic relic of kyanite wrapped by white mica is observed (Fig. 24f). Staurolite is fine-grained, in a very low modal amount, and often related to garnet rims. Rutile is enclosed in garnet, and in the matrix it is usually rimmed by ilmenite.

The relationships among minerals suggest three metamorphic stages, $M_{LN}1$, $M_{LN}2$, and $M_{LN}3$, for the Liberdade Nappe micaschist (Fig. 28). The $M_{LN}1$ stage is Syn-S_2, related to prograde/peak metamorphism and it is characterized by quartz+plagioclase+white mica+biotite+garnet+rutile+kyanite(?) as the equilibrium assemblage in the rock. The $M_{LN}2$ stage, in which quartz+plagioclase+white mica+biotite+garnet+kyanite(?)+ilmenite is inferred to be stable, represents a post-peak mineral assemblage. Finally, sillimanite and staurolite are retrograde minerals that grew during the late stage of the metamorphic path ($M_{LN}3$ and Post-S_2).

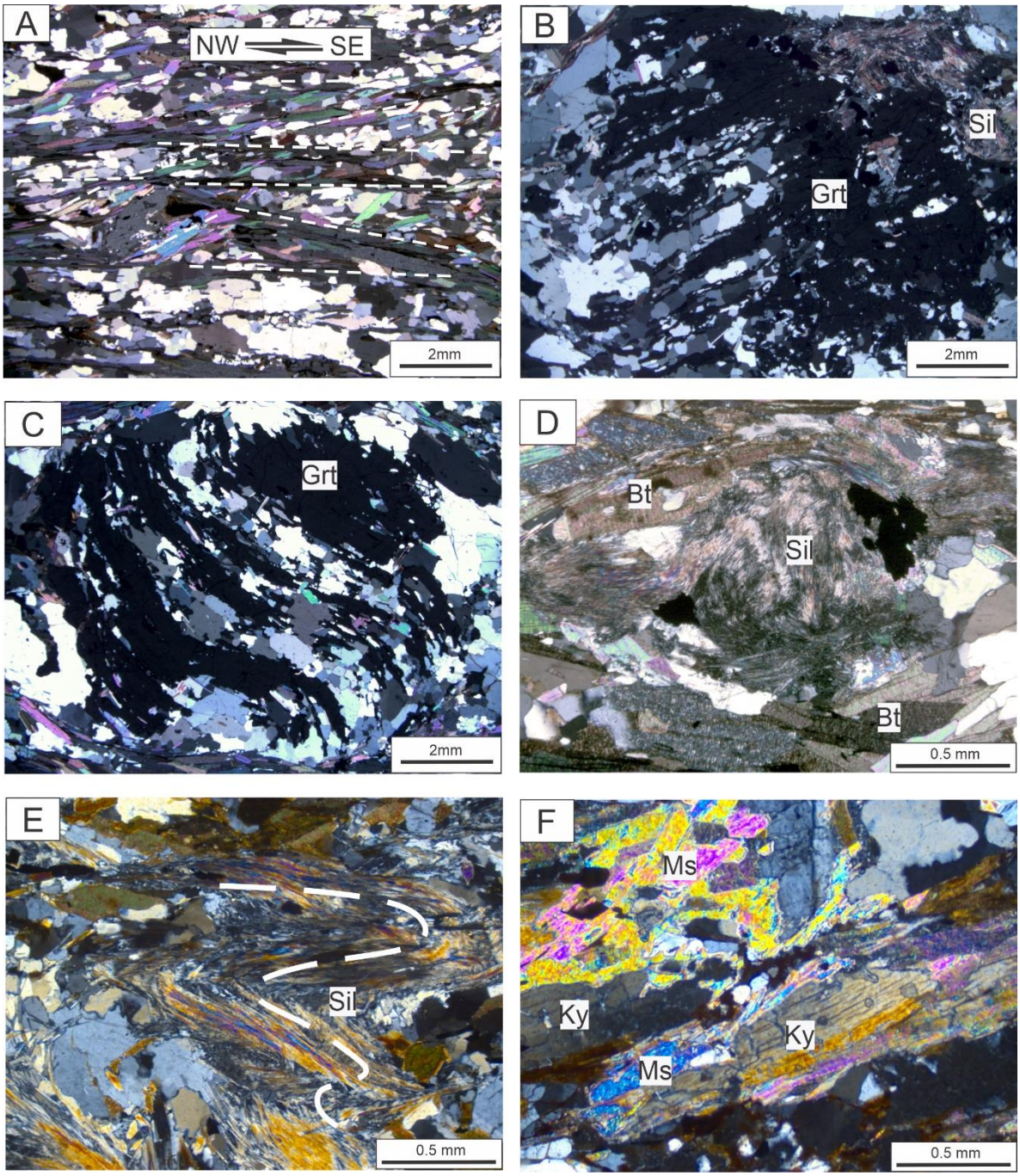

Figure 24 - - Liberdade Nappe (LN) photomicrographs. a) S-C fabric indicating a top-to-the-SE sense of shear (UTM 521535/7560145); b) Skeletal garnet and decussate fibrolite (UTM 521535/7560145); c) Garnet porphyroblast with spiral internal foliation (UTM 521535/7560145); d) Garnet pseudomorph replaced completely by fibrolite (UTM 521535/7560145); e) Isoclinal fold marked by fibrolite orientation (UTM 519472/ 7549550); f) Kyanite relic overgrown by white mica (UTM 5110028/7561820).

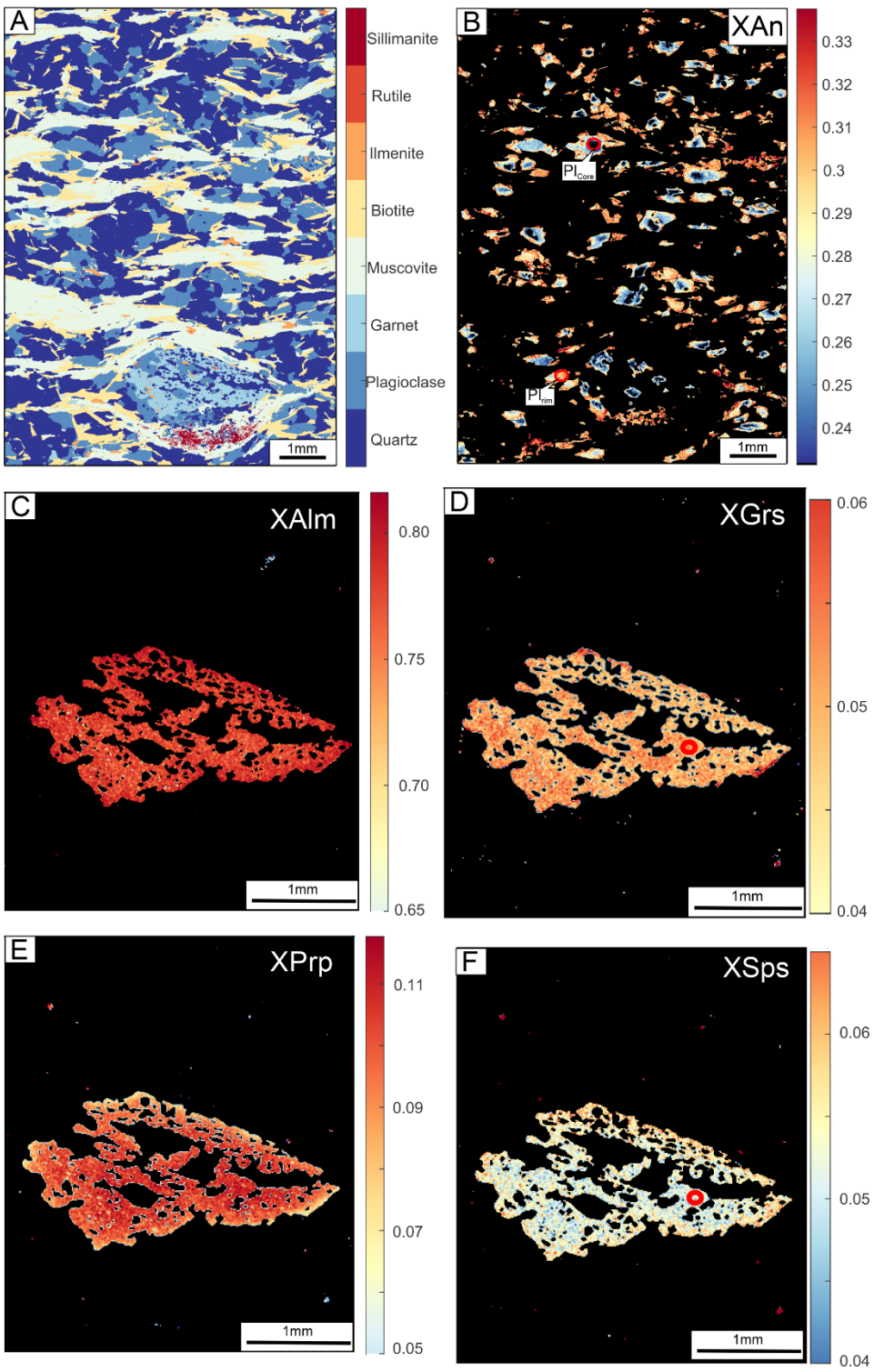

Figure 25 - Quantitative compositional maps for the sample NESG-388 of the Liberdade Nappe a) Mineral map of the investigated thin-section area showing the mineral phases in the mapped area; b) Anorthite (X_{An}) content in plagioclase map; c)-f) Almandine (X_{Alm}), grossular (X_{Grs}), pyrope (X_{Prp}) and spessartine (X_{Sps}) zoning in garnet.). The red circles indicate the area used to perform the Qcmp maps for garnet, plagioclase core and rim.

Sample NESG-388 (Fig. 23a, table 8, and supplementary figure B1) was selected for the LN mineral chemistry investigation and petrological modeling. The NESG-388 is a white mica+biotite+garnet+ilmenite-bearing mylonitic schist with sillimanite, rutile, and staurolite as accessory phases (Fig. 25a). Plagioclase is compositionally zoned, and its anorthite content increases from core to rim (X_{An} –0.20-0.32) (Fig. 25b). Garnet displays a homogeneous chemical composition, in which its end-members vary slightly from core to rim: almandine (X_{Alm})=0.81-0.79, pyrope (X_{Prp})=0.11-0.07, spessartine (X_{Sps}) =0.05-0.06 and grossular (X_{Grs})=0.05-0.06 (Fig.25c-f). The Ti (a.p.f.u) in biotite decreases toward the rim, ranging from 0.14 to 0.09, whereas the #Mg (Mg/Fe^{+2}+Mg) ratio displays an inverse correlation, increasing toward the rims, varying from 0.37 to 0.43 (supplementary figure B2). The Si^{+4} (a.p.f.u) of white mica varies from 3.04 to 3.15 (supplementary figure B2d) .

4.4.2 Andrelândia Nappe

The Andrelândia Nappe micaschist is constituted by the major phases quartz+plagioclase+biotite+white mica+garnet+kyanite+ilmenite(±sillimanite±staurolite) and tourmaline+apatite+monazite+zircon+rutile as accessories. The main foliation (S_2) is characterized by discontinuous millimetric compositional layers of granoblastic, made by quartz and plagioclase, and lepidoblastic, constituted by white mica and biotite with subordinate garnet and kyanite. The micaschist close to the contact with the Liberdade Nappe is affected by shearing and displays a mylonitic fabric (post-S_2). The kinematic indicators described in the sheared micaschist are *S-C* shear band and white mica-fish, which point to a top-to-the-E/ESE sense of shear (Fig. 26a). Quartz is a medium- to coarse-grained mineral with irregular and lobate contacts, typical of the GBM recrystallization mechanism (Law, 2014).

Garnet is present as porphyroblast (≤2 cm in size) (Fig. 26b). Discontinuous inclusion trails of opaque minerals within garnet, with respect to the S_2 fabric, testify to the inter-tectonic nature of this mineral (Fig. 26b and d). Thin graphite crystals, ilmenite, and rutile are the typical inclusions in garnet, and staurolite, quartz, plagioclase, biotite, and white mica are subordinate. Kyanite is a coarse-grained subidiomorphic crystal with a long axis aligned along the main external foliation (Syn-S_2) (Fig. 26b). Twinning in kyanite is observed. Late

fibrolite growth along shear bands and replacing biotite crystals are observed (Fig. 26c and d). Two generations of staurolite were observed, the first is characterized by tiny crystals enclosed in garnet. Whereas the second is in the matrix, often around garnet rims. A staurolite with biotite and sillimanite inclusions aligned with the external foliation, made by sillimanite, quartz, and biotite, denotes a syn-tectonic origin regarding the post-S_2 fabric (Fig. 26d). The contact between staurolite and garnet, as well as the abrupt change of the internal foliation of both minerals, suggest a pattern of porphyroblasts amalgamated (Fig. 26d, e.g., Passchier and Trouw, 2005).

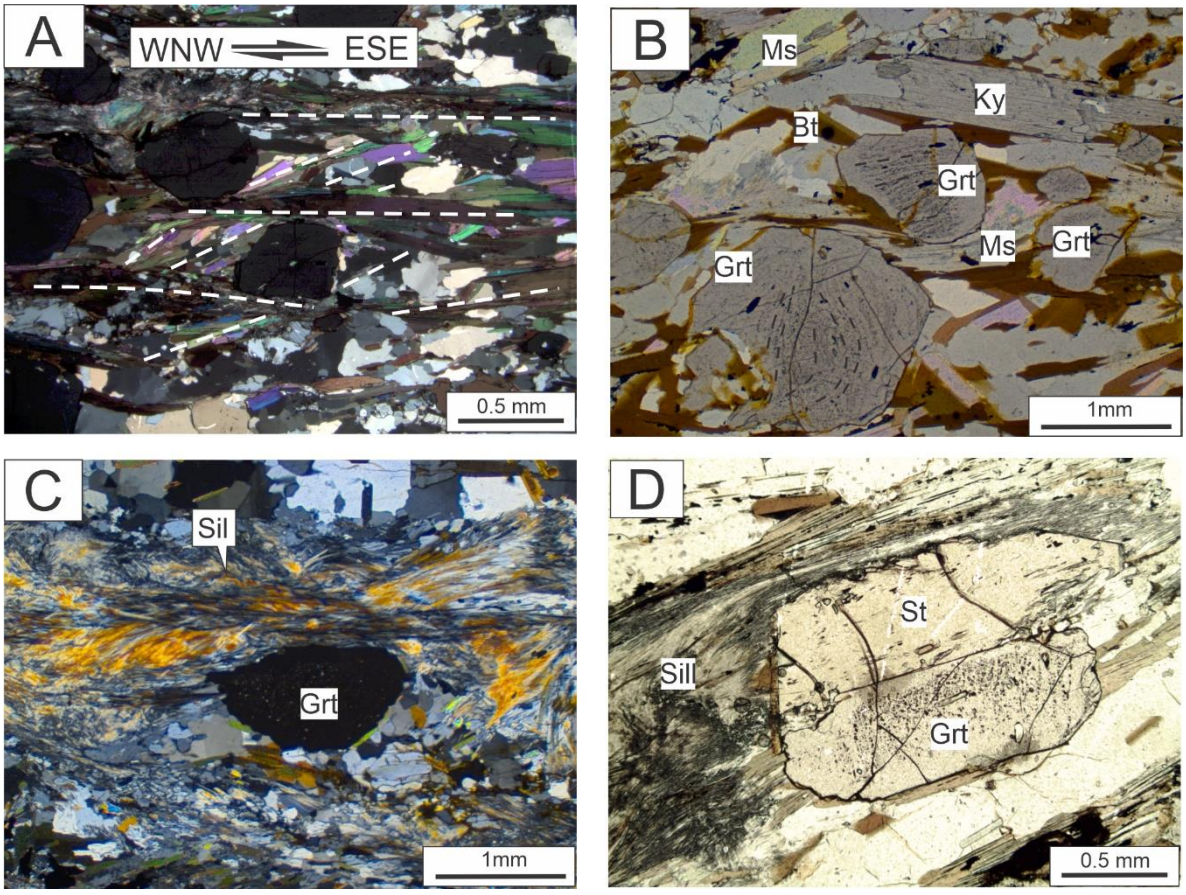

Figure 26- Andrelândia Nappe (AN) photomicrographs. a) S-C fabric indicating a top-to-the-ESE sense of shearing (UTM 513937/7565930); b) Garnet porphyroblast with opaque inclusion trails, and kyanite aligned according to the external foliation (UTM 516960/7565691); c) Fibrolite growth along a shear band (UTM 516960/7565691); d) Garnet with opaque inclusion trails oblique to the external foliation (post-S_2) made by sillimanite, quartz and biotite. Staurolite with internal foliation in line with the external one. Fibrolite replacing biotite crystals (UTM 516960/7565691).

Based on the above description, three main stages of mineral equilibration were recognized (Fig. 28). The early prograde assemblage ($M_{AN}1$), preserved in garnet core inclusions, is constituted by Grt(core)+Qz+Pl+Bt+Ms+St+Rt. The peak assemblage ($M_{AN}2$) is coeval with the S_2 foliation and is marked by the appearance of kyanite and ilmenite and the consumption of staurolite and rutile. The $M_{AN}3$ assemblage corresponds to retrograde metamorphic path, characterized by a second growth of staurolite around garnet rims together with the late fibrolite appearance.

Sample NESG-401 was chosen for a detailed chemical investigation (Fig. 23a, table 8, and supplementary figure B1). The micaschist is composed of Qz+Pl+Bt+Ms+Grt+Ilm and minor apatite (Fig. 27a). This sample is white mica-poor, which is restricted to the garnet strain shadow zones (supplementary figure B1 and Fig. 27a). The plagioclase is zoned with Ca-poor cores (X_{An} -0.22) and Ca-rich rims (X_{An} -0.32). The highest Ca-content (X_{An} -0.34) occurs in crystals that bound garnet (Fig. 27b). There are two garnet crystals in the X-ray mapped area. The large garnet porphyroblast displays a bell shape profile, whereas the smaller one presents an almost flat profile (Fig. 27c, d, e, and f). Garnet porphyroblast shows an increase in almandine and pyrope toward the rim, whereas spessartine and grossular display the inverse pattern (Core- X_{Alm}-0.6, X_{Prp}-0.06, X_{Sps} -0.1, X_{Grs}-0.22; Rim- X_{Alm}-0.72, X_{Prp}-0.13, X_{Sps}-0.03, X_{Grs}-0.08) (Fig. 27c, d, e, and f). Spessartine displays a sharp increase in the outermost rim (X_{Sps}-0.09/0.1) in both garnet crystals. The biotite composition varies according to its structural position. Crystals close to garnet have higher #Mg and lower Ti (a.p.f.u) compared to grains far from garnet (Bt near garnet XMg- 0.54-0.52 and $Ti_{(a.p.f.u)}$- 0.8-0.10; Bt in matrix XMg-0.5-0.51 and $Ti_{(a.p.f.u)}$- 0.11-0.12 ; supplementary figure B3). The $Si^{+4}_{(a.p.f.u)}$ content in white mica is close to the muscovite end-member, between 3.00-3.03 (supplementary figure B3d).

Table 8- Representative Electron Microprobe (EMPA) analyses of minerals from samples NESG-388 and NESG-401. (b.d.l. - below detection limit).

	Liberdade Nappe - NESG-388						Andrelândia Nappe - NESG-401						
	Grt (core)	Grt (rim)	Pl (core)	Pl(rim)	Ms	Bt	Grt (core)	Grt (mantle)	Grt (rim)	Pl (core)	Pl(rim)	Ms	Bt
SiO2	36.93	37.40	64.35	60.89	46.19	34.97	36.98	37.05	36.97	62.16	59.91	45.73	35.15
TiO2	0.04	b.d.l	b.d.l	b.d.l	0.91	2.34	0.06	b.d.l	b.d.l	b.d.l	b.d.l	0.68	2.05
Al2O3	20.85	20.68	23.40	25.59	36.45	19.13	20.47	20.87	20.68	23.99	25.09	35.81	18.76
FeO_{Tot}	35.81	35.92	0.06	0.26	1.27	21.41	28.37	34.78	34.03	1.09	1.14	2.54	18.88
MnO	2.28	2.65	b.d.l	b.d.l	0.02	0.04	4.92	2.1	4.56	b.d.l	b.d.l	0.01	0.06
MgO	2.69	2.17	b.d.l	b.d.l	0.61	7.67	1.42	3.54	2.72	b.d.l	b.d.l	0.53	10.44
CaO	1.80	1.79	4.20	6.53	0.01	b.d.l	7.92	2.52	2.12	4.37	6.69	b.d.l	0.05
Na2O	b.d.l	b.d.l	8.96	7.73	0.80	0.18	b.d.l	b.d.l	b.d.l	8.37	7.51	1.08	0.21
K2O	b.d.l	b.d.l	0.09	0.06	9.51	8.71	b.d.l	0.01	b.d.l	0.05	0.05	9.08	8.80
Totals	100.4	100.6	101.1	101.1	95.8	94.5	100.1	100.9	101.1	100.0	100.4	95.5	94.4
Oxygens	12	12	8	8	11	11	12	12	12	8	8	11	11
Si	2.982	3.015	2.807	2.679	3.041	2.701	2.977	2.961	2.968	2.751	2.664	3.032	2.683
Ti	0.002	-	-	-	0.045	0.136	0.003	-	-	-	-	0.034	0.118
Al	1.985	1.966	1.203	1.327	2.830	1.742	1.943	1.966	1.958	1.251	1.315	2.799	1.688
Fe3	0.004	0.004	0.002	0.002	0.003	0.004	0.064	0.064	0.064	0.035	0.035	0.053	0.061
Fe2	2.414	2.418	-	0.007	0.067	1.379	1.839	2.253	2.214	0.001	0.003	0.082	1.137
Mn	0.156	0.181	-	-	0.001	0.003	0.336	0.142	0.310	-	-	0.001	0.004
Mg	0.324	0.261	-	-	0.060	0.883	0.171	0.422	0.325	-	-	0.052	1.187
Ca	0.155	0.155	0.196	0.308	0.001	-	0.683	0.216	0.182	0.207	0.319	-	0.004
Na	-	-	0.758	0.660	0.102	0.028	-	-	-	0.718	0.647	0.139	0.031
K	-	-	0.005	0.003	0.799	0.858	-	0.001	-	0.003	0.003	0.768	0.857
Sum	8.02	8.00	4.97	4.99	6.949	7.734	8.02	8.02	8.02	4.97	4.99	6.96	7.77
XAlm	0.79	0.80	XAn-0.20	XAn-0.32	XMg-0.47	XMg-0.39	0.61	0.74	0.73	XAn-0.22	XAn-0.33	XMg-0.39	XMg-0.51
XPrp	0.11	0.09					0.06	0.14	0.11				
XSps	0.05	0.06					0.11	0.05	0.10				
XGrs	0.05	0.05					0.23	0.07	0.06				

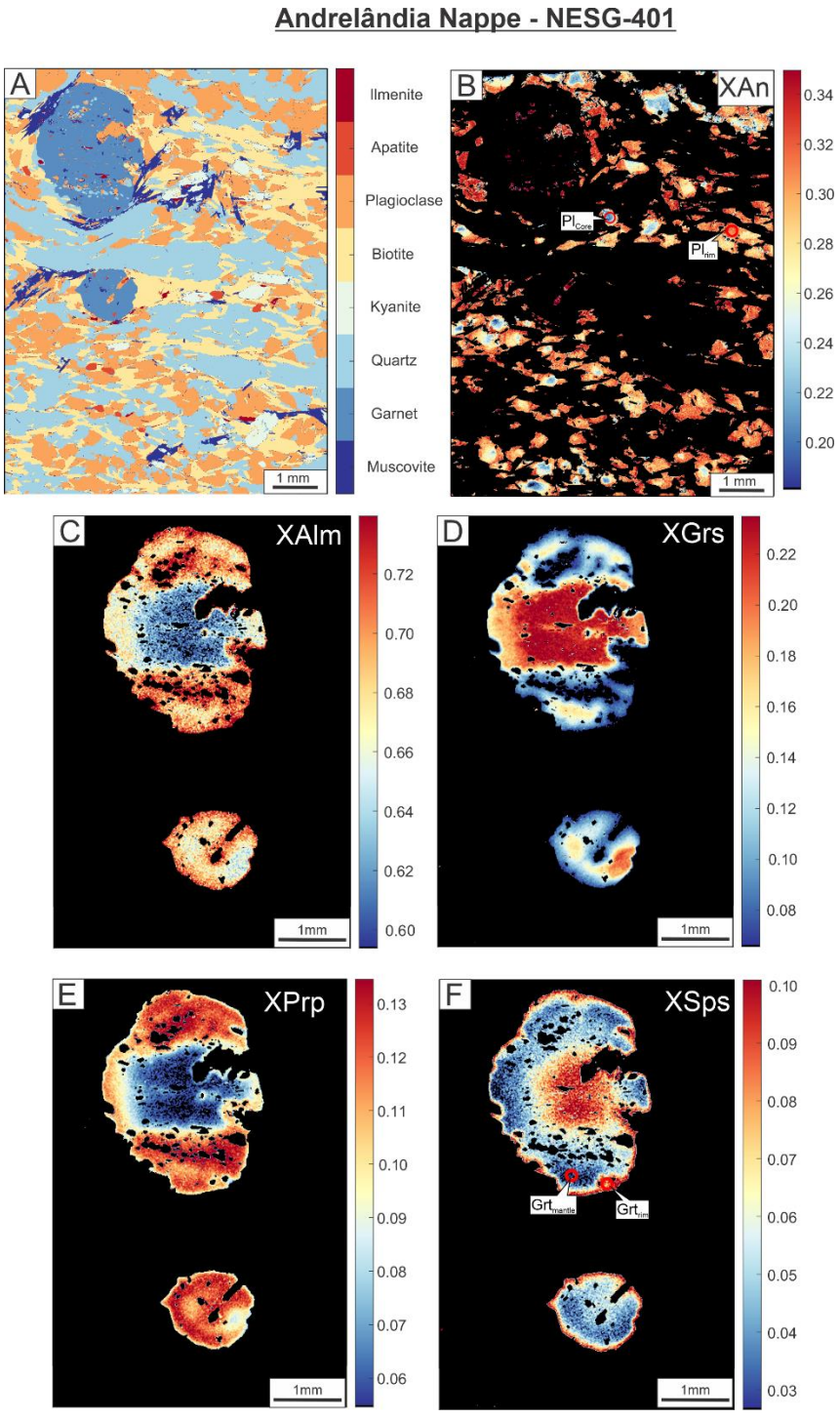

Figure 27 - Quantitative compositional maps for sample NESG-401 of the Andrelândia Nappe; a) Mineral map of the investigated thin-section area showing the mineral phases in the mapped area; b) Anorthite (XAn) content in plagioclase map; c)-f) Almandine (XAlm), grossular (XGrs), pyrope (XPrp) and spessartine (XSps) zoning in garnet. The red circles indicate the area used to perform the Qcmp maps for garnet, plagioclase core and rim..

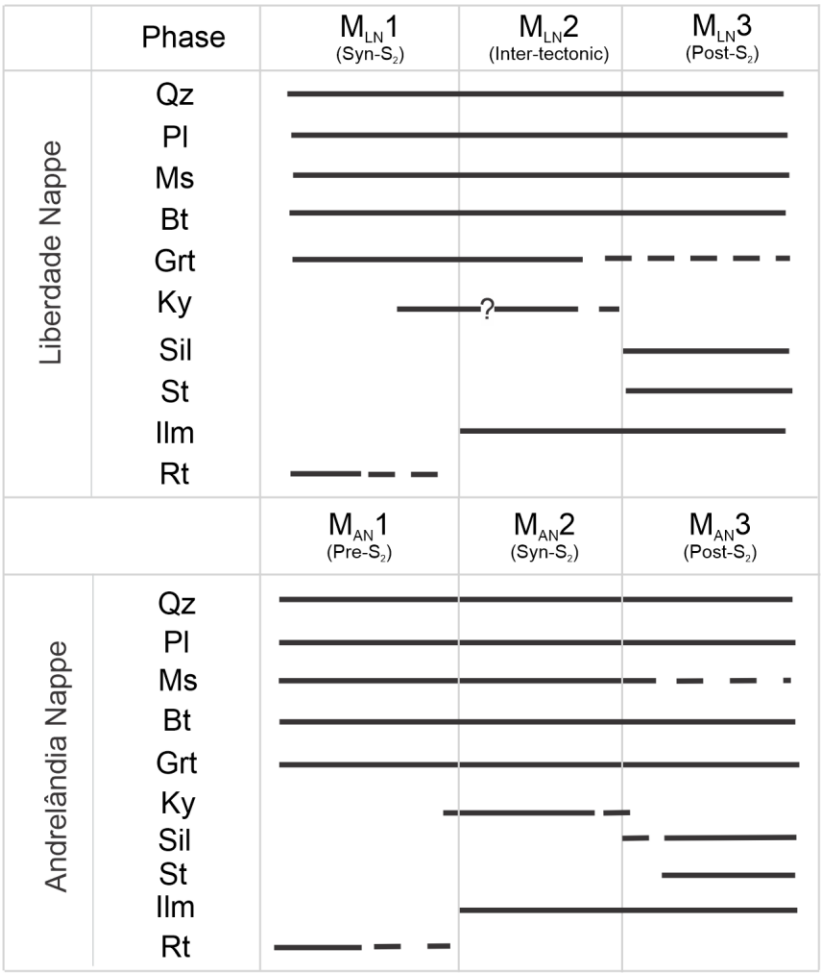

Figure 28- Blastesis-deformation relationships in the Liberdade and Andrelândia Nappes.

4.5 Iterative thermodynamic modeling (ITM) and *P-T* path

The iterative thermodynamic modeling (ITM) integrated with quantitative compositional mapping was applied as the strategy for setting up the metamorphic story of the Andrelândia and Liberdade Nappes using the software Bingo-Antidote a XMapTools add-on (Duesterhoeft and Lanari, 2020; Lanari and Duesterhoeft, 2019; Lanari and Hermann, 2021). This approach provides a means of investigating rocks that were not fully re-equilibrated during their metamorphic paths. Through the quantitative compositional maps, areas\phases within a sample that best represents the reactive phases can be selected for the local bulk composition (LBC) calculation. Furthermore, the Bingo-Antidote software provides a series of statistics routines that compare the model results with the observed mineral assemblage, modes, and phase compositions for the LBC studied. The bingo routines

calculate the model quality, assessing as much as it matches with the LBC mineral assemblage (Q_{asm}), mineral modes (Q_{mode}), and mineral compositions (Q_{cmp}). The quality factors Q_{asm}, Q_{mode}, and Q_{cmp} vary from 0%, which means there is no match between the model and LBC observations, and 100%, meaning that the model perfectly reproduces the LBC features. In addition, the antidote provides routines to evaluate how the quality factors change within the model *P-T(-X)*. The Andrelândia and Liberdade Nappes thin-section areas investigated for obtaining LBCs are displayed in Fig. 25a and 27a. The maps of quality factors from both samples are shown in **appendix B** figures B4, B5, and B6.

The isochemical diagrams were calculated for the local bulk composition (LBC) obtained by the Bingo-Antidote using the Theriak-Domino software (Capitani and Petrakakis, 2010; de Capitani and Brown, 1987) to illustrate the stability of mineral fields. The calculations were performed in the chemical system MnO-Na_2O-CaO-K_2O-FeO-MgO-Al_2O_3-TiO_2-SiO_2-H_2O. The water amount was chosen in order to optimize the quality factors using the antidote recipe 14. The diagrams were calculated for the *P-T* range of 4-12 kbar and 550-725 °C. The database tc55 (Holland and Powell, 1998), provided and employed in the Bingo-Antidote software, was used for the isochemical diagrams calculations. The respective solution models were utilized: feldspar (Baldwin et al., 2005), garnet (White et al., 2005), biotite (White et al., 2005), staurolite (Holland and Powell, 1998), cordierite (Holland and Powell, 1998), white mica (Coggon and Holland, 2002), ilmenite (White et al., 2007) and melt (White et al., 2007).

4.5.1 Sample NESG-388 - Liberdade Nappe

The calculated isochemical diagram for the Liberdade Nappe LBC is presented in Fig. 29a. The observed peak mineral assemblage, quartz+plagioclase+white mica+biotite+ilmenite, is stable in the penta-variant field constrained in the *P-T* range of 6.5-12 kbar and 600-670°C. Assuming the mineral phase equilibrium, the optimal *P-T* condition is expected to be achieved at 628°C and 7.5 kbar. At this condition, the quality factors for the mode (Q_{mode}) is 92%, and the system mineral chemistry (Q_{cmp}) is 86% (Fig. 29b).

The mineral *P-T* chemistry composition maps, corresponding to the areas displayed in the Fig. 25 **and appendix B** figure B2, are presented in **appendix B** figure B4. They display a more complex story used to trace the *P-T* path (Fig. 29b). The An-poor plagioclase

core compositions ($Q_{cmp=}$100%) are stable in higher pressure, 8.5 kbar up to 11.5 kbar, in large temperature conditions, from 500°C to 700°C. On the contrary, plagioclase rim composition records a lower pressure condition, down to 8 kbar, and temperatures from 590°C to 660°C. Although the optimal *P-T* conditions obtained by the antidote, peak conditions are better constrained by plagioclase rim composition (Q_{cmp} =100%), around 650°C and 9.5-10 kbar. The Na-Ca diffusion in plagioclase is considered slower than garnet Ca-Fe-Mg-Mn in temperatures above 600°C (Caddick et al., 2010; Lanari and Hermann, 2021). These described diffusional behaviors are the likely causes of plagioclase core records better the prograde conditions rather than garnet.

Plagioclase rim (Q_{cmp} =100%), and garnet (Q_{cmp} =90-100%) mineral chemistry compositions in addition with the mineral modes (Q_{mode} =100%) intersect at the hexa-variant field in which Qz+Pl+Bt+Grt+Ms+Ky+Ilm are the stable phases. The intersection is around 650°C and 7-7.5 kbar, suggesting an almost isothermal decompression path. Relics of kyanite are described in LN (Fig. 24f), supporting that this mineral was stable in some moment of the LN *P-T* path. Lastly, the *P-T* path later stage is recorded by the compositional match between plagioclase rim and muscovite (Pl-Q_{cmp} =100%; Ms- Q_{cmp} =95%) in the hexa-variant field in which Qz+Pl+Grt+Bt+Ms+Ilm+Sil+H_2O are stable. A *P-T* path (Fig. 29b) is suggested based on the above mineral chemistry and mode optimal quality factors fields, and the $M_{LN}1$, $M_{LN}2$, and $M_{LN}3$ metamorphic stages described in section 4.4.1. The quantitative map of the Ti-in-biotite thermometer (Henry et al., 2005) was applied (**appendix B** figure B2c). It displays values from 650 to 580°C consistent with the findings obtained by the ITM approach.

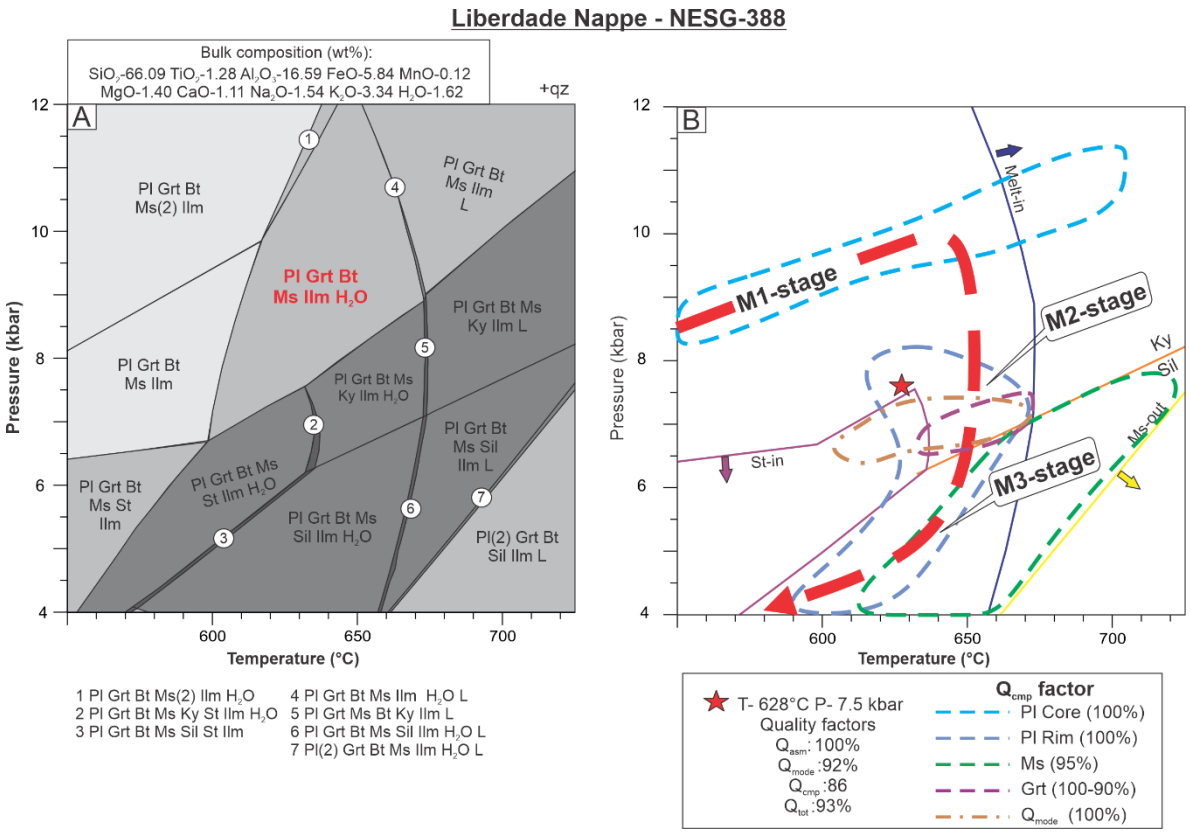

Figure 29 - a) P-T isochemical phase diagram in the MnNCKFMASHT system for the Liberdade Nappe (NESG-388); b) P-T path based on optimal conditions of mineral chemistry composition (Qcmp) and mode (Qmode) maps. The red star corresponds to the optimal P-T conditions obtained by the antidote.

4.5.2 Sample NESG-401 – Andrelândia Nappe

Fig. 30a displays the isochemical diagram built for the Andrelândia Nappe LBC that better represents the peak conditions. Bulk compositions that consider phases that are not fully equilibrated in the system, such as minerals relics or displaying compositional zoning, can affect the thermodynamic models quality (Konrad-Schmolke et al., 2008; Lanari and Engi, 2017; Spear, 1988). Once one garnet of the LBC is strongly zoned and likely its core was unreactive at peak condition, for avoiding the question described above, the garnet core area was subtracted and is not considered in the bulk composition. Although, the isochemical diagram taking into account the garnet core composition and the *P-T* stability field map for garnet core composition (garnet core Q_{cmp}) are provided in the **appendix B** figure B5. Therefore, the $M_{AN}1$ stage, which corresponds to a mineral assemblage preserved in the garnet core, does not appear in the suggested *P-T* path.

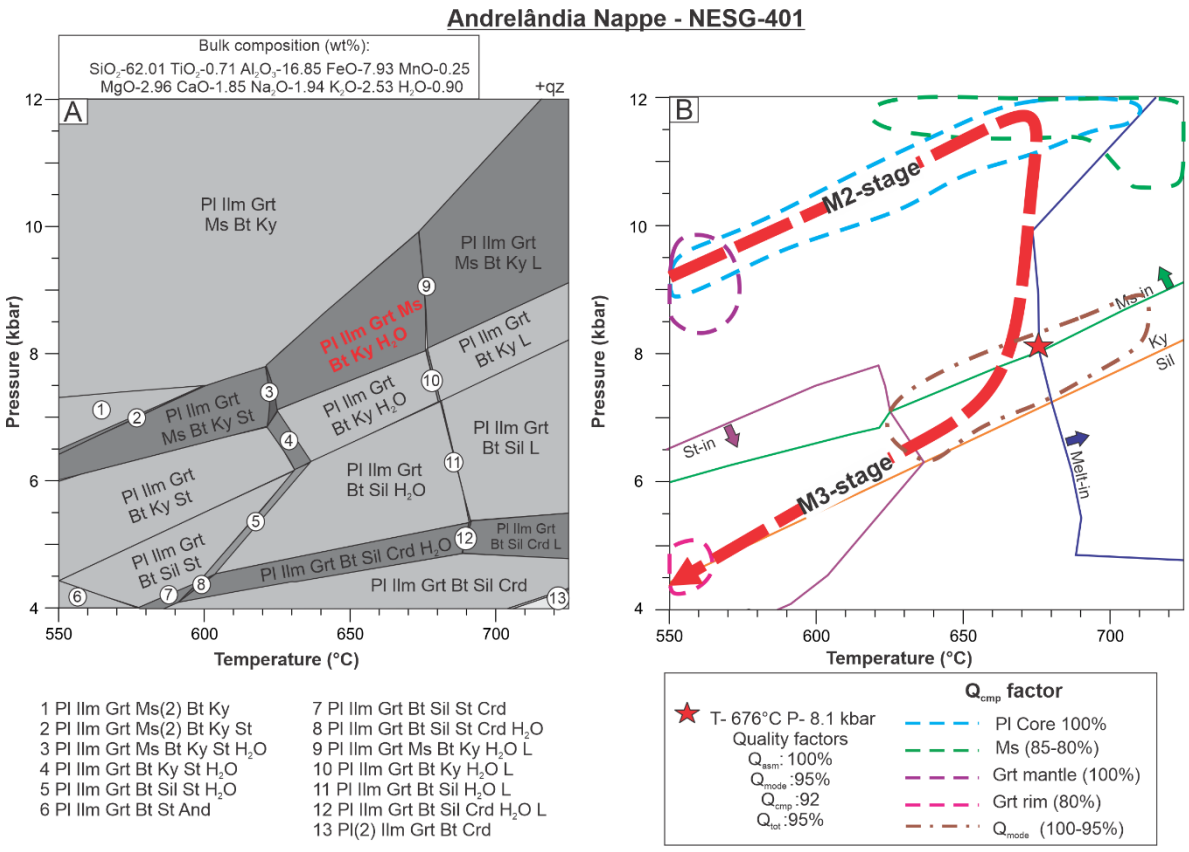

Figure 30 - a) P-T isochemical phase diagram in the MnNCKFMASHT system for the Andrelândia Nappe (NESG-401); b) P-T path based on optimal conditions for mineral chemistry composition (Q_{cmp}) and mode (Q_{mode}) maps. The red star corresponds to the optimal P-T conditions obtained by the antidote.

The peak mineral assemblage, Qz+Pl+Bt+Grt+Ky+Ms+Ilm+H_2O, was constrained in the quadri-variant field delimitated in the *P-T* range of 620°C-675°C and 7-10 kbar. The optimal *P-T* condition obtained is 676°C and 8.1 kbar with $Q_{cmp=}$ 92% and Q_{mode}=95% (Fig. 30b). The mineral phases chemical composition of the sample NESG-401 preserves three stages of the metamorphic path, the prograde, decompression, and cooling (Fig. 30b), which were traced using *P-T* stability field maps (**appendix B** figure B6). The prograde path was traced taking into account the compositions of garnet mantle (Q_{cmp} =100%), which records early stages of amphibolite facies around 550-570°C and 8-9 kbar, plagioclase core (Q_{cmp} =100%), and white mica (Q_{cmp} =85-80%). Indeed, the antidote optimal conditions calculations seem to underestimate the peak condition. The plagioclase core and white mica chemical composition provide a better constrain, crossing at *ca.* 660°C-670°C and 11.5-12 kbar, at these conditions, Qz+Pl+Bt+Grt+Ky+Ms+Ilm are the stable phases ($M_{AN}2$ stage). An almost isothermal decompression is suggested based on the mineral modes (Q_{mode}= 95-

100%) field of stability, which is at lower pressure of 6-8 kbar but at almost the same temperature range, from 625 to 680 °C. At last, garnet rim chemical composition (Q_{cmp} =80%) provided information about the AN cooling stage. It is equilibrated at 550°C and 4.5 kbar in the stability field of Qz+Pl+Grt+Bt+Ilm+St+Sil ($M_{AN}3$ stage; Fig. 30b). The Ti-in-biotite thermometer map (**appendix B** figure B3) displays temperatures ranging from 630 to 560 °C, in agreement with the retrograde temperature conditions obtained by ITM.

4.6 EMPA Monazite petrochronology

To constrain the timing of metamorphic and deformation events, *in-situ* U-(Th)-Pb monazite chemical dating was carried out by EMPA (e.g., Dahl et al., 2005; Dumond et al., 2015; Williams et al., 2007, 2006; Williams and Jercinovic, 2002). The analytical procedures are described in **appendix B**.

4.6.1 Sample NESG-388 – Liberdade Nappe

Monazites from sample NESG-388 are between quartz, plagioclase, white mica, and biotite from the matrix. Ten crystals were chosen to perform X-ray maps and trace element analysis. The results are illustrated in Fig. 31. Most of the crystals display an elongated shape parallel to the mylonitic foliation, varying in size from 70 to 250 µm, except the Mnz 4, associated with ilmenite which shows an irregular lobate shape. In some crystals, small quartz (e.g., Mnz 4, Mnz 5, and Mnz 6) inclusions were observed, but most monazites are inclusions free. The monazites display a sectorial core-rim internal zoning (e.g., Mnz 1, 2, 6 and 7). A remarkable feature that might be highlighted is the core and rim zonation pattern that is well-aligned (e.g., Mnz1, 2, 6, 8, and 10) with the main foliation, suggesting a pre- to syn-mylonitic growth related to the rock fabric. In addition, the Mnz 7 occurred on the S-plane of a *S-C* fabric.

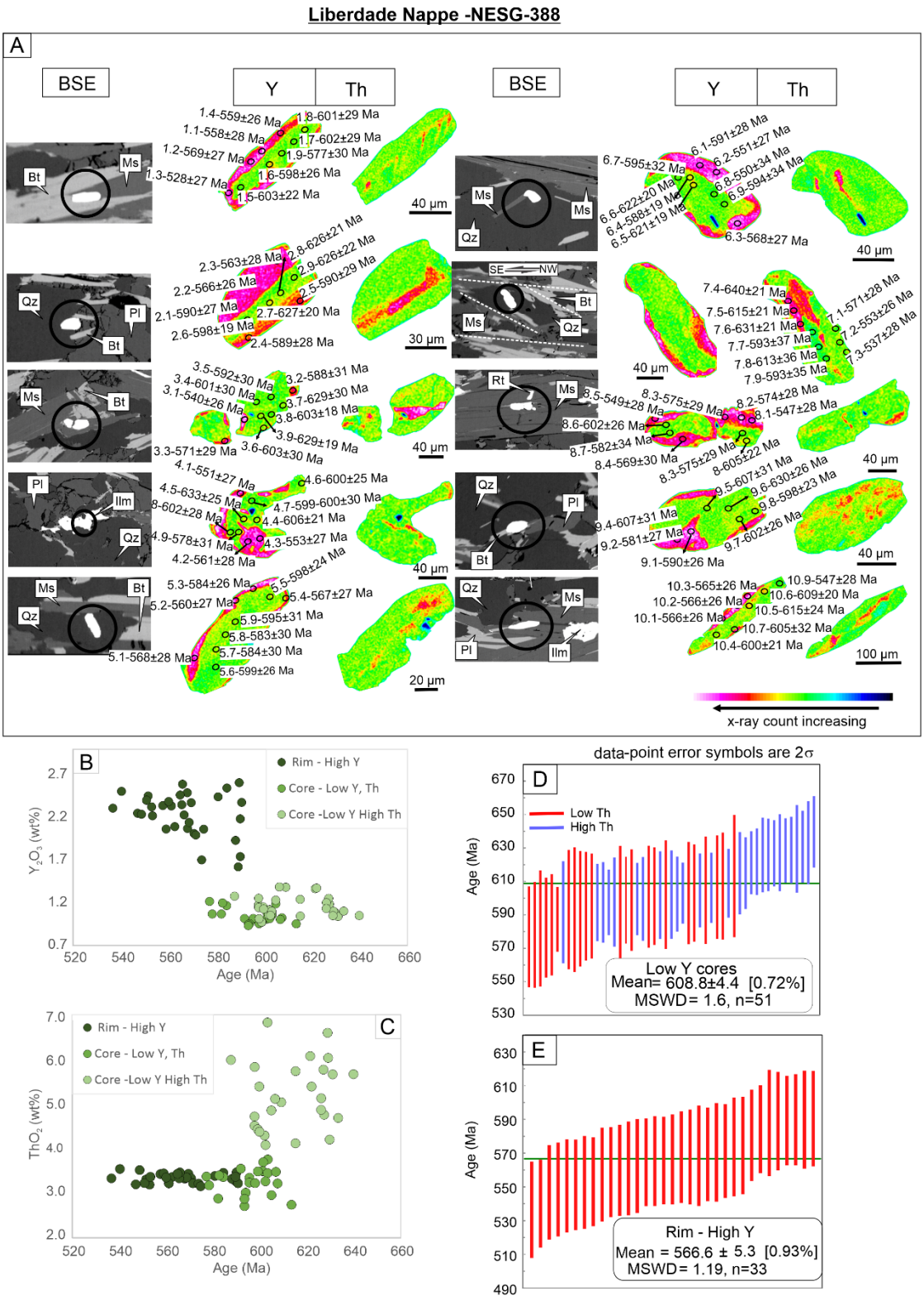

Figure 31 - Liberdade Nappe (sample NESG-388): a) BSE images, X-ray maps (Y and Th) of monazites showing structural position, textural relationships, and internal zoning; b) Y2O3 (wt%) vs. age plot; c) ThO2 (wt%) vs. age plot; d) weighted average diagram for monazite core dates (domain 1 and 2); e) weighted average diagram for monazite rim dates (domain 3).

Three chemical domains are distinguished based on the X-ray maps, mainly of Y and Th distribution (Fig. 31a, b, and c). Domain 1, characterized by high-Th and low-Y cores, are small patchy (e.g., Mnz 9), and straight (e.g., Mnz 2). The Y_2O_3 content (wt%) varies from 1.02 to 1.39, and the ThO_2 (wt%) values are very spread, ranging from 4.00 to 6.95. Domain 2 is related to core characterized by low-Y and -Th. The Y_2O_3 (wt%) and ThO_2 (wt%) amounts vary respectively in a narrow range of 0.93-1.22 and 2.29-3.80. The third domain (domain 3) is associated with monazite rims showing high-Y, in which the Y_2O_3 (wt%) amounts are spread in a broad range from 1.62 up to 2.61, and ThO_2 (wt%) variation is concentrated between 3.18-3.59.

In total, 84 punctual EMPA spots were acquired in the different chemical domains for the chemical dating calculation. Obtained dates span from 640 to 540 Ma. Domain 1, characterized by high-Th and low-Y core, dates range from 640±21Ma to 588±19 Ma. Domain 2, with low-Th and Y cores, has dates spread from 613 Ma±36 Ma to 550±33 Ma. Owing to ages from domains 1 and domain 2 being relative to core, they were plotted in the same weighted average diagram (Fig. 31d) and yielded a mean age of 609±4 Ma (n=55; MSWD=1.6). Domain 3, related to high-Y rims, has dates from 590±28 Ma to 540±26 Ma and yields a mean weighted average age of 567±5 Ma (n=33; MSWD=1.19; Fig. 31e).

4.6.2 Sample NESG-401 – Andrelândia Nappe

Fig. 32a displays the mapped monazite crystals (n=8) from the sample NESG-401, the elements analysis spots position, and the results of chemical dating. The monazites occur between the matrix minerals, hosted in quartz, plagioclase, biotite, and white mica (e.g., Mnz 1, 3, and 5); one crystal is enclosed in kyanite (Mnz 4), and three are located in apatite rims (Mnz 2, 5 and 8). The size of crystals varies from 50 µm up to 100 µm. Monazite shape varies from rounded to elongated. Quartz inclusions are observed in Mnz 1 and Mnz 7. Regarding the monazite compositional zoning, they are very homogenous. The crystals display intermediate Y_2O_3 contents varying from 1.3 to 2.9 wt% and variable Th amounts, varying the ThO_2 between 1.9 and 5.4 wt% (Fig. 32a, b and c). The exception is represented by rims significantly enriched in Th (with ThO_2 content between 6.7-13.1 wt%) observed in crystals associated with apatite (Fig. 32c).

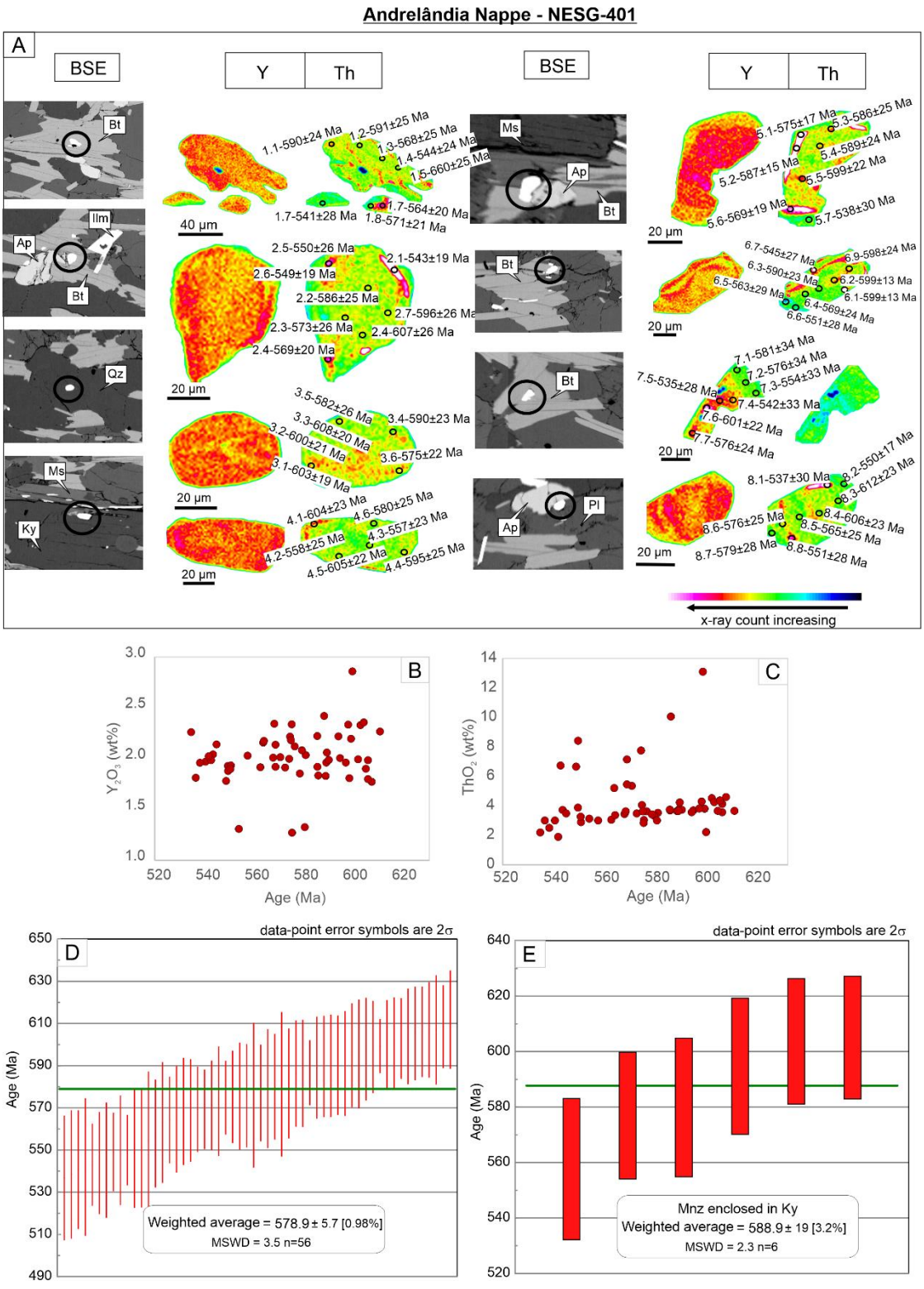

Figure 32 - Andrelândia Nappe (sample NESG-401): a) BSE images, X-ray maps (Y and Th) of monazites showing structural position, textural relationships, and internal zoning; b) Y2O3 (wt%) vs. age plot; c) ThO2 (wt%) vs. age plot; d) weighted average diagram for monazite core dates; e) weighted average diagram for monazite enclosed in Ky.

A total of 56 chemical spots of EMPA were carried out. The obtained U-(Th)-Pb chemical dates range from 612±23 Ma to 535±28 Ma. The dates are plotted in the weighted average diagram (Fig. 32d), and they yield a mean age of 579±5.7 Ma (MSWD=3.5). Of particular interest is the crystal enclosed in kyanite (Mnz 4), which can report worthy information about tectonic and metamorphic events undergone by this rock since the kyanite is considered coeval with the main foliation of the study sample. The dates vary from 605±22 Ma to 558±25 Ma and yield a mean age of 589±19 Ma (MSWD=2.3; Fig. 32e).

4.7 Discussion

4.7.1 Monazite chemical dating interpretation

The *in-situ* monazite dating combined with the X-ray trace elements maps (e.g., Y and Th) allows correlating monazite growth episodes with metamorphic reactions and deformation stages (Bosse and Villa, 2019; Iaccarino et al., 2020, 2017; Spear and Pyle, 2002; Williams et al., 2007; Williams and Jercinovic, 2012, 2002). The Y and HREE concentration in monazite mostly depends on the garnet presence in the system, once this mineral is the preferential sink for these elements (Spear and Pyle, 2002). Whereas the Th concentration is controlled by a Th-rich phase breakdown responsible for releasing this element in the system, preferentially partitioned into monazite structure (Benetti et al., 2021; Catlos, 2013; Kohn and Malloy, 2004; Williams et al., 2022). Moreover, monazite can be a fabric-forming mineral in deformed rocks and behaves as a porphyroclast rotated and with inclusion trails (Dumond et al., 2008; Williams et al., 2007). Therefore, the *in-situ* dating allows us to relate the monazite with its microstructural position, providing means to constrain the deformation time.

At subsolidus conditions, two main metamorphic reactions will control the monazite chemistry. Firstly, the allanite breakdown is responsible for releasing most of the REE necessary for the monazite precipitation (Gasser et al., 2012; Janots et al., 2008; Kohn and Malloy, 2004; Palin et al., 2012; Spear and Pyle, 2010; Wing et al., 2003). This reaction occurs between the greenschist-to amphibolite facies transition, in temperature conditions around 550°C (Gasser et al., 2012; Janots et al., 2008; Spear and Pyle, 2010). At these conditions, if monazite grows coeval or previous than garnet is a stable phase, the monazite will display intermediate-to high-Y content. In contrast, if garnet is already a reactive phase,

the Y will be partitioned toward it, and the monazite will be Y-depleted. In addition, due to allanite being a Th-rich mineral, the monazite that grows soon after its breakdown tends to be Th-enriched (Benetti et al., 2021; Catlos, 2013; Kohn and Malloy, 2004). Another monazite generation is expected during the rock decompression path, in which garnet breakdown releases Y and HREE in the system, and the monazite precipitating from this reaction will display enriched signatures in these elements (Gasser et al., 2012; Kohn et al., 2005; Williams et al., 2007).

Considering the monazite behavior during the sub-solidus metamorphism and deformation described above, two episodes of its growth can be identified in sample NESG-388 from the Liberdade Nappe. The first episode is correlated with Y-depleted cores with a wide range of Th amounts (domains 1 and 2). These dates are associated with prograde metamorphism in which monazite grew post-garnet crystallization in the system and yielded mean chemical age of 608±4 Ma. The Th-enriched domains (domain 1) can likely be linked to the early prograde path, soon after the allanite-to-monazite transition, releasing Th in the system and reproducing the oldest dates. The weighted mean age of 567±5 Ma, represented by Y-enriched monazite rims (domain 3), is interpreted as linked with garnet resorption during the rock decompression. Furthermore, the growth orientation of some high-Y rims aligned with the mylonitic foliation (e.g., Mnz 1 and 2), and the crystal in the *S-C* band (Mnz 7) rotated during the shearing suggest that the decompression was coeval with the development of the mylonitic fabric (Post-S_2) related with top-to-the-SE motion.

The monazites from sample NESG-401 of the Andrelândia Nappe are homogenous with intermediate Y and Th-depleted. They are interpreted as growing coeval with the garnet during the prograde metamorphism, at a minimum age of 578.9±5.7 Ma. The Mnz 4 is enclosed in kyanite and parallel to the AN micaschist main fabric, providing time constraints for main foliation-forming deformation (Syn-S_2) and kyanite growth during the *P-T* path. This single crystal yields mean age of 588.9±19 (n=6), consequently interpreted as corresponding to the time of deformation, and taking into account the age standard deviation, is considered contemporary to the prograde metamorphism. Rims highly enriched in Th (Mnz 2, 5, and 8) are attributable to exchange reactions between apatite and monazite and have no signatures that can associate them with any significant tectono-metamorphic event.

4.7.2 Tectono-metamorphic evolution of the Andrelândia Nappe System (ANS)

The microstructural descriptions, *P-T* path traced through thermodynamic metamorphic modeling, and monazite petrochronological data presented here elucidated the complex ANS framework in the southern sector of the SBO. Both the Liberdade and Andrelândia Nappes evolved from a clockwise sub-solidus *P-T* path characterized by burial and heating, followed by nearly isothermal decompression, and lastly, cooling and decompression. The Liberdade Nappe (NESG-388) $M_{LN}1$ stage assemblage (Qz+Pl+Grt+Bt+Ms+Ilm) records its prograde metamorphic path, which achieved peak conditions at *ca*. 650°C and 9.5-10 kbar and has a minimum age of 609±4 Ma. The further stages are the $M_{LN}2$ (Qz+Pl+Grt+Bt+Ms+Ilm±Ky) and the $M_{LN}3$ (Qz+Pl+Grt+Bt+Ms+Ilm+Sil+St), which represent respectively the early isothermal exhumation and late exhumation/cooling episodes related with the nappe migration, whose the minimum age is constrained at 567±5 Ma.

The micaschist from Andrelândia Nappe (NESG-401) records a prograde burial path from ~550°C and 9.0-9.5 kbar up to ~680 °C and 11-12 kbar ($M_{AN}2$ stage). The minimum age for prograde metamorphism was estimated at 578.9±5.7 Ma, and within the uncertainties is considered coeval with the main deformation (S_2) event underwent by this rock. It was followed by an almost isothermal decompression, in which the pressure conditions decreased from 12 kbar down to 8.0-7.0 kbar. Lastly, the $M_{AN}3$ stage related to staurolite and sillimanite appearance in the system was constrained in the *P-T* range of 670-550°C and 8.0-4.5 kbar.

A compilation of literature *P-T* paths from the ANS is provided in Fig. 33. Even though the different approaches adopted by the other authors (e.g., inverse and forward thermodynamic modeling), and considering the different methods-related uncertainties, peak conditions constrained for the Andrelândia and Liberdade Nappes in this contribution are in agreement with those previously reported by Coelho et al. (2017), Motta and Moraes (2017), Reno et al. (2012), Santos et al. (2004). However, there are differences between the *P-T* path traced here and those interpreted by these authors. For instance, Reno et al. (2021) suggested two episodes of isobaric cooling separated by a near-isothermal decompression phase to the Carmo da Cachoeira Nappe, the Andrelândia Nappe equivalent in the SBO northern sector. Moreover, Santos et al. (2004) considered that Andrelândia Nappe underwent heating during

exhumation, while the Liberdade Nappe evolved from an isothermal decompression. These *P-T* path contrasts can be assigned to different interpretations regarding blastesis-deformation relationships and distinct approaches used by each of the authors.

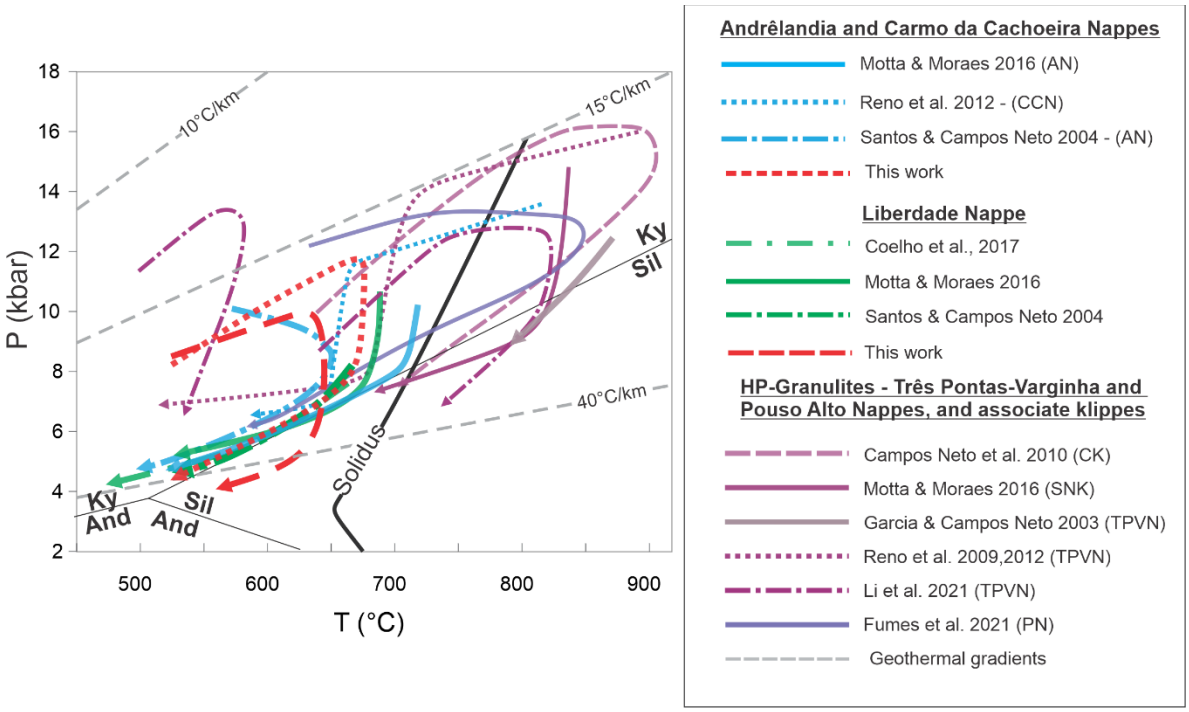

Figure 33 - Summary of Andrelândia Nappe System (ANS) P-T paths. Grey dotted lines display different geothermal gradients trends. Solidus curve from Spear et al. (1999) in the NaKFMASH system.

4.7.3 Tectonic implications

Our present findings shed new light on some critical points regarding the tectono-metamorphic events experienced by the ANS. The first point is related to the Andrelândia and Liberdade Nappes *P-T* paths. Microstructural observations and thermodynamic modeling show that the staurolite and sillimanite in the matrix are related to decompression and cooling stages, rather than a heating stage as considered by Coelho et al. (2017), Fontainha et al. (2020), Peternel et al. (2005), Trouw et al. (2013). Furthermore, the baric and thermic peaks of the suggested metamorphic paths, in both nappes, occur almost simultaneously. These suggested paths are not consistent with a second heating episode at lower pressure related to the Central Ribeira Orogeny.

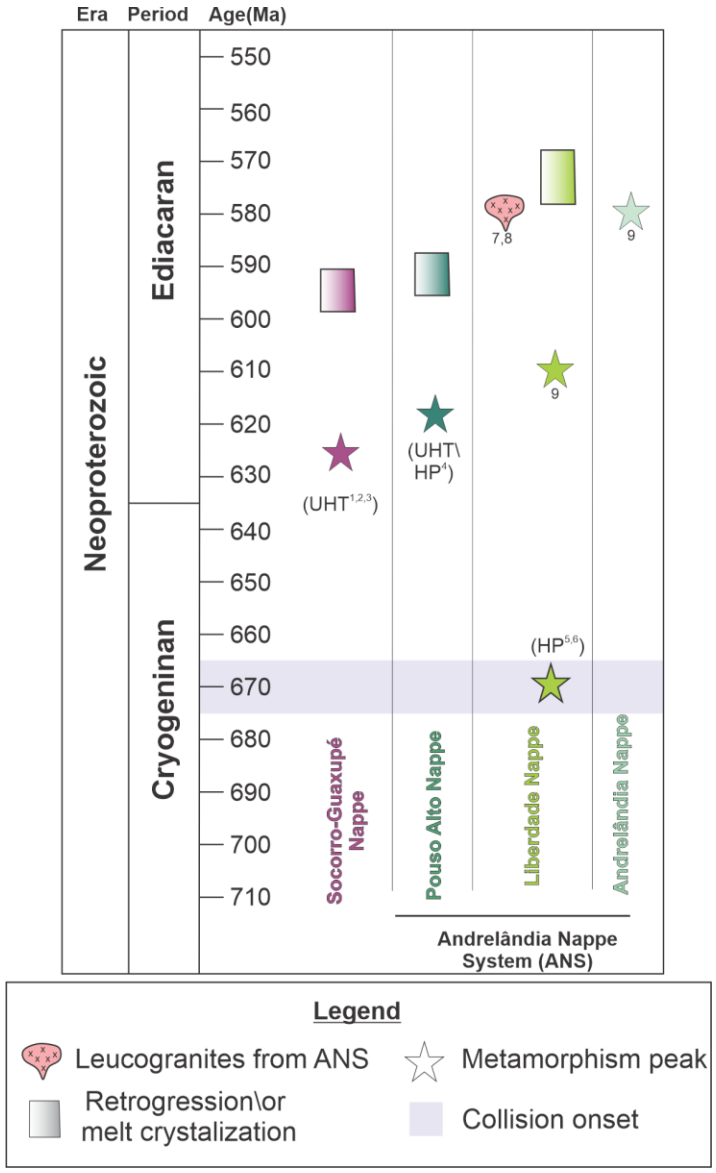

Figure 34 - Time-metamorphism synoptic plot illustrating the spread of SBO nappes prograde and retrograde ages. Geochronologic information is based on (1,2) Rocha et al. (2018, 2017); (3)Motta et al. (2021); (4) Benetti in prep.; (5) Frugis et al. (2018); (6) Reno et al. (2009), (7) Campos Neto et al. (2011); (8) Coelho et al. (2017); (9) this contribution. UHT-ultrahigh-temperature metamorphism, HP-high pressure metamorphism.

The second critical point concerns the time constraints of metamorphism and deformation (Fig. 34). The Liberdade Nappe attained amphibolite facies at ~610 Ma, nearly 20-30 Ma before the Andrelândia Nappe. Although the sample from Andrelândia Nappe does not have dates related to exhumation, the spread dates from the Liberdade Nappe linked with the exhumation mostly overlap the prograde monazite dates in the Andrelândia Nappe, structurally below. Hence, it is possible to claim that when the Liberdade Nappe onset its decompression path, the Andrelândia Nappe was still experiencing prograde conditions and

was likely exhumed afterward compared to the Liberdade Nappe. In other words, the dates around 590-570 Ma in the Liberdade Nappe are related to its exhumation and tectonic transport toward SE. In contrast, such time span is linked with prograde burial metamorphic conditions (coeval with kyanite growth) in the Andrelândia Nappe.

These achievements demonstrate a progressive rejuvenation of metamorphic ages toward the bottom of the ANS stack (Fig. 34). Indeed, the spread of ages from 630 Ma to 570 Ma within the SBO record a temporal variation in when the nappes attended their prograde/retrograde metamorphic stage (Fig. 34) rather than a second younger tectonic event as demonstrated here. Such findings corroborate that the SBO evolved from a single but progressive continent-continent collision event of the Paranapanema and São Francisco Cratons.

4.8 Conclusion

The *P-T-t-D* data provided here document the metamorphic and deformational history of the micaschists from the Andrelândia and Liberdade Nappes. The Liberdade Nappe attained prograde metamorphism at *ca.* 610 Ma and achieved peak conditions at ~650°C and 9.5-10 kbar. This stage was followed by a near-isothermal decompression with a minimum age of *ca*. 570 Ma. Meanwhile, the Andrelândia Nappe structurally below the Liberdade Nappe experienced prograde metamorphism later, at *ca.* 580 Ma, reaching the peak condition at *ca*. 680°C and 11.5-12 kbar. These achievements demonstrate that the spread of ages within the ANS is related to different periods in which each nappe from the ANS attained prograde and retrograde metamorphism. A rejuvenation of prograde and retrograde ages is observed towards the ANS bottom. This new dataset reinforces the idea that SBO evolved by the progressive evolution of the continental collision between the Paranapanema and São Francisco blocks.

CHAPTER 5

HP-UHT GRANULITE FROM POUSO ALTO NAPPE, SE BRAZIL: INSIGHTS INTO THE HEAT DRIVERS AND EXHUMATION OF LOWER CRUST

5.1 Abstract

The Pouso Alto Nappe (PAN) is part of the Southern Brasilia Orogen (SBO) hinterland and is mainly constituted by a K-feldspar+garnet+kyanite+rutile-bearing paragneiss interpreted as a residual HP-granulite. A study was addressed to the PAN granulite by combining detailed microstructural descriptions with monazite petrochronology, thermodynamic modeling, and trace elements thermometry. By integrating these data, it was possible to reconstruct the PAN granulite *P-T-t* trajectory and recognize for the first time a rock that experienced HP-UHT metamorphism within the SBO. Our results reveal that the prograde subsolidus metamorphic conditions occurred between *ca.* 670 and 620 Ma. Later, the granulite underwent undersaturated-water partial melting during heating and burial, achieving peak conditions of *ca.*1050-1150°C and 18-19 kbar at a maximum age of *ca.*620 Ma. The retrograde path evolved from continuous cooling and decompressing, in which the final melt crystallization took place at *ca.* 590 Ma. The obtained *P* data indicates that likely this rock was part of the continental subduction channel and reached crustal depths of *ca.* 70 km, corresponding to the interface between lower crust and lithospheric mantle in a double thickened crust. It is suggested that the UHT metamorphism was attained by combining heat production elements accumulation and minor mantle heat flow. The exhumation and cooling of the melt-weakened material are thought to begin after the delamination of denser material of the subduction conduit toward the mantle. Consecutively, the previous melt-weakened granulite onset its flow outward, likely driven by the gravitational force, with the exhumation and cooling rates estimated respectively of ~14°C/Ma and ~0.15 cm/yr. Lastly, it is suggested that the PAN granulite would record the transition from a wedge-shaped orogenic belt to an orogenic plateau during the continental collision development.

5.2 Introduction

Metapelites that experienced the high pressure (HP)-granulites facies have been recognized as part of the large hot orogens assemblage, such as in the European Variscan Belt (O'Brien, 2008; O'Brien and Rötzler, 2003), the Greenville Orogen (Indares, 2020; Indares et al., 2008; Rivers, 2012), and the Himalaya Belt (Groppo et al., 2007; Guilmette et al., 2011; Iaccarino et al., 2017; Lombardo and Rolfo, 2000). At HP-granulite facies (P>10 kbar) the characteristic mineral assemblage, related to pelitic protholits, is

quartz+garnet+kyanite+K-feldspar (O'Brien and Rötzler, 2003). This metamorphic condition is associated with crust subduction into lower crust/mantle depths during a continental collision (O'Brien and Rötzler, 2003). Therefore, the study of metamorphic rocks which experienced HP-granulite conditions can provide wealthy information about the composition and processes occurring in the deep crust during orogenesis, such as crustal thickening, partial melting, and lower crust flow.

The Southern Brasilia Orogen (SBO), localized in southeast Brazil, is one of the orogenic belts linked to the Gondwana supercontinent assembly. HP-granulites, that are part of the SBO hinterland, crop out in the Passos, Três Pontas-Varginha, Pouso Alto Nappes, and the Auiruoca, Carvalhos and Serra da Natureza klippes (Campos Neto et al., 2010; Campos Neto and Caby, 2000; Cioffi et al., 2012; Fumes et al., 2021; Li et al., 2021; Reno et al., 2012, 2009). Most of the petrochronological studies performed on the HP-granulites were focused on the Três Pontas-Varginha Nappe, with just a few data reported from other localities where they crop out, for instance, the Passos Nappe, Carvalhos, and Serra da Natureza Klippes (Campos Neto et al., 2010; Fumes et al., 2021; Motta and Moraes, 2017)

This chapter addressed a detailed investigation of the Pouso Alto Nappe (PAN) felsic granulite. We combined detailed textural and microstructural studies with monazite petrochronology, thermodynamic modeling, and trace elements thermometry. By integrating these data, we were able to reconstruct the PAN *P-T-t* trajectory and recognize for the first-time rocks that experienced HP-UHT metamorphism within the SBO. These results allowed insights into the metamorphism heat sources, deep crust subduction, and exhumation of the Pouso Alto Nappe, which were integrated into the tectonic evolution of the Southern Brasilia Orogen.

5.3 Pouso Alto Nappe (PAN) petrography, microstructural relationships, and mineral chemistry

The Pouso Alto Nappe (PAN) crops out in the south of Minas Gerais, southeastern Brazil (Fig. 23). The PAN is bounded in the south by the Socorro-Guaxupé Nappe and in the north by the Liberdade Nappe and Pouso Alegre Complex (Fig. 23). The PAN main lithotype is a medium-to coarse-grained K-feldspar+garnet+kyanite+rutile(±ilmenite)-bearing gneiss. The main foliation strike varies to NE-SW and dips toward NW in the northwest, NW-SE in

the northeast sector with the dip direction to NE, and in the north, the strike is E-W dipping to N. Such strike and dip direction variation of the main foliation is interpreted as cylindrical synform, SW-orientated. The general tectonic transport was toward NE, evidenced by the W-SW plunging of object lineation.

The main foliation is a spaced disjunctive foliation, mainly marked by coarse-grained and stretched quartz forming ribbons monomineralic completely recrystallized (Fig. 35a, 36a, and b). The matrix is mainly formed by K-feldspar and quartz (Fig. 35a and 36b). Kyanite forms elongated blades with long axis orientated along the main foliation, which can be folded wrapping garnet (Fig. 35b). Garnet porphyroblast has inclusions of quartz, biotite, rutile, kyanite, K-feldspar, and plagioclase, and ilmenite (Fig. 36c and d). Biotite is scarce in the matrix, and when observed, it is randomly orientated, usually associated with garnet rims and forming symplectites with quartz (Fig. 35b, g, and 36f). Rutile is observed enclosed in kyanite and garnet rims (Fig. 35c). In the latter case, it is usually aligned along the main foliation and with ilmenite corona (Fig. 35c). Few mylonitic structures and kinematic indicators are preserved within the main rock fabric. At the microscale, the kinematic indicators are represented by K-feldspar with core-mantle structure and asymmetric myrmekite growth along its boundaries, and mineral-fish such as kyanite and garnet (Fig. 35c, d, and e).

Several microstructures described in the literature associated with melt crystallization (Guilmette et al., 2011; Holness et al., 2011; Indares et al., 2008; Vernon, 2018, 2011) are observed. For instance, garnet with a reactive corona of granophyric texture (Fig. 35f). In this case, the garnet is interpreted as a peritectic mineral product of the biotite-dehydration reaction, in which Bt+Ky+Qz+Pl → Grt+Kfs+Rt+Melt. The granophyric corona, an intergrowth between quartz and K-feldspar, is a late product of the back reaction described above, between the peritectic garnet and cooling melt (Vernon, 2011 and references therein). Other examples described include: (i) biotite symplectic growth with quartz (Fig. 35g and 36f) replacing garnet and K-feldspar, (ii) tiny films of quartz+feldspar surrounding kyanite crystal (Fig. 35h) interpreted as melt-pseudomorphs.

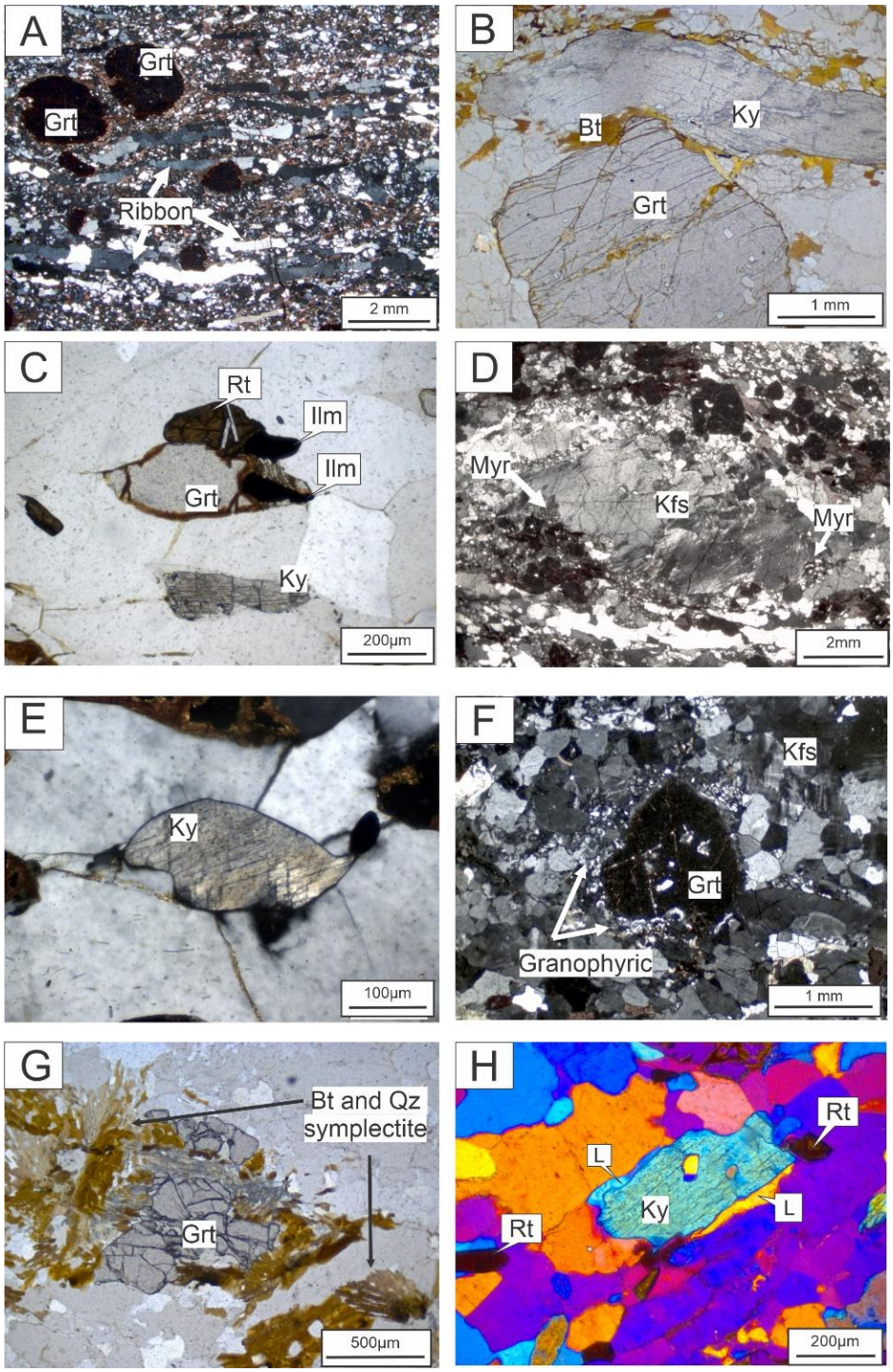

Figure 35 - Pouso Alto Nappe (PAN) granulite photomicrographs. a) Spaced disjunctive foliation marked by recrystallized quartz ribbons (UTM 506542/7546895); b) folded kyanite blade wrapping the garnet porphyroblasts (UTM 497499/7546556); c) garnet fish with rutile rim. Garnet and rutile shows ilmenite tails (UTM 503642/7548277); d) K-feldspar with core-mantle microstructure, and asymmetric myrmekite in its rim (UTM 503702/7548858); e) kyanite fish with ilmenite tail (UTM 503642/7548277); f) Garnet with reaction rim displaying the granophyric texture, made by an intergrowth between quartz and K-feldspar (UTM 497499/7546556); g) symplectite growth between quartz and biotite (UTM 503948/7548898) at the expense of garnet and K-feldspar; h) melt-film pseudomorphs (L) surrounding kyanite (UTM 496429/7547117).

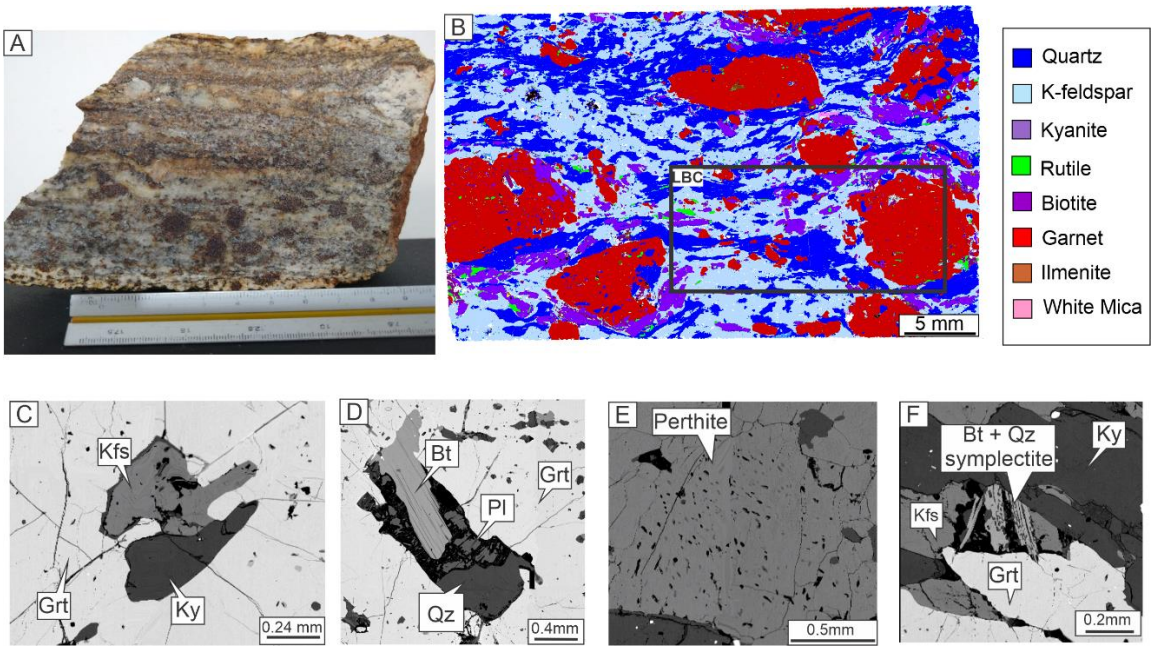

Figure 36 - K-feldspar-garnet-kyanite-rutile-bearing paragneiss, sample PA-16 (UTM 496150/7548121). a) Hand sample aspect; b) full thin-section map carried out using the SEM-MLA. The black square represents the X-ray mapped area used to calculate the local bulk composition (LBC); c-f) backscattered electron (BSE) images showing mineral microstructures; c) kyanite and K-feldspar enclosed in garnet; d) polymineralic pockets, constituted by biotite, plagioclase, and quartz, enclosed in garnet porphyroblasts; e) K-feldspar with perthite; f) quartz and biotite symplectite around garnet rim.

A representative sample of the K-feldspar+garnet+kyanite+rutile-bearing paragneiss (sample PA-16; UTM 496150\7548121; Fig. 36) from the Pouso Alto Nappe (PAN) was chosen for detailed investigation. The whole analytical procedure carried out is described in **appendix C**. The garnet occurs as medium-grained crystals (<1 mm) in the matrix and as porphyroblasts with a size of 0.5 cm up to 1.5 cm. The porphyroblasts have inclusions of quartz, kyanite, K-feldspar, plagioclase, rutile, biotite, ilmenite, and polymineralic pockets (Fig. 36c and d). Quantitative compositional maps show that the garnet porphyroblast is zoned, especially regarding the grossular and pyrope end-member variations (Fig. 37b, c, and d). From core to mantle garnet displays a bell-shaped profile, where almandine (X_{Alm}=Fe/Fe+Mg+Ca) and pyrope (X_{Prp}=Mg/Mg+Fe+Ca) increase, whereas the grossular (X_{Grs}=Ca/Ca+Fe+Mg) decreases (Core- X_{Alm}-0.63-0-.64, X_{Prp}- 0.21-0.22, X_{Grs}-0.08-0.09; Rim- X_{Alm}-0.70, X_{Prp}-0.25-0.26, X_{Grs}-0.04-0.05; Fig. 37b, c and d; table 9). In contrast, from the mantle to the rim, the garnet end-members have the opposite behavior, in which almandine (X_{Alm} =0.66) and pyrope (X_{Prp} =0.24-0.23) decrease while grossular increases

(X_{Grs} =0.09-0.08) (Fig. 37b, c, and d). The medium-grained garnets from the matrix display a homogenous composition similar to the porphyroblast rim (Fig. 37b, c, and d).

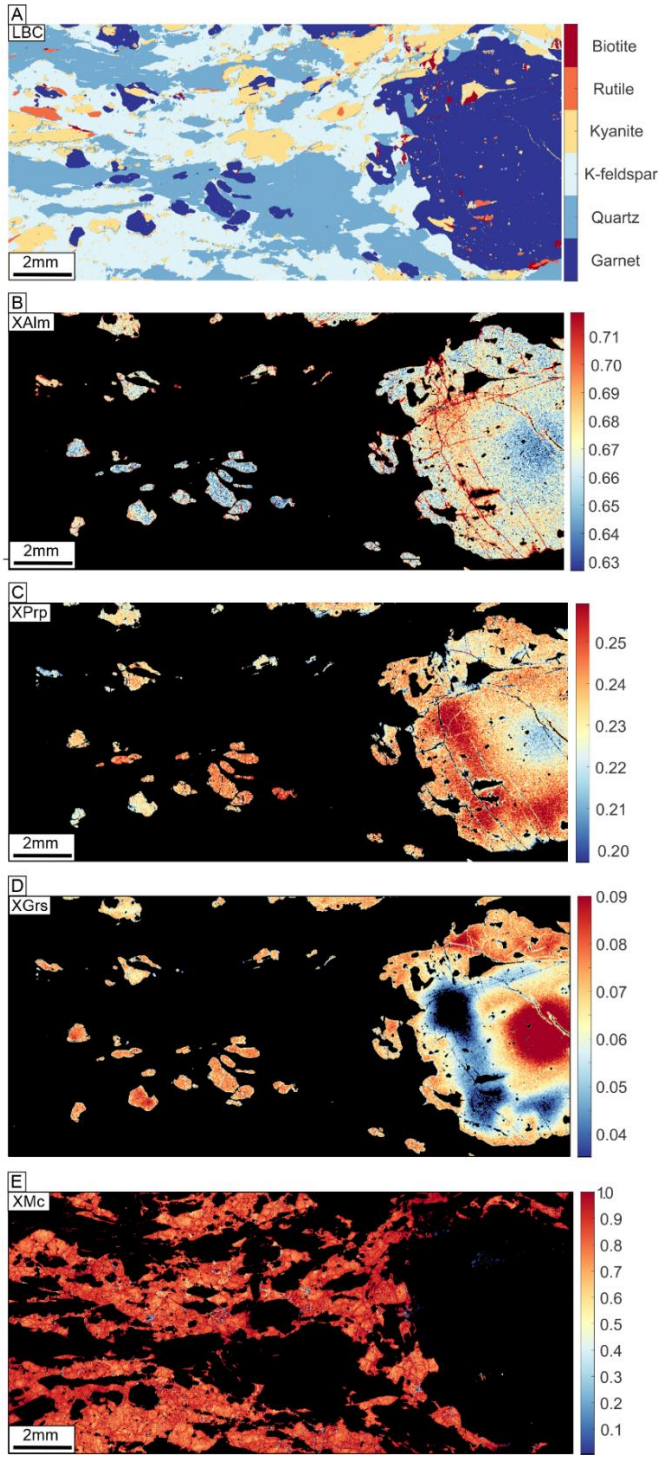

Figure 37- Quantitative compositional maps for sample PA-16; a) mineral map of the investigated thin-section area; b)-d) almandine (X_{Alm}), pyrope (X_{Prp}), and grossular (X_{Grs}) zoning in garnet; e) map of microcline (X_{Mic}) content in K-feldspar map.

Table 9- Representative Electron Microprobe (EMP) analyses of minerals from sample PA-16. (b.d.l. - below detection limit).

	Pouso Alto Nappe - PA-16					
	Grt (core)	Grt (mantle)	Grt (rim)	Kfs	Pl	Bt
SiO_2	38.68	38.4	38.62	65.6	61.76	37.93
TiO_2	b.d.l	0.01	0.01	b.d.l	b.d.l	4.24
Al_2O_3	21.84	21.81	21.65	18.85	24.31	17.42
FeO_{Tot}	30.39	32.18	31.38	0.19	0.21	11.56
MnO	0.89	0.64	0.82	b.d.l	b.d.l	0.01
MgO	5.99	6.62	6.11	b.d.l	b.d.l	14.62
CaO	3.15	1.19	2.38	0.09	5.58	0.04
Na_2O	0.04	0.01	0.03	1.17	7.73	0.15
K_2O	b.d.l	b.d.l	b.d.l	14.63	0.78	9.43
Totals	101.0	100.9	101.0	100.5	100.4	95.38
Oxygens	12	12	12	8	8	11
Si	3.004	2.992	3.005	2.994	2.734	2.768
Ti	-	-	-	-	-	0.233
Al	2.000	2.003	1.986	1.014	1.269	1.498
Fe3	0.010	0.01	0.010	0.006	0.006	0.009
Fe2	1.962	2.086	2.031	0.001	0.001	0.695
Mn	0.058	0.042	0.054	-	-	-
Mg	0.693	0.769	0.709	-	-	1.590
Ca	0.262	0.099	0.199	0.004	0.265	0.003
Na	0.006	-	0.004	0.103	0.664	0.021
K	-	-	-	0.852	0.044	0.878
Sum	8.00	8.00	8.00	4.97	4.98	7.70
XAlm	0.67	0.71	0.69	XMic-0.89	XAb-0.68	XMg-0.70
XPrp	0.24	0.26	0.24			
XGrs	0.09	0.03	0.07			

The feldspar in the matrix is essentially K-feldspar with small perthitic growth (Fig. 36e). Plagioclase is preserved only inside garnet, associated with the polymineralic pocket (Fig. 36d). The XMic (=K/K+Ca+Na) content in K-feldspar varies from 0.60 to 0.90 (table 9). The XAb (=Na/Na+Ca+K) in perthites and in plagioclase enclosed in the garnet range from 0.52 to 0.70 (table 9). Biotite is very scarce in the sample. It is observed enclosed in garnet as relics and within the polymineralic pocket (Fig. 36d), as well as close to garnet edges forming symplectite with quartz (Fig. 36f). The biotite $Ti_{(a.p.f.u)}$ varies from 0.15 to 0.24 on the basis of 11O and XMg (=Mg\Mg+Fe^{+2}) ranges from 0.60 to 0.75 (table 9).

5.4 Metamorphic modeling and *P-T* paths

Four different methodologies were applied to the selected sample, PA-16 (Fig.36a and b), in order to constrain the *P-T* history of the Pouso Alto Nappe granulite. They are: the multi-equilibrium average*T* (Holland and Powell, 2011; software THERMOCALC version 3.50 and dataset ds62), phase equilibria modeling (de Capitani and Brown, 1987; de Capitani and Petrakakis, 2010; software THERIAK-DOMINO version 11.03.2020), and the trace element-based thermometers, the Zr-in-rutile (Kohn, 2020) and the Ti-in-quartz (Thomas et al., 2010). The complete methodology applied is described in the **appendix C**.

Owing to the sample has been regarded as a residual granulite, some amount of melt is expected to have been lost during its *P-T* path. Therefore, the sample current bulk composition does not represent the pristine protolith and can only be used to estimate peak- to retrograde *P-T* path. In order to address this issue, two sets of isochemical diagrams were calculated. Firstly, an area of the thin-section that best represents the granulite residual composition, mineral mode, and containing the reactive phases (Grt+Rt+Kfs+Ky±Ilm±Bt) during its *P-T* path was selected for performing X-ray maps (Fig. 36b and 37). Further, the mapped area was treated using the software XMapTools (Lanari et al., 2014; Lanari and Engi, 2017) in order to obtain the local bulk composition (LBC; Fig. 36b and 37a). Then, the first isochemical diagram was calculated using the local bulk composition (LBC) after subtracting the garnet core. The second isochemical diagram was done to constrain the rock prograde history. For this reason, the garnet core and the melt composition were reintegrated into the LBC. The single-step melt-reintegration approach was applied (Bartoli, 2017; Groppo et al., 2013; Indares et al., 2008; Lasalle and Indares, 2014). The isochemical diagrams calculations were performed using the internally consistent database of Holland & Powell (1998) (update 5.5, tcds55_p07 download in https://dtinkham.net/peq.html) and the solution models of White et al. (2007) for garnet, biotite, and melt, White et al. (2000) for ilmenite, White et al. (2002) for orthopyroxene and spinel, Coggon & Holland (2002) for white mica, Holland & Powell (2003) for feldspar (plagioclase and K-feldspar), and Holland & Powell (1998) for cordierite. The obtained results for *P-T* estimates are summarized in Fig. 38.

Obtaining peak conditions in high-temperature rocks can be a challenge due to most of the minerals have chemistry compositions modified by post-peak diffusion reactions (Spear

and Florence, 1992). The diffusion extension at high temperatures will be dependent on the mineral size, phases and elements considered, etc (Caddick et al., 2010; Spear and Florence, 1992). For instance, Ca diffuses at several orders of magnitude sluggish than Fe-Mg-Mn (Caddick et al., 2010; Spear and Florence, 1992). Another example is given by Caddick et. al. (2010) who calculate the effects of diffusion modification in garnet, their calculations indicate that porphyroblasts with diameters higher than 500 μm can preserve unmodified zoning for several tens of millions of years. Indeed, owing to the factors described above several authors report that garnet from HP-granulites tends to preserve the prograde grossular zoning (e.g., Fumes et al., 2021; Hollis et al., 2006; Indares, 2020; Indares et al., 2008; Štípská and Powell, 2005). In the LBC studied, the small garnets from the matrix display a flat pattern and are interpreted here as being diffusion modified. However, the garnet porphyroblast, which has a diameter of *ca.* 7.5 mm, has a strongly zoned pattern considering the grossular and pyrope end-members. Then, taking into account the above considerations, it is regarded that the grossular zoning of the garnet porphyroblast may conserve prograde growth information.

The PAN granulite peak assemblage, Qz+Kfs+Grt+Ky+Rt+L, is predicted to be stable in the penta-variant field delimitated by the Ms-out/solidus curve toward temperatures <850°C, and by the Ky-in at pressure below 18 kbar (Fig. 38a), according to the phase equilibria modeling. The intersection between garnet grossular mantle isopleth (X_{Grs}= 0.04-0.05) and garnet modal proportions (20 vol%) is located at *ca.* 1050-1150°C and 17-19 kbar (Fig. 38b), and it provides an approximation of peak conditions. Furthermore, the garnet grossular (XGrs=0.07) and pyrope (X_{Prp}= 0.23) isopleths for rim composition cross at *ca.* 820°C and 11 kbar on the biotite-out/solidus curve (Fig.38b). In order to reconstruct the prograde-to-peak *P-T* path, 25 mol% of melt were reintegrated into the local bulk composition (LBC) for the solidus H_2O-saturated curve appears (Fig. 38c and d; melt-in curve). This amount of melt added is consistent with the rock residual feature. The intersection of pyrope (X_{Prp}=0.23) and grossular (X_{Grs}=0.09-0.08) garnet core compositions is *ca.* 800°C and 13 kbar. The isopleths match on this field is consistent with the mineral assemblage, Qz+Fsp+Rt+Bt+Ky+L, observed enclosed in garnet, interpreted as the early prograde stage (Fig. 38d). In addition, the multi-equilibrium average*T* calculation yields

temperature of 1036±37°C at 18 kbar (sigfit=1.9; Fig. 38d) supporting the peak *P-T* data obtained above.

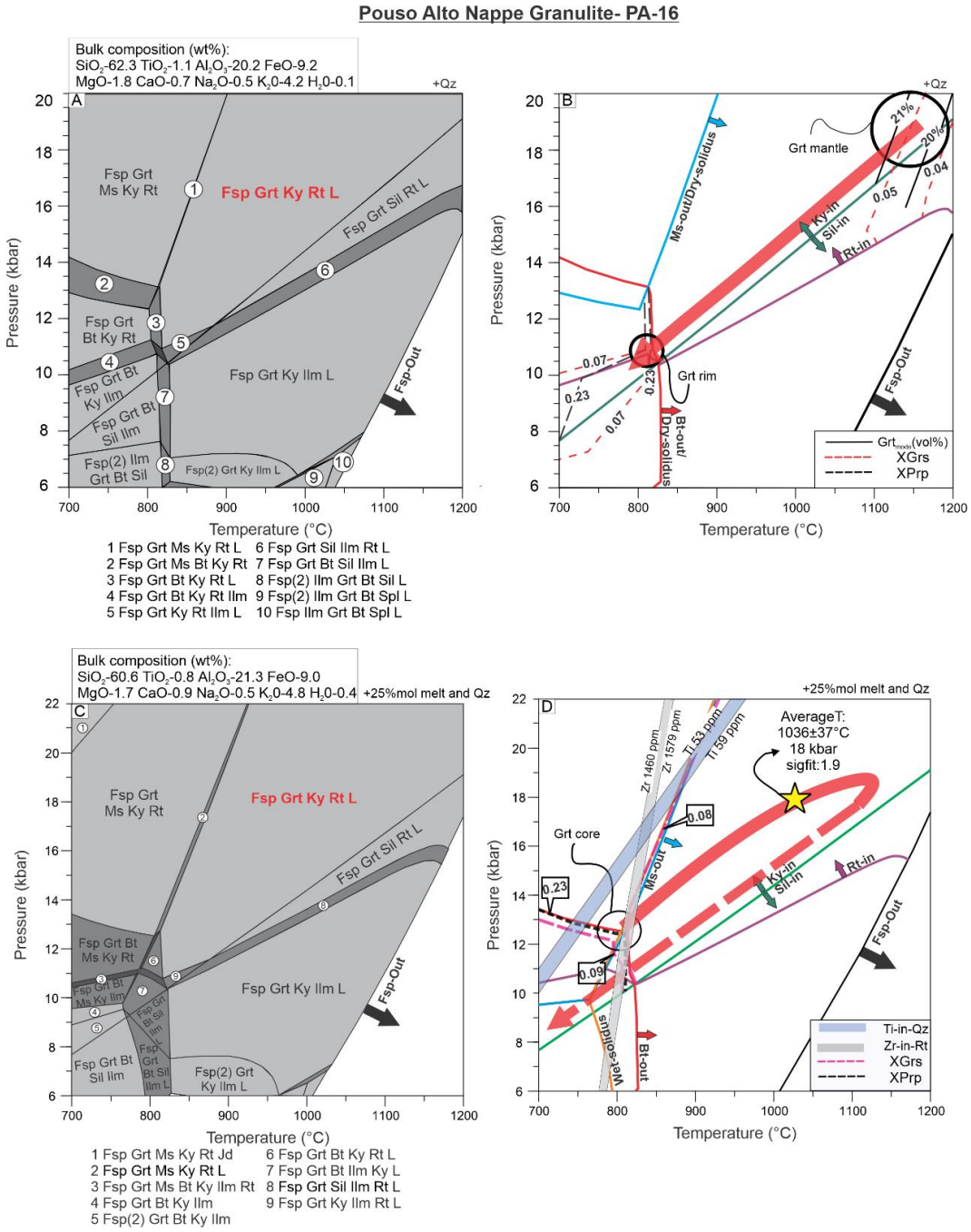

Figure 38– P-T isochemical phase diagrams in the MnNCKFMASHT system for the Pouso Alto granulite (PA-16). a) Isochemical diagram calculated after removing garnet core composition; b) P-T diagram displaying the main minerals stability curves relative to diagram reported in (a) and the retrograde path based on garnet mode and mineral composition isopleths; c) melt-reintegrated isochemical diagram calculated using a reintegrated composition (garnet core and melt); d) P-T diagram displaying the main minerals stability curves relative to the diagram reported in (c), the Zr-in-rutile and Ti-in-quartz isopleths for composition above the 90th percentile, and the suggested metamorphic path.

Trace element based thermometry results are summarized in table 10 showing estimates of Zr-in-rutile and Ti-in-quartz thermometers. The temperatures were calculated for pressure of 10 kbar using the calibrations of Kohn, (2020) for the Zr-in-rutile and Thomas et al. (2010) for the Ti-in-quartz (table 10). The *P-T* range for the Zr-in-rutile and Ti-in-quartz composition related to the 90th percentile, corresponding to1460-1579 ppm of Zr and 53-59 ppm of Ti, are displayed in Fig. 38d. Both thermometers retrieve temperatures consistent with late stages of the retrograde metamorphic path, related to cooling and decompression.

Table 10- Summary of Ti-in-Qz (Thomas et al., 2010) *and Zr-in-Rt* (Kohn, 2020) *data of the sample PA-16.*

		Number	Min	Max	1st quartile	Median	3st quartile	Mean	Std
Zr-in-Rt	Zr(ppm)	26	487	1579	696	960	1351	941	338
	T (ºC) - 10 kbar	26	675	806	708	745	784	745	40
Ti-in-Qz	Ti(ppm)	16	34	59	39	44	46	43	6
	T (ºC) - 8 kbar	16	606	656	617	628	633	627	13

In summary, we suggested a clockwise *P-T* evolution for the Pouso Alto Nappe granulite, which is shown in Fig. 38d. The onset of suprasolidus conditions is estimated at around 800°C and 13 kbar, during the prograde metamorphism, and evolved until reaching coeval temperature and pressure peak conditions around 1050-1150°C and 18-19 kbar. After, the rock underwent cooling and decompression, linked to exhumation, in which the melt final crystallization took place around 820ºC and 11 kbar.

5.5 Monazite petrochronology

In situ monazite dating was performed on the same thin-section (PA-16) studied for mineral chemistry and *P-T* constrain of the Pouso Alto Nappe. Fig. 39 displays the analyzed monazites microstructural and spots (REE and U-Pb) positions through BSE images, and X-ray maps of Y and Th. Monazite of sample PA-16 varies in size from 85 µm up to 300 µm. Crystals are observed in different microstructural positions, including grains partially or completely enclosed in garnet (Mnz 1, 2, 3, 6, and 10), and located at the boundaries of quartz and K-feldspar in the matrix (Mnz 4, 5, and 9). Two monazites are found within kyanite crystals (Mnz 7 and 8). The monazite rims are usually associated with quartz, K-feldspar, biotite, and rutile (Mnz 3, 7, 8, and 10). Regarding the chemical zoning (Y and Th), some monazites are homogeneous (e.g., Mnz 4 and 9), while others show a core-rim (e.g., Mnz 1, and 5) and complex patchy (e.g., Mnz 8 and 9) zonation (Fig. 39).

Two chemical domains were identified in the granulite from Pouso Alto Nappe (Fig. 40). Domain 1 is recorded in concentric and irregular cores, such as the Mnz 5, 7 and 8, and homogenous crystals enclosed in garnet porphyroblast (Mnz 3 and 10). This chemical domain is enriched in HREE (Dy_{CN}/Yb_{CN}= 20.35- 188.18), it has flat to weak Eu anomalies, Eu/Eu*(=$Eu_{CN}/(Sm_{CN}*Gd_{CN})^{1/2}$) between 048-0.72, and Th/U ratio ranging from 4.89 to 20.35 (Fig. 40a and b). The dates from this domain (Domain 1) range from 669±9 Ma to 617±3 Ma, and yield a concordia age of 629.1±3.8 Ma (MSWD=1.7; n=19; Fig. 40c; table 9).

Domain 2 is observed in homogenous matrix crystals (Mnz 4 and 9; Fig. 40) and forming rims in the zoned ones (Mnz 1, 5, 7 and 8; Fig. 40). It is characterized by HREE depletion (Dy_{CN}/Yb_{CN}= 58.08-116.19), prominent negative Eu anomalies (Eu/Eu*=0.22-0.45), and an increase in Th/U from 17.51 to 105.60 (Fig. 40a and b). Dates associated with Domain 2 are spread between 619±14 Ma and 593±13 Ma and yield a concordia age of 607.4±3.7 Ma (MSWD=0.79; n=27; Fig. 40c; table 9).

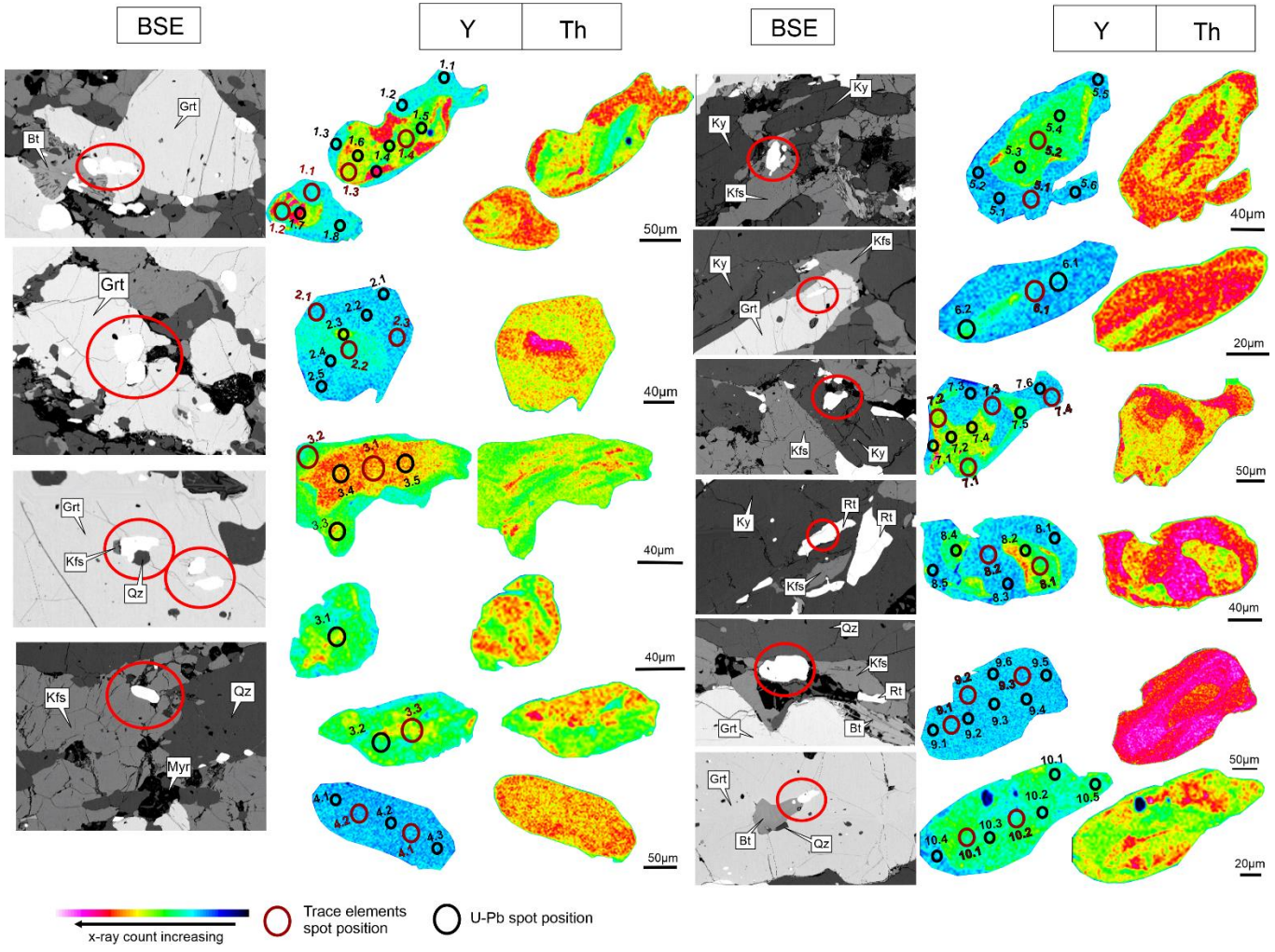

Figure 39 - Backscattered electron (BSE) photomicrographs indicating the microstructural setting of analyzed monazites and respective X-ray maps for Y and Th.

Table 11 - LA-ICP-MS U-(Th)-Pb in situ geochronological results for sample PA-16.

			ISOTOPES RATIOS								AGE ESTIMATES (Ma)							
Mnz grain	Textural position	Domain	$^{207}Pb/^{206}Pb$	2σ %	$^{207}Pb/^{235}U$	2σ %	$^{206}Pb/^{238}U$	2σ %	$^{208}Pb/^{232}Th$	2σ %	$^{207}Pb/^{206}Pb$	2σ abs	$^{207}Pb/^{235}U$	2σ abs	$^{206}Pb/^{238}U$	2σ abs	$^{208}Pb/^{232}Th$	2σ abs
1.1	partially enclosed in Grt	Domain 2	0.05890	0.00176	0.81711	0.02422	0.10064	0.00199	0.03127	0.00040	563.4	16.83	606.4	17.98	618.2	12.20	622.4	7.94
1.2		Domain 2	0.05898	0.00176	0.80028	0.02370	0.09843	0.00195	0.03050	0.00039	566.4	16.91	597.0	17.68	605.2	11.96	607.3	7.80
1.3		Domain 2	0.06190	0.00184	0.84169	0.02477	0.09863	0.00195	0.03043	0.00039	670.7	19.94	620.1	18.25	606.4	11.98	605.9	7.78
1.4		Domain 1	0.06081	0.00192	0.83315	0.02596	0.09940	0.00199	0.03032	0.00039	632.5	19.98	615.4	19.17	610.9	12.25	603.7	7.76
1.5		Domain 1	0.06669	0.00220	0.92015	0.02983	0.10011	0.00205	0.03085	0.00039	828.1	27.32	662.4	21.47	615.1	12.59	614.1	7.86
1.6		Domain 1	0.06299	0.00194	0.83763	0.02537	0.09646	0.00192	0.03096	0.00040	707.9	21.75	617.8	18.71	593.6	11.81	616.3	7.88
1.7		Domain 2	0.06285	0.00187	0.85677	0.02519	0.09889	0.00195	0.03042	0.00039	703.2	20.93	628.4	18.47	607.9	12.00	605.7	7.78
1.8		Domain 2	0.05771	0.00172	0.78287	0.02317	0.09840	0.00193	0.03048	0.00039	518.8	15.51	587.1	17.38	605.0	11.89	606.9	7.79
2.1	enclosed in Grt	Domain 2	0.05995	0.00235	0.79622	0.03044	0.09635	0.00209	0.03039	0.00039	601.8	23.55	594.7	22.73	593.0	12.85	605.1	7.78
2.2		Domain 2	0.05901	0.00236	0.79988	0.03128	0.09833	0.00215	0.03021	0.00039	567.5	22.74	596.8	23.34	604.6	13.23	601.6	7.74
2.3		Domain 2	0.05826	0.00185	0.79924	0.02506	0.09952	0.00199	0.03069	0.00039	539.6	17.12	596.4	18.70	611.6	12.25	611.0	7.83
2.4		Domain 2	0.05981	0.00256	0.81010	0.03367	0.09828	0.00222	0.03031	0.00039	596.7	25.49	602.5	25.04	604.3	13.64	603.5	7.76
2.5		Domain 2	0.06063	0.00232	0.83929	0.03151	0.10041	0.00216	0.03086	0.00039	626.1	24.00	618.8	23.23	616.8	13.30	614.3	7.86
3.1	enclosed in Grt	Domain 1	0.06521	0.00205	0.90794	0.02819	0.10100	0.00203	0.03151	0.00040	781.1	24.59	656.0	20.37	620.3	12.44	627.1	7.98
3.2		Domain 1	0.06270	0.00196	0.86159	0.02656	0.09969	0.00199	0.03172	0.00041	698.1	21.77	631.0	19.45	612.6	12.20	631.2	8.23
3.3		Domain 1	0.06250	0.00194	0.87459	0.02674	0.10152	0.00202	0.03162	0.00040	691.3	21.44	638.1	19.51	623.3	12.41	629.2	8.00
3.4		Domain 1	0.06219	0.00193	0.86277	0.02646	0.10063	0.00200	0.03117	0.00040	680.6	21.16	631.6	19.37	618.1	12.27	620.4	7.92
3.5		Domain 1	0.06292	0.00197	0.89069	0.02757	0.10269	0.00205	0.03100	0.00040	705.5	22.11	646.7	20.02	630.2	12.57	617.1	7.89
4.1	matrix	Domain 2	0.05899	0.00219	0.80254	0.02914	0.09869	0.00209	0.03036	0.00039	566.7	21.05	598.3	21.72	606.7	12.86	604.5	7.77
4.2		Domain 2	0.05784	0.00303	0.79263	0.04014	0.09942	0.00248	0.03104	0.00041	523.7	27.45	592.7	30.02	611.0	15.22	617.8	8.10
4.3		Domain 2	0.06001	0.00273	0.83364	0.03684	0.10078	0.00235	0.03121	0.00040	603.9	27.43	615.6	27.21	619.0	14.40	621.2	7.93
5.1	matrix	Domain 1	0.05905	0.00245	0.81372	0.03275	0.09996	0.00221	0.03085	0.00039	568.9	23.57	604.5	24.33	614.2	13.59	614.1	7.86
5.2		Domain 2	0.06166	0.00253	0.86355	0.03456	0.10160	0.00226	0.03100	0.00040	662.3	27.19	632.1	25.29	623.8	13.87	617.1	7.89
5.3		Domain 1	0.06718	0.00217	0.95527	0.03021	0.10316	0.00208	0.03191	0.00041	843.4	27.21	680.8	21.53	632.9	12.75	634.9	8.06
5.4		Domain 1	0.06649	0.00214	0.95265	0.03021	0.10393	0.00209	0.03174	0.00040	821.8	26.47	679.5	21.55	637.4	12.80	631.6	8.03
5.5		Domain 2	0.06081	0.00206	0.82154	0.02722	0.09800	0.00201	0.03100	0.00040	632.5	21.40	608.9	20.18	602.7	12.35	617.1	7.89
5.6		Domain 2	0.05796	0.00260	0.77461	0.03371	0.09695	0.00222	0.03047	0.00039	528.3	23.68	582.4	25.34	596.5	13.64	606.7	7.79
6.1	enclosed in Grt	Domain 2	0.06528	0.00276	0.90490	0.03696	0.10056	0.00226	0.03088	0.00041	783.4	33.13	654.3	26.73	617.7	13.88	614.7	8.08
6.2		Domain 1	0.06425	0.00326	0.91916	0.04496	0.10377	0.00257	0.03068	0.00040	749.9	38.07	661.9	32.38	636.5	15.75	610.8	8.04

Cont. Table 11 - LA-ICP-MS U-(Th)-Pb in situ geochronological results for sample PA-16.

			ISOTOPES RATIOS								AGE ESTIMATES (Ma)							
Mnz grain	Textural position	Domain	$^{207}Pb/^{206}Pb$	2σ %	$^{207}Pb/^{235}U$	2σ %	$^{206}Pb/^{238}U$	2σ %	$^{208}Pb/^{232}Th$	2σ %	$^{207}Pb/^{206}Pb$	2σ abs	$^{207}Pb/^{235}U$	2σ abs	$^{206}Pb/^{238}U$	2σ abs	$^{208}Pb/^{232}Th$	2σ abs
7.1	enclosed in Ky	Domain 1	0.06191	0.00213	0.86372	0.03054	0.10120	0.00122	0.03100	0.00044	671.0	23.05	632.2	22.35	621.4	7.46	617.1	8.77
7.2		Domain 1	0.05883	0.00234	0.81689	0.03299	0.10072	0.00142	0.03098	0.00044	560.8	22.35	606.3	24.49	618.6	8.70	616.7	8.76
7.3		Domain 2	0.05868	0.00267	0.82396	0.03746	0.10184	0.00163	0.03123	0.00044	555.2	25.28	610.3	27.74	625.2	9.98	621.6	8.82
7.4		Domain 1	0.06104	0.00227	0.84833	0.03210	0.10081	0.00131	0.03108	0.00045	640.6	23.80	623.7	23.60	619.2	8.02	618.6	8.97
7.5		Domain 1	0.06335	0.00249	0.95593	0.03799	0.10944	0.00151	0.03145	0.00045	720.0	28.31	681.2	27.07	669.5	9.22	625.9	8.87
7.6		Domain 2	0.05719	0.00241	0.80767	0.03436	0.10244	0.00151	0.03069	0.00044	498.9	21.06	601.1	25.58	628.7	9.29	611.0	8.70
8.1	enclosed in Ky	Domain 1	0.06049	0.00267	0.84382	0.03740	0.10118	0.00159	0.03104	0.00044	621.1	27.44	621.3	27.54	621.3	9.74	617.8	8.78
8.2		Domain 1	0.06636	0.00246	0.93887	0.03535	0.10263	0.00133	0.03178	0.00046	817.8	30.30	672.3	25.31	629.8	8.15	632.3	9.12
8.3		Domain 2	0.06057	0.00298	0.83116	0.04052	0.09953	0.00174	0.03032	0.00043	624.0	30.66	614.3	29.94	611.7	10.67	603.7	8.62
8.4		Domain 1	0.06633	0.00257	0.91939	0.03592	0.10055	0.00136	0.03108	0.00044	816.8	31.59	662.0	25.86	617.6	8.36	618.6	8.79
8.5		Domain 2	0.05942	0.00265	0.80137	0.03577	0.09782	0.00154	0.03073	0.00044	582.5	26.01	597.6	26.67	601.6	9.49	611.8	8.71
9.1	matrix	Domain 2	0.05838	0.00276	0.77577	0.03640	0.09641	0.00158	0.03067	0.00044	544.1	25.74	583.1	27.36	593.3	9.72	610.6	8.70
9.2		Domain 2	0.05805	0.00302	0.79050	0.04050	0.09877	0.00179	0.03046	0.00043	531.6	27.66	591.5	30.30	607.2	11.02	606.5	8.65
9.3		Domain 2	0.05908	0.00361	0.81796	0.04875	0.10043	0.00214	0.03059	0.00044	570.0	34.79	606.9	36.18	616.9	13.16	609.0	8.68
9.4		Domain 2	0.06008	0.00305	0.82166	0.04113	0.09921	0.00177	0.03071	0.00044	606.5	30.80	609.0	30.48	609.8	10.90	611.4	8.70
9.5		Domain 2	0.06189	0.00349	0.82179	0.04534	0.09629	0.00192	0.03001	0.00043	670.3	37.76	609.0	33.60	592.6	11.84	597.6	8.55
9.6		Domain 2	0.06130	0.00317	0.84268	0.04287	0.09970	0.00181	0.03074	0.00044	649.8	33.61	620.6	31.57	612.7	11.14	612.0	8.71
10.1	enclosed in Grt interplay with Bt	Domain 1	0.06330	0.00255	0.86854	0.03499	0.09952	0.00136	0.03115	0.00045	718.3	28.90	634.8	25.57	611.6	8.35	620.0	8.99
10.2		Domain 1	0.06116	0.00243	0.84742	0.03375	0.10049	0.00136	0.03114	0.00044	644.9	25.66	623.2	24.82	617.3	8.36	619.8	8.80
10.3		Domain 1	0.06436	0.00267	0.89769	0.03708	0.10117	0.00142	0.03125	0.00045	753.5	31.24	650.5	26.87	621.3	8.70	622.0	9.01
10.4		Domain 1	0.05957	0.00266	0.82738	0.03672	0.10075	0.00155	0.03100	0.00044	588.0	26.21	612.2	27.17	618.8	9.51	617.1	8.77
10.5		Domain 1	0.06256	0.00263	0.86974	0.03642	0.10085	0.00144	0.03144	0.00045	693.3	29.20	635.4	26.61	619.4	8.82	625.7	9.05

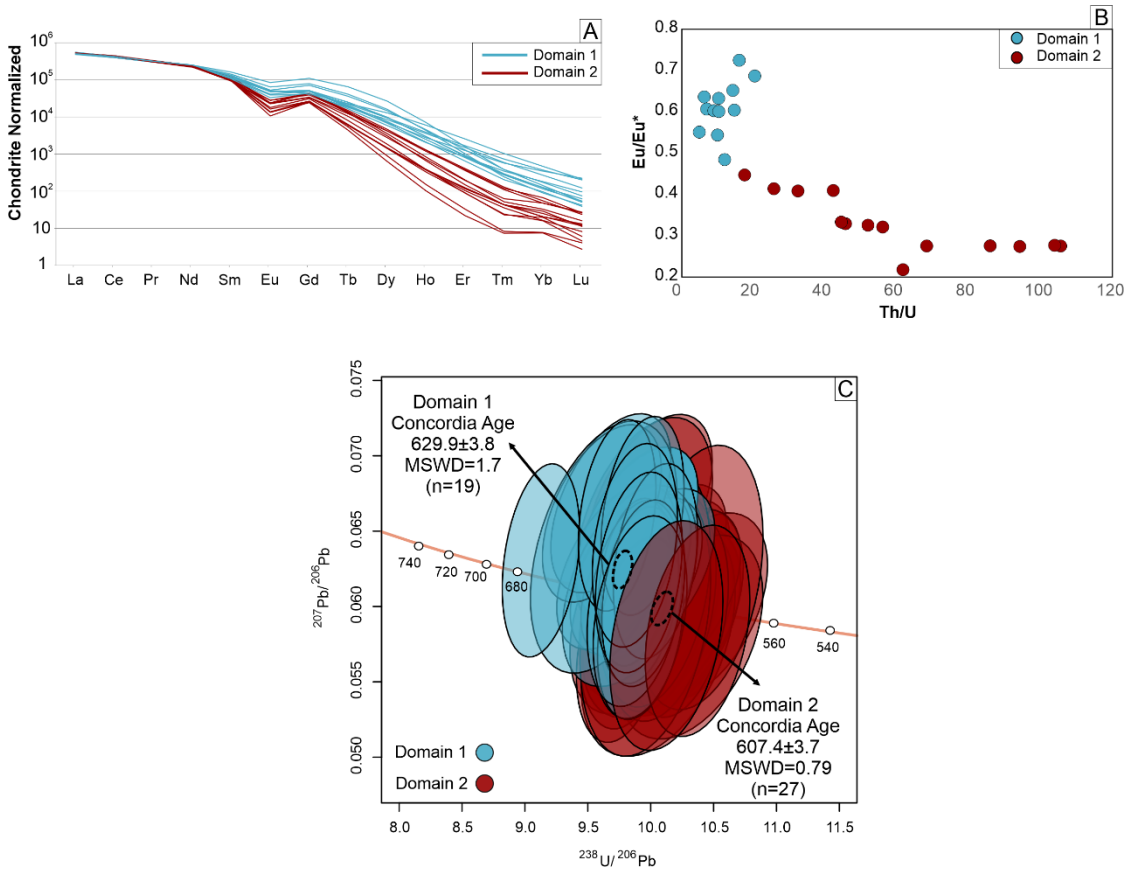

Figure 40 - Monazite chemistry and U-(Th)-Pb data of the PAN granulite, sample PA-16. a) Monazite REE plot, normalized to chondritic values of McDonough and Sun (1995)*; b) diagram of Eu/Eu* vs. Th/U; c) Tera-Wasserburg plot.*

5.6 Discussion

5.6.1 Linking monazite ages to the P-T path

Several studies reported the HP-granulite monazite ages from the Southern Brasilia Orogen (Campos Neto et al., 2010; Fumes et al., 2021; Li et al., 2021; Motta and Moraes, 2017; Reno et al., 2012). The monazite ages reported by these authors are spread in a wide time range, from 660 down to 590 Ma, which were also obtained in this contribution. Indeed, in rocks that reached HT-UHT metamorphic conditions, the spread of monazites dates can be hampered to interpret (Weller et al., 2020; Yakymchuk and Brown, 2014). At this extreme suprasolidus conditions, it is expected that the monazites would be partial to completely dissolved in the system and to reprecitate from the melt presenting complex textures and REE signatures (Johnson et al., 2021; Taylor et al., 2016; Weller et al., 2020; Yakymchuk and

Brown, 2019, 2014). With petrochronology advent, a lot of advances have been done in order to understand the monazite geochemistry signatures during the suprasolidus reactions, such as the peritectic garnet growth and biotite dehydration-melting reactions. Moreover, the *in-situ* dating provides the characterization of the monazite microstructural position and its textural relationships, that in conjunction with its geochemistry signature, allow the most accurate approach for linking the age with the metamorphic path (Engi, 2017; Kohn et al., 2017; Williams and Jercinovic, 2002, 2012).

The PAN granulite oldest monazite dates, from 669±9 Ma to 617±3 Ma, are characterized by enriched HREE, minor to flat Eu anomaly, and low Th\U rates (Fig. 41d). Based on textural and chemistry criterium, these dates are interpreted to be related to monazite growth during the sub-solidus prograde path, before biotite dehydration melting reaction (Fig. 41d). This interpretation is supported by: (1) the interplay between Mnz10, which has a chemistry signature comprised in the domain 1, and biotite suggesting both phases contemporaneity; (2) this monazite population is hosted mainly in garnet porphyroblasts (e.g., Mnz 1, 3 and 10) and kyanite (e.g., Mnz 7 and 8) indicating that these minerals likely played a role in shielding this monazite population from being completely dissolved during the partial melting reactions; (3) the dates from domain 1 are the oldest and located into crystals cores; (4) the high HREE content and low Th\U rate trend are consistent with sub-solidus conditions before peritectic garnet growth.

The low-HREE, steep Eu anomaly, and increasing Th\U rate trend associated with homogenous crystals and rims of the zoned ones returned the youngest ages, from 619±14 Ma and 593±13 Ma (domain 2). This change in monazite chemical pattern can be correlated to the suprasolidus conditions experienced by the PAN granulite. In this scenario, the monazite composition is controlled by the Bt-breakdown melting reaction, which has garnet+K-feldspar+melt as products (Dumond et al., 2015; Rocha et al., 2017). During this water-undersaturated partial melting reaction, the HREE partitioned into the peritectic garnet structure (Pyle and Spear, 2003; Rubatto et al., 2013), the Eu fractionates toward K-feldspar (Buick et al., 2010; Rubatto et al., 2013), whereas Th is incorporated by monazite rather than melt (Stepanov et al., 2012; Watt and Harley, 1993; Williams et al., 2022). Therefore, this monazite domain is interpreted to have been developed during a close peak to retrograde

metamorphic path due to melt crystallization (Fig. 41d). The oldest age reported for this monazite domain, of 619±14 Ma, is here considered a maximum approximation of peak conditions.

5.6.2 UHT metamorphic heating drivers

The increase of UHT rocks studies in the past decades improved our knowledge about the heat drives to reach such extreme metamorphic conditions (Clark et al., 2015, 2011; Horton et al., 2021, 2016; Kelsey, 2008; Kelsey and Hand, 2015). The crustal temperature change during the time is dependent on conduction and advection flow, as well as the heat production by radioactive elements accumulation and shearing, and endothermic reactions, of heat consumption, such as partial melting (Clark et al., 2011; Kelsey and Hand, 2015 and references therein).

The heat production in the crust is mainly due to the concentration of the radioactive elements K, Th, and U, the heat-producing elements (HPE). In the studied sample, the K-feldspar, a K repository, represents *ca.* 25% of the rock volume. Indeed, in the sample here investigated, the K_2O concentration is 4.18 wt%, which is about twice higher than the average concentration estimated for the entire crust by Rudnick and Gao (2003). Furthermore, in high-grade metapelites monazite is recognized as the main Th host (Bea, 2012, 1996; Yakymchuk and Brown, 2019). As discussed above (see section 5.6.1), during the fluid-absent partial melting the Th is partitioned into monazite structure, as recorded in monazite domain 2, suggesting Th entrapment in the residuum rather than be lost during melt migration. Although the calculation of radioactive heat production rate to the PAN granulite is beyond the scope of this work, the evidence discussed above suggests a high concentration of HPE, mostly of K and Th.

Partial melting reactions are typically endothermic and have a thermal buffering effect on the crust (Clark et al., 2011; Kelsey and Hand, 2015). The crust thermal buffer effect can be overcome, in order to achieve UHT conditions, in rocks that were pre-conditioned by being melt-depleted owing to a prior HT\UHT event (Clark et al., 2011; Kelsey and Hand, 2015; Vielzeuf et al., 1990). A pre-conditioned crust by a previous (U)HT event hypothesis is hard to reconcile in the SBO evolution, once there are no clues of it until the moment. In addition, a single metamorphic event in which the heat source was maintained for a

protracted-time period can also play this role (Brown and Kothonen, 2009; Korhonen et al., 2013). For instance, Clark et al. (2011) investigated UHT conditions through 1-D numerical model, according to the latter authors, it is necessary a high radiogenic heat production of ~3µW m^{-3} during a period of *ca*. 60 Ma for achieving temperature conditions larger than 900°C. In the SBO, the collision onset is estimated to take place at ~670 Ma (Frugis et al., 2018; Reno et al., 2009), and we suggested, based on petrochronology and petrology, that the PAN granulite reaches the metamorphic peak at ~620 Ma. Therefore, the SBO underwent crustal thickening and temperature rise during a time span of *ca.*50 Ma until achieving the HP-UHT metamorphic conditions.

Along the *P-T* path, experienced by our sample, it is observed that the temperature increases proportionally to the pressure raise. The maximum pressure recorded is ~19-18 kbar, and assuming an average crust density of $2.8x10^3$ km/m^3, it is equivalent to a burial depth of *ca.*70 km (Fig. 41b). This maximum depth can be related to the interface between the lower crust and lithospheric mantle (i.e., Moho) in a double thickness crust (Fig. 8b) as documented nowadays for instance in the Himalaya (Hirn et al., 1984). The hypothesis that PAN granulite was buried into the lithospheric mantle is discarded, once there is no evidence of mantle lithologies associated, such as ultramafic rocks, with the PAN granulite. In addition, assuming an average density of 4,130 kg/m^3 for garnet, 3,610 kg/m^3 for kyanite, 2,620 kg/m^3 for quartz, 2,560 kg/m^3 for K-feldspar, and 4,250 kg/m^3 for rutile, an average density of 3,130 kg/m^3 for the sample PA-16 is calculate by the XMapTools. This average density calculated is compatible with rocks from the lower crust (Hacker et al., 2015 and references therein). Therefore, at depth consistent with the Moho interface, the lithospheric mantle heat flow must play some role in temperature increase, even if possibly in a minimal way.

The PAN granulite shows microstructures indicating that it was affected by non-coaxial shearing development (Fig. 35c, d, and e) and in principle, a shearing heating effect could be invocated. Although, it is very unlikely that it has contributed to temperature increase >600°C, owing to rock strength decrease after undergoing partial melting producing negative feedback (Clark et al., 2011). Moreover, the quartz cathodoluminescence map shows homogenous spectra intensity to quartz (**Appendix C** figure C4), and in conjunction with

microstructural observations indicates that its phase was completely recrystallized during its retrograde, syn-shearing metamorphic path. The Ti-in-quartz isopleths show that the recrystallization occurred during the late exhumation and cooling path, at temperatures ≤700ºC (Fig. 38d). Hence, it is suggested that the shearing heating may have contributed after melt crystallization, during the exhumation and could have led to a decrease in the cooling rate, but not to the UHT conditions.

5.6.3 Continental subduction

The integration of the PAN granulite *P-T-t-D* dataset provides us insights into the geodynamic processes that take place in the deep crust. We propose that the Pouso Alto granulite is a witness to the continental subduction (Fig. 41a and b). The interpreted *P-T* path (Fig. 41d) suggests that the PAN granulite was part of the material detached and incorporated into the lithosphere subduction conduit. During its path toward the down into the continental subduction channel, it was heated and had its density increased, while the crust was thickened (Fig. 41a and b). At the moment when PAN granulite achieved the interface between the lower crust and the Moho, this process would have been interrupted, likely due to delamination of the denser material from the continental subduction channel (Fig. 41b). Notwithstanding, the PAN granulite would be less dense than the lithospheric mantle, but at the same time denser than the middle and upper crust rocks. This density contrast between the PAN granulite and the lithosphere layers led it to remain in the lower crust depth.

5.6.4 Lower ductile crust flow and exhumation

The crust strength decreases exponentially at even small melt amounts owing to the connectivity between melt films (Jamieson et al., 2011a; Rosenberg and Handy, 2005). At melt volume ≥7vol%, the crust reaches a threshold (MCT-melt connectivity threshold) which leads to a rheological transition, characterized by its significant weakening (Rosenberg and Handy, 2005). This crustal answer to partial melt assumes a first-order control in orogen growth and its flow. For instance, the partial melt of the middle and lower crust during an orogen development can lead to the weakening of these crustal levels and, further ductile lateral and\or upward flow (Beaumont et al., 2001; Jamieson et al., 2011b, 2004; Jamieson and Beaumont, 2013; Vanderhaeghe, 2012, 2009). The reconstructed prograde path indicates that the biotite dehydration melt reaction produces around 15-25 vol% of melt (**Appendix C**

Figure C2). Although is unlikely that this melt amount was accumulated, owing to melt extraction mechanisms, we consider that the melt connectivity threshold was achieved. The channel flow model has been proposed by several authors as the main mechanism for the Andrelândia Nappe System ductile motion (Campos Neto et al., 2011; Coelho et al., 2017; Frugis et al., 2018; Westin et al., 2021). According to this model, the high topographies could not be sustained by the partially molten and weakened lower crust, inducing the lateral flow of the middle and lower crust (Beaumont et al., 2001; Jamieson and Beaumont, 2013). The lower crust melt weakened followed by its gravity-driven flow would record the transition from a wedge-shaped orogenic belt to an orogenic plateau (Fig. 41c; Vanderhaeghe, 2012; Vanderhaeghe et al., 2003).

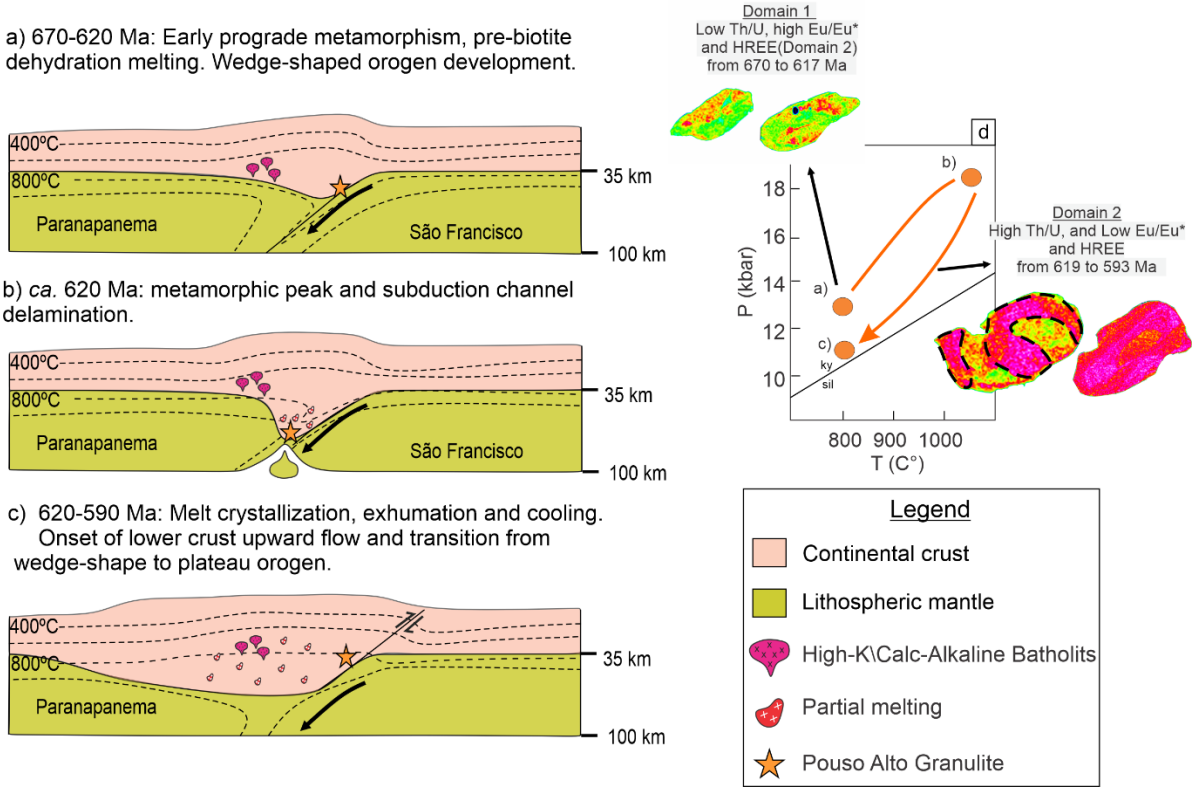

Figure 41- Simplified sketches of the SBO proposed tectonic and P-T evolution. a) From 670 to 620: early prograde metamorphism, pre-biotite dehydration melting. At this time onset the development of a wedge-shape orogen; b) ca. 620: maximum metamorphic peak age in which the Pouso Alto rock reached close Moho depth in a double thickening crust. Delamination of denser material from the subduction conduit toward the mantle; c) from 620 to 590: melt crystallization, cooling, and exhumation. During this period the melt-weakened crust onset its flow outward, likely triggered by the pressure gradient of the double thickness crust and its surroundings. The outward lower crust flow would record the transition from wedge-shaped orogen to plateau; d) P-T-t metamorphic path highlighting the monazite (X-ray maps of Th) textural zoning.

Furthermore, the lower crust lateral flow, exhumation, and cooling evolved at slow rates. The monazite U-(Th)-Pb ages, obtained in this work, indicate that cooling and decompression occurred from 619(±14) Ma to 593(±13) Ma, in this time range the rock temperature decreased ~280°C (from ~1000-1100°C to 820°C) and ~8-7 kbar (from ~19-18 kbar to 11 kbar). The estimated minimum cooling and exhumation rates, for crust density of $2.8x10^3$ km/m^3, are respectively ~14°C/Ma and ~0.15 cm/yr. Fumes et al. (2021) reported slow cooling rates also for HP-granulite from the Passos Nappe. This slow cooling rate is compatible with the low thermal diffusivity and conduction of the lower crust and mantle (Kelsey and Hand, 2015 and references therein), which means that once the rock achieved these extreme thermal conditions it will remain for a long period of time.

5.7 Conclusion

The PAN granulite reveals a complex history of orogen evolution during the continental collision which took place in the deep crust. During the continental collision, the PAN granulite is interpreted here as being part of the continental subduction channel. The granulite was buried and heated during its path, and after *ca.* 50 Ma of collision onset, around 620 Ma, it achieved peak conditions around 1000-1100°C and 18-19 kbar. Our *P* data indicate that this rock reached crustal depths of *ca.* 70 km, corresponding to the interface between lower crust and lithospheric mantle in a crust double thickened. It is suggested that the UHT metamorphic condition was attained by a combination of heat production elements accumulation (HPE) and possibly by minor mantle heat flow. Once the PAN granulite reached Moho depths, the denser material from the subduction conduit is delaminated toward the mantle, while the less dense rocks remained in lower crust depths. Consecutively, the previous melt-weakened material onset its flow outward, with a slow exhumation and cooling rates estimated rate respectively of ~14°C/Ma and ~0.15 cm/yr. We, therefore, suggested that the granulite from the Pouso Alto Nappe documented the transition from a wedge-shaped orogenic belt to an orogenic plateau during the continental collision development.

CHAPTER 6

CONCLUSION

The comparative study of orogenic belts provided interesting insights into the lithosphere evolution and modifications during processes linked to mountain belt. The Himalayan Orogen, a young mountain belt where the collision is still an ongoing process, provides more complete information about the structure and composition of a mountain during the large hot orogenesis process which can be linked with geophysical data and direct geomorphological observations. In the Himalayan Orogen direct information about the lower crust are largely lacking. Whereas lower crust exhibitions can be directly observed in older orogens, such as the Southern Brasilia where deep roots of the orogen are now exposed. Moreover, the multidisciplinary approach applied for studying the large hot orogens, in which structural data of different scales are integrated with metamorphic petrology and petrochronology results provided us the elementary information to unravel these complex tectonic frameworks. By integrating the *P-T-t-D* data, it was possible to assess how the lithosphere evolved during the continental convergence in two distinct scenarios, a nearly orthogonal collision(e.g., the Himalaya Orogen), and an oblique collision inserted within a supercontinent cycle (e.g., the Southern Brasilia Orogen). The results presented in this thesis contribute to understanding the evolution of the middle and lower crust within two different large hot orogens (LHO), the Himalayan and Southern Brasilia. The addressed research questions were discussed separately for each one of the studied orogens within the thesis chapters. Below, these questions will be taken up and discussed, taking into account a comparative view of each of the large hot orogens during this mature stage of the continental collision.

> *How is the architecture of the orogenic hinterland? Is there any evidence of a plateau formation in the Southern Brasilia Orogen such as the current Tibet in the Himalaya orogen?*

The large hot orogens (LHO) have been described as mountain belts in which an orogenic plateau is underlain by thickened crust (~60-80 km) and flanked by external wedges (Jamieson and Beaumont, 2013). The hinterland is part of the orogenic wedge and is constituted by melt-weakened material from the middle crust, decoupled from the strong upper crust and lithospheric mantle. The Greater Himalayan Sequence (GHS), the Himalayan Orogen wedge's hinterland, is very continuous ~2000 km along the strike. The *P-T* data

conditions reported here for a GHS section in NW Himalaya, consistent with other works, show that they vary from 550 to 750ºC and 8-12 kbar. Such conditions are compatible with the middle crust within an LHO. In addition, localized exposures of rocks that underwent eclogite facies metamorphism, with a strong granulite to amphibolite facies overprint (Groppo et al., 2007; Grujic et al., 2011; Lombardo and Rolfo, 2000; Wang et al., 2021; Warren et al., 2011) crop out from W Himalaya to southern Tibet, eastern Nepal, and northwestern Bhutan. These middle and lower crust sections crop out in the plateau flank external wedges (Jamieson and Beaumont, 2013). They are separated from the other belt units by two opposite sense crustal-scale shear zones, the Main Central Thrust (MCT) and the South Tibetan Detachment System (STDS). Internally, the GHS is divided by High Himalayan Discontinuity into two structural units.

The Andrelândia Nappe System (ANS), the Southern Brasilia Orogen wedge's hinterland, displays a fold-nappe structure with an estimated displacement of 85 km toward E-NE (Campos Neto et al., 2020). The Southern Brasilia Orogen has been the product of a lateral collision, and part of the Gondwana supercontinent assemblage resulted in a more complex architecture compared to the Himalayan Orogen. The ANS is divided into two parts by a tectonic window exposing the Archean-Paleoproterozoic migmatitic orthogneiss from the basement. The nappes from the ANS are separated by tectonic contacts, mainly marked by thrust sense shear zones. The ANS *P-T* constraints are between 19-10 kbar and 1100-650 ºC, compatible with conditions in the middle and lower crust. This observation contrasts with the Himalayan Orogen, in which there are just localized exposures of lower crust rocks, and the hinterland is mainly constituted by middle crust exhibitions. Moreover, assuming an average crust density of $2.8x10^3$ km/m^3, the ANS maximum record of pressure was at ~19-18 kbar is equivalent to a burial depth of *ca.*70 km. This burial depth suggested that the crust was likely doubled in thickness during the continental collision. The exhumation onset of the HP-UHT rocks (Pouso Alto Nappe granulite) would record the moment in which the crust could not sustain the orogen weight and started a transition from a wedge-shaped to plateau orogenic belt.

How varies the P-T gradient within the orogenic hinterland? Which are the structures controlling its change?

The hinterland rocks from both the Himalaya Orogen and Southern Brasilia Orogen have field geothermal gradients consistent with the Barrovian metamorphic field (England and Thompson, 1984; Jamieson et al., 1998) of *ca.* 20 °C/km. In the studied section of the Himalaya Orogen, the modeled rock of the Lower GHS, in the Badrinath shear zone footwall, registered peak conditions of 700 ºC and 10-11 kbar. This result is within the kyanite stability field and can be converted into an apparent geothermal gradient of ~70 ºC/kbar. In addition, the sample from the Badrinath Shear Zone hanging wall in the Upper GHS was equilibrated in the sillimanite field constrained at 700-720ºC and 8 kbar. It corresponds to an apparent geothermal gradient of ~90ºC/kbar. It is suggested that this observed difference of apparent geothermal gradients between the upper and lower GHS is controlled by the High Himalayan Discontinuity. The onset of the High Himalayan Discontinuity contractional activity led to a perturbation in the paleo-isotherms. At this time, while the rocks from the Upper GHS started their exhumation path, the ones from the Lower GHS continued to be buried.

The Andrelândia Nappe System (ANS) is divided into three nappes, which are, in the studied area, from the top to the bottom of the stack, the Pouso Alto, Liberdade, and Andrelândia. The calculated apparent geothermal gradients for them are ~60ºC/kbar for the Pouso Alto, ~65ºC/kbar for the Liberdade, and ~60ºC/kbar for the Andrelândia. Considering the uncertainties of the *P-T* calculations, we can consider that the temperature varies uniformly according to the depth in the studied sections of the ANS. Notwithstanding, the ANS does not record continuous slices of the lower and middle crust. The pressure difference between the top nappe, Pouso Alto, which records peak pressure around 19-18 kbar, and the middle and lower nappes, the Liberdade and Andrelândia, whose reached respectively peak pressure values around 10 and 12 kbar, indicates a pressure gap of ~7-6 kbar. Considering an average crustal density of $2.8x10^3$ km/m^3, this pressure difference can be translated into a lack of *ca.* 23-27 km of crust between the bottom and middle nappes. A possible explanation for this discontinuity would be a rheological heterogeneous crust in the Southern Brasilia Orogen. In this scenario, it is likely that the melt-weakened material overthrust stronger crustal rocks, forming a fold-nappe geometry (Beaumont et al., 2006 and references therein).

A similar explanation is given for the fold-nappe structure and lower crust exposures in the Greenville Orogen (Jamieson et al., 2010, 2007).

> *How long was the incubation time for each one of the studied LHO? Was it enough to generate widespread partial melting and weaken the middle and lower crust?*

In addition to being dependent on the heat source distribution, the crust response to the collisional process is also conditioned by the time in which the heat is available during this process (England and Thompson, 1984). The incubation time is the interval time between tectonic thickening of the crust during contractional orogenesis, in which the isotherms are perturbed, and the subsequent re-equilibration (Beaumont et al., 2006). In addition, it is estimated that a period of *ca.* 20-25 m.y since the collision onset is needed for the rocks stored within the orogenic wedge's hinterland to achieve temperatures equal to or higher than 700°C to be partially molten (Beaumont et al., 2006; Jamieson and Beaumont, 2013). The collision onset in the Himalayan orogen is estimated to have taken place at ~59-54 Ma. Moreover, thermal equilibration started in the Greater Himalayan Sequence, in the Alaknanda Valley, at ~23 Ma. Therefore, an incubation time around 35-31 Ma is estimated. Thus, the Greater Himalaya Sequence incubation time could be considered sufficient to accumulate heat production elements in substantial volume for the middle and lower crusts to be melt-weakened. The *P-T* results obtained for the Badrinath Shear Zone pointed out that the partial melting occurred in water-saturated conditions, at 700-720°C and 8-10 kbar, and produced around 5-15 vol% of melt. Although, rocks that underwent partial melting and reached T>700ºC are mostly observed in the Upper Greater Himalayan Sequence structural unit. Hence, the Badrinath Shear Zone could be regarded as a rheological boundary, present at 24-19 Ma, between a weak migmatitic hanging-wall and a strong footwall.

Regarding the Southern Brasilia Orogen, the collision onset is estimated at ~670 Ma. The oldest obtained age for the onset of isotherms re-equilibration was ~620 Ma for the Pouso Alto Nappe. Thus, the minimum incubation time was around 50 Ma for the Southern Brasilia Orogen. In the three studied units of the Andrelândia Nappe System, rocks that underwent anatexis were recognized only within the Pouso Alto Nappe. The data obtained for the Pouso Alto Nappe granulite indicated that anatexis occurred in undersaturated-water conditions, at ~800ºC and 13 kbar, and produced around 30 vol% of melt. Although the long incubation

time of the Andrelândia and Liberdade Nappes, they did not have records of partial melting in the studied section of the Andrelândia Nappe System. However, several works reported anatectic features in the other nappes from the system, especially in the lower portion of the Andrelândia Nappe and in the Três Pontas-Varginha Nappe (Campos Neto et al., 2011; Coelho et al., 2017; Garcia and Campos Neto, 2003; Li et al., 2021; Motta and Moraes, 2017; Reno et al., 2012).

How was the strain distributed in such LHO? What was the flow mode acting in each one of the studied LHO systems?

The Greater Himalayan Sequence and the Andrelândia Nappe System record deformational structures related to the prograde and retrograde metamorphic paths. The prograde path structures are related to the kyanite stability field and are usually overprinted and preserved as relics by the exhumation-related structures within the sillimanite stability field. In both orogenic belts, the deformation is heterogeneously partitioned giving rise to the development of foliations, folds, and concentrated into shear zones. In summary, they evolved from progressive deformation and metamorphism due to a single continental collision. For instance, the Himalaya orogen tectono-metamorphic evolution is resulted of the India-Asia collision. Even though the Southern Brasilia Orogent has been built during the Pan African-Brasilian event, in which a series of almost diachronic collisions occurred against the São Francisco-Congo Craton, the results presented here point to a tectono-metamorphic evolution owing to a single continent-continent collision, of the Paranapanema and São Francisco blocks. Moreover, the addressed meso- and microstructural studies suggest that the deformation took place at a high-temperature ductile regime above 650ºC (Passchier and Trouw, 2005).

The shear zones accomplish a first-order role in accommodating deformation during the exhumation in these collisional orogens. The High Himalayan Discontinuity, an internal shear zone within the Greater Himalayan Sequence whose branch in the Alaknanda Valley, the Badrinath Shear Zone, is described in this thesis. It accommodates the deformation during the early stages of Greater Himalayan Sequence exhumation. The Main Central Thrust and South Tibetan Detachment System, the two opposite sense crustal-scale shear zones bounding the Greater Himalayan Sequence, were interpreted as the lower and upper boundary

of a channel from where the rocks from mid-crust were exhumed. However, since the identification of the High Himalayan Discontinuity early motion, before the Main Central Thrust and the South Tibetan Detachment System, the models of mid-crust exhumation were questioned. Our observations support the "in-sequence shearing" model in which the deformation was driven by high-temperature shear zones during progressive mid-crust exhumation from top to bottom in the Greater Himalayan Sequence toward the orogen foreland. It is suggested that the early shortening stages in the upper GHS by the High Himalayan Discontinuity contractional activity could have led to crustal thickening. The early High Himalayan Discontinuity motion may have caused the later activation of the South Tibetan Detachment System coeval with Main Central Thrust in order to re-equilibrate the system as regarded in the critical taper model.

In the Southern Brasilia Orogen, the fold nappes from the Andrelândia System are separated by tectonic contacts usually marked by shear zones. Even though the pioneer works in the Southern Brasilia Orogen were focused on the deformation phases descriptions, studies in which macro- and microstructural aspects of the fold nappes motion are linked with *P-T* constraints and geochronology are still scarce. In the Pouso Alto region, the ductile motion of the Pouso Alto and the Liberdade Nappes were constrained in this thesis. Both Nappes have activities related to the exhumation path during a single tectonic-metamorphic event. A rejuvenation of both prograde/burial (Pre-nappe migration) and decompression/retrograde (Syn-nappe migration) ages is observed towards the ANS bottom. These achievements support an "in-sequence" propagation of the nappes stack toward the São Francisco Craton south. Furthermore, the outward flow of the melt-weakened lower crust rocks is pointed as it has been driven by the gradient lithostatic between the orogenic belt and its foreland as suggested in the channel flow model.

In conclusion, in both orogenic systems the Himalaya (the archetypical example of continental collisional belt and a modern LHO) and in the SBO (an example of fossil LHO), and despite their own particularities, they have hinterlands with a wedge-shaped (i.e., Himalaya Orogen) and fold-nappe (i.e., Southern Brasilia Orogen) structure constituted by heterogeneous distributed melt-weakened middle and lower crust rocks, which evolved within the Barrovian field during the time range of 35 to 50 Ma, until the isotherms onset re-equilibrate. The progressive deformation at a high-temperature ductile regime (>650ºC) was resulted from a single continent-continent collision in Himalayan and Southern Brasilia Orogens. Finally, the studied examples of large hot orogens followed an "in-sequence" propagation pattern from the hinterland toward the foreland driven by the gravitational force, although different active mechanisms were suggested, such as the critical tapper (i.e., Himalaya Orogen) and channel flow (i.e., Southern Brasilia Orogen).

7 REFERENCES

Agustsson, K.S., Gordon, S.M., Long, S.P., Seward, G.G.E., Zeiger, K., Penfold, M., 2016. Pressure–temperature–structural distance relationships within Greater Himalayan rocks in eastern Bhutan: implications for emplacement models. Journal of Metamorphic Geology 34, 641–662. https://doi.org/10.1111/jmg.12197

Alkmim, F.F., Marshak, S., Fonseca, M.A., 2001. Assembling West Gondwana in the Neoproterozoic: Clues from the São Francisco craton region, Brazil. Geology 29, 319–322. https://doi.org/10.1130/0091-7613(2001)029<0319:AWGITN>2.0.CO;2

Andrade, V. De, Vidal, O., Lewin, E., O'Brien, P., Agard, P., 2006. Quantification of electron microprobe compositional maps of rock thin sections: an optimized method and examples. Journal of Metamorphic Geology, 24(7), 655–668. https://doi.org/10.1111/J.1525-1314.2006.00660.X

Antolín, B., Appel, E., Montomoli, C., Dunkl, I., Ding, L., Gloaguen, R., Bay, R. el, 2011. Kinematic evolution of the eastern Tethyan Himalaya: Constraints from magnetic fabric and structural properties of the Triassic flysch in SE Tibet. Geological Society Special Publication 349, 99–121. https://doi.org/10.1144/SP349.6

Armijo, R., Lacassin, R., Coudurier-Curveur, A., Carrizo, D., 2015. Coupled tectonic evolution of Andean orogeny and global climate. Earth-Science Reviews 143, 1–35. https://doi.org/10.1016/J.EARSCIREV.2015.01.005

Baldwin, J. A., Powell, R., Brown, M., Moraes, R., Fuck, R. A., 2005. Modelling of mineral equilibria in ultrahigh-temperature metamorphic rocks from the Anápolis–Itauçu Complex, central Brazil. Journal of Metamorphic Geology, 23(7), 511–531. https://doi.org/10.1111/J.1525-1314.2005.00591.X

Bartoli, O., 2017. Phase equilibria modelling of residual migmatites and granulites: An evaluation of the melt-reintegration approach. Journal of Metamorphic Geology, 35(8), 919–942. https://doi.org/10.1111/JMG.12261

Bea, F., 1996. Residence of REE, Y, Th and U in Granites and Crustal Protoliths; Implications for the Chemistry of Crustal Melts. Journal of Petrology, 37(3), 521–552. https://doi.org/10.1093/PETROLOGY/37.3.521

Bea, F., 2012. The sources of energy for crustal melting and the geochemistry of heat-producing elements. Lithos, 153, 278–291. https://doi.org/10.1016/J.LITHOS.2012.01.017

Beaumont, C., Jamieson, R.A., Nguyen, M.H., Lee, B., 2001. Himalayan tectonics explained by extrusion of a low-viscosity crustal channel coupled to focused surface denudation. Nature 414, 738–742. https://doi.org/10.1038/414738a

Beaumont, C., Nguyen, M.H., Jamieson, R.A., Ellis, S., 2006. Crustal flow modes in large hot orogens, in: Geological Society Special Publication. pp. 91–145. https://doi.org/10.1144/GSL.SP.2006.268.01.05

Benetti, B., Montomoli, C., Iaccarino, S., Langone, A., Carosi, R., 2021. Mapping tectono-metamorphic discontinuities in orogenic belts: implications for mid-crust exhumation in NW Himalaya. Lithos, 392–393, 106129. https://doi.org/10.1016/j.lithos.2021.106129

Bird, P.C., Cartwright, J.A., Davies, T.L., 2015. Basement reactivation in the development of rift basins: An example of reactivated caledonide structures in the West Orkney Basin. Journal of the Geological Society 172, 77–85. https://doi.org/10.1144/jgs2013-098

Bosse, V., Villa, I. M., 2019. Petrochronology and hygrochronology of tectono-metamorphic events. Gondwana Research, 71, 76–90.

Bradley, D.C., McCauley, A.D., Stillings, L.L., 2017. Mineral-deposit model for lithium-cesium-tantalum pegmatites. Scientific Investigations Report. https://doi.org/10.3133/SIR20105070O

Brito Neves, B., Campos Neto, M., Fuck, R., 1999. From Rodinia to Western Gondwana: an approach to the Brasiliano-Pan African Cycle and orogenic collage. Episodes-Newsmagazine of the International Union of Geological Sciences 22, 155–166.

Brown, M., 1993. P–T–t evolution of orogenic belts and the causes of regional metamorphism. Journal of Geological Society of London 150, 227–241. https://doi.org/10.1144/GSJGS.150.2.0227

Brown, M., 2002. Retrograde processes in migmatites and granulites revisited. Journal of Metamorphic Geology 20, 25–40. doi:10.1046/j.0263-4929.2001.00362.x

Brown, M., 2007a. Metamorphic Conditions in Orogenic Belts: A Record of Secular Change. International Geology Review 49, 193–234. https://doi.org/10.2747/0020-6814.49.3.193

Brown, M., 2007b. Metamorphism, Plate Tectonics, and the Supercontinent Cycle. Earth Science Frontiers 14, 1–18. https://doi.org/10.1016/S1872-5791(07)60001-3

Brown, M., Johnson, T., 2018. Secular change in metamorphism and the onset of global plate tectonics. American Mineralogist 103, 181–196. https://doi.org/10.2138/AM-2018-6166

Brown, M., Kothonen, F. J., 2009. Some Remarks on Melting and Extreme Metamorphism of Crustal Rocks. Physics and Chemistry of the Earth's Interior, 67–87. https://doi.org/10.1007/978-1-4419-0346-4_4

Brun, J.P., Faccenna, C., 2008. Exhumation of high-pressure rocks driven by slab rollback. Earth and Planetary Science Letters 272, 1–7. https://doi.org/10.1016/J.EPSL.2008.02.038

Buick, I. S., Clark, C., Rubatto, D., Hermann, J., Pandit, M., Hand, M., 2010. Constraints on the Proterozoic evolution of the Aravalli–Delhi Orogenic belt (NW India) from monazite geochronology and mineral trace element geochemistry. Lithos, 120(3–4), 511–528. https://doi.org/10.1016/J.LITHOS.2010.09.011

Burchfiel, B.C., Chen, Z., Hodges, K.V., Liu, Y., Royden, L.H., Changrong, D., Xu, L., 1992. The South Tibetan detachment system, Himalayan Orogen: Extension contemporaneous with and parallel to shortening in a Collisional mountain belt. Special Paper of the Geological Society of America 269, 1–41. https://doi.org/10.1130/SPE269-p1

Bürgmann, R., Dresen, G., 2008. Rheology of the Lower Crust and Upper Mantle: Evidence from Rock Mechanics, Geodesy, and Field Observations. Annual Review of Earth and Planetary Sciences 36, 531–567. https://doi.org/10.1146/annurev.earth.36.031207.124326

Caddick, M. J., Konopásek, J., Thompson, A. B., 2010. Preservation of Garnet Growth Zoning and the Duration of Prograde Metamorphism. Journal of Petrology, 51(11), 2327–2347. https://doi.org/10.1093/PETROLOGY/EGQ059

Campagna, D.J., Aydin, A., 1994. Basin genesis associated with strike-slip faulting in the Basin and Range, southeastern Nevada. Tectonics 13, 327–341. https://doi.org/10.1029/93TC02723

Campos Neto, M. da C., 2000. Orogenic systems from SW-Gondwana: an approach to Brasiliano-Pan African cycle and orogenic collage in SE-Brazil, in: Tectonic Evolution of South America. pp. 335–365.

Campos Neto, M. da C., Basei, M.A.S., Assis Janasi, V. de, Moraes, R., 2011. Orogen migration and tectonic setting of the Andrelândia Nappe system: An Ediacaran western Gondwana collage, south of São Francisco craton. Journal of South American Earth Sciences 32, 393–406. https://doi.org/10.1016/j.jsames.2011.02.006

Campos Neto, M. da C., Caby, R., 2000. Terrane accretion and upward extrusion of high-pressure granulites in the Neoproterozoic nappes of southeast Brazil: Petrologic and structural constraints. Tectonics, 19(4), 669–687. https://doi.org/10.1029/1999TC900065

Campos Neto, M. da C., Cioffi, C.R., Moraes, R., da Motta, R.G., Siga, O., Basei, M.A.S., 2010. Structural and metamorphic control on the exhumation of high-P granulites: The Carvalhos Klippe example, from the oriental Andrelândia Nappe System, southern portion of the Brasília Orogen, Brazil. Precambrian Research 180, 125–142. https://doi.org/10.1016/j.precamres.2010.05.010

Campos Neto, M. da C., Cioffi, C.R., Westin, A., Rocha, B.C., Frugis, G.L., Tedeschi, M., Pinheiro, M.A.P., 2020. O Orógeno Brasília Meridional, in: Geocronologia e Evolução Tectônica Do Continente Sul-Americano: A Contribuição de Umberto Giuseppe Cordani.

Campos Neto, M. da C., Stipp Basei, M.A., Farias Vlach, S.R., Caby, R., Szabó, G.A.J., Vasconcelos, P., 2004. Orogen migration and superposition of orogenesis: An overview of Brasiliano orogenic collage of the Southern San Francisco Craton, southeastern Brazil. Geologia USP - Serie Cientifica. https://doi.org/10.5327/s1519-874x2004000100002

Campos Neto, M.da C., Caby, R., 1999. Neoproterozoic high-pressure metamorphism and tectonic constraint from the nappe system south of the Sao Francisco Craton, southeast Brazil. Precambrian Research 97, 3–26. https://doi.org/10.1016/S0301-9268(99)00010-8

Carosi, R., Lombardo, B., Molli, G., Musumeci, G., Pertusati, P.C., 1998. The south Tibetan detachment system in the Rongbuk Valley, Everest region. Deformation features and geological implications. Journal of Asian Earth Sciences 16, 299–311. https://doi.org/10.1016/S0743-9547(98)00014-2

Carosi, R., Montomoli, C., Iaccarino, S., 2018. 20 years of geological mapping of the metamorphic core across Central and Eastern Himalayas. Earth-Science Reviews 177, 124–138. https://doi.org/10.1016/j.earscirev.2017.11.006

Carosi, R., Montomoli, C., Iaccarino, S., Massonne, H.J., Rubatto, D., Langone, A., Gemignani, L., Visonà, D., 2016. Middle to late Eocene exhumation of the Greater Himalayan Sequence in the Central Himalayas: Progressive accretion from the Indian plate. Geological Society of America Bulletin 128, 1571–1592. https://doi.org/10.1130/B31471.1

Carosi, R., Montomoli, C., Iaccarino, S., Visonà, D., 2019. Structural evolution, metamorphism and melting in the greater Himalayan sequence in central-Western Nepal. Geological Society of London Special Publication 483, 305–323. https://doi.org/10.1144/SP483.3

Carosi, R., Montomoli, C., Langone, A., Turina, A., Cesare, B., Iaccarino, S., Fascioli, L., Visonà, D., Ronchi, A., Rai, S.M., 2015. Eocene partial melting recorded in peritectic garnets from kyanite-gneiss, Greater Himalayan Sequence, central Nepal. Geological Society of London Special Publication 412, 111–129. https://doi.org/10.1144/SP412.

Carosi, R., Montomoli, C., Rubatto, D., Visonà, D., 2010. Late Oligocene high-temperature shear zones in the core of the Higher Himalayan Crystallines (Lower Dolpo, western Nepal). Tectonics 29, 1–20. https://doi.org/10.1029/2008TC002400

Carosi, R., Montomoli, C., Visonà, D., 2007. A structural transect in the Lower Dolpo: Insights on the tectonic evolution of Western Nepal. Journal of Asian Earth Sciences 29, 407–423. https://doi.org/10.1016/j.jseaes.2006.05.001

Carrapa, B., 2009. Tracing exhumation and orogenic wedge dynamics in the European Alps with detrital thermochronology. Geology, 37(12), 1127–1130.

Catlos, E. J., 2013. Generalizations about monazite: Implications for geochronologic studies. American Mineralogist, 98(5–6), 819–832. https://doi.org/10.2138/am.2013.4336

Catlos, E. J., Lovera, O. M., Kelly, E. D., Ashley, K. T., Harrison, T. M., Etzel, T., 2018. Modeling High-Resolution Pressure-Temperature Paths Across the Himalayan Main Central Thrust (Central Nepal): Implications for the Dynamics of Collision. Tectonics, 37(8), 2363–2388. https://doi.org/10.1029/2018TC005144

Célérier, J., Harrison, T.M., Beyssac, O., Herman, F., Dunlap, W.J., Webb, A.G., 2009. The Kumaun and Garwhal Lesser Himalaya, India: Part 2: Thermal and deformation histories. Geological Society of America Bulletin 121, 1281–1297. https://doi.org/10.1130/B26343.1

Chakraborty, S., Mukul, M., Mathew, G., Pande, K., 2019. Major shear zone within the Greater Himalayan Sequence and sequential evolution of the metamorphic core in Sikkim, India. Tectonophysics 770, 228183. https://doi.org/10.1016/j.tecto.2019.228183

Chardon, D., Gapais, D., Cagnard, F., 2009. Flow of ultra-hot orogens: A view from the Precambrian, clues for the Phanerozoic. Tectonophysics 477, 105–118. https://doi.org/10.1016/J.TECTO.2009.03.008

Chen, J., Carosi, R., Cao, H., Montomoli, C., Iaccarino, S., Langone, A., Li, G., 2018. Structural setting of the Yalaxiangbo dome, SE Tibet (China).Italian Journal of Geosciences,137(2), 330-347.

Cioffi, C. R., Campos Neto, M. da C., Rocha, B. C. da, Moraes, R., Henrique-Pinto, R., 2012. Geochemical signatures of metasedimentary rocks of high-pressure granulite facies and their relation with partial melting: Carvalhos Klippe, Southern Brasília Belt, Brazil. Journal of South American Earth Sciences, 40, 63–76. https://doi.org/10.1016/j.jsames.2012.09.007

Cioffi, C.R., Campos Neto, M. da C., Möller, A., Rocha, B.C., 2019. Titanite petrochronology of the southern Brasília Orogen basement: Effects of retrograde net-transfer reactions on titanite trace element compositions. Lithos 344–345, 393–408. https://doi.org/10.1016/j.lithos.2019.06.035

Cioffi, C.R., Campos Neto, M. da C., Möller, A., Rocha, B.C., 2016a. Paleoproterozoic continental crust generation events at 2.15 and 2.08Ga in the basement of the southern Brasília Orogen, SE Brazil. Precambrian Research 275, 176–196. https://doi.org/10.1016/j.precamres.2016.01.007

Cioffi, C.R., Campos Neto, M. da C., Möller, A., Rocha, B.C., 2016b. Tectonic significance of the Meso- to Neoarchean complexes in the basement of the southern Brasília Orogen. Precambrian Research 287, 91–107. https://doi.org/10.1016/j.precamres.2016.10.009

Clark, C., Fitzsimons, I. C. W., Healy, D., Harley, S. L., 2011. How Does the Continental Crust Get Really Hot? Elements, 7(4), 235–240.

Clark, C., Healy, D., Johnson, T., Collins, A. S., Taylor, R. J., Santosh, M., Timms, N. E., 2015. Hot orogens and supercontinent amalgamation: A Gondwanan example from southern India. Gondwana Research, 28(4), 1310–1328. https://doi.org/10.1016/J.GR.2014.11.005

Clarke, G.L., White, R.W., Lui, S., Fitzherbert, J.A., Pearson, N.J., 2007. Contrasting behaviour of rare earth and major elements during partial melting in granulite facies migmatites, Wuluma Hills, Arunta Block, central Australia. Journal of Metamorphic Geology 25, 1–18. doi:10.1111/j.1525-1314.2006.00673.x

Coelho, M.B., Trouw, R.A.J., Ganade, C.E., Vinagre, R., Mendes, J.C., Sato, K., 2017. Constraining timing and P-T conditions of continental collision and late overprinting in the Southern Brasília Orogen (SE-Brazil): U-Pb zircon ages and geothermobarometry of the Andrelândia Nappe System. Precambrian Research 292, 194–215. https://doi.org/10.1016/j.precamres.2017.02.001

Coggon, R., & Holland, T. J. B., 2002. Mixing properties of phengitic micas and revised garnet-phengite thermobarometers. Journal of Metamorphic Geology, 20(7), 683–696. https://doi.org/10.1046/J.1525-1314.2002.00395.X

Coney, P.J., 1970. The Geotectonic Cycle and the New Global Tectonics, Geological Society of America Bulletin.

Connolly, J.A.D., 2005. Computation of phase equilibria by linear programming: A tool for geodynamic modeling and its application to subduction zone decarbonation. Earth and Planetary Science Letters 236, 524–541. https://doi.org/10.1016/j.epsl.2005.04.033

Cordani, U.G., D'agrella-Filho, M.S., Brito-Neves, B.B., Trindade, R.I.F., 2003. Tearing up Rodinia: the Neoproterozoic palaeogeography of South American cratonic fragments. Terra Nova 15, 350–359. https://doi.org/10.1046/j.1365-3121.2003.00506.x

Cordani, U.G., Pimentel, M.M., De Araujo, C.E.G., Basei, M.A.S., Fuck, R.A., Girardi, V.A.V., 2013. Was there an ediacaran clymene ocean in central south America? American journal of science. American Journal of Science 313, 517–539. https://doi.org/10.2475/06.2013.01

Cottle, J.M., Larson, K.P., Kellett, D.A., 2015. How does the mid-crust accommodate deformation in large, hot collisional orogens? A review of recent research in the Himalayan orogen. Journal of Structural Geology 78, 119–133. https://doi.org/10.1016/j.jsg.2015.06.008

Dahl, P. S., Terry, M. P., Jercinovic, M. J., Williams, M. L., Hamilton, M. A., Foland, K. A., Clement, S. M., Friberg, L. V. M. 2005. Electron probe (Ultrachron) microchronometry of metamorphic monazite: Unraveling the timing of polyphase thermotectonism in the easternmost Wyoming Craton (Black Hills, South Dakota). American Mineralogist, 90(11–12), 1712–1728. https://doi.org/10.2138/am.2005.2002

Dahlen, F.A., 1990. Critical taper model of fold-and-thrust belts and accretionary wedges. Annual Review of Earth and Planetary Sciences 18, 55–99.

Daly, M.C., Chorowicz, J., Fairhead, J.D., 1989. Rift basin evolution in Africa: The influence of reactivated steep basement shear zones. Geological Society Special Publication 44, 309–334. https://doi.org/10.1144/GSL.SP.1989.044.01.17

de Capitani, C., Brown, T. H., 1987. The computation of chemical equilibrium in complex systems containing non-ideal solutions. Geochimica et Cosmochimica Acta, 51(10), 2639–2652. https://doi.org/10.1016/0016-7037(87)90145-1

de Capitani, C., Petrakakis, K., 2010. The computation of equilibrium assemblage diagrams with Theriak/Domino software. American Mineralogist, 95(7), 1006–1016. https://doi.org/10.2138/AM.2010.3354

DeCelles, P. G., Mitra, G., 1995. History of the Sevier orogenic wedge in terms of critical taper models, northeast Utah and southwest Wyoming . Geological Society of America Bulletin, 107(4), 454–462.

Decelles, P.G., Kapp, P., Gehrels, G.E., Ding, L., 2014. Paleocene-Eocene foreland basin evolution in the Himalaya of southern Tibet and Nepal: Implications for the age of initial India-Asia collision. Tectonics 33, 824–849. https://doi.org/10.1002/2014TC003522

Del Lama, E.A., Zanardo, A., Oliveira, M.A.F., Morales, N., 2000. Exhumation of high-pressure granulites of the Guaxupé Complex, southeastern Brazil. Geological Journal 35, 231–249. https://doi.org/10.1002/gj.859

Dewey, J.F., Bird, J.M., 1970. Mountain belts and the new global tectonics. Journal of Geophysical Research 75, 2625–2647. https://doi.org/10.1029/JB075i014p02625

Dewey, J.F., Burke, K.C.A., 1973. Tibetan, Variscan, and Precambrian Basement Reactivation: Products of Continental Collision. The Journal of Geology 81, 683–692. https://doi.org/10.1086/627920

Dielforder, A., Hampel, A., 2021. Force-Balance Analysis of Stress Changes During the Subduction-Collision Transition and Implications for the Rise of Mountain Belts. Journal of Geophysical Research: Solid Earth 126, e2020JB020914. https://doi.org/10.1029/2020JB020914

Dielforder, A., Hetzel, R., Oncken, O., 2020. Megathrust shear force controls mountain height at convergent plate margins. Nature 2020 582:7811 582, 225–229. https://doi.org/10.1038/s41586-020-2340-7

Duesterhoeft, E., Lanari, P., 2020. Iterative thermodynamic modelling—Part 1: A theoretical scoring technique and a computer program (Bingo-Antidote). Journal of Metamorphic Geology, 38(5), 527–551. https://doi.org/10.1111/JMG.12538

Dumond, G., Goncalves, P., Williams, M. L., Jercinovic, M. J., 2015. Monazite as a monitor of melting, garnet growth and feldspar recrystallization in continental lower crust. Journal of Metamorphic Geology, 33(7), 735–762. https://doi.org/10.1111/jmg.12150

Dumond, G., McLean, N., Williams, M.L., Jercinovic, M.J., Bowring, S.A., 2008. High-resolution dating of granite petrogenesis and deformation in a lower crustal shear zone: Athabasca granulite terrane, western Canadian Shield. Chemical Geology 254, 175–196. https://doi.org/10.1016/j.chemgeo.2008.04.014

Dunkl, I., Antolín, B., Wemmer, K., Rantitsch, G., Kienast, M., Montomoli, C., Ding, L., Carosi, R., Appel, E., El Bay, R., Xu, Q., von Eynatten, H., 2011. Metamorphic evolution of the Tethyan Himalayan flysch in SE tibet. Geological Society Special Publication 353, 45–69. https://doi.org/10.1144/SP353.4

Engi, M., 2017. Petrochronology Based on REE-Minerals: Monazite, Allanite, Xenotime, Apatite. Reviews in Mineralogy and Geochemistry, 83(1), 365–418. https://doi.org/10.2138/RMG.2017.83.12

England, P.C., Thompson, A.B., 1984. Pressure-Temperature-Time Paths of Regional Metamorphism I. Heat Transfer during the Evolution of Regions of Thickened Continental Crust. Journal of Petrology 25, 894–928. https://doi.org/10.1093/petrology/25.4.894

Faccenda, M., Gerya, T. V., Chakraborty, S., 2008. Styles of post-subduction collisional orogeny: Influence of convergence velocity, crustal rheology and radiogenic heat production. Lithos 103, 257–287. https://doi.org/10.1016/j.lithos.2007.09.009

Fletcher, R.C., 1972. Application of a mathematical model to the emplacement of mantled gneiss domes. American Journal of Science 272, 197–216.

Fontainha, M.V.F., Trouw, R.A.J., Peternel, R., de Paula, R.R., Polo, H.J.O., Negrão, A.P., Furtado, P.C., Telles, R.C.M., 2020. A case study of superposed structures in the tectonic interference zone between the Southern Brasília and Ribeira orogens, southeastern Brazil. Journal of South American Earth Sciences 104, 102718. https://doi.org/10.1016/j.jsames.2020.102718

Fossen, H., Cavalcante, G.C.G., 2017. Shear zones – A review. Earth-Science Reviews 171, 434–455. https://doi.org/10.1016/j.earscirev.2017.05.002

Foster, G., Kinny, P., Vance, D., Prince, C., Harris, N., 2000. The significance of monazite U-Th-Pb age data in metamorphic assemblages; a combined study of monazite and garnet chronometry. Earth and Planetary Science Letters 181, 327–340. https://doi.org/10.1016/S0012-821X(00)00212-0

Frugis, G.L., Campos Neto, M. da C., Lima, R.B., 2018. Eastern Paranapanema and southern São Francisco orogenic margins: Records of enduring Neoproterozoic oceanic convergence and collision in the southern Brasília Orogen. Precambrian Research 308, 35–57. https://doi.org/10.1016/j.precamres.2018.02.005

Fuck, R.A., Pimentel, M.M., Alvarenga, C.J.S., Dantas, E.L., 2017. The Northern Brasília Belt. Springer, Cham, pp. 205–220. https://doi.org/10.1007/978-3-319-01715-0_11

Fuhrman, M.L., Lindsley, D.H., 1988. Ternary-Feldspar Modeling and Thermometry. American Mineralogist 73, 201–2015.

Fumes, R.A., Luvizotto, G.L., Moraes, R., Lanari, P., Valeriano, C. de M., Zack, T., Caddick, M.J., Simões, L.S.A., 2021. Petrochronology of high-pressure granulite facies rocks from Southern Brasília Orogen, SE Brazil: Combining quantitative compositional mapping, single-element thermometry and geochronology. Journal of Metamorphic Geology 1–36. https://doi.org/10.1111/JMG.12637

Ganade De Araujo, C.E., Rubatto, D., Hermann, J., Cordani, U.G., Caby, R., Basei, M.A.S., 2014. Ediacaran 2,500-km-long synchronous deep continental subduction in the West Gondwana Orogen. Nature Communications 5, 1–8. https://doi.org/10.1038/ncomms6198

Garcia, M. da G.M., Campos Neto, M. da C., 2003. Contrasting metamorphic conditions in the Neoproterozoic collision-related Nappes south of São Francisco Craton, SE Brazil. Journal of South American Earth Sciences 15, 853–870. https://doi.org/10.1016/S0895-9811(02)00147-5

Garzanti, E., 1999. Stratigraphy and sedimentary history of the Nepal Tethys Himalaya passive margin. Journal of Asian Earth Sciences 17, 805–827. https://doi.org/10.1016/S1367-9120(99)00017-6

Garzanti, E., Baud, A., Mascle, G., 1987. Sedimentary record of the northward flight of india and its collision with eurasia (ladakh himalaya, India). Geodinamica Acta 1, 297–312. https://doi.org/10.1080/09853111.1987.11105147

Gasser, D., Bruand, E., Rubatto, D., Stüwe, K., 2012. The behaviour of monazite from greenschist facies phyllites to anatectic gneisses: An example from the Chugach Metamorphic Complex, southern Alaska. Lithos 134–135, 108–122. https://doi.org/10.1016/j.lithos.2011.12.003

Gerya, T., 2014. Precambrian geodynamics: Concepts and models. Gondwana Research 25, 442–463. https://doi.org/10.1016/J.GR.2012.11.008

Godin, L., Grujic, D., Law, R.D., Searle, M.P., 2006. Channel flow, ductile extrusion and exhumation in continental collision zones: An introduction. Geological Society Special Publication 268, 1–23. https://doi.org/10.1144/GSL.SP.2006.268.01.01

Godin, L., Roche, R.S. LA, Waffle, L., Harris, L.B., 2019. Influence of inherited indian basement faults on the evolution of the himalayan orogen. Geological Society Special Publication 481, 251–276. https://doi.org/10.1144/SP481.4

Goscombe, B., Gray, D., Foster, D.A., 2018. Metamorphic response to collision in the Central Himalayan Orogen. Gondwana Research 57, 191–265. https://doi.org/10.1016/j.gr.2018.02.002

Groppo, C., Lombardo, B., Rolfo, F., Pertusati, P., 2007. Clockwise exhumation path of granulitized eclogites from the Ama Drime range (Eastern Himalayas). Journal of Metamorphic Geology 25, 51–75. https://doi.org/10.1111/j.1525-1314.2006.00678.x

Groppo, C., Rolfo, F., Lombardo, B., 2009. P-T evolution across the main central thrust zone (Eastern Nepal): Hidden discontinuities revealed by petrology. Journal of Petrology 50, 1149–1180. doi:10.1093/petrology/egp036

Groppo, C., Rolfo, F., Mosca, P., 2013. The cordierite-bearing anatectic rocks of the higher Himalayan crystallines (eastern Nepal): Low-pressure anatexis, melt productivity, melt loss and the preservation of cordierite. Journal of Metamorphic Geology, 31(2), 187–204. https://doi.org/10.1111/jmg.12014

Grujic, D., Casey, M., Davidson, C., Hollister, L.S., Kündig, R., Pavlis, T., Schmid, S., 1996. Ductile extrusion of the Higher Himalayan Crystalline in Bhutan: Evidence from quartz microfabrics. Tectonophysics 260, 21–43. https://doi.org/10.1016/0040-1951(96)00074-1

Grujic, D., Warren, C.J., Wooden, J.L., 2011. Rapid synconvergent exhumation of Miocene-aged lower orogenic crust in the eastern Himalaya. Lithosphere 3, 346–366. https://doi.org/10.1130/L154.1

Guilmette, C., Indares, A., Hébert, R., 2011. High-pressure anatectic paragneisses from the Namche Barwa, Eastern Himalayan Syntaxis: Textural evidence for partial melting, phase equilibria modeling and tectonic implications. Lithos, 124(1–2), 66–81. https://doi.org/10.1016/j.lithos.2010.09.003

Hacker, B. R., Kelemen, P. B., Behn, M. D., 2015. Continental Lower Crust. Annual Review of Earth and Planetary Sciences, 43, 167–205. https://doi.org/10.1146/annurev-earth-050212-124117

Hackspacher, P.C., Fetter, A.H., Teixeira, W., Dantas, E.L., Ebert, H.D., Trouw, R.A.J., Vasconcelos, P., 2004. Final stages of the Brasiliano Orogenesis in SE Brazil: U-Pb and 40Ar/39Ar evidence for overprinting of the Brasília Belt by the Ribeira Belt Tectonics. Journal of the Virtual Explorer 17.

Hasalová, P., Štípská, P., Powell, R., Schulmann, K., Janousek, V., Lexa, O., 2007. Transforming mylonitic metagranite by open-system interactions during melt flow. Journal of Metamorphic. Geology 26,55-80. doi:10.1111/j.1525-1314.2007.00744.x

Henry, D. J., Guidotti, C. V., Thomson, J. A., 2005. The Ti-saturation surface for low-to-medium pressure metapelitic biotites: Implications for geothermometry and Ti-substitution mechanisms. American Mineralogist, 90(2–3), 316–328. https://doi.org/10.2138/AM.2005.1498

Hirn, A., Lepine, J. C., Jobert, G., Sapin, M., Wittlinger, G., Zhong Xin, X., En Yuan, G., Xiang Jing, W., Ji Wen, T., Shao Bai, X., Pandey, M. R., Tater, J. M., 1984. Crustal structure and variability of the Himalayan border of Tibet. Nature 1984 307:5946, 307, 23–25. https://doi.org/10.1038/307023a0

Hirth, G., Kohlstedf, D., 2003. Rheology of the upper mantle and the mantle wedge: A view from the experimentalists.

Hodges, K. V, 2000. Tectonics of the Himalaya and southern Tibet from two perspectives. Geological Society of America Bulletin 112, 324–350.

Hodges, K. V., Silverberg, D.S., 1988. Thermal evolution of the Greater Himalaya, Garhwal, India. Tectonics 7, 583–600. https://doi.org/10.1029/TC007i003p00583

Hollis, J. A., Harley, S. L., White, R. W., & Clarke, G. L. (2006). Preservation of evidence for prograde metamorphism in ultrahigh-temperature, high-pressure kyanite-bearing granulites, South Harris, Scotland. Journal of Metamorphic Geology, 24(3), 263–279. https://doi.org/10.1111/J.1525-1314.2006.00636.X

Holland, T. J. B., Powell, R., 1998. An internally consistent thermodynamic data set for phases of petrological interest. Journal of Metamorphic Geology, 16(3), 309–343. https://doi.org/10.1111/J.1525-1314.1998.00140.X

Holland, T.J.B., Powell, R., 2011. An improved and extended internally consistent thermodynamic dataset for phases of petrological interest, involving a new equation of state for solids. Journal of Metamorphic Geology 29, 333–383. https://doi.org/10.1111/j.1525-1314.2010.00923.x

Horton, F., Hacker, B., Kylander-Clark, A., Holder, R., Jöns, N., 2016. Focused radiogenic heating of middle crust caused ultrahigh temperatures in southern Madagascar. Tectonics, 35(2), 293–314. https://doi.org/10.1002/2015TC004040

Horton, F., Holder, R. M., Swindle, C. R., 2021. An extensive record of orogenesis recorded in a Madagascar granulite. Journal of Metamorphic Geology. https://doi.org/10.1111/JMG.12628

Hu, X., Garzanti, E., Wang, J., Huang, W., An, W., Webb, A., 2016. The timing of India-Asia collision onset – Facts, theories, controversies. Earth-Science Reviews. https://doi.org/10.1016/j.earscirev.2016.07.014

Hu, X.M., Garzanti, E., An, W., Hu, X.F., 2015. Provenance and drainage system of the Early Cretaceous volcanic detritus in the Himalaya as constrained by detrital zircon geochronology. Journal of Palaeogeography 4, 85–98. https://doi.org/10.3724/SP.J.1261.2015.00069

Hunter, N.J.R., Weinberg, R.F., Wilson, C.J.L., Luzin, V., Misra, S., 2018. Microscopic anatomy of a “hot-on-cold” shear zone: Insights from quartzites of the Main Central Thrust in the Alaknanda region (Garhwal Himalaya). Geological Society of America Bulletin 130, 1519–1539. https://doi.org/10.1130/B31797.1

Hunter, N.J.R., Weinberg, R.F., Wilson, C.J.L., Luzin, V., Misra, S., 2019. Quartz deformation across interlayered monomineralic and polymineralic rocks: A comparative analysis. Journal of Structural Geology 119, 118–134. https://doi.org/10.1016/j.jsg.2018.12.005

Iaccarino, S., Montomoli, C., Carosi, R., Massonne, H.J., Langone, A., Visonà, D., 2015. Pressure-temperature-time-deformation path of kyanite-bearing migmatitic paragneiss in the Kali Gandaki valley (Central Nepal): Investigation of Late Eocene-Early Oligocene melting processes. Lithos 231, 103–121. https://doi.org/10.1016/j.lithos.2015.06.005

Iaccarino, S., Montomoli, C., Carosi, R., Massonne, H.J., Visonà, D., 2017a. Geology and tectono-metamorphic evolution of the Himalayan metamorphic core: insights from the Mugu Karnali transect, Western Nepal (Central Himalaya). Journal of Metamorphic Geology 35, 301–325. https://doi.org/10.1111/jmg.12233

Iaccarino, S., Montomoli, C., Carosi, R., Montemagni, C., Massonne, H.J., Langone, A., Jain, A.K., Visonà, D., 2017b. Pressure-Temperature-Deformation-Time Constraints on the South Tibetan Detachment System in the Garhwal Himalaya (NW India). Tectonics 36, 2281–2304. https://doi.org/10.1002/2017TC004566

Iaccarino, S., Montomoli, C., Montemagni, C., Massonne, H.-J., Langone, A., Jain, A.K., Visonà, D., Carosi, R., 2020. The main central thrust zone along the Alaknanda and Dhauli Ganga valleys (Garhwal Himalaya, NW India): Insights into an inverted metamorphic sequence. Lithos 105669. https://doi.org/10.1016/j.lithos.2020.105669

Indares, A., 2020. Deciphering the metamorphic architecture and magmatic patterns of large hot orogens: Insights from the central Grenville Province. Gondwana Research, 80, 385–409. https://doi.org/10.1016/J.GR.2019.10.013

Indares, A., White, R. W., Powell, R., 2008. Phase equilibria modelling of kyanite-bearing anatectic paragneisses from the central Grenville Province. Journal of Metamorphic Geology, 26(8), 815–836. https://doi.org/10.1111/J.1525-1314.2008.00788.X

Jain, A.K., Shreshtha, M., Seth, P., Kanyal, L., Carosi, R., Montomoli, C., Iaccarino, S., Mukherjee, P.K., 2014. The higher himalayan crystallines, Alaknanda – Dhauli ganga valleys, Garhwal Himalaya, India. Journal of the Virtual Explorer 47. https://doi.org/10.3809/jvirtex.2014.00349

Jamieson, R. A., Beaumont, C., 2013. On the origin of orogens. Bulletin of the Geological Society of America, 125(11–12), 1671–1702. https://doi.org/10.1130/B30855.1

Jamieson, R. A., Beaumont, C., Medvedev, S., Nguyen, M. H., 2004. Crustal channel flows: 2. Numerical models with implications for metamorphism in the Himalayan-Tibetan orogen. Journal of Geophysical Research: Solid Earth, 109(6), 1–24. https://doi.org/10.1029/2003JB002811

Jamieson, R. A., Unsworth, M. J., Harris, N. B. W., Rosenberg, C. L., Schulmann, K., 2011a. Crustal melting and the flow of mountains. Elements, 7(4), 253–260. https://doi.org/10.2113/gselements.7.4.253

Jamieson, R.A., Beaumont, C., Fullsack, P., Lee, B., 1998. Barrovian regional metamorphism: where's the heat? Geological Society, London, Special Publications 138, 23–51. https://doi.org/10.1144/GSL.SP.1996.138.01.03

Jamieson, R.A., Beaumont, C., Medvedev, S., Nguyen, M.H., 2004. Crustal channel flows: 2. Numerical models with implications for metamorphism in the Himalayan-Tibetan orogen. Journal of Geophysical Research: Solid Earth 109, 1–24. https://doi.org/10.1029/2003JB002811

Jamieson, R.A., Beaumont, C., Nguyen, M.H., Culshaw, N.G., 2007. Synconvergent ductile flow in variable-strength continental crust: Numerical models with application to the western Grenville orogen. Tectonics 26. https://doi.org/10.1029/2006TC002036

Jamieson, R.A., Beaumont, C., Nguyen, M.H., Lee, B., 2002. Interaction of metamorphism, deformation and exhumation in large convergent orogens. Journal of Metamorphic Geology 20, 9–24. https://doi.org/10.1046/J.0263-4929.2001.00357.X

Jamieson, R.A., Beaumont, C., Warren, C.J., Nguyen, M.H., 2010. The Grenville Orogen explained? Applications and limitations of integrating numerical models with geological and geophysical data. Canadian Journal of Earth Sciences 47, 517–539. https://doi.org/10.1139/E09-070/ASSET/IMAGES/E09-070T3H.GIF

Janots, E., Engi, M., Berger, A., Allaz, J., Schwarz, J.-O., Spandler, C., 2008. Prograde metamorphic sequence of REE minerals in pelitic rocks of the Central Alps: implications for allanite–monazite–xenotime phase relations from 250 to 610 °C. Journal of Metamorphic Geology 26, 509–526. https://doi.org/10.1111/j.1525-1314.2008.00774.x

Johnson, M., Harley, S.H., 2012. Orogenesis: The Making of mountains . Cambridge University Press.

Johnson, T., Yakymchuk, C., Brown, M., 2021. Crustal melting and suprasolidus phase equilibria: From first principles to the state-of-the-art. Earth-Science Reviews, 221. https://doi.org/10.1016/J.EARSCIREV.2021.103778

Kellett, D.A., Grujic, D., Coutand, I., Cottle, J., Mukul, M., 2015. The South Tibetan detachment system facilitates ultra rapid cooling of granulite-facies rocks in Sikkim Himalaya. Tectonics 32, 252–270. https://doi.org/10.1002/tect.20014

Kelsey, D. E., 2008. On ultrahigh-temperature crustal metamorphism. Gondwana Research, 13(1), 1–29. https://doi.org/10.1016/J.GR.2007.06.001

Kelsey, D. E., Hand, M., 2015. On ultrahigh temperature crustal metamorphism: Phase equilibria, trace element thermometry, bulk composition, heat sources, timescales and tectonic settings. Geoscience Frontiers, 6(3), 311–356. https://doi.org/10.1016/J.GSF.2014.09.006

Khanal, G., Wang, J.M., Wu, F.Y., Wang, J.G., Yang, L., 2020. In-sequence buoyancy extrusion of the Himalayan metamorphic core, central Nepal: Constraints from monazite petrochronology and thermobarometry. Journal of Asian Earth Sciences 199, 104406. https://doi.org/10.1016/j.jaesx.2020.100025

Kind, R., Yuan, X., Saul, J., Nelson, D., Sobolev, S. V., Mechie, J., Zhao, W., Kosarev, G., Ni, J., Achauer, U., Jiang, M., 2002. Seismic Images of Crust and Upper Mantle Beneath Tibet: Evidence for Eurasian Plate Subduction. Science (1979) 298, 1219–1221. https://doi.org/10.1126/SCIENCE.1078115

Kohn, M. J., Engi, M., Lanari, P., 2017. Petrochronology: Methods and applications. In Petrochronology (Vol. 83). De Gruyter. https://doi.org/10.1515/9783110561890/HTML

Kohn, M. J., Malloy, M. A., 2004. Formation of monazite via prograde metamorphic reactions among common silicates: Implications for age determinations. Geochimica et Cosmochimica Acta, 68(1), 101–113. https://doi.org/10.1016/S0016-7037(03)00258-8

Kohn, M. J., Wieland, M. S., Parkinson, C. D., Upreti, B. N., 2005. Five generations of monazite in Langtang gneisses: Implications for chronology of the Himalayan metamorphic core. Journal of Metamorphic Geology, 23(5), 399–406. https://doi.org/10.1111/j.1525-1314.2005.00584.x

Kohn, M.J., 2008. P-T-t data from central Nepal support critical taper and repudiate large-scale channel flow of the Greater Himalayan Sequence. Geological Society of America Bulletin 120, 259–273. https://doi.org/10.1130/B26252.1

Kohn, M.J., 2014. Himalayan Metamorphism and Its Tectonic Implications. Annual Review of Earth and Planetary Sciences 42, 381–419. https://doi.org/10.1146/annurev-earth-060313-055005

Kohn, M.J., 2016. Metamorphic chronology - A tool for all ages: Past achievements and future prospects. American Mineralogist 101, 25–42. https://doi.org/10.2138/am-2016-5146

Kohn, M. J., 2020. A refined zirconium-in-rutile thermometer. American Mineralogist, 105(6), 963–971. https://doi.org/10.2138/AM-2020-7091

Konrad-Schmolke, M., O'Brien, P. J., de Capitani, C., Carswell, D. A., 2008. Garnet growth at high- and ultra-high pressure conditions and the effect of element fractionation on mineral modes and composition. Lithos, 103(3–4), 309–332. https://doi.org/10.1016/J.LITHOS.2007.10.007

Korhonen, F. J., Clark, C., Brown, M., Bhattacharya, S., Taylor, R., 2013. How long-lived is ultrahigh temperature (UHT) metamorphism? Constraints from zircon and monazite geochronology in the Eastern Ghats orogenic belt, India. Precambrian Research, 234, 322–350. https://doi.org/10.1016/J.PRECAMRES.2012.12.001

Lanari, P., Duesterhoeft, E., 2019. Modeling Metamorphic Rocks Using Equilibrium Thermodynamics and Internally Consistent Databases: Past Achievements, Problems and Perspectives. Journal of Petrology, 60(1), 19–56. https://doi.org/10.1093/PETROLOGY/EGY105

Lanari, P., Engi, M., 2017. on Metamorphic Mineral Assemblages. Reviews in Mineralogy and Geochemistry, 83, 55–102.

Lanari, P., Hermann, J., 2021. Iterative thermodynamic modelling-Part 2: Tracing equilibrium relationships between minerals in metamorphic rocks. Journal of Metamorphic Geology, 39, 651–674. https://doi.org/10.1111/jmg.12575

Lanari, P., Vho, A., Bovay, T., Airaghi, L., Centrella, S., 2019. Quantitative compositional mapping of mineral phases by electron probe micro-analyser. Geological Society, London, Special Publications, 478(1), 39–63. https://doi.org/10.1144/SP478.4

Lanari, P., Vidal, O., de Andrade, V., Dubacq, B., Lewin, E., Grosch, E. G., Schwartz, S., 2014. XMapTools: A MATLAB©-based program for electron microprobe X-ray image processing and geothermobarometry. Computers & Geosciences, 62, 227–240. https://doi.org/10.1016/J.CAGEO.2013.08.010

Larson, K.P., Ambrose, T.K., Webb, A.G., Cottle, J.M., Shrestha, S., 2015. Reconciling Himalayan midcrustal discontinuities: The Main Central thrust system. Earth and Planetary Science Letters 429, 139–146. https://doi.org/10.1016/j.epsl.2015.07.070

Larson, K.P., Godin, L., Price, R.A., 2010. Relationships between displacement and distortion in orogens: Linking the Himalayan foreland and hinterland in central Nepal. Geological Society of America Bulletin 122, 1116–1134. https://doi.org/10.1130/B30073.1

Lasalle, S., Indares, A., 2014. Anatectic record and contrasting P–T paths of aluminous gneisses from the central Grenville Province. Journal of Metamorphic Geology, 32(6), 627–646. https://doi.org/10.1111/JMG.12083

Law, R.D., 2014. Deformation thermometry based on quartz c-axis fabrics and recrystallization microstructures: A review. Journal of Structural Geology 66, 129–161. https://doi.org/10.1016/j.jsg.2014.05.023

Law, R.D., Stahr, D.W., Francsis, M.K., Ashley, K.T., Grasemann, B., Ahmad, T., 2013. Deformation temperatures and flow vorticities near the base of the greater himalayan series, sutlej valley and shimla klippe, NW india. Journal of Structural Geology 54, 21–53. https://doi.org/10.1016/j.jsg.2013.05.009

Le Fort, P., 1975. Himalayas: the collided range. Present knowledge of the continental arc. American Journal of Science 275, 1–44.

Leech, M.L., Singh, S., Jain, A.K., Klemperer, S.L., Manickavasagam, R.M., 2005. The onset of India-Asia continental collision: Early, steep subduction required by the timing of UHP metamorphism in the western Himalaya. Earth and Planetary Science Letters 234, 83–97. https://doi.org/10.1016/j.epsl.2005.02.038

Li, B., Massonne, H.J., Hartmann, L.A., Zhang, J., Luo, T., 2021. Kyanite-garnet granulite from the Andrelândia nappe system, Brasília belt, registers two late Neoproterozoic metamorphic cycles. Precambrian Research 355, 106086. https://doi.org/10.1016/j.precamres.2020.106086

Li, C., van der Hilst, R.D., Meltzer, A.S., Engdahl, E.R., 2008. Subduction of the Indian lithosphere beneath the Tibetan Plateau and Burma. Earth and Planetary Science Letters 274, 157–168. https://doi.org/10.1016/J.EPSL.2008.07.016

Lombardo, B., Rolfo, F., 2000. Two contrasting eclogite types in the Himalayas: implications for the Himalayan orogeny. Journal of Geodynamics 30, 37–60. https://doi.org/10.1016/S0264-3707(99)00026-5

Machado, N., Valladares, C., Heilbron, M., Valeriano, C., 1996. U-Pb geochronology of the central Ribeira belt (Brazil) and implications for the evolution of the Brazilian Orogeny. Precambrian Research 79, 347–361. https://doi.org/10.1016/0301-9268(95)00103-4

Marimon, R.S., Trouw, R.A.J., Dantas, E.L., Ribeiro, A., Santos, P., Kuster, K., Vinagre, R., 2021. Provenance of passive-margin and syn-collisional units: Implications for the geodynamic evolution of the Southern Brasília Orogen, West Gondwana. Sedimentary Geology 413, 105823. https://doi.org/10.1016/j.sedgeo.2020.105823

Massonne, H.J., 2014. Wealth of P-T-t information in medium-high grade metapelites: Example from the Jubrique Unit of the Betic Cordillera, S Spain. Lithos 208, 137–157. https://doi.org/10.1016/j.lithos.2014.08.027

McDonough, W. F., Sun, S. s., 1995. The composition of the Earth. Chemical Geology, 120(3–4), 223–253. https://doi.org/10.1016/0009-2541(94)00140-4

Medvedev, S., 2002. Mechanics of viscous wedges: Modeling by analytical and numerical approaches. Journal of Geophysical Research: Solid Earth, 107(B6), ETG 9-1. https://doi.org/10.1029/2001JB000145

Miao, Y., Herrmann, M., Wu, F., Yan, X., Yang, S., 2012. What controlled Mid–Late Miocene long-term aridification in Central Asia? — Global cooling or Tibetan Plateau uplift: A review. Earth-Science Reviews 112, 155–172. https://doi.org/10.1016/J.EARSCIREV.2012.02.003

Montemagni, C., Carosi, R., Fusi, N., Iaccarino, S., Montomoli, C., Villa, I.M., Zanchetta, S., 2020. Three-dimensional vorticity and time-constrained evolution of the Main Central Thrust zone, Garhwal Himalaya (NW India). Terra Nova 32, 215–224. https://doi.org/10.1111/ter.12450

Montemagni, C., Iaccarino, S., Montomoli, C., Carosi, R., Jain, A., Villa, I.M., 2018b. Age constraints on the deformation style of the South Tibetan Detachment System in Garhwal Himalaya. Italian Journal of Geosciences 137, 1–14. https://doi.org/10.3301/IJG.2018.07

Montemagni, C., Montomoli, C., Iaccarino, S., Carosi, R., Jain, A.K., Massonne, H.J., Villa, I.M., 2018a. Dating protracted fault activities: Microstructures, microchemistry and geochronology of the Vaikrita thrust, main central thrust zone, Garhwal Himalaya, NW India. Geological Society of London Special Publication 481, 127–146.

Montomoli, C., Carosi, R., Iaccarino, S., 2015. Tectonometamorphic discontinuities in the Greater Himalayan Sequence: A local or a regional feature? Geological Society of London Special Publication 412, 25–41. https://doi.org/10.1144/SP412.3

Montomoli, C., Carosi, R., Rubatto, D., Visonà, D., Iaccarino, S., 2017a. Tectonic activity along the inner margin of the South Tibetan Detachment constrained by syntectonic leucogranite emplacement in Western Bhutan. Italian Journal of Geosciences 136, 5–14. https://doi.org/10.3301/IJG.2015.26

Montomoli, C., Iaccarino, S., Antolin, B., Appel, E., Carosi, R., Dunkl, I., Lin, D., Visonà, D., 2017b. Tectono-metamorphic evolution of the Tethyan Sedimentary Sequence (Himalayas, SE Tibet). Italian Journal of Geosciences 136, 73–88. https://doi.org/10.3301/IJG.2015.42

Montomoli, C., Iaccarino, S., Carosi, R., Langone, A., Visonà, D., 2013. Tectonometamorphic discontinuities within the Greater Himalayan Sequence in Western Nepal (Central Himalaya): Insights on the exhumation of crystalline rocks. Tectonophysics, 608, 1349–1370. https://doi.org/10.1016/j.tecto.2013.06.006

Mooney, W.D., Vidale, J.E., 2003. Thermal and chemical variations in subcrustal cratonic lithosphere: evidence from crustal isostasy. Lithos 71, 185–193. https://doi.org/10.1016/J.LITHOS.2003.07.004

Motta, R. G., Moraes, R., 2017. Pseudo- and real-inverted metamorphism caused by the superposition and extrusion of a stack of nappes: a case study of the Southern Brasília Orogen, Brazil. International Journal of Earth Sciences, 106(7), 2407–2427. https://doi.org/10.1007/s00531-016-1436-7

Motta, R.G., Fitzsimons, I.C.W., Moraes, R., Johnson, T.E., Schuindt, S., Benetti, B.Y., 2021. Recovering P–T–t paths from ultra-high temperature (UHT) felsic orthogneiss: An example from the Southern Brasília Orogen, Brazil. Precambrian Research 359, 106222. https://doi.org/10.1016/j.precamres.2021.106222

Mottram, C. M., Cottle, J. M., Kylander-Clark, A. R. C., 2019. Campaign-style U-Pb titanite petrochronology: Along-strike variations in timing of metamorphism in the Himalayan metamorphic core. Geoscience Frontiers, 10(3), 827–847. https://doi.org/10.1016/J.GSF.2018.09.007

Mukherjee, P.K., Jain, A.K., Singhal, S., Singha, N.B., Singh, S., Kumud, K., Seth, P., Patel, R.C., 2019. U-Pb zircon ages and Sm-Nd isotopic characteristics of the Lesser and Great Himalayan sequences, Uttarakhand Himalaya, and their regional tectonic implications. Gondwana Research 75, 282–297. https://doi.org/10.1016/j.gr.2019.06.001

O'Brien, P. J., 2008. Challenges in high-pressure granulite metamorphism in the era of pseudosections: reaction textures, compositional zoning and tectonic interpretation with examples from the Bohemian Massif. Journal of Metamorphic Geology, 26(2), 235–251. https://doi.org/10.1111/J.1525-1314.2007.00758.X

O'Brien, P. J., Rötzler, J., 2003. High-pressure granulites: formation, recovery of peak conditions and implications for tectonics. Journal of Metamorphic Geology, 21(1), 3–20. https://doi.org/10.1046/J.1525-1314.2003.00420.X

Palin, R. M., Searle, M. P., Waters, D. J., Horstwood, M. S. A., Parrish, R. R., 2012. Combined thermobarometry and geochronology of peraluminous metapelites from the Karakoram metamorphic complex, North Pakistan; New insight into the tectonothermal evolution of the Baltoro and Hunza Valley regions. Journal of Metamorphic Geology, 30(8), 793–820. https://doi.org/10.1111/J.1525-1314.2012.00999.X

Palin, R.M., Santosh, M., 2021. Plate tectonics: What, where, why, and when? Gondwana Research 100, 3–24. https://doi.org/10.1016/J.GR.2020.11.001

Palin, R.M., Santosh, M., Cao, W., Li, S.S., Hernández-Uribe, D., Parsons, A., 2020. Secular change and the onset of plate tectonics on Earth. Earth-Science Reviews 207, 103172. https://doi.org/10.1016/J.EARSCIREV.2020.103172

Palin, R.M., Searle, M.P., St-Onge, M.R., Waters, D.J., Roberts, N.M.W., Horstwood, M.S.A., Parrish, R.R., Weller, O.M., Chen, S., Yang, J., 2014. Monazite geochronology and petrology of kyanite- and sillimanite-grade migmatites from the northwestern flank of the eastern Himalayan syntaxis. Gondwana Research. 26, 323–347. doi:10.1016/j.gr.2013.06.022

Parrish, R.R., 1990. U-Pb dating of monazite and its application to geological problems. Canadian Journal of Earth Sciences 27, 1431–1450. https://doi.org/10.1139/e90-152

Passchier, C.W., Trouw, R.A.J., 2005. Microtectonics, 2nd ed. Berlin:Springer Verlag.

Peternel, R., Allard, R., Trouw, J., Da, R., Schmitt, S., Xavier, F., 2005. Interferência entre duas faixas móveis Neoproterozóicas: O caso das faixas Brasília e Ribeira no sudeste do Brasil. Revista Brasileira de Geociências, 35(3), 297–310.

Phillips, E.R., Ransom, D.M., Vernon, R.H., 1972. Myrmekite and muscovite developed by retrograde metamorphism at Broken Hill, New South Wales. Mineralogical Magazine 38, 570–578.

Piccolo, A., Faccenda, M., Carosi, R., Montomoli, C., Visonà, D., 2018. Crustal strength control on structures and metamorphism in collisional orogens. Tectonophysics 746, 470–492. https://doi.org/10.1016/J.TECTO.2017.09.018

Powell, R., Holland, T., 2008. On thermobarometry. Journal of Metamorphic Geology 26, 155–179. https://doi.org/10.1111/j.1525-1314.2007.00756.x

Pyle, J. M., Spear, F. S., 2003. Four generations of accessory-phase growth in low-pressure migmatites from SW New Hampshire. American Mineralogist, 88(2–3), 338–351. https://doi.org/10.2138/am-2003-2-311

Ramsay, J.G., 1980. Shear zone geometry: A review. Journal of Structural Geology 2, 83–99. https://doi.org/10.1016/0191-8141(80)90038-3

Reno, B.L., Brown, M., Kobayashi, K., Nakamura, E., Piccoli, P.M., Trouw, R.A.J., 2009. Eclogite-high-pressure granulite metamorphism records early collision in West Gondwana: New data from the Southern Brasília Belt, Brazil. Journal of the Geological Society of London 166, 1013–1032. https://doi.org/10.1144/0016-76492008-140

Reno, B.L., Piccoli, P.M., Brown, M., Trouw, R.A.J., 2012. In situ monazite (U-Th)-Pb ages from the Southern Brasília Belt, Brazil: constraints on the high-temperature retrograde evolution of HP granulites. Journal of Metamorphic Geology 30, 81–112. https://doi.org/10.1111/j.1525-1314.2011.00957.x

Rey, P., Vanderhaeghe, O., Teyssier, C., 2001. Gravitational collapse of the continental crust: definition, regimes and modes. Tectonophysics 342, 435–449. https://doi.org/10.1016/S0040-1951(01)00174-3

Richards, J.P., 2015. Tectonic, magmatic, and metallogenic evolution of the Tethyan orogen: From subduction to collision. Ore Geology Reviews 70, 323–345. https://doi.org/10.1016/J.OREGEOREV.2014.11.009

Ring, U., Brandon, M.T., Willett, S.D., Lister, G.S., 1999. Exhumation processes. Geological Society, London, Special Publications 154, 1–27. https://doi.org/10.1144/GSL.SP.1999.154.01.01

Rivers, T., 2012. Upper-crustal orogenic lid and mid-crustal core complexes: Signature of a collapsed orogenic plateau in the hinterland of the Grenville Province. Canadian Journal of Earth Sciences, 49(1), 1–42. https://doi.org/10.1139/E11-014/ASSET/IMAGES/E11-014IEQ38.GIF

Robinson, D.M., DeCelles, P.G., Copeland, P., 2006. Tectonic evolution of the Himalayan thrust belt in western Nepal: Implications for channel flow models. Bulletin of the Geological Society of America 118, 865–885. https://doi.org/10.1130/B25911.1

Rocha, B. C., Moraes, R., Möller, A., Cioffi, C. R., 2018. Magmatic inheritance vs. UHT metamorphism: Zircon petrochronology of granulites and petrogenesis of charnockitic leucosomes of the Socorro–Guaxupé nappe, SE Brazil. Lithos, 314–315, 16–39. https://doi.org/10.1016/j.lithos.2018.05.014

Rocha, B. C., Moraes, R., Möller, A., Cioffi, C. R., Jercinovic, M. J., 2017. Timing of anatexis and melt crystallization in the Socorro–Guaxupé Nappe, SE Brazil: Insights from trace element composition of zircon, monazite and garnet coupled to U–Pb geochronology. Lithos, 277(March), 337–355. https://doi.org/10.1016/j.lithos.2016.05.020

Rodrigues, S.W. de O., Martins-Ferreira, M.A.C., Faleiros, F.M., Campos Neto, M. da C., Yogi, M.T.A.G., 2019. Deformation conditions and quartz c-axis fabric development along nappe boundaries: The Andrelândia Nappe System, Southern Brasília Orogen (Brazil). Tectonophysics 766, 283–301. https://doi.org/10.1016/J.TECTO.2019.06.014

Rosenberg, C.L., Handy, M.R., 2005. Experimental deformation of partially melted granite revisited: implications for the continental crust. Journal of Metamorphic Geology 23, 19–28. https://doi.org/10.1111/J.1525-1314.2005.00555.X

Rubatto, D., Chakraborty, S., Dasgupta, S., 2013. Timescales of crustal melting in the Higher Himalayan Crystallines (Sikkim, Eastern Himalaya) inferred from trace element-constrained monazite and zircon chronology. Contributions to Mineralogy and Petrology, 165(2), 349–372. https://doi.org/10.1007/s00410-012-0812-y

Rudnick, R. L., Fountain, D. M., 1995. Nature and composition of the continental crust: A lower crustal perspective. Reviews of Geophysics, 33(3), 267. https://doi.org/10.1029/95RG01302

Rudnick, R. L., Gao, S., 2003. Composition of the continental crust. In H. D. Holland, R. L. Rudnick, S. Gao, & K. K. Turekian (Eds.), The crust (Vol. 3, pp. 1–64).

Sachan, H.K., Kohn, M.J., Saxena, A., Corrie, S.L., 2010. The Malari leucogranite, Garhwal Himalaya, Northern India: Chemistry, age, and tectonic implications. Geological Society of America Bulletin 122, 1865–1876. https://doi.org/10.1130/B30153.1

Salazar Mora, C.A., Campos Neto, M. da C., Basei, M.A.S., 2014. Syn-collisional lower continental crust anatexis in the Neoproterozoic Socorro-Guaxupé Nappe System, southern Brasília Orogen, Brazil: Constraints from zircon U-Pb dating, Sr-Nd-Hf signatures and whole-rock geochemistry. Precambrian Research 255, 847–864. https://doi.org/10.1016/j.precamres.2014.10.017

Sandiford, M., McLaren, S., 2002. Tectonic feedback and the ordering of heat producing elements within the continental lithosphere. Earth and Planetary Science Letters 204, 133–150. https://doi.org/10.1016/S0012-821X(02)00958-5

Santos, L.P., da Costa Campos Neto, M., Grohmann, C.H., 2004. Metamorphic path constrained by metapelitic rocks from the inner Aiuruoca-Andrelândia nappe, south of the São Francisco craton, SE Brazil. Journal of South American Earth Sciences 16, 725–741. https://doi.org/10.1016/j.jsames.2003.12.006

Searle, M.P., Law, R.D., Godin, L., Larson, K.P., Streule, M.J., Cottle, J.M., Jessup, M.J., 2008. Defining the Himalayan Main Central Thrust in Nepal. Journal of Geological Society of London 165, 523–534. https://doi.org/10.1144/0016-76492007-081

Searle, M.P., Simpson, R.L., Law, R.D., Parrish, R.R., Waters, D.J., 2003. The structural geometry, metamorphic and magmatic evolution of the Everest massif, High Himalaya of Nepal-South Tibet. Journal of Geological Society of London 160, 345–366. https://doi.org/10.1144/0016-764902-126

Searle, M.P., Windley, B.F., Coward, M.P., Cooper, D.J.W., Rex, A.J., Rex, D., Tingdong, L., Xuchang, X., Jan, M.Q., Thakur, V.C., Kumar, S., 1987. The closing of Tethys and the tectonics of the Himalaya. Geological Society of America Bulletin 98, 678–701.

Sen, K., Chaudhury, R., Pfänder, J., 2015. 40Ar-39Ar age constraint on deformation and brittle-ductile transition of the Main Central Thrust and the South Tibetan Detachment zone from Dhauliganga valley, Garhwal Himalaya, India. Journal of Geodynamics 88, 1–13. https://doi.org/10.1016/j.jog.2015.04.004

Simonetti, M., Carosi, R., Montomoli, C., Corsini, M., Petroccia, A., Cottle, J.M., Iaccarino, S., 2020b. Timing and kinematics of flow in a transpressive dextral shear zone, Maures Massif (Southern France). International Journal of Earth Sciences 109, 2261–2285. https://doi.org/10.1007/s00531-020-01898-6

Simonetti, M., Carosi, R., Montomoli, C., Cottle, J.M., Law, R.D., 2020a. Transpressive Deformation in the Southern European Variscan Belt: New Insights From the Aiguilles Rouges Massif (Western Alps). Tectonics 39. https://doi.org/10.1029/2020TC006153

Sizova, E., Gerya, T., Brown, M., 2014. Contrasting styles of Phanerozoic and Precambrian continental collision. Gondwana Research 25, 522–545. https://doi.org/10.1016/J.GR.2012.12.011

Spear, F. S., 1988. Metamorphic fractional crystallization and internal metasomatism by diffusional homogenization of zoned garnets. Contributions to Mineralogy and Petrology , 99(4), 507–517. https://doi.org/10.1007/BF00371941

Spear, F. S., Florence, F. P., 1992. Thermobarometry in granulites: pitfalls and new approaches. Precambrian Research, 55(1–4), 209–241. https://doi.org/10.1016/0301-9268(92)90025-J

Spear, F. S., Kohn, M. J., & Cheney, J. T., 1999. P-T paths from anatectic pelites. Contributions to Mineralogy and Petrology 1999 134:1, 134(1), 17–32. https://doi.org/10.1007/S004100050466

Spear, F. S., Pyle, J. M., 2002. Apatite, monazite, and xenotime in metamorphic rocks. Reviews in Mineralogy and Geochemistry, 48, 293–335. https://doi.org/10.2138/rmg.2002.48.7

Spear, F. S., Pyle, J. M., 2010. Theoretical modeling of monazite growth in a low-Ca metapelite. Chemical Geology, 273(1–2), 111–119. https://doi.org/10.1016/j.chemgeo.2010.02.016

Spear, F., 1995. Metamorphic Phase Equilibria and Pressure-Temperature-Time Paths, Second. ed. Mineralogical Society of America.

Spear, F.S., 2010. Monazite-allanite phase relations in metapelites. Chemical Geology 279, 55–62. https://doi.org/10.1016/j.chemgeo.2010.10.004

Spencer, C.J., Harris, R.A., Dorais, M.J., 2012a. Depositional provenance of the Himalayan metamorphic core of Garhwal region, India: Constrained by U-Pb and Hf isotopes in zircons. Gondwana Research 22, 26–35. https://doi.org/10.1016/j.gr.2011.10.004

Spencer, C.J., Harris, R.A., Dorais, M.J., 2012b. The metamorphism and exhumation of the Himalayan metamorphic core, eastern Garhwal region, India. Tectonics 31, 1–18. https://doi.org/10.1029/2010TC002853

Squire, R.J., Campbell, I.H., Allen, C.M., Wilson, C.J.L., 2006. Did the Transgondwanan Supermountain trigger the explosive radiation of animals on Earth? Earth and Planetary Science Letters 250, 116–133. https://doi.org/10.1016/J.EPSL.2006.07.032

Stepanov, A. S., Hermann, J., Rubatto, D., Rapp, R. P., 2012. Experimental study of monazite/melt partitioning with implications for the REE, Th and U geochemistry of crustal rocks. Chemical Geology, 300–301, 200–220. https://doi.org/10.1016/J.CHEMGEO.2012.01.007

Stipp, M., Stünitz, H., Heilbronner, R., Schmid, S.M., 2002a. The eastern Tonale fault zone: A "natural laboratory" for crystal plastic deformation of quartz over a temperature range from 250 to 700 °C. Journal of Structural Geology 24, 1861–1884. https://doi.org/10.1016/S0191-8141(02)00035-4

Štípská, P., & Powell, R. (2005). Constraining the P–T path of a MORB-type eclogite using pseudosections, garnet zoning and garnet-clinopyroxene thermometry: an example from the Bohemian Massif. Journal of Metamorphic Geology, 23(8), 725–743. https://doi.org/10.1111/J.1525-1314.2005.00607.X

St-Onge, M.R., Rayner, N., Palin, R.M., Searle, M.P., Waters, D.J., 2013. Integrated pressure-temperature-time constraints for the Tso Morari dome (Northwest India): Implications for the burial and exhumation path of UHP units in the western Himalaya. Journal of Metamorphic Geology 31, 469–504. https://doi.org/10.1111/jmg.12030

Taylor, R. J. M., Kirkland, C. L., Clark, C., 2016. Accessories after the facts: Constraining the timing, duration and conditions of high-temperature metamorphic processes. Lithos, 264, 239–257. https://doi.org/10.1016/J.LITHOS.2016.09.004

Tedeschi, M., Lanari, P., Rubatto, D., Pedrosa-Soares, A., Hermann, J., Dussin, I., Pinheiro, M.A.P., Bouvier, A.S., Baumgartner, L., 2017. Reconstruction of multiple P-T-t stages from retrogressed mafic rocks: Subduction versus collision in the Southern Brasília orogen (SE Brazil). Lithos 294–295, 283–303. https://doi.org/10.1016/j.lithos.2017.09.025

Tedeschi, M., Pedrosa-Soares, A., Dussin, I., Lanari, P., Novo, T., Pinheiro, M.A.P., Lana, C., Peters, D., 2018. Protracted zircon geochronological record of UHT garnet-free granulites in the Southern Brasília orogen (SE Brazil): Petrochronological constraints on magmatism and metamorphism. Precambrian Research 316, 103–126. https://doi.org/10.1016/j.precamres.2018.07.023

Thakur, S.S., Madhavan, K., Patel, S.C., Rameshwar Rao, D., Singh, A.K., Pandey, S., Nandini, P., 2018. Yttrium-zoning in garnet and stability of allanite in metapelites from the Main Central Thrust Zone and adjacent higher Himalayan crystallines along the Alaknanda Valley, NW Himalaya. Lithos 320, 1–19. https://doi.org/10.1016/j.lithos.2018.09.002

Thakur, S.S., Patel, S.C., Singh, A.K., 2015. A P–T pseudosection modelling approach to understand metamorphic evolution of the Main Central Thrust Zone in the Alaknanda valley, NW Himalaya. Contributions to Mineralogy and Petrology 170, 1–26. https://doi.org/10.1007/s00410-015-1159-y

Thomas, J. B., Watson, E. B., Spear, F. S., Shemella, P. T., Nayak, S. K., Lanzirotti, A., 2010. TitaniQ under pressure: The effect of pressure and temperature on the solubility of Ti in quartz. Contributions to Mineralogy and Petrology, 160(5), 743–759. https://doi.org/10.1007/S00410-010-0505-3/FIGURES/9

Tommasi, A., Vauchez, A., Femandes, L.A.D., Porcher, C.C., 1994. Magma-assisted strain localization in an orogen-parallel transcurrent shear zone of southern Brazil. Tectonics 13, 421–437. https://doi.org/10.1029/93TC03319

Trouw, R. A. J., Peternel, R., Ribeiro, A., Heilbron, M., Vinagre, R., Duffles, P., Trouw, C. C., Fontainha, M., Kussama, H. H., 2013. A new interpretation for the interference zone between the southern Brasília belt and the central Ribeira belt, SE Brazil. Journal of South American Earth Sciences, 48, 43–57. https://doi.org/10.1016/j.jsames.2013.07.012

Trouw, R.A.J., Heilbron, M., Ribeiro, A., Paciullo, F., Valeriano, C.M., Almeida, J.C.H., Tupinambá, M., Andreis, R.R., 2000. The central segment of the Ribeira Belt, in: Tectonic Evolution of South America. pp. 287–310.

Turlin, F., Deruy, C., Eglinger, A., Vanderhaeghe, O., André-Mayer, A.-S., Poujol, M., Moukhsil, A., Solgadi, F., 2018. A 70 Ma record of suprasolidus conditions in the large, hot, long-duration Grenville Orogen. Terra Nova 30, 233–243. https://doi.org/10.1111/ter.12330

Valeriano, C. de M., 2017. The Southern Brasília Belt in: São Francisco Craton, Eastern Brazil. Springer, Cham, pp. 189–203. https://doi.org/10.1007/978-3-319-01715-0_10

Valeriano, C.M., Machado, N., Simonetti, A., Valladares, C.S., Seer, H.J., Simões, L.S.A., 2004. U-Pb geochronology of the southern Brasília belt (SE-Brazil): Sedimentary provenance, Neoproterozoic orogeny and assembly of West Gondwana. Precambrian Research 130, 27–55. https://doi.org/10.1016/j.precamres.2003.10.014

Valladares, C.S., Machado, N., Heilbron, M., Gauthier, G., 2004. Ages of detrital zircon from siliciclastic successions south of the São Francisco Craton, Brazil: Implications for the evolution of Proterozoic basins. Gondwana Research 7, 913–921. https://doi.org/10.1016/s1342-937x(05)71074-1

van Achterbergh, E., Ryan, C.G., Jackson, S.E., Griffin, W., 2001. Data reduction software for LA-ICP-MS. In: P.Sylvester, I. (Ed.), Laser Ablation-ICPMS in the Earth Science:Principles and Applications. Mineralogical Association of Canada , 239–243.

Vanderhaeghe, O., 2009. Migmatites, granites and orogeny: Flow modes of partially-molten rocks and magmas associated with melt/solid segregation in orogenic belts. Tectonophysics 477, 119–134. https://doi.org/10.1016/J.TECTO.2009.06.021

Vanderhaeghe, O., 2012. The thermal-mechanical evolution of crustal orogenic belts at convergent plate boundaries: A reappraisal of the orogenic cycle. Journal of Geodynamics 56–57, 124–145. https://doi.org/10.1016/j.jog.2011.10.004

Vanderhaeghe, O., Medvedev, S., Fullsack, P., Beaumont, C., Jamieson, R. A., 2003. Evolution of orogenic wedges and continental plateaux: insights from crustal thermal–mechanical models overlying subducting mantle lithosphere. Geophysical Journal International, 153(1), 27–51. https://doi.org/10.1046/J.1365-246X.2003.01861.X

Vanderhaeghe, O., Teyssier, C., 2001. Partial melting and flow of orogens. Tectonophysics 342, 451–472. https://doi.org/10.1016/S0040-1951(01)00175-5

Vannay, J.C., Hodges, K. v., 1996. Tectonometamorphic evolution of the Himalayan metamorphic core between the Annapurna and Dhaulagiri, central Nepal. Journal of Metamorphic Geology 14, 635–656. https://doi.org/10.1046/j.1525-1314.1996.00426.x

Vauchez, A., Tommasi, A., Mainprice, D., 2012. Faults (shear zones) in the Earth's mantle. Tectonophysics 558–559, 1–27. https://doi.org/10.1016/j.tecto.2012.06.006

Vermeesch, P., 2018. IsoplotR: A free and open toolbox for geochronology. Geoscience Frontiers 9, 1479–1493. https://doi.org/10.1016/j.gsf.2018.04.001

Vernon, R. H., 2011. Microstructures of melt-bearing regional metamorphic rocks. Geological Society of America Memoirs, 207, 1–11.

Vielzeuf, D., Clemens, J. D., Pin, C., Moinet, E., 1990. Granites, Granulites, and Crustal Differentiation. In Granulites and crustal evolution (pp. 59–85). Springer, Dordrecht. https://doi.org/10.1007/978-94-009-2055-2_5

Visonà, D., Carosi, R., Montomoli, C., Tiepolo, M., Peruzzo, L., 2012. Miocene andalusite leucogranite in central-east Himalaya (Everest-Masang Kang area): Low-pressure melting during heating. Lithos 144–145, 194–208. https://doi.org/10.1016/j.lithos.2012.04.012

Visonà, D., Lombardo, B., 2002. Two-mica and tourmaline leucogranites from the Everest-Makalu region (Nepal - Tibet). Himalayan leucogranite genesis by isobaric heating? Lithos 62, 125–150. https://doi.org/10.1016/S0024-4937(02)00112-3

Wang, J.M., Lanari, P., Wu, F.Y., Zhang, J.J., Khanal, G.P., Yang, L., 2021. First evidence of eclogites overprinted by ultrahigh temperature metamorphism in Everest East, Himalaya: Implications for collisional tectonics on early Earth. Earth and Planetary Science Letters 558, 116760. https://doi.org/10.1016/J.EPSL.2021.116760

Wang, J.M., Rubatto, D., Zhang, J.J., 2015. Timing of partial melting and cooling across the Greater Himalayan Crystalline Complex (Nyalam, central Himalaya): In-sequence thrusting and its implications. Journal of Petrology 56, 1677–1702. https://doi.org/10.1093/petrology/egv050

Warren, C.J., 2013. Exhumation of (ultra-)high-pressure terranes: Concepts and mechanisms. Solid Earth 4, 75–92. https://doi.org/10.5194/se-4-75-2013

Warren, C.J., Grujic, D., Kellett, D.A., Cottle, J., Jamieson, R.A., Ghalley, K.S., 2011. Probing the depths of the India-Asia collision: U-Th-Pb monazite chronology of granulites from NW Bhutan. Tectonics 30. https://doi.org/10.1029/2010TC002738

Waters, D.J., 2019. Metamorphic constraints on the tectonic evolution of the high Himalaya in Nepal: The art of the possible. Geological Society of London Special Publication 483, 325–375. https://doi.org/10.1144/SP483-2018-187

Watt, G. R., Harley, S. L., 1993. Accessory phase controls on the geochemistry of crustal melts and restites produced during water-undersaturated partial melting. Contributions to Mineralogy and Petrology 1993 114:4, 114(4), 550–566. https://doi.org/10.1007/BF00321759

Weinberg, R.F., 2016. Himalayan leucogranites and migmatites: nature, timing and duration of anatexis. Journal of Metamorphic Geology 34, 821–843. https://doi.org/10.1111/jmg.12204

Weinberg, R.F., Podladchikov, Y., 1994. Diapiric ascent of magmas through power law crust and mantle. Journal of Geophysical Research: Solid Earth 99, 9543–9559. https://doi.org/10.1029/93JB03461

Weinberg, R.F., Schmeling, H., 1992. Polydiapirs: multiwavelength gravity structures. Journal of Structural Geology 14, 425–436. https://doi.org/10.1016/0191-8141(92)90103-4

Weller, O. M., Jackson, S., Miller, W. G. R., St-Onge, M. R., Rayner, N., 2020. Quantitative elemental mapping of granulite-facies monazite: Textural insights and implications for petrochronology. Journal of Metamorphic Geology, 38(8), 853–880. https://doi.org/10.1111/JMG.12552

Wernicke, B., 1981. Low-angle normal faults in the Basin and Range Province: nappe tectonics in an extending orogen. Nature 291, 645–648.

Westin, A., Campos Neto, M. C., Hollanda, M. H. B. M., Salazar-Mora, C. A., Queiroga, G. N., Frugis, G. L., de Castro, M. P., 2021. The fast exhumation pattern of a Neoproterozoic nappe system built during West Gondwana amalgamation: Insights from thermochronology. Precambrian Research, 355, 106115. https://doi.org/10.1016/j.precamres.2021.106115

Westin, A., Campos Neto, M.C., Cawood, P.A., Hawkesworth, C.J., Dhuime, B., Delavault, H., 2019. The Neoproterozoic southern passive margin of the São Francisco craton: Insights on the pre-amalgamation of West Gondwana from U-Pb and Hf-Nd isotopes. Precambrian Research 320, 454–471. https://doi.org/10.1016/j.precamres.2018.11.018

Westin, A., Campos Neto, M.C., Hawkesworth, C.J., Cawood, P.A., Dhuime, B., Delavault, H., 2016. A paleoproterozoic intra-arc basin associated with a juvenile source in the Southern Brasilia Orogen: Application of U-Pb and Hf-Nd isotopic analyses to provenance studies of complex areas. Precambrian Research 276, 178–193. https://doi.org/10.1016/j.precamres.2016.02.004

Westin, A., Campos Neto, M.da C., 2013. Provenance and tectonic setting of the external nappe of the Southern Brasília Orogen. Journal of South American Earth Sciences 48, 220–239. https://doi.org/10.1016/j.jsames.2013.08.006

White, R. W., Pomroy, N. E., Powell, R., 2005. An in situ metatexite–diatexite transition in upper amphibolite facies rocks from Broken Hill, Australia. Journal of Metamorphic Geology, 23(7), 579–602. https://doi.org/10.1111/J.1525-1314.2005.00597.X

White, R. W., Powell, R., Holland, T. J. B., 2007. Progress relating to calculation of partial melting equilibria for metapelites. Journal of Metamorphic Geology, 25(5), 511–527. https://doi.org/10.1111/J.1525-1314.2007.00711.X

White, R.W., Powell, R., Holland, T.J.B., Johnson, T.E., Green, E.C.R., 2014. New mineral activity-composition relations for thermodynamic calculations in metapelitic systems. Journal of Metamorphic Geology 32, 261–286. https://doi.org/10.1111/jmg.12071

Whitney, D. L., Evans, B. W., 2010. Abbreviations for names of rock-forming minerals. American Mineralogist, 95, 185–187. https://doi.org/10.2138/am.2010.3371

Williams, M. A., Kelsey, D. E., Rubatto, D., 2022. Thorium zoning in monazite: a case study from the Ivrea–Verbano Zone, NW Italy. Journal of Metamorphic Geology, 1–28. https://doi.org/10.1111/JMG.12656

Williams, M. L., Jercinovic, M. J., 2002. Microprobe monazite geochronology: Putting absolute time into microstructural analysis. Journal of Structural Geology, 24(6–7), 1013–1028. https://doi.org/10.1016/S0191-8141(01)00088-8

Williams, M. L., Jercinovic, M. J., 2012. Tectonic interpretation of metamorphic tectonites: Integrating compositional mapping, microstructural analysis and in situ monazite dating. Journal of Metamorphic Geology, 30(7), 739–752. https://doi.org/10.1111/j.1525-1314.2012.00995.x

Williams, M. L., Jercinovic, M. J., Goncalves, P., Mahan, K., 2006. Format and philosophy for collecting, compiling, and reporting microprobe monazite ages. Chemical Geology, 225(1–2), 1–15. https://doi.org/10.1016/j.chemgeo.2005.07.024

Williams, M. L., Jercinovic, M. J., Hetherington, C. J., 2007. Microprobe Monazite Geochronology: Understanding Geologic Processes by Integrating Composition and Chronology. Annual Review of Earth and Planetary Sciences, 35(1), 137–175. https://doi.org/10.1146/annurev.earth.35.031306.140228

Wilson, J.Tu., 1966. Did the Atlantic close and then re-open? Nature 676–681.

Wing, B.A., Ferry, J.M., Harrison, M., 2003. Prograde destruction and formation of monazite and allanite during contact and regional metamorphism of pelites: petrology and geochronology. Contributions to Mineralogy and Petrology 145, 228–250. https://doi.org/10.1007/s00410-003-0446-1

Wortel, M.J.R., Spakman, W., 2000. Subduction and Slab Detachment in the Mediterranean-Carpathian Region. Science (1979) 290, 1910–1917.

Yakymchuk, C., Brown, M., 2014. Behaviour of zircon and monazite during crustal melting. Journal of the Geological Society, 171(4), 465–479. https://doi.org/10.1144/JGS2013-115

Yakymchuk, C., Brown, M., 2019. Divergent behaviour of Th and U during anatexis: Implications for the thermal evolution of orogenic crust. Journal of Metamorphic Geology, 37(7), 899–916. https://doi.org/10.1111/JMG.12469

Yi, Z., Huang, B., Yang, L., Tang, X., Yan, Y., Qiao, Q., Zhao, J., Chen, L., 2015. A quasi-linear structure of the southern margin of Eurasia prior to the India-Asia collision: First paleomagnetic constraints from Upper Cretaceous volcanic rocks near the western syntaxis of Tibet. Tectonics 34, 1431–1451. https://doi.org/10.1002/2014TC003571

Zeiger, K., Gordon, S.M., Long, S.P., Kylander-Clark, A.R.C., Agustsson, K., Penfold, M., 2015. Timing and conditions of metamorphism and melt crystallization in Greater Himalayan rocks, eastern and central Bhutan: insight from U–Pb zircon and monazite geochronology and trace-element analyses. Contributions to Mineralogy and Petrology 169, 47. https://doi.org/10.1007/s00410-015-1143-6

Zhu, D.C., Wang, Q., Zhao, Z.D., Chung, S.L., Cawood, P.A., Niu, Y., Liu, S.A., Wu, F.Y., Mo, X.X., 2015. Magmatic record of India-Asia collision. Scientific Reports 5, 14289. https://doi.org/10.1038/srep14289

APPENDIX A

Supplementary material of Chapter 3

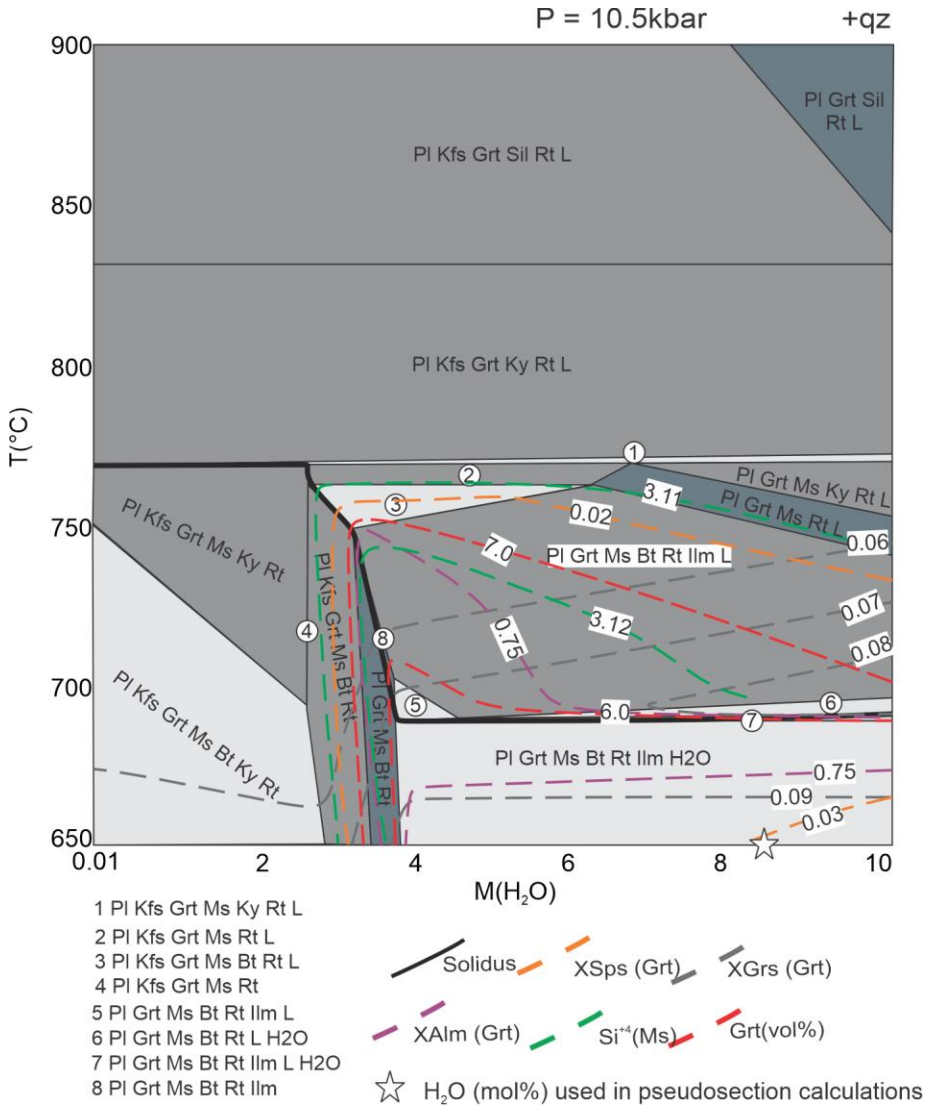

Figure A1- T- M(H_2O) pseudosection for the sample AK18-31 at 10.5 kbar contoured for XSps, XGrs, XAlm, Grt (vol%) and Si^{+4} (Ms). M=mol%.

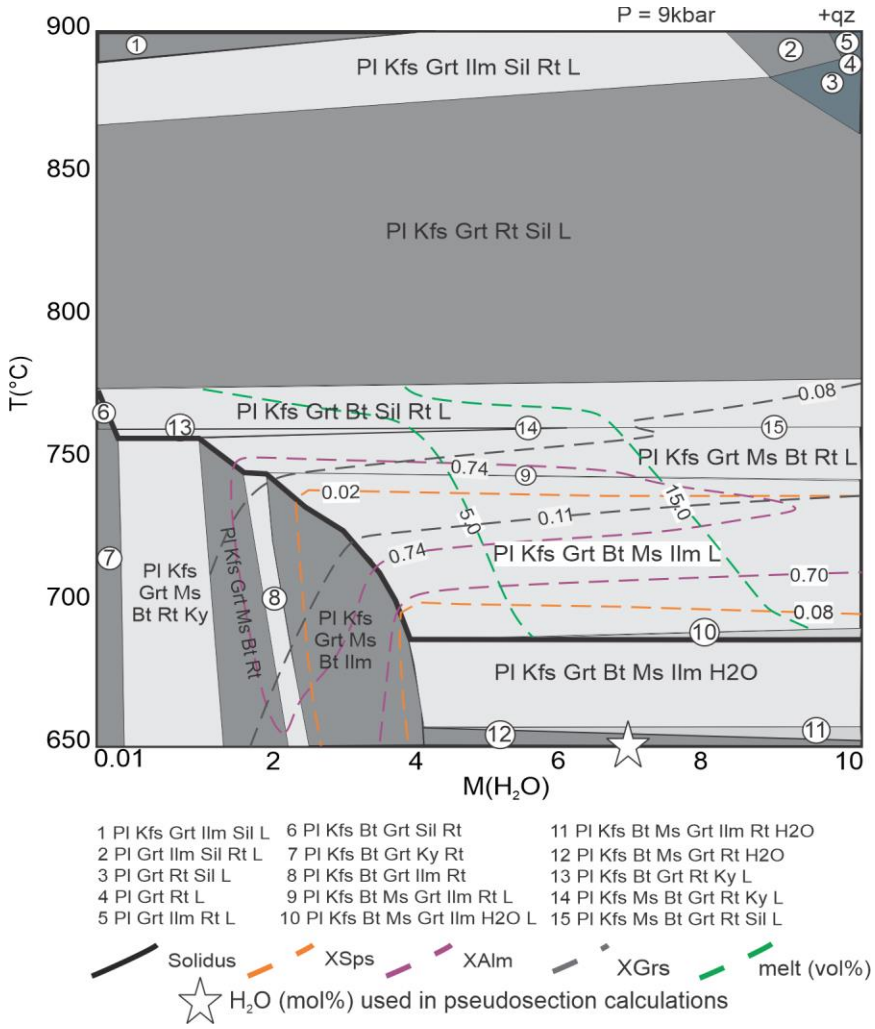

Figure A2- T- M(H2O) pseudosection for the sample AK18-48 at 9 kbar contoured for XSps, XGrs. XAlm and melt (vol%) . M=mol%.

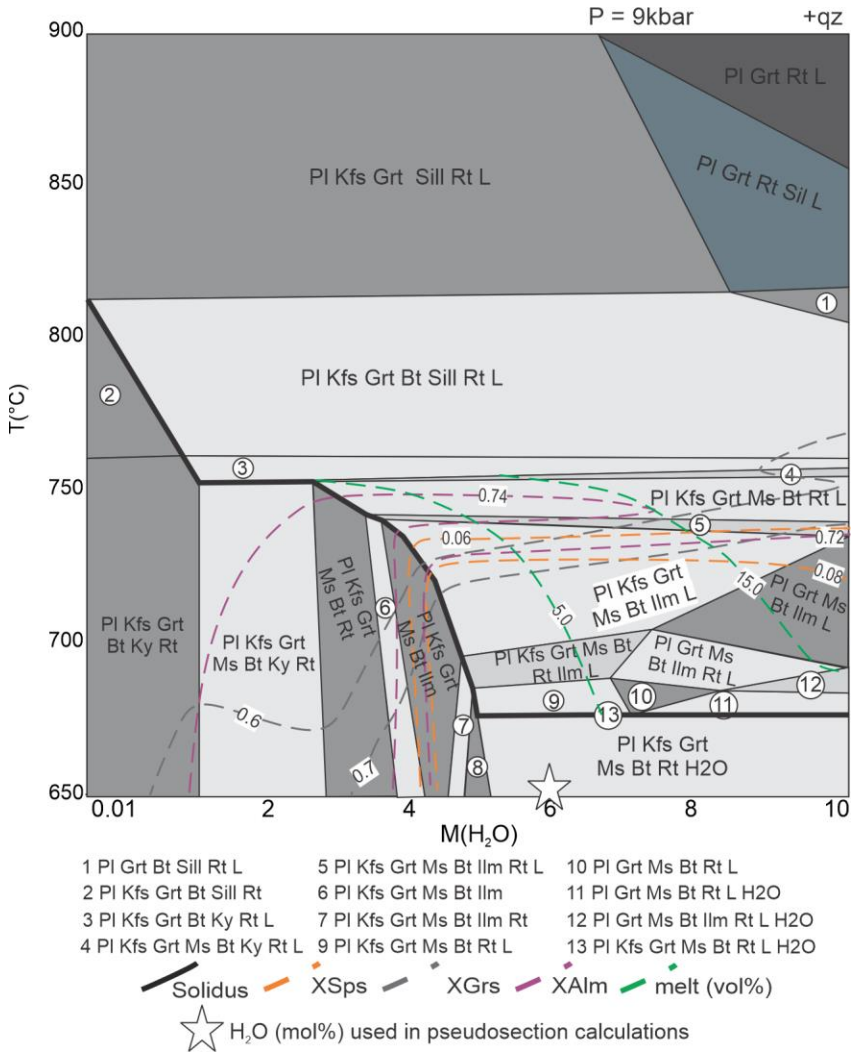

Figure A3- T- M(H2O) pseudosection for the sample AK18-53 at 9 kbar contoured for XSps, XGrs. XAlm and melt (vol%). M=mol%.

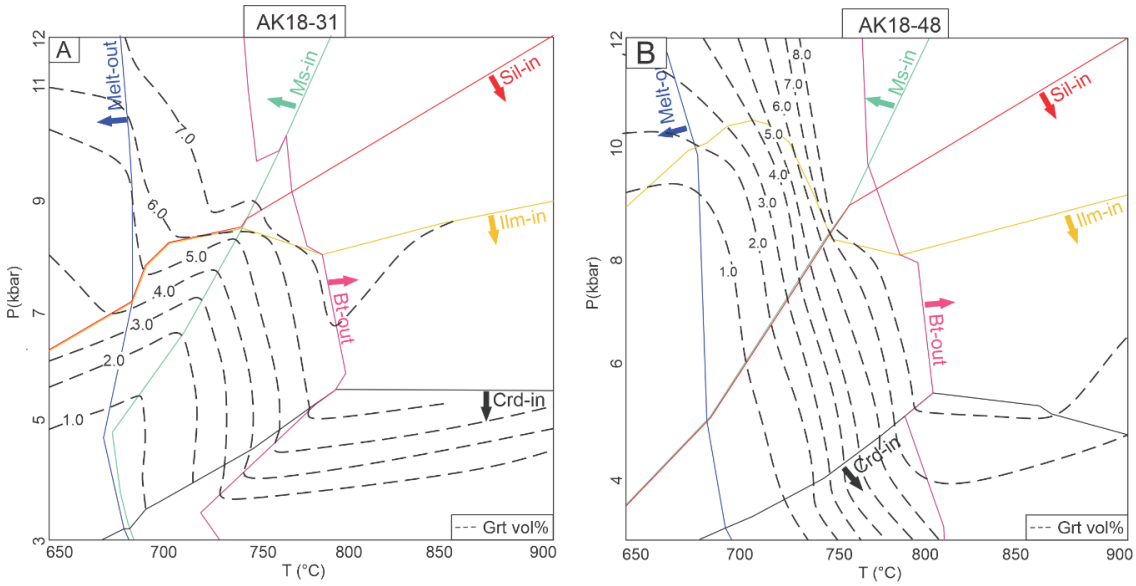

Figure A4- a) Main mineral stability curves of sample AK18-31 and contoured for vol% of garnet. b) Main mineral stability curves of sample AK18-48 and contoured for vol% of garnet.

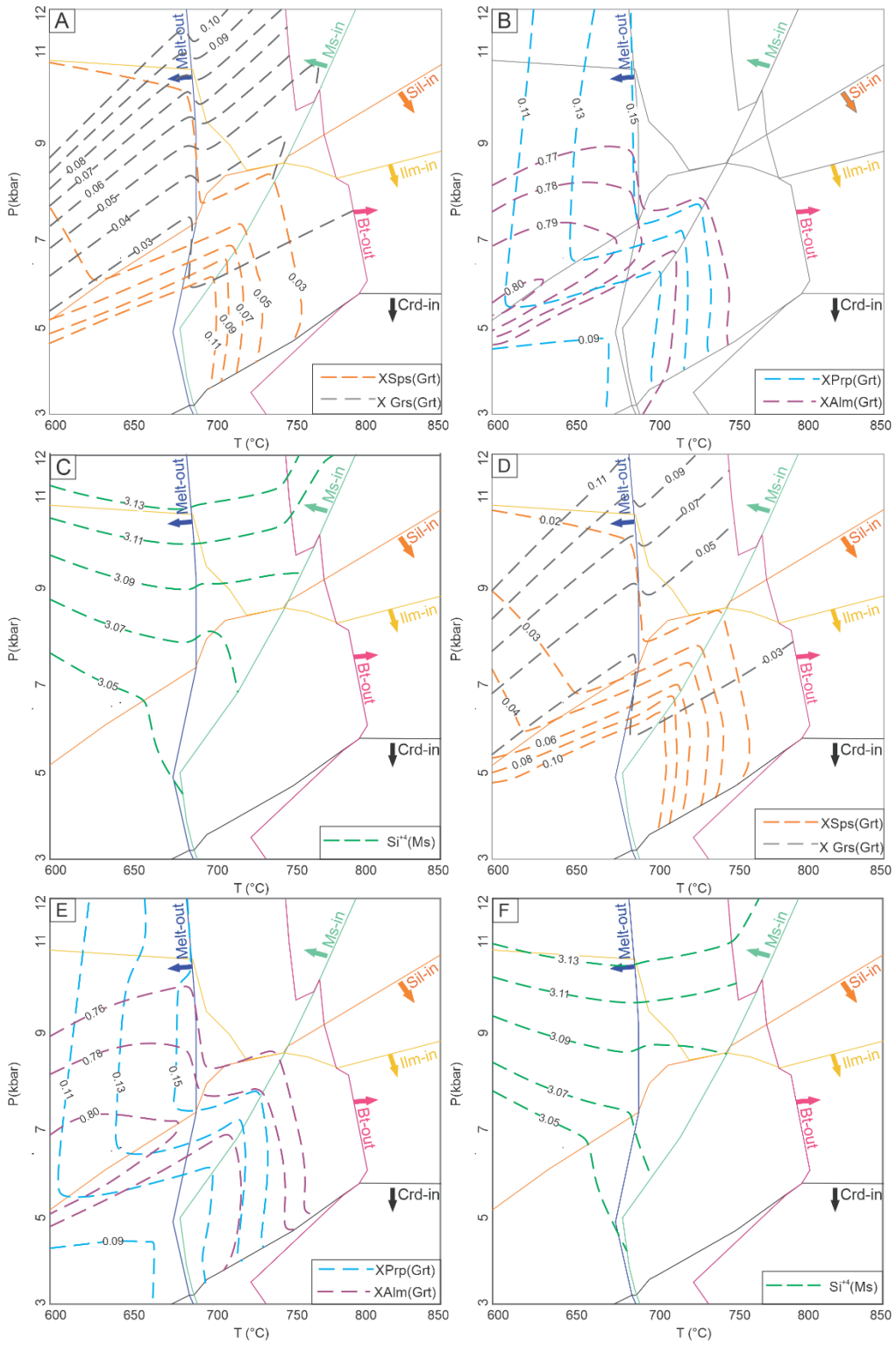

Figure A5- Main mineral stability curves of Figure 9, sample AK18-31 (XGrs, XSps, XAlm, XPrp and white mica (Si4+). A), B) and C) calculated with the bulk composition and D), E) and F) calculated after garnet core subtracted by the bulk composition.

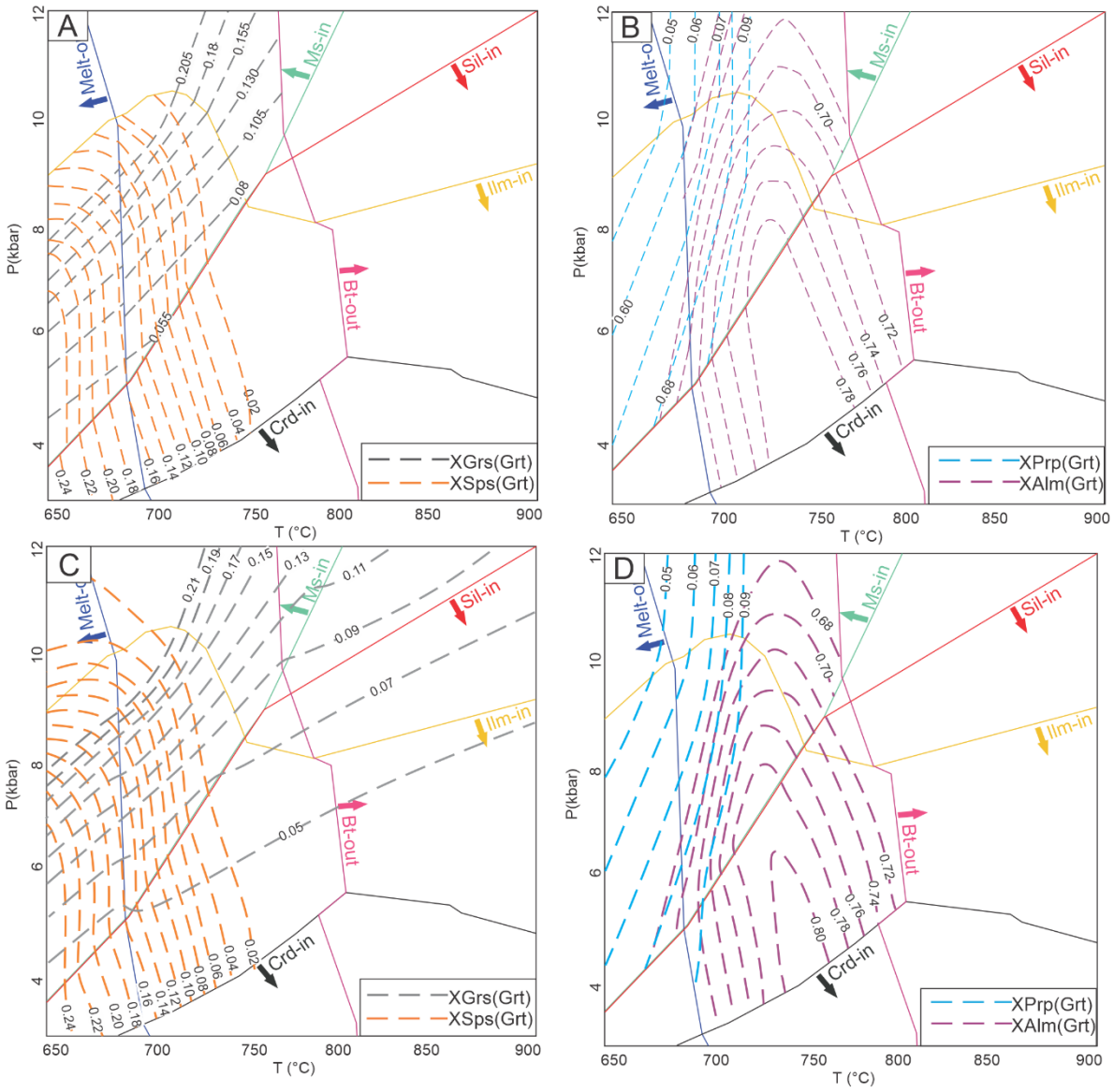

Figure A6- Main mineral stability curves of Figure 7, sample AK18-48, countered for compositional isopleths of garnet (XGrs, XSps, XAlm, XPrp). A) and B) calculated with the bulk composition and C) and D) calculated after garnet core subtracted by the bulk composition.

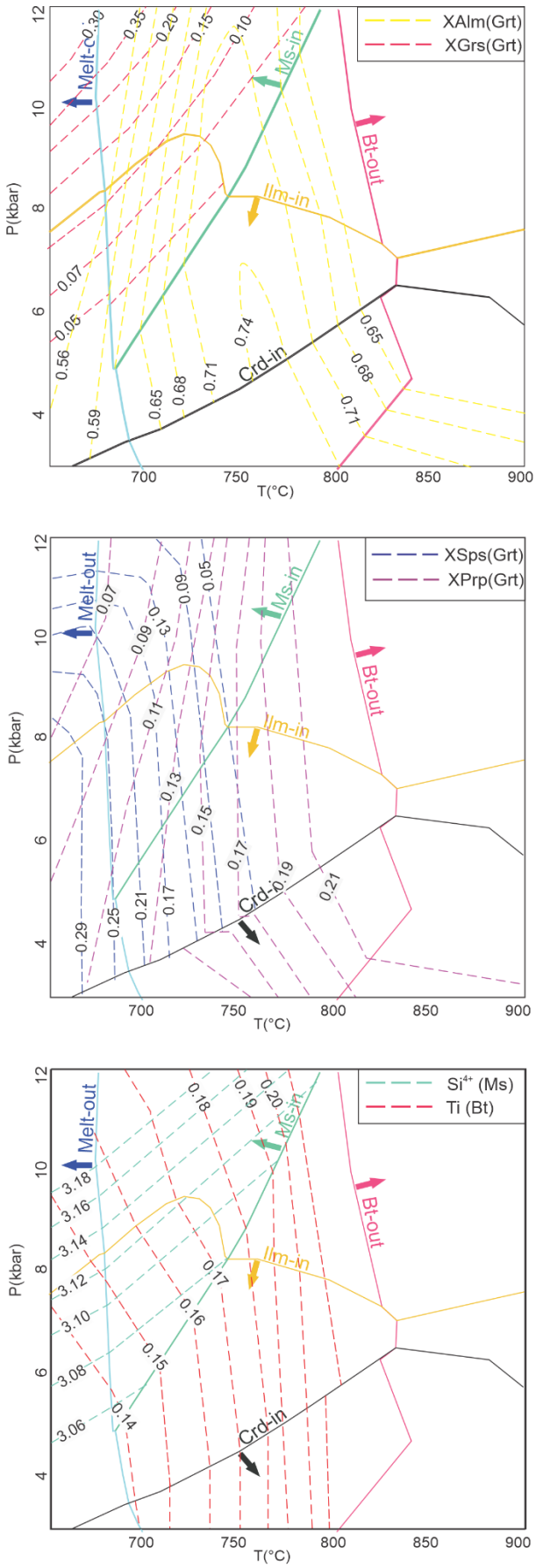

Figure A7- Main mineral stability curves of Figure 8, sample AK18-53, countered for compositional isopleths of garnet (XGrs, XSps, XAlm, XPrp), biotie (Ti) and white mica (Si^{4+}).

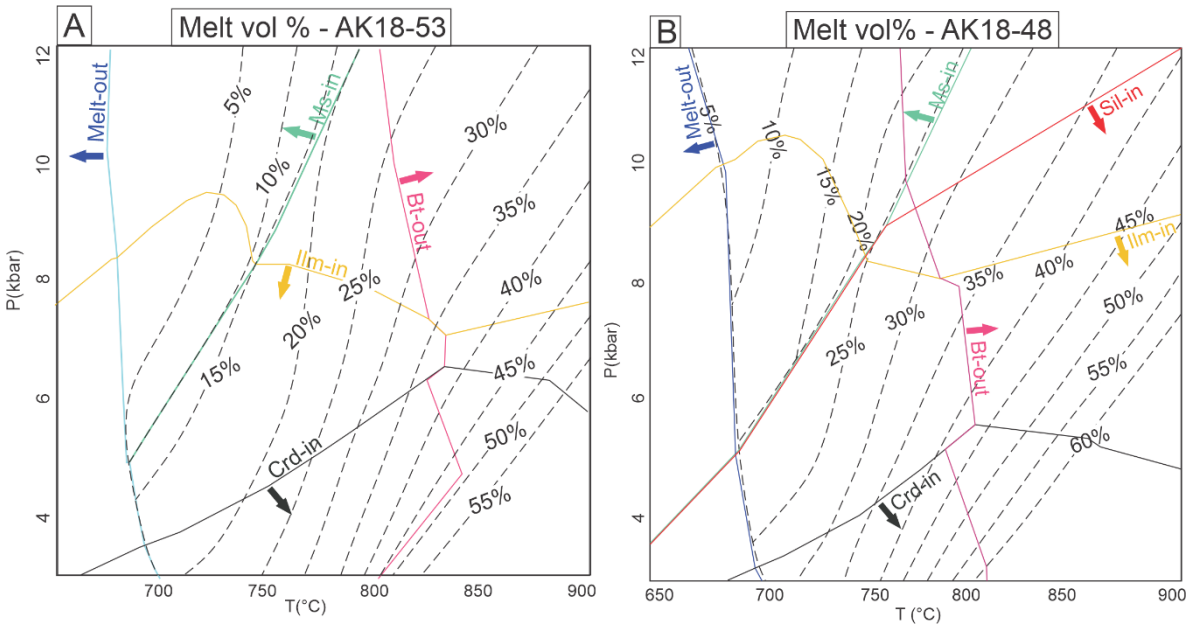

Figure A8 – a) Main mineral stability curves of sample AK18-53 and contoured for vol% of melt. b) Main mineral stability curves of sample AK18-48 and contoured for vol% of melt.

APPENDIX B

Supplementary material of Chapter 4

ANALYTICAL METHODS

The equipment employed in the trace elements, quantitative mineral analyses, and compositional maps is a JEOL JXA-8230 Electron Probe Micro Analyzer (EPMA) equipped with five wavelengths dispersive spectrometry (WDS) detectors hosted at the Department of Geology at the State of São Paulo University (UNESP). The compositional maps were obtained through X-rays maps, which were further classified and calibrated using the internal standardization procedure and the pseudo-background correction available in the XMapTools 3.4 (Lanari et al., 2019, 2014). The x-ray maps for Mg, Na, Ca, K, and Fe were acquired by the WDS detectors, whereas for Al, Si, P, S, Ti, Mn, and Zr by the energy dispersive-spectrometry (EDS). The x-ray maps were carried out with an accelerating voltage of 15Kv, a current beam of 100nA, and a dwell of 100 ms.

Monazite U-(Th)-Pb chemistry dating was performed using the same equipment cited above. The crystals were firstly identified through full thin-sections maps acquired using the Scanning Electron Microscopy and Mineral Liberation Analyzer (SEM-MLA). Considering the monazite structural position and textural relationships some crystals were selected to perform high-resolution compositional X-ray maps of Y, Al, Th, U, Pb, Si, Ca, Fe, La, and Ce. The acquisition conditions were 15 kV, 100 nA, 100 ms dwell time and 10 μm electron beam size and step. Trace elements spots analyses were performed in the different domains identified with helping of the X-ray maps. The moacyr monazite standard was used after each 10 to 20 punctual analyses, and their results are displayed in the supplementary figure file A7. The dates were plotted in the weighted average diagram using the Isoplot program (Ludwig, 2008). The full analytical procedure is described in detail by (Fumes et al., 2021).

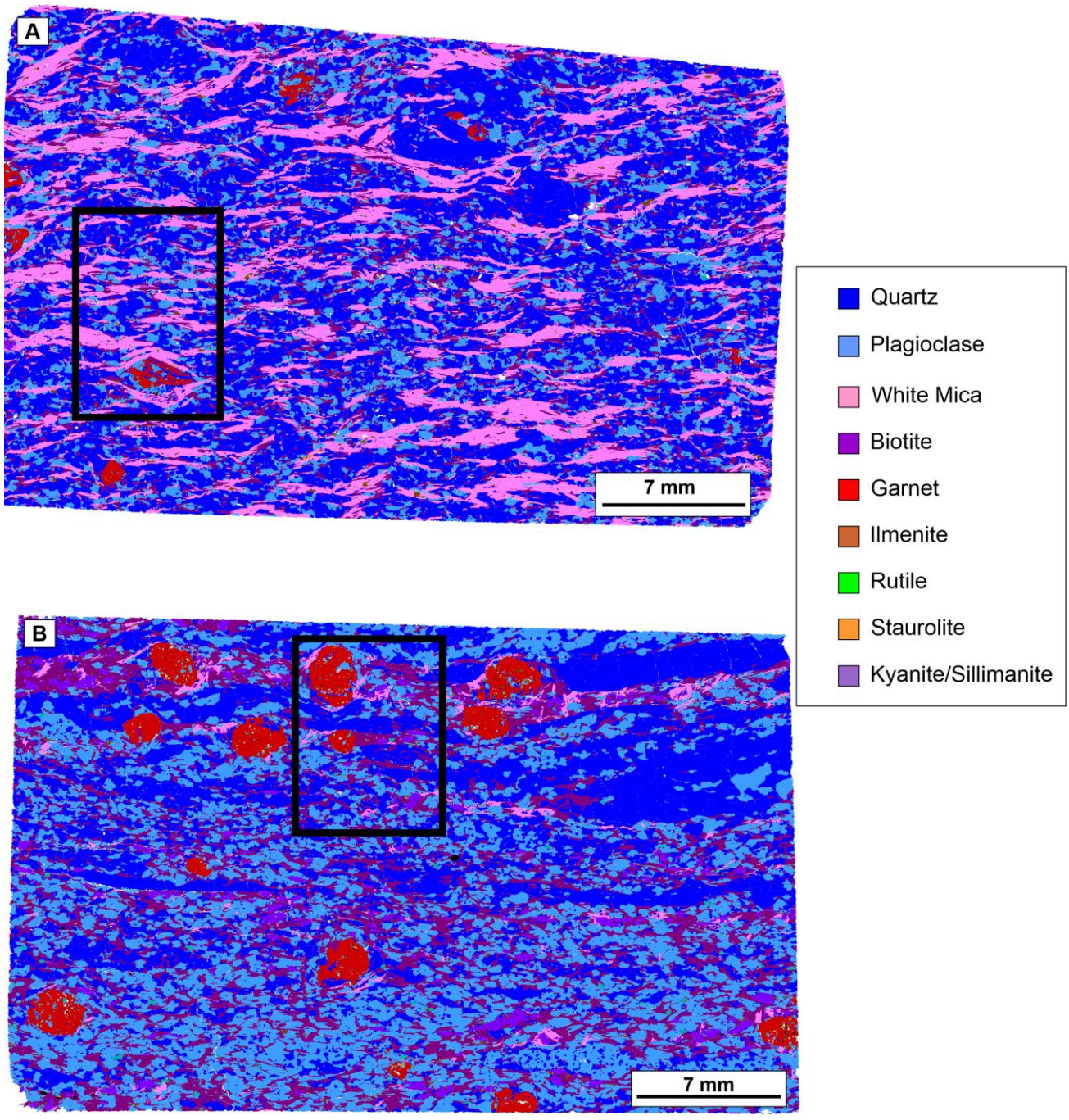

Figure B1 - Full thin-sections maps acquired using the Scanning Electron Microscopy and Mineral Liberation Analyzer (SEM-MLA). Black square represents the local bulk composition (LBC) investigated. a) Sample NESG-388 from Liberdade Nappe; b) Sample NESG-401 from Andrelândia Nappe.

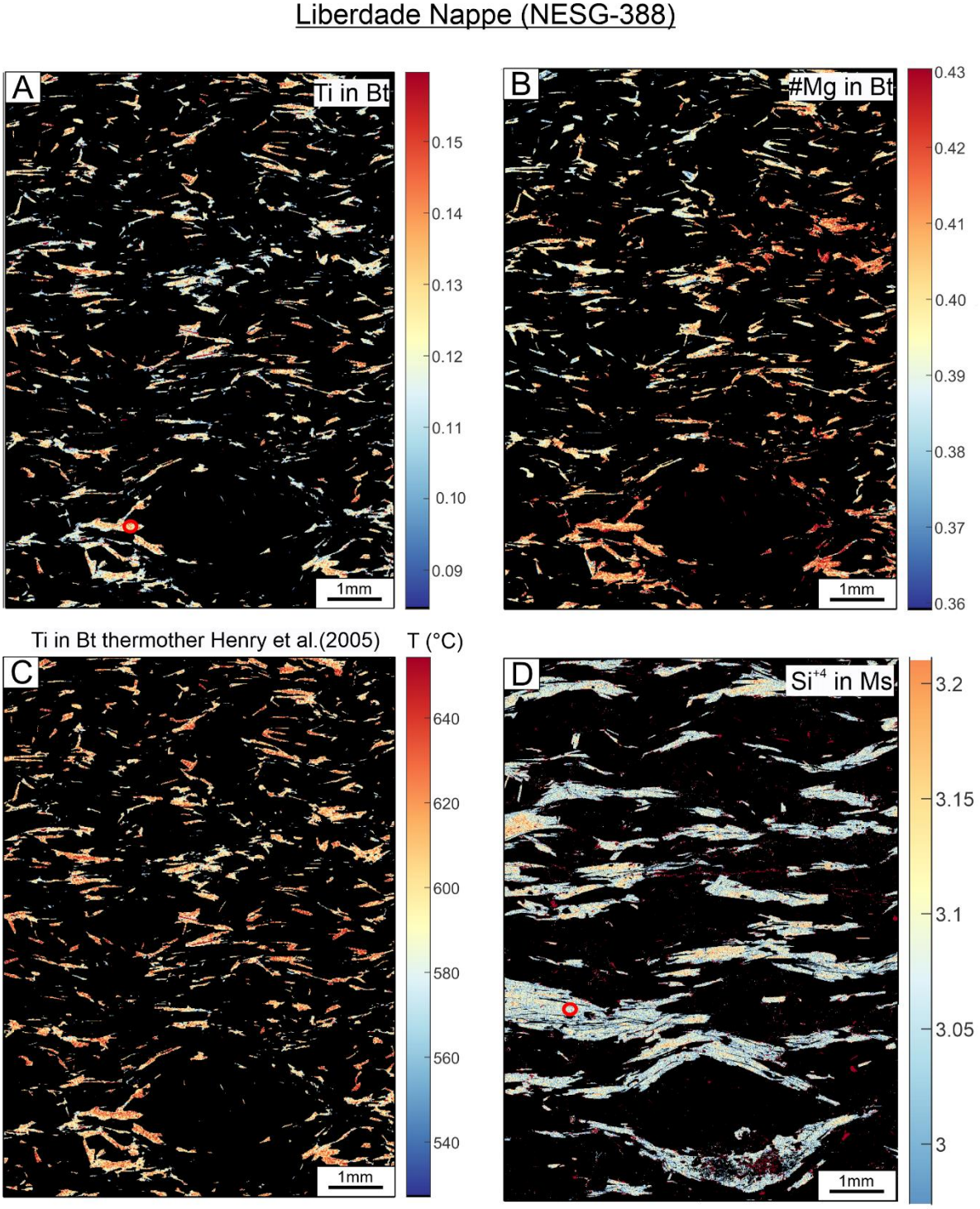

Figure B2 – Quantitative compositional maps for the sample NESG-388 from Liberdade Nappe. a) Map of Ti content in biotite (a.p.f.u); b) Map of #Mg in biotite; c) Map of Ti in biotite thermometer of Henry et al. (2005);d) Map of Si^{+4} content in white mica (a.p.f.u). Red circle indicate the area used to perform the Qcmp maps.

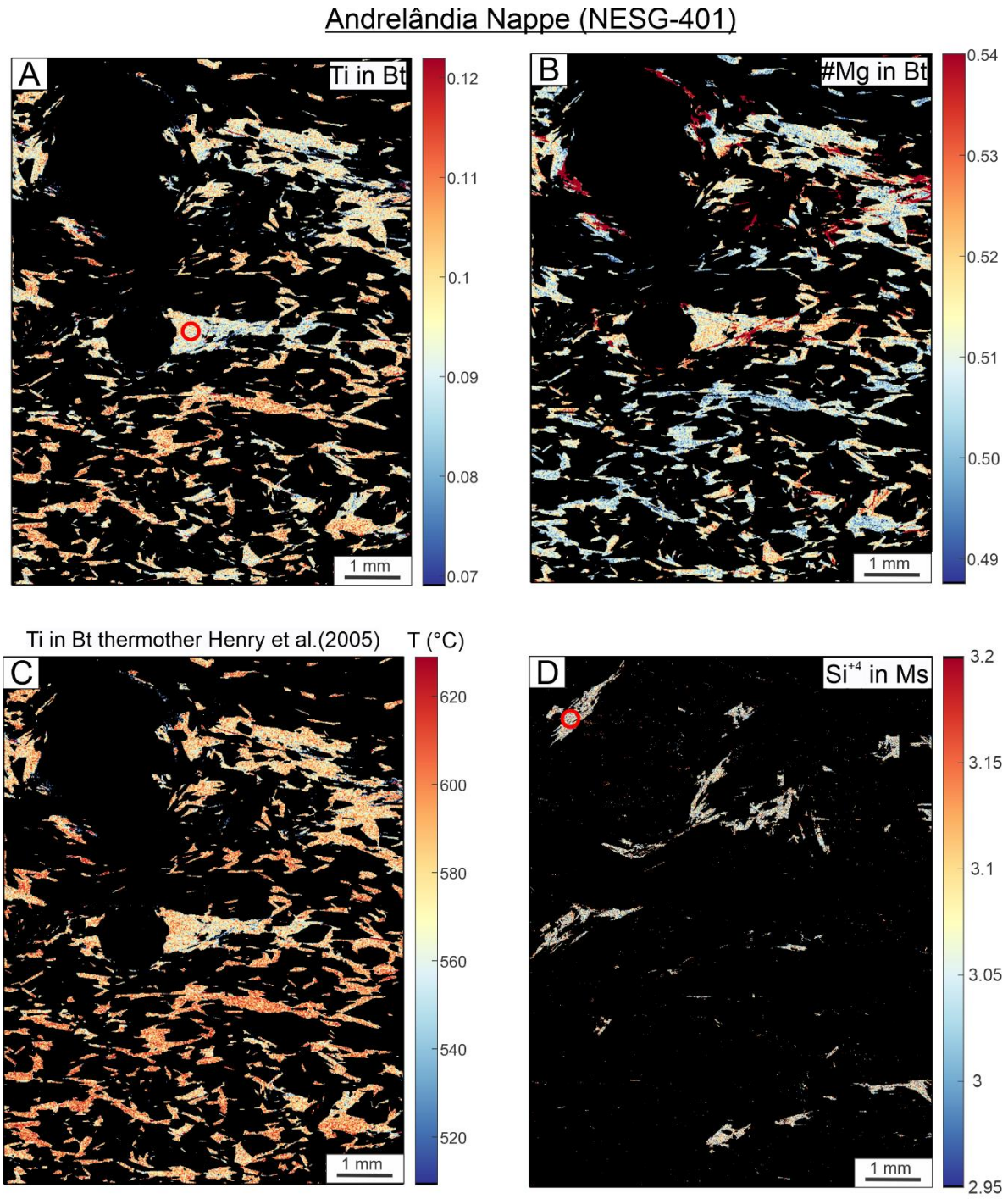

Figure B3 – Quantitative compositional maps for the sample NESG-401 from Andrelândia Nappe. a) Map of Ti content in biotite (a.p.f.u); b) Map of #Mg in biotite; c) Map of Ti in biotite thermometer of Henry et al. (2005). Red circle indicate the area used to perform the Qcmp maps.

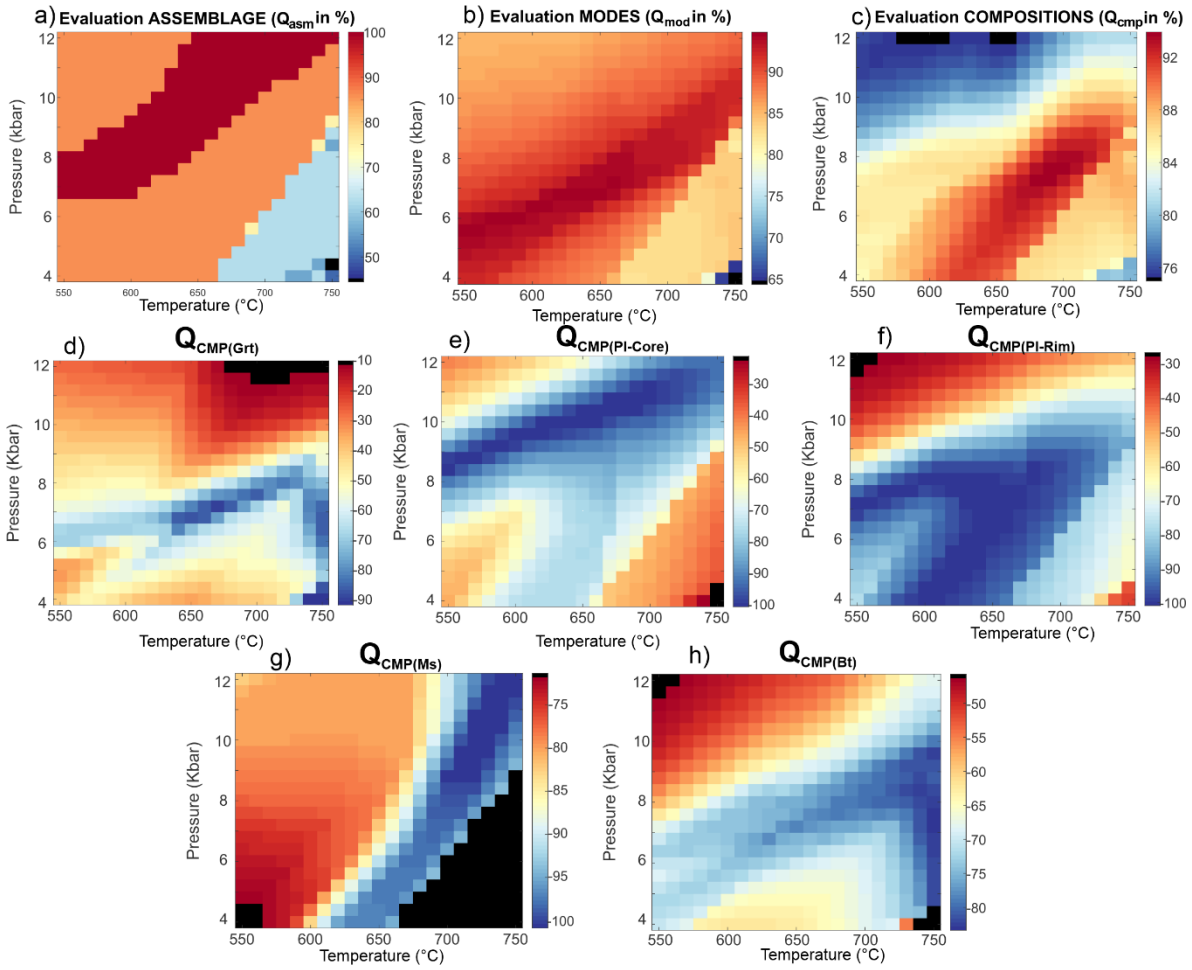

Figure B4- Maps of quality factors by Antidote for Liberdade Nappe. a) Q_{asm}; b)Q_{mod}; c) Q_{cmp} for the LBC bulk composition; d)Q_{cmp} for garnet composition; e) Q_{cmp} for plagioclase core composition; f) Q_{cmp} for plagioclase rim composition; g) Q_{cmp} for white mica composition; h) Q_{cmp} for biotite composition.

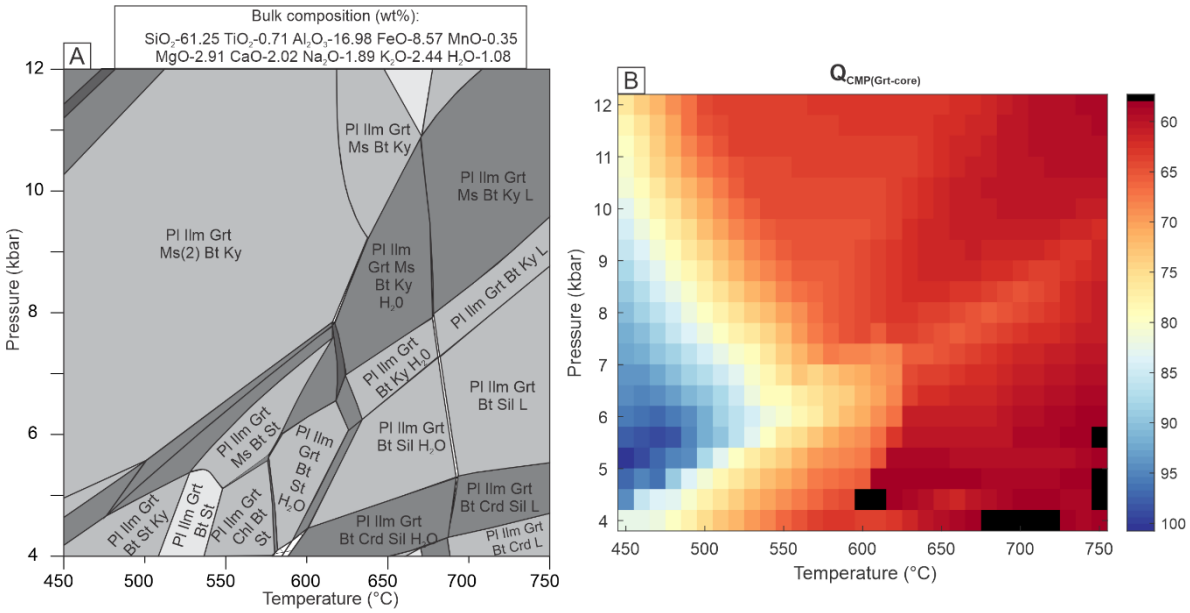

Figure B5- a) P-T isochemical phase diagram in the MnNCKFMASHT system for the Andrelândia Nappe (NESG-401) for the LBC including garnet core composition; b) Map of quality factor Q_{cmp} by Antidote for AN garnet core composition.

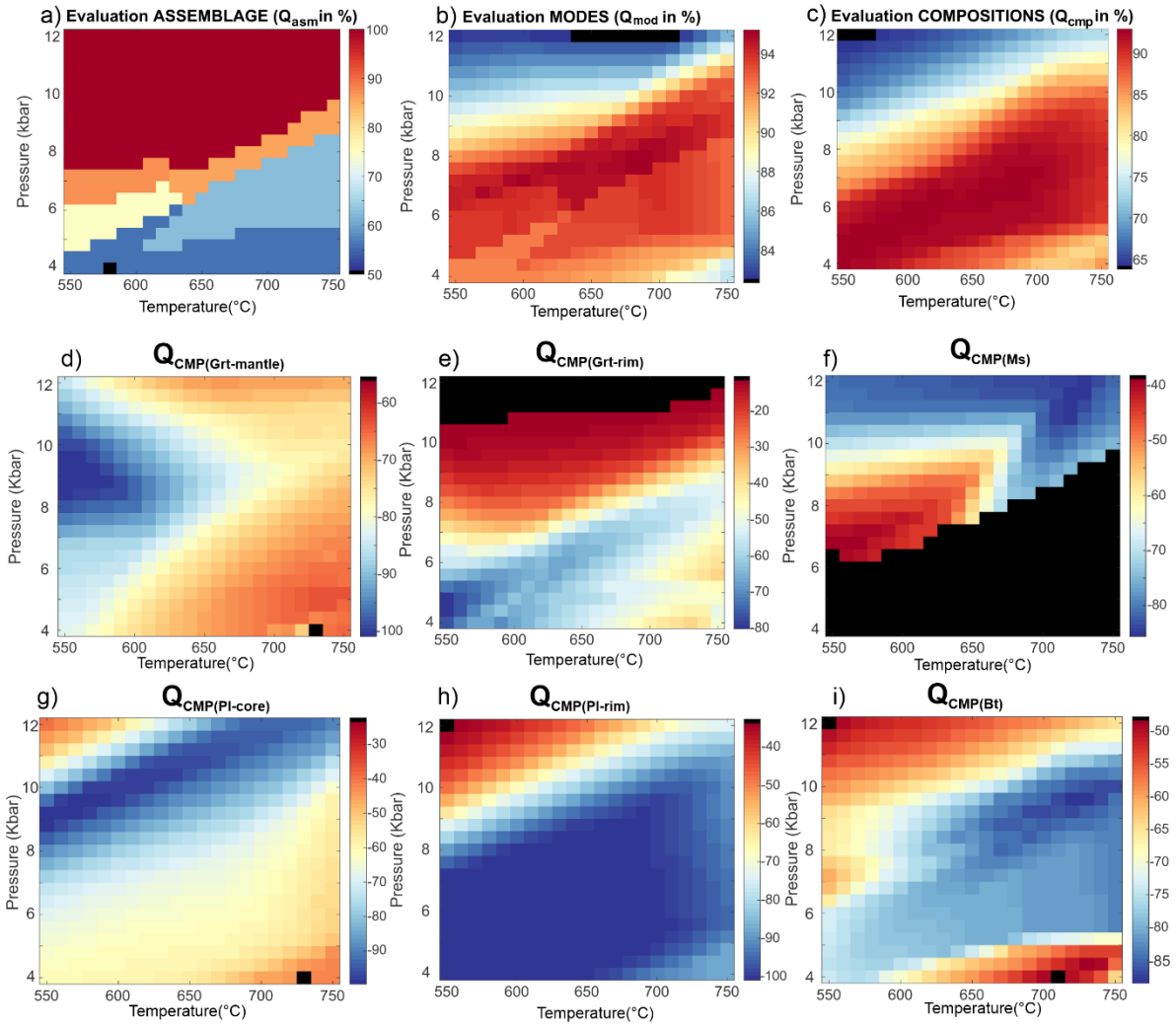

Figure B6- Maps of quality factors by Antidote for Andrelândia Nappe. a) Q_{asm}; b)Q_{mod}; c) Q_{cmp} for the LBC bulk composition; d) Q_{cmp} for garnet mantle composition; e) Q_{cmp} for garnet rim composition; f) Q_{cmp} for white mica composition; g) Q_{cmp} for plagioclase core composition; h) Q_{cmp} for plagioclase rim composition; i) Q_{cmp} for biotite composition.

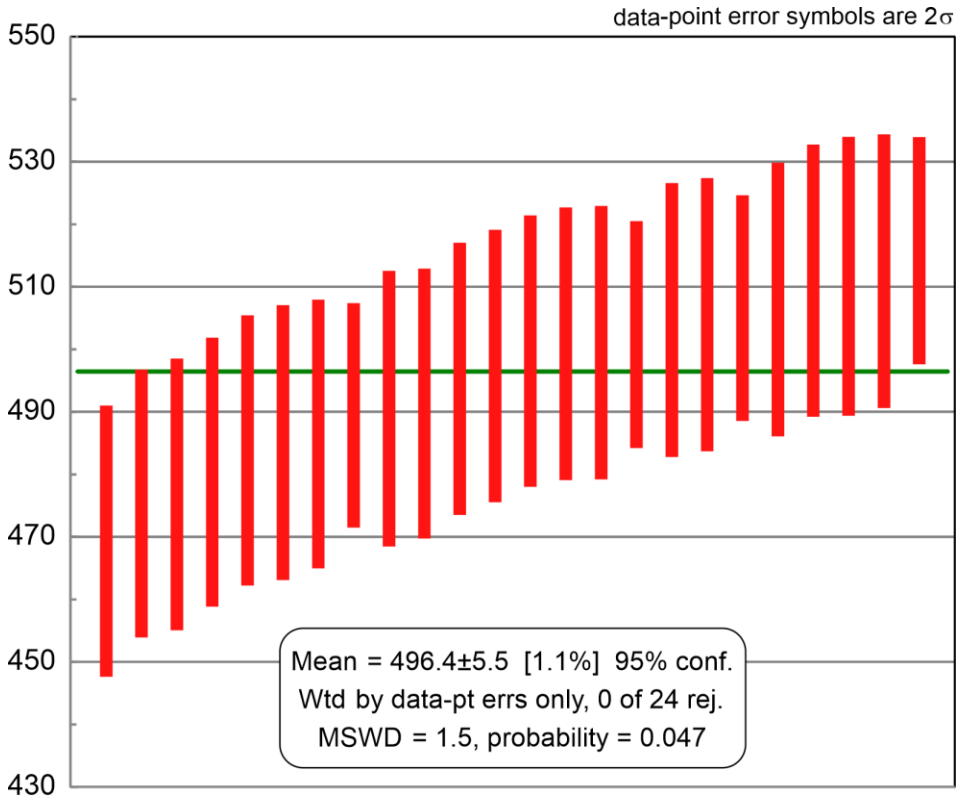

Figure B7 – Weight mean plot for Moacyr monazite standard.

APPENDIX C

Supplementary material of Chapter 5

ANALYTICAL METHODS

1. Imaging, mineral chemistry, and quantitative compositional mapping

A full-thin section map was acquired using the Scanning Electron Microscopy and Mineral Liberation Analyzer (SEM-MLA; Fig. 36b). In addition, an area of the thin-section, used to calculate the local bulk composition (LBC; Fig. 36b) was selected for performing X-ray maps (Mg, Na, Ca, K, Fe, Al, Si, P, S, Ti, Mn, and Zr) with helping of an electron probe micro-analyzer (EMPA). The EMPA equipment utilized is a JEOL JXA-8230 equipped with five wavelengths dispersive spectrometry (WDS) detectors at the Geology Department of UNESP. The x-rays maps were calibrated with punctual analysis and converted into oxide weight percentage maps applying internal standards (Andrade et al., 2006) in the software XMapTools 3.4 (Lanari et al., 2014, 2019; Fig. 37).

2. Inverse and forward thermodynamic modeling

The inverse thermodynamic modeling (or multi-equilibrium *P-T* calculation) uses an internally consistent thermodynamic database to calculate an independent set of reactions between the end-members phases of a particular assemblage. The *P-T* condition was constrained using the THERMOCALC software version 3.50 and the thermodynamic dataset ds62 (Holland & Powell, 2011). Once the sample PA-16 underwent partial melting, and most of these reactions are temperature dependent, the average*T* mode was used in the calculation. The punctual analysis of minerals composition from garnet mantle, biotite with the highest Ti (a.p.f.u), and K-feldspar with highest $X_{Mic,}$ were used for the calculations. Those compositions were chosen taking into account textural and chemical criteria, and likely they may represent the closest approximation of metamorphic peak equilibrium. The calculation was performed considering the H_2O as a pure fluid composition (a_{H2O}=1).

The forward thermodynamic modeling (or phase equilibrium modeling) was applied for building isochemical diagrams using the THERIAK-DOMINO software, version 11.03.2020 (de Capitani & Brown, 1987; de Capitani & Petrakakis, 2010). The isochemical diagram was calculated in the system NCKFMASHT. The Mn and Fe^{+3} were not considered, respectively due to the small amount in the sample (Mn<0.1) and a lack of Fe^{3+} rich oxides and the rutile is a stable phase in the system. The first isochemical diagram was built using the bulk composition obtained by integrating the density-corrected maps (LBC) through the software XMapTools subtracting the garnet core composition. A T-M_{H2O} pseudosection was built, at pressure conditions of 16 kbar, in order to assess the modeled assemblage sensitivity to the used H_2O contents (Figure C1). Hence, the H_2O content was fixed at 0.1 (wt%) owing to the sample anhydrous feature. The second isochemical diagram was built using the single-step melt-reintegration approach and adding the garnet core composition subtracted in the

previous one. The melt composition at the peak was reintegrated into the bulk composition until the appearance of the H_2O-saturated solidus.

3. Trace element thermometry – Zr-in-Rutile and Ti-in-quartz

The trace elements analysis from sample PA-16 were carried out in the same EPMA equipment used for performing the X-ray maps and silicates punctual analysis. For the Zr-in-rutile thermometer, the following elements were analyzed: Si, Al, Cr, Nb, Ta, Fe, Zr and Ti, using 20 kV of accelerating voltage and a current of 80 nA. The methodology used followed the routine described by Luvizotto et al. (2009). The rutile crystals are presented in the matrix, as well as enclosed in garnet, and vary from micro- to millimetric in size (Figure C3). In some crystals are observed ilmenite in the rutile rims or forming lamellae. Small zircons close to the rutile rim were observed in two of the analyzed rutiles. The Zr content range from 487 to 1579 ppm (n=26), and the values above the 90^{th} percentile are above 1485 ppm. Due to the pressure dependence of the calibration, results are shown in the *P-T* diagram Fig. 38d (isopleths for the 90^{th} percentile) using the Kohn (2020) equation.

For the Ti-in-quartz thermometry, firstly a cathodoluminescence map was acquired in order to identify the quartz spectra intensity changes and guide the further spot analysis position (Figure C4). The punctual analysis were performed using 15kV voltage and 200nA beam current, and the detailed methodology is described in Fumes et al.(2021). The Cl map shows a homogeneous intensity for the quartz crystals, pointing out that they were completely recrystallized (Figure C4). The Ti content in quartz range from 34 to 59 ppm (n=16). The *P-T* compositional stability field of the Ti-in-quartz above the 90^{th} percentile is displayed in Fig. 38d using the calibration of Thomas et al. (2010).

4. U-(Th)-Pb monazite geochronology

The monazite crystals were first identified during the full thin-section mapping described in section 1. Further, based on microstructural position and textural relationships, some crystals were selected to perform high-resolution compositional X-ray maps of Y, Al, Th, U, Pb, Si, Ca, Fe, La, and Ce, in order to identify different chemical domains. The acquisition conditions were 15 kV, 100 nA, 100ms dwell time and 10µm electron beam size and step. Isotopic *in situ* analyses of trace elements and U-(Th)-Pb were performed using a laser-ablation, inductively coupled, plasma mass spectrometry (LA-ICP-Ms) at CNR-Istituto di Geoscienze e Georisorse U.O. Pavia (Italy). The equipment used was Ar-F 193-nm excimer (Geolas 102 from Microlas) coupled with 8900 triple quadrupole ICP-MS (Agilent). The spot size for U-(Th)-Pb and trace analyses were respectively, 10µm and 25 µm. The Moacyr monazite and NIST-612 standard materials were used for the U-(Pb)-Th and trace elements analyses. The software GLITTER ® was used for data reduction. The data treatment was done with IsoplotR (Vermeesch, 2018). Uncertainties of the corrected $^{207}Pb/^{206}Pb$ and $^{238}U/^{206}Pb$ ratios are quoted at the 2σ.

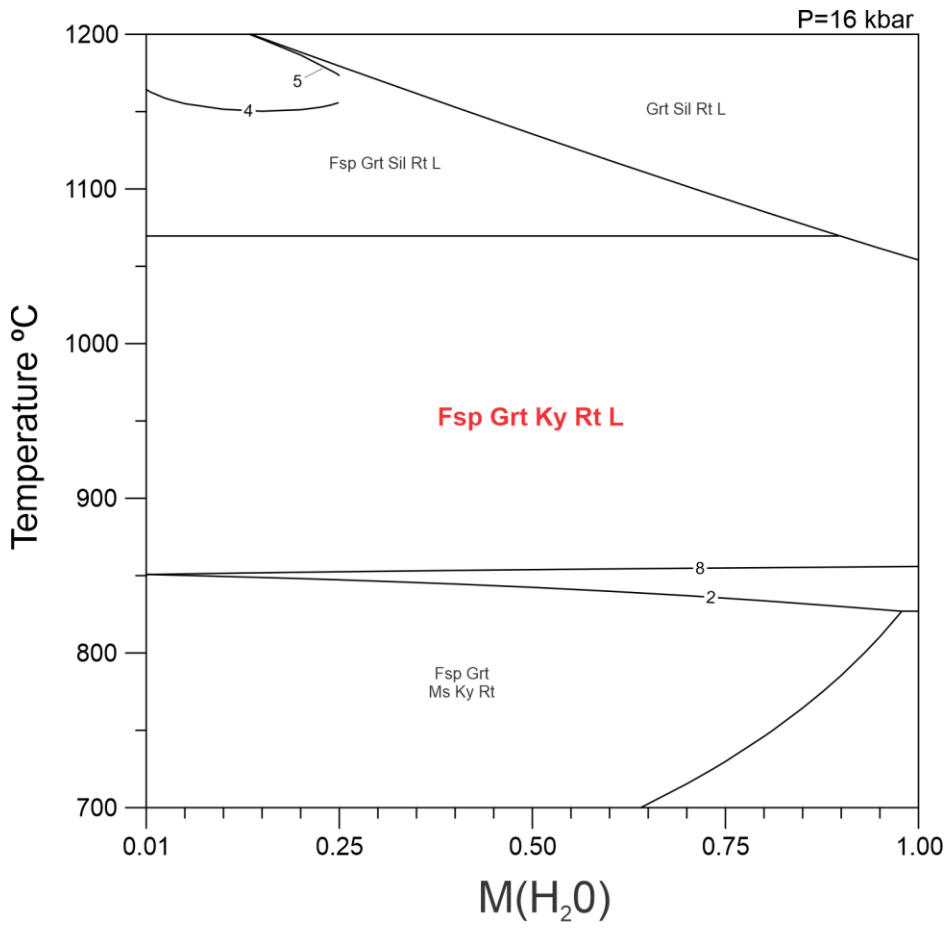

Figure C1- T-M_{H2O} pseudosection for the sample PA-16 at 16 kbar.

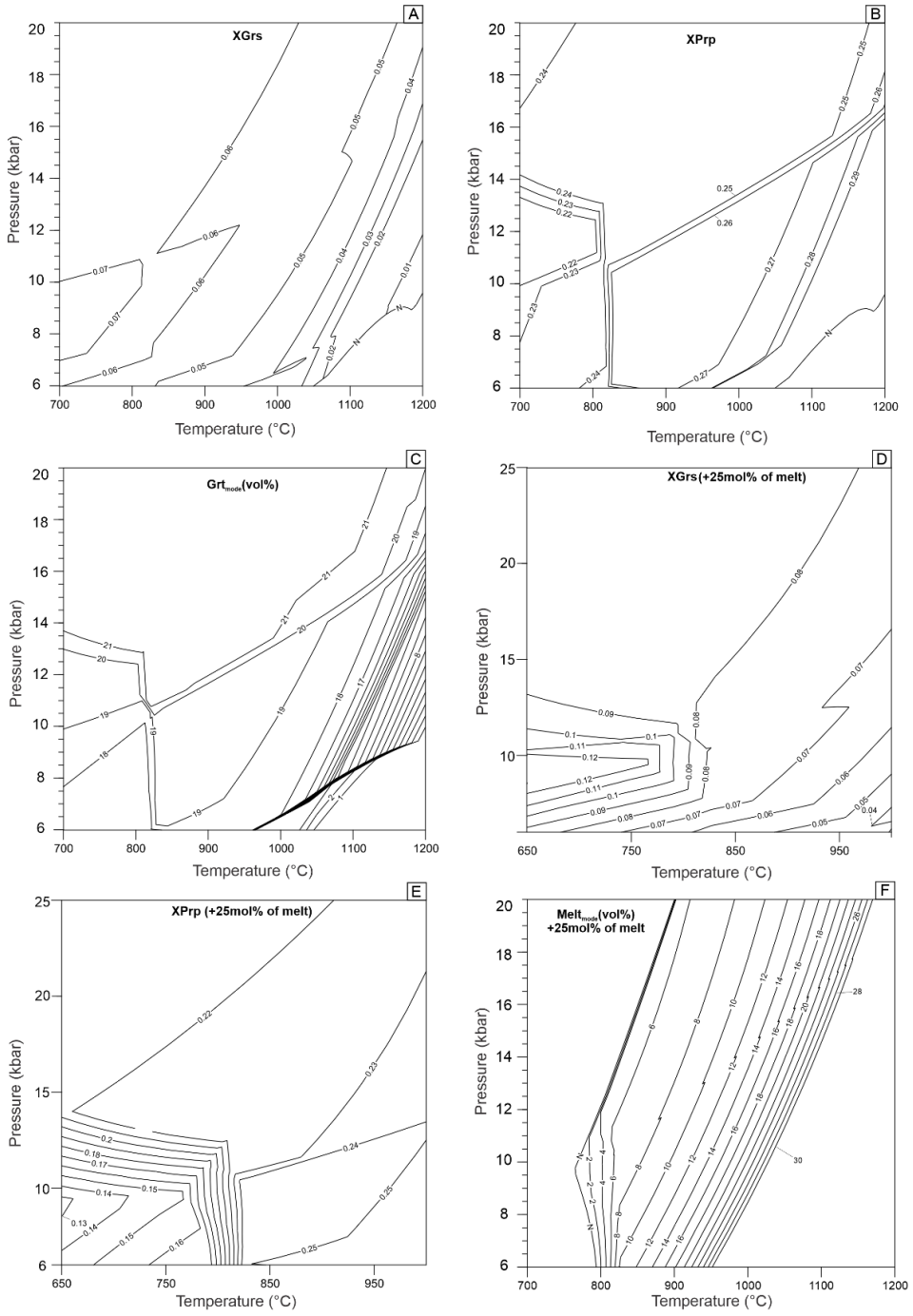

Figure C2- Compositional isopleths for the Pouso Alto granulite (PA-16). a) to c)- Isopleths corresponding to isochemical diagram displayed in Fig.5a, and d) to f) correspond to isochemical diagram of Fig.5c; a) XGrs compositional isopleths calculated for Local Bulk composition (LBC) after removing the garnet core; b) XPrp compositional isopleths calculated for LBC after removing the garnet core; c) Garnet mode (vol%) curves calculated for LBC after removing the garnet core; d) XGrs compositional isopleths calculated using a bulk reintegrated composition (+25mol% of melt and garnet core); e) XPrp compositional isopleths calculated using a bulk reintegrated composition; f) Melt mode (vol%) curves calculated using a bulk reintegrated composition.

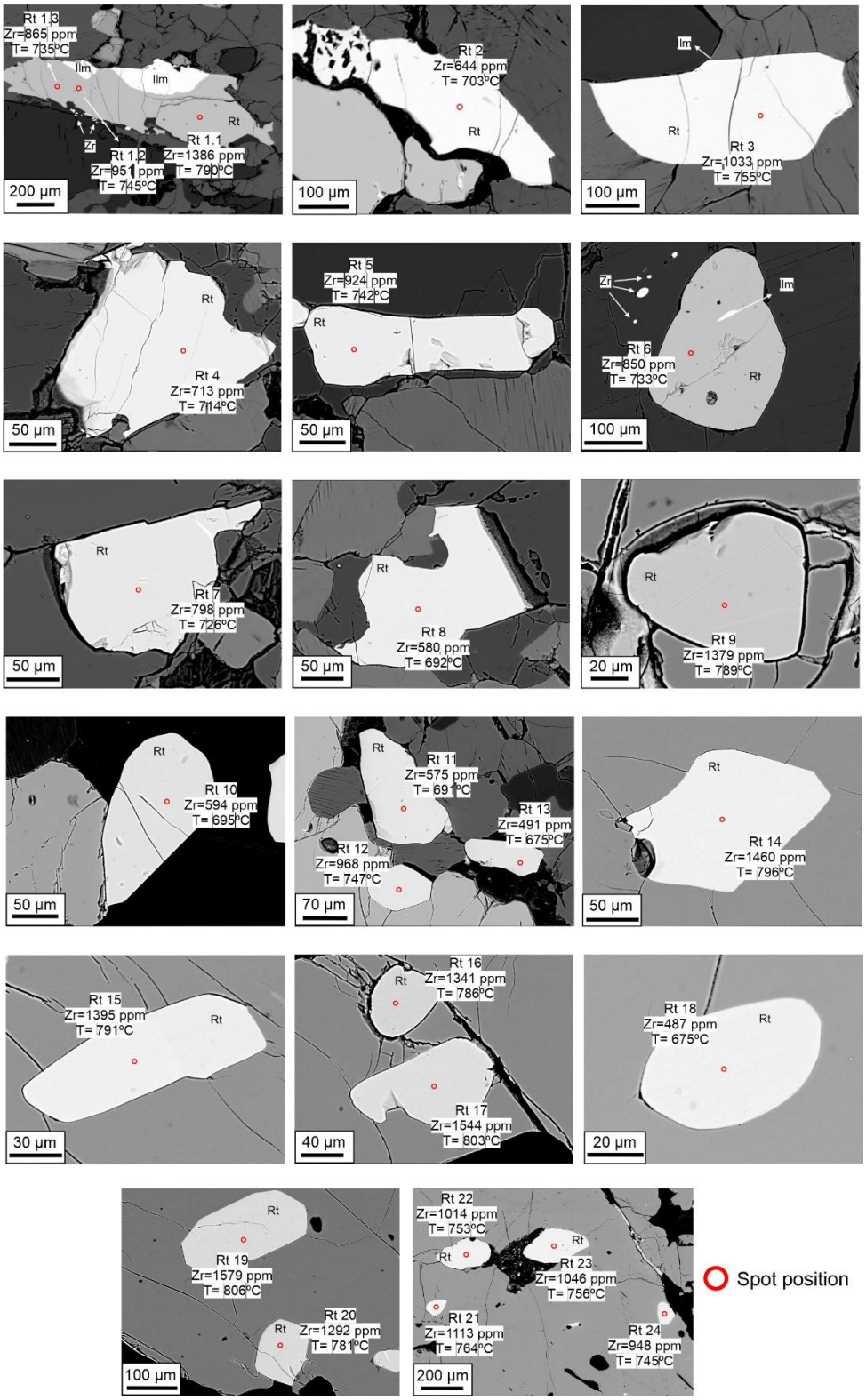

Figure C3- BSE images of analyzed rutiles for Zr-in-rutile thermometry. Temperatures were calculated using Kohn (2020) calibration at 10 kbar.

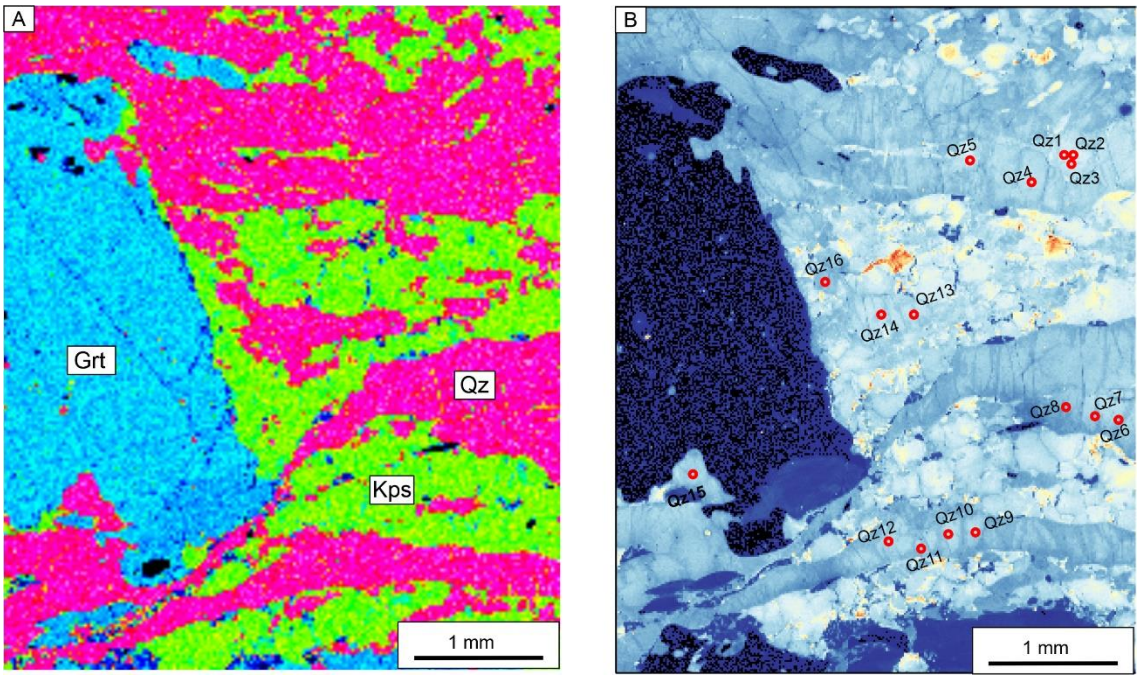

Figure C4- a) X-ray map for Si of the area investigated for Ti-in-quartz thermometry; c) Cathodoluminescence (CL) map of the area investigated for Ti-in-quartz thermometry and spots position.